



Magnetic Resonance Imaging Clinics

[Register](#) or Login:

Password:

 Auto-Login [[Reminder](#)]

Search _____ for _____

[Advanced Search](#) - [MEDLINE](#) - [My Recent Searches](#) - [My Saved Searches](#) - [Search Tips](#)
[CLINIC HOME](#)
[CURRENT ISSUE](#)
[PREVIOUS ISSUES](#)
[SEARCH THIS CLINIC](#)
[FORTHCOMING ISSUES](#)

CLINIC INFORMATION

- [Consulting Editor](#)
- [Author Information](#)
- [Abstracting/Indexing](#)
- [Contact Information](#)
- [Media Information](#)
- [Permissions](#)
- [Buy Back Issues](#)

[RELATED SITES](#)
More periodicals:
[FIND A PERIODICAL](#)
[FIND A PORTAL](#)
[GO TO PRODUCT CATALOG](#)

Issue

 Alert me when new journal issues are available. [Add TOC Alert](#)
November 2003 (Vol. 11, Issue 4)

[← previous issue](#)

MR Neuroimaging: Current and Newer Techniques II

Guest Editor: M. Castillo

[View Selected](#)

[Abstracts](#)

Display:

Table of contents

pages v-vii
[PDF \(26 KB\)](#)

Forthcoming issues

page viii
[PDF \(21 KB\)](#)

Preface

MR neuroimaging: current and newer techniques II

by Castillo M

page xi
[Full Text](#) | [PDF \(40 KB\)](#)

Review article

Functional MR imaging: paradigms for clinical preoperative mapping

by Moritz C, Haughton V

pages 529-542
[Full Text](#) | [PDF \(788 KB\)](#)

Review article

MR myelography of the spine and MR peripheral nerve imaging

by Stone JA

pages 543-558
[Full Text](#) | [PDF \(823 KB\)](#)

Review article

MR angiography of the spine: update

by Bowen BC, Saraf-Lavi E, Pattany PM

pages 559-584
[Full Text](#) | [PDF \(1363 KB\)](#)

Review article

MR angiography of the extracranial circulation

by Jewells V, Castillo M

pages 585-597
[Full Text](#) | [PDF \(395 KB\)](#)

Review article

Contrast-enhanced MR angiography of the intracranial circulation

by Sohn CH, Sevick RJ, Frayne R

pages 599-614
[Full Text](#) | [PDF \(741 KB\)](#)

Review article

Practical consideration for 3T imaging

by Lin W, An H, Chen Y, Nicholas P, Zhai G, Gerig G, Gilmore J, Bullitt E

pages 615-639

[Full Text](#) | [PDF \(1322 KB\)](#)

Review article

MR microscopy of normal human brain

by Fatterpekar GM, Delman BN, Boonn WW, Gultekin S H, Fayad ZA, Hoff PR, Naidich TP

pages 641-653

[Full Text](#) | [PDF \(937 KB\)](#)

Cumulative index

pages 655-671

[PDF \(115 KB\)](#)

[View Selected](#)



[Abstracts](#)

Display:

CONTENTS

Preface	xi
Mauricio Castillo	

Functional MR Imaging: Paradigms for Clinical Preoperative Mapping	529
Chad Moritz and Victor Haughton	

Clinical applications of functional MR imaging include mapping of brain functions in relationship to intracranial tumors, seizure foci, or vascular malformations to determine the risk for performing surgical excision, the need for intraoperative mapping during excision, and selecting the optimal surgical approach to a lesion. A variety of paradigms are used to produce a blood-oxygen-level-dependent response in various brain regions, which can be identified with functional MR imaging. The paradigms used include active motor, language, or cognitive tasks, and passive tactile, auditory, or visual stimuli. Activation usually indicates the location of eloquent cortex. Lack of function in a region cannot be assumed when functional MR imaging shows absence of activation within the region.

MR Myelography of the Spine and MR Peripheral Nerve Imaging	543
Jeffrey A. Stone	

MR myelography is a useful tool to evaluate compression of spinal nerves and may also be used for evaluation of other spinal pathology. Current echo-planar imaging techniques allow for rapid myelographic MR imaging to be easily added to routine spine imaging sequences without significant additional time constraints. MR peripheral nerve imaging is another useful but underused tool for evaluating patients with peripheral nerve symptoms, particularly when routine spinal axis imaging fails to demonstrate an abnormality. This article reviews the current technique and application of both MR myelography and MR peripheral nerve imaging.

MR Angiography of the Spine: Update	559
Brian C. Bowen, Efrat Saraf-Lavi, and Pradip M. Pattany	

Spinal MR angiography is usually implemented as a three-dimensional (3D) contrast-enhanced gradient-echo technique, with older "standard" 3D contrast-enhanced MR angiography, requiring 5 to 10 minutes per 3D volume, and newer "fast" (bolus/dynamic) 3D contrast-enhanced MR angiography, requiring tens of seconds per 3D volume, depending on k-space sampling schemes. Normal intradural vessels detected on standard

contrast-enhanced MR angiography are primarily veins (medullary and median), whereas arteries and veins are detected on fast contrast-enhanced MR angiography. With standard MR angiography added to a conventional MR imaging study, the correct level of dural arteriovenous fistula plus or minus one vertebral segment was identified in 73% of true positive patients—a significant increase compared with MR imaging alone. Preliminary results indicate that the fast technique may further improve characterization of normal and abnormal intradural vessels.

MR Angiography of the Extracranial Circulation

585

Valerie Jewells and Mauricio Castillo

In this article, the authors present a brief history of MR angiography (MRA) of the neck with emphasis on the techniques developed, particularly recent ones, to improve image quality. The goal of MRA is to eventually replace catheter angiography. The use of MRA, particularly contrast enhanced MRA with regards to pathology (atherosclerotic disease/plaque formation, dissection and post-traumatic aneurysm) involving the extra-cranial carotid and vertebral arteries is addressed. The authors also comment on computed tomographic angiography and sonography and how they compare with contrast enhanced MRA when pertinent.

Contrast-enhanced MR Angiography of the Intracranial Circulation

599

Chul-Ho Sohn, Robert J Sevick, and Richard Frayne

Syllabus time-of-flight (TOF) and phase-contrast (PC) MR angiographic (MRA) techniques have been used to study the intracranial circulation since the late 1980s. Both TOF and PC MRA are completely non-invasive relying on naturally occurring mechanisms to generate blood-to-background image contrast. Both techniques, however, suffer from several deleterious effects, most notably signal loss in regions with slow or disturbed flow. The injection of MR contrast agents containing the paramagnetic ion gadolinium has been shown to reduce this signal loss. In this article the authors summarize the use of contrast-enhanced MRA (CE MRA) in imaging the intracranial circulation, including the use of post-contrast TOF, dynamic CE MRA and time-resolved CE MRA techniques to study acute ischemic stroke, aneurysms, and vascular malformations.

Practical Consideration for 3T Imaging

615

Weili Lin, Hongyu An, Yasheng Chen, Peter Nicholas, GuiHua Zhai, Guido Gerig, John Gilmore, and Elizabeth Bullitt

In the past 10 to 15 years, 1.5T has been one of the most commonly used field strengths for day-to-day clinical operations. However, recent advances in high field technology and the increased availability of high field (>1.5T) human scanners have opened the doors for a variety of exciting improvements in clinical and research applications of MR imaging. In particular, 3T has continued to gain wide acceptance as one of the main field strengths for clinical and research studies. Therefore, in this article the authors focus on the pros and cons of 3T imaging and comparisons between results obtained at 3T and 1.5T.

MR Microscopy of Normal Human Brain

641

Girish M. Fatterpekar, Bradley N. Delman, William W. Boonn, Humayun S. Gultekin, Zahi A. Fayad, Patrick R. Hoff, and Thomas P. Naidich

MR microscopy at 9.4T depicts the architecture of the brain in exquisite detail, including the individual laminae of the cortex, the individual nuclei of the basal ganglia, the

thalami, subthalami and metathalami, and the orientations and relationship among the dominant nuclei and white matter tracts of the brain. The authors believe that these anatomic relations will ultimately be displayed in vivo as clinical MR scanners begin to operate at field strengths of 4.7T, 7T, and 8T. Then, those familiar with this anatomy will be able to interpret patient images with far greater sophistication.

FORTHCOMING ISSUES

February 2004

Shoulder MR Imaging

Marco Zanetti, MD, and
Juerg Hodler, MD, *Guest Editors*

May 2004

MR Imaging of the Upper Extremity

Javier Beltran, MD, *Guest Editor*

RECENT ISSUES

August 2003

**MR Neuroimaging: Current and
Newer Techniques I**

Mauricio Castillo, MD, *Guest Editor*

May 2003

MR Imaging of Sports-Related Injuries

Lynne S. Steinbach, MD, *Guest Editor*

February 2003

Cardiac MR Imaging

Pamela K. Woodard, MD, *Guest Editor*

THE CLINICS ARE NOW AVAILABLE ONLINE!

Access your subscription at:
www.TheClinics.com



Preface

MR neuroimaging: current and newer techniques II



Mauricio Castillo, MD
Guest Editor

“The only constant is change.”

—Buddha

“We cannot understand the possibilities that we choose to ignore.”

—The Oracle to Neo in *The Matrix Reloaded*

In 1998, I edited an issue of the *Magnetic Resonance Imaging Clinics of North America* entitled “New Techniques in MR Neuroimaging.” That issue covered topics varying from MR spectroscopy to diffusion-weighted imaging to MR neurography. It turns out that it was a very popular one! In the 5 years since that issue, MR imaging has advanced, and thus the editors of the *Clinics* and I thought that it would be a good idea to bring our readers up-to-date by reviewing the changes that have happened since then. As such, I have asked some of the same authors to update their previous articles and have asked other authors to contribute with different articles. The authors range from well-established academicians to younger and extremely bright individuals. It certainly has been a pleasure to work with them all, and I thank them for their efforts.

The need to cover many topics resulted in the publication of two separate issues of the *Clinics*

on MR neuroimaging. In the first part, the readers will find articles that focus on techniques (perfusion, diffusion, and so forth) and specific areas (head and neck and pediatrics). The second part includes articles on functional and spinal imaging, MR angiography, and imaging at higher field strengths.

A few months ago, I met one of our residency professors (who despite being well into his retirement years continues to work). He told me that he was “still young enough to be amazed by the changes in radiology and liked to keep current with them.” I believe that his attitude reflects that of many radiologists and that this attitude is what makes our specialty a healthy and challenging one. I hope that readers find these articles to be entertaining, informative, helpful, and, why not... amazing!

Mauricio Castillo, MD
Department of Radiology
University of North Carolina at Chapel Hill
3326 Old Infirmary Building, CB 7510
Chapel Hill, NC 27599-7510, USA
E-mail address: castillo@med.unc.edu



Functional MR imaging: paradigms for clinical preoperative mapping

Chad Moritz, Victor Haughton, MD*

Department of Radiology, University Hospitals and Clinics, University of Wisconsin, 600 Highland Avenue, E3/311 CSC, Madison, WI 53792, USA

Over the last decade, functional MR (fMR) imaging has progressed from a research tool for noninvasively studying brain function to an established technique for evaluating a variety of clinical disorders through the use of motor, sensory, and cognitive activation paradigms. Although positron emission tomography (PET), and, more recently, magnetoencephalography (MEG), also have provided opportunities to assess brain function noninvasively, the combined spatial and temporal resolution of fMR imaging, the wider availability of MR imaging scanners, and the broad range of available activation paradigms confer distinct advantages over these alternative approaches to functional neuroimaging.

fMR imaging uses blood-oxygen-level-dependent (BOLD) [1] effects to localize regional cerebral blood flow changes temporally and spatially coupled with changes in neuronal activity. When groups of neurons are active, the blood flow to the active neurons increases in excess of what is needed to provide the additional oxygen consumed metabolically. The net result of increased neuronal activity is a decrease in paramagnetic deoxygenated hemoglobin in the veins and capillaries within the vicinity of the active neurons. The amount of change depends on many factors including the nature of the task and the region of brain affected. The decrease in deoxy-hemoglobin produces a small change in signal intensity, which is typically less than 5% in T2*-weighted images acquired at 1.5 Tesla. These

slight changes in signal intensity (“activation”) are detected by post-processing statistical analysis techniques [2–4] that identify the task-related hemodynamic responses. The derived maps of spatially localized fMR imaging responses can then be color-coded to reflect the degree of statistical significance and overlaid on the subject’s own co-registered structural MR imaging anatomical images. Numerous post-processing procedures are involved in state-of-the-art fMR imaging analysis, and their detailed description is beyond the scope of this fMR imaging paradigm review.

One clinical application of fMR imaging is the mapping of brain functions in relationship to intracranial tumors, seizure foci, or vascular malformations before surgical excision. The goal of functional mapping procedures is to maximize resection of pathological tissue, spare eloquent cortices, and reduce surgical risk. Localizing eloquent cortex merely by means of the anatomic landmarks identified in structural MR images is inexact, because of the frequent anatomic variations in the brain and to displacement of normal landmarks when a mass lesion is present. Pre-surgical fMR imaging can provide accurate mapping of functional brain responses to various stimuli or tasks, even close to lesions [5,6]. These fMR imaging maps also can be used to aid in the planning of a surgical approach, shorten the operative procedure by obviating intraoperative awake mapping, and help determine whether operative or non-operative treatment would be optimal for the patient. The whole-brain volumetric capability of fMR imaging allows functional mapping beyond the limits of the exposed cortical surface available for intra-operative mapping.

* Corresponding author.

E-mail address: Vhaughton@mail.radiology.wisc.edu (V. Haughton).

Published studies have verified the accuracy of fMR imaging presurgical mapping compared with intraoperative electrocortical stimulation [7–10].

A variety of paradigms are used to produce pre-surgical BOLD response in various brain regions. The paradigms used include active motor, language, or cognitive tasks, and passive tasks using tactile, auditory, or visual stimuli. “Eloquent” regions in which activation can be demonstrated include the sensory and motor cortices, supplementary and pre-supplementary motor areas, basal ganglia, primary and association visual cortices, primary and association auditory cortices, Wernicke’s area, Broca’s area, and executive areas of the brain. The intent of this overview is to describe clinically proven clinical fMR imaging paradigms.

A routine clinical fMR imaging session typically includes three to six different paradigms, with each paradigm chosen to activate a cortical region anatomically related to the lesion or jeopardized by the treatment, either by surgery or ionizing radiation. For example, a patient with a lesion in the vicinity of left precentral gyrus could perform one or two sensorimotor fMR imaging paradigms to localize the sensorimotor homunculus and supplementary motor area. The same patient could also perform one or two language paradigms to identify fMR imaging responses for Broca’s area, Wernicke’s area, and pre-supplementary motor area (SMA). Thus, the optimal clinical fMR imaging program requires a “menu” of different paradigms, from which a selection is made that is appropriate to each patient’s mapping requirements.

Usually the paradigms for clinical preoperative fMR imaging mapping are designed as “blocks” rather than “events” or “single-trial”. The primary interest of presurgical fMR imaging is the localization of functional response, and block paradigms yield a greater detection power than event-related paradigms [11,12]. The duration for each fMR imaging scan is a compromise between the need to acquire sufficient data for reliable statistical mapping and to limit the time a patient spends inside the magnet. A task design which includes 4 to 10 blocks of stimulus condition, each with 4 to 12 image acquisitions per block, interleaved with similar length blocks of rest or control condition, should provide adequate data for demonstrating fMR imaging localization. Such a task design can be achieved within a total scan duration of three to five minutes. A combination of high-resolution structural MR imaging

images and several fMR imaging paradigms can be obtained within an hour or less of scanning time.

Paradigms for clinical use must be designed so that even patients with neurologic impairments are able to perform the task. Tasks that are too difficult or complicated result in poor patient compliance and suboptimal activation [13]. During the fMR imaging acquisition, patient task performance can be monitored visually (for motor tasks), or with button presses on an MR imaging compatible recording device (for language or cognitive tasks). However, the performance of some simple covert paradigms (such as silent word generation) cannot be monitored. For tasks that are not monitored, poor patient compliance might not be evident until the weak or absent activation is demonstrated in the processed images. Similarly, small amounts of head motion, that could compromise fMR image quality, may go undetected during the fMR imaging acquisition. Therefore, it is imperative that the patient is well coached before the scan session to help ensure their understanding and compliance with task directions, and careful attention must be given to measures for preventing head motion.

Motor paradigms

The network of primary cortical motor control is an important concern for fMR imaging assessment when regions of pre- and post-central gyri are at risk from surgical procedures on the brain. A variety of paradigms are available for the localization of fMR imaging motor task responses, including flexion or extension, supination or pronation, and joystick manipulation. The large finger or hand area of the sensorimotor homunculus yields a robust BOLD response during the performance of simple or complex finger tapping (thumb to finger opposition) [14]. Similarly, a foot or ankle or lip or tongue movement paradigm [15] can be used to map the corresponding region along the central sulcus. Typically, when such tasks are performed in a block paradigm, fMR imaging responses can be localized to the corresponding regions of contralateral primary sensorimotor cortex (Fig. 1), supplementary motor area, and ipsilateral superior cerebellum. fMR imaging responses in basal ganglia (Fig. 2) and thalamus may also be mapped with motor paradigms [16]. A complex opposition of each finger to the thumb yields a greater extent of response in primary

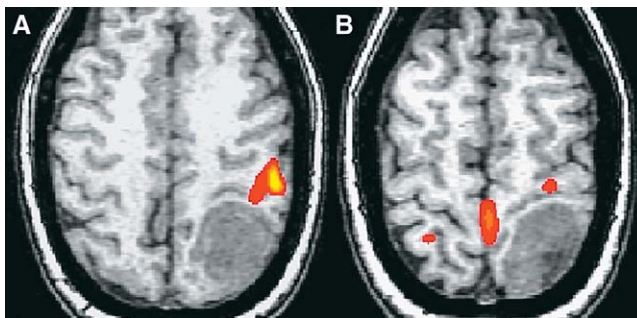


Fig. 1. fMRI responses during performance of a finger-tapping (A) and foot or ankle motor tasks (B) in a patient with a left parietal low grade glioma. The activation for the finger task is on the lateral convexity in the superior genu of the central sulcus. The activation for the foot task is near the interhemispheric fissure.

sensorimotor cortex than a simple thumb to index finger opposition. For patients with compromised motor ability that may have difficulty performing complex finger tapping, the simpler thumb to index finger opposition can be used. Generally, the more complex the finger motor task the greater the activation in the SMA [17].

Motor tasks of the upper or lower limbs may be performed unilaterally, bilaterally, or alternating right and left limbs. Alternating- or bilateral-limb motor task paradigms can demonstrate comparative fMR imaging responses between the affected hemisphere (in proximity to a lesion) and the unaffected hemisphere. Alternating-limb paradigms allow a separate comparison of the response from each limb, which can be useful to observe the functional relationship of sensorimotor cortex across hemispheres in the presence of tumor mass effects (Fig. 3). As with all fMR imaging procedures, care must be taken to assure that head motion does not occur during the performance of motor tasks, because even slight

amounts of task-correlated motion can cause confounding false-positives in statistical analysis. For sufficient BOLD contrast between the active and resting task conditions, the patient should be instructed to fully relax during the scan rest periods.

Tactile stimulation paradigms

As an alternative to motor tasks, the sensorimotor regions can be mapped with passive fMR imaging tactile stimulation paradigms [18]. Passive stimulus paradigms are useful in patients who are unable to perform a motor task, either because of age, disability, or the administration of anesthesia (Fig. 4). The BOLD response from tactile stimulation of the palm produces a fMR imaging localization similar to that produced by finger tapping [19], including contralateral primary sensorimotor cortex and supplementary motor area. Other regions, such as the lower limb or face, can also be mapped by means of a passive

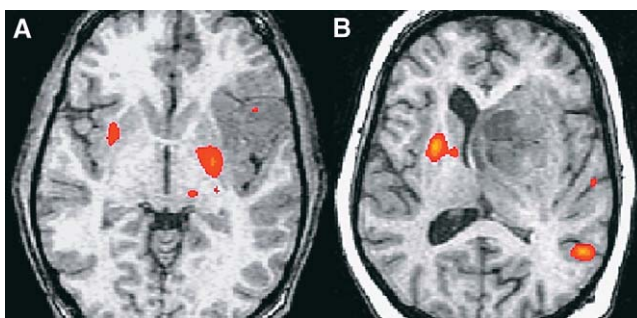


Fig. 2. Basal ganglia (putamen) fMRI responses during performance of a finger motor task shown in patients with a left frontal temporal tumor (A) and mesial left frontal gliomas (B).

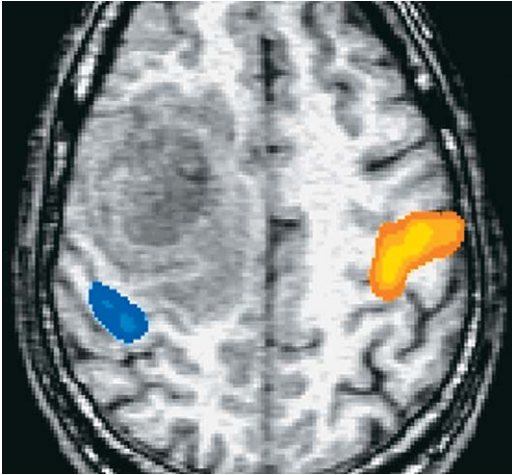


Fig. 3. fMRI responses during performance of an alternating-hand finger motor task in a patient with a right frontal tumor. Activation for the right hand movement is colored yellow or orange and left hand movement cyan or blue. Sensorimotor cortex is activated bilaterally.

tactile stimulus (Fig. 5). The source of the tactile stimulus can be as simple as the investigator's fingertips, a plastic toothbrush or wooden dowel, or as sophisticated as a MR imaging-compatible air-puff delivery system. Care should be taken that the stimulus mechanism does not cause task-

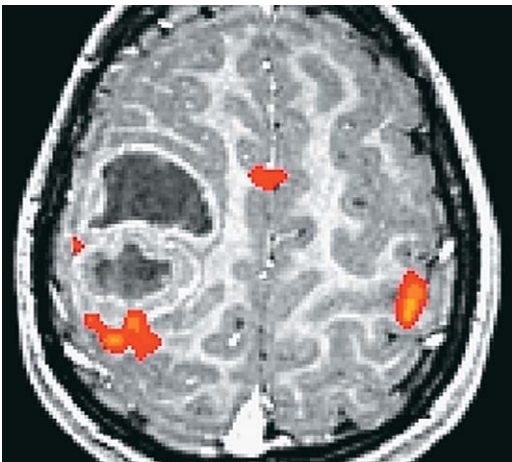


Fig. 4. fMRI responses during a bilateral palm tactile stimulus paradigm in a 3-year-old patient with a right frontal tumor. FMRI was performed with Propofol general anesthesia. Bilateral primary sensorimotor and SMA activation is demonstrated.

correlated artifacts, which are encountered even when the mechanism is outside the imaged volume [20]. Tactile stimulation paradigms provide a degree of flexibility to clinical fMR imaging applications, because impaired, unconscious, or even severely injured patients can be successfully mapped [21].

Auditory stimulation paradigms

MR imaging scanners can generate a great amount of ambient acoustic noise because of the rapid rate of gradient switching. Nevertheless, it is possible to map primary and association auditory cortices in patients with fMR imaging using headphones or combination earplugs or ear-phones to attenuate background scanner noise [22–24]. Stimuli such as pure tones, complex sounds, music, or speech can be used; different stimuli yield varying patterns of fMR imaging response. A simple paradigm that combines both auditory and receptive language stimulus can be accomplished by the auditory rendition of narrated text. An advantage of text listening is that the audible characteristics of the spoken word are sufficiently different from the background scanner noise, making it easier for the patient to discriminate the auditory stimulus compared with pure tones. When the patient is listening to text, fMR imaging responses in bilateral regions of lateral superior temporal gyri and transverse temporal gyri are demonstrated (Fig. 6). An auditory narrated text stimulus can also be expected to invoke receptive language responses, including Wernicke's area in posterior superior temporal or inferior parietal regions, and possibly Broca's area in inferior or middle frontal gyri.

To help ensure the patient's concentration on the narrated text, a magazine or book the patient would normally read or enjoy can be chosen as the source of the text. The choice of material is especially important in pediatric patients. Robust activation can be obtained in pediatric patients with appropriately chosen text, even when the patient is apparently asleep [25] or sedated. For fMR imaging in adult patients, a small collection of recorded text narrations is useful in the scanning area. When the auditory stimulus is conveyed to the patients by way of the MR imaging-compatible intercom system, the fit of the headphones or the earphones and earplugs should be checked carefully to ensure optimal delivery of sound and damping of ambient sound.

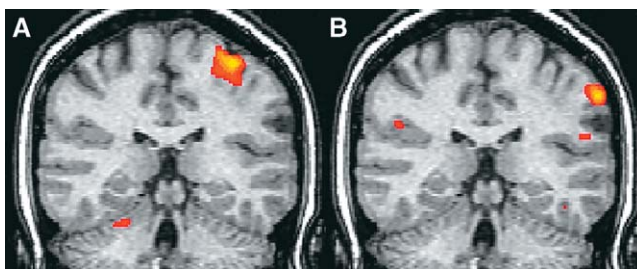


Fig. 5. fMRI responses during a finger motor task (A); and a face tactile paradigm (B) in a patient with a left frontal tumor. The activations conform to the expected locations along the sensorimotor strip.

Visual stimulation paradigms

Visual presentations of stimuli or paradigm cues offer many opportunities for fMR imaging application. Visual stimuli can be delivered to the patient by way of MR imaging-compatible video goggles, a video screen, or a combination of mirrors and a rear-projection screen. Primary and association visual cortex fMR imaging responses can be elucidated by presentation of a suitable stimulus, such as an 8 Hz reversing checkerboard pattern alternating in blocks with a fixation and gray background (Fig. 7) [26]. The response to this primary visual stimulus can identify regions of eloquent cortex in proximity to occipital lobe lesions, especially along the striate cortex and calcarine fissure.

Visual stimuli of a more complex nature, such as words, text, scenes or faces, can also evoke fMR imaging responses in dorsal and ventral visual association cortices. Visual stimuli are used in fMR imaging paradigms designed to map memory, language, and cognitive functions in the human brain. Examples of paradigms using

complex visual cues are illustrated under the headings of language and cognitive paradigms.

Language paradigms

Linguistic mapping often is a priority for fMR imaging presurgical referrals, because injury in a region with language function produces substantial clinical deficit and the location of language cortex may be difficult to predict. fMR imaging replaces the more invasive Wada test to determine the hemispheric dominance of language in many patients [27–30]. fMR imaging paradigms can produce not only an assessment of hemispheric dominance, but can also reveal the localization of intrahemispheric cortical foci for expressive and receptive language function. A variety of language paradigms have been used for preoperative fMR imaging, including word generation, [31,32] word comprehension [33], and rhyme discrimination [34,35]. Because of the complexity of language-related functions, it has been suggested that the performance of

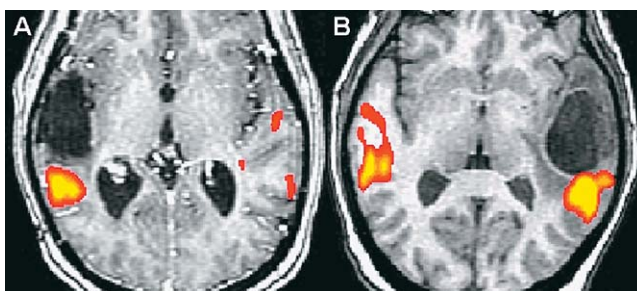


Fig. 6. Temporal lobe auditory responses during a text listening paradigm shown in a patient with a right temporo-parietal tumor (A); and a patient with a left fronto-temporal tumor (B). These activations are robust despite being in close proximity to the lesions.

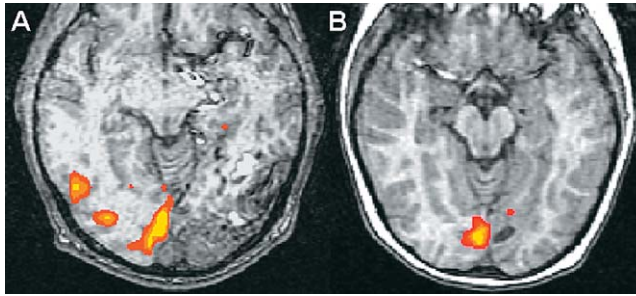


Fig. 7. fMRI responses from an 8 Hz reversing checkerboard visual stimulus paradigm in a patient with left occipital AVM (A) and a patient with left occipital lesion and epileptogenic focus (B). In (B) little functional visual cortex was evident in the left hemisphere. The child did not have a demonstrably greater visual deficit following surgery.

multiple and diverse fMR imaging paradigms can more fully represent the varied neuroanatomical responses of language function [36,37]. While a variety of paradigms can be used for language mapping, some of the simplest for patients to perform include word generation, text reading, and listening to narrated text. Word generation paradigms can be performed with a variety of cues, including: word-stem completion, verb generation from a given noun or picture, word generation from a given alphabet letter, word generation from a given category or antonym generation from a given word. Auditory or visual presentations can be used to provide task cues, alternating with blocks of rest or control condition. Visual presentation offers greater flexibility and avoids interference from acoustic noise generated by the scanner. To minimize lip, tongue, and head motion that occur during overt word production, the patient can be instructed to generate words from the provided cues covertly (silently).

Word generation paradigms produce a robust fMR imaging response in expressive language regions of lateral inferior and middle frontal gyrus in the language dominant hemisphere (Broca's area) (Fig. 8), and the medial superior frontal gyrus (pre-SMA) (see Fig. 10). Text reading paradigms can also produce fMR imaging response in Broca's area, but are especially useful for their sensitivity to receptive language regions of posterior superior temporal gyrus and inferior parietal lobe (Wernicke's area) (Fig. 9). Narrated text can invoke fMR imaging responses in Broca's and Wernicke's areas, but will also produce an auditory response in adjacent auditory cortices of superior temporal gyri. Since it is difficult to distinguish adjacent auditory and language regions of superior temporal gyrus, a contrasting control task such as backward text must be used in an auditory narrated text paradigm to isolate Wernicke's area response [38].

Expressive language paradigms, such as word generation tasks reliably produce a fMR imaging

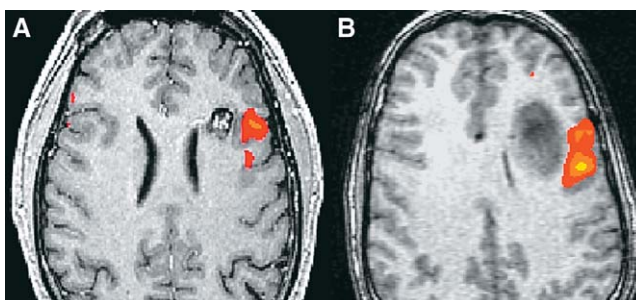


Fig. 8. fMRI responses during performance of word generation expressive language paradigms in (A) a patient with left frontal cavernous angioma; and (B) a patient with left frontal tumor. In both cases, the lesions have close proximity to language cortex. In the patient with the cavernous hemangiomas, surgery was not offered to the patient and in B tumor resection was tailored to minimize the risk for postoperative language deficit.

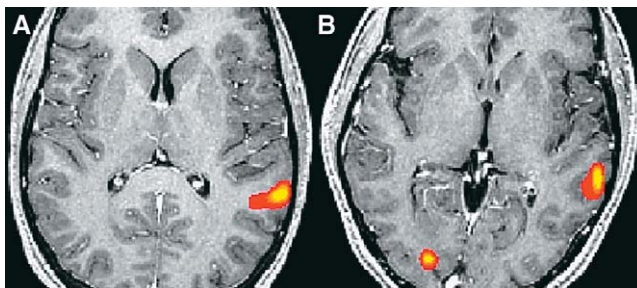


Fig. 9. (A, B) fMRI response to a text reading receptive language paradigm in two patients. Activation is evident in the left inferior parietal lobe. Both patients were studied before resection of cavernous hemangiomas, not shown in the images.

response in the medial superior frontal gyrus in addition to that in Broca's area. This response is typically situated slightly rostral to the site of the SMA activation during a motor task (Fig. 10). It is referred to as pre-SMA. Injury to the SMA or pre-SMA may produce a profound language deficit such as aphasia. Therefore mapping of the SMA is sometime requested in patients evaluated for resection of a frontal lobe tumor. Proximity of the SMA activation to the surgical target predicts a higher risk for postoperative neurologic deficits for motor or speech function [39].

Patient task performance can be a factor in successful language response mapping, especially if word generation tasks are performed covertly. Patient cooperation during a language task may be variable, so it is reasonable to have a patient perform at least two tasks for language mapping. Multiple language paradigms can be designed to evoke different language-related responses (eg,

expressive and receptive language). Confirmation and increased confidence of fMR imaging language mapping is attained when a concurrence of response localization occurs across multiple paradigms (Fig. 11).

Accurate results with language tasks require careful preparation of the tasks and instructions to the patient. At the authors' facility, the antonym word generation paradigm is commonly used with five blocks of single words presented visually on a screen (two seconds per word) alternating with blank screen fixation. The words are selected for this task to have a high degree of imageability. The patient is instructed to covertly generate an antonym for each word presentation. Similarly, single alphabet letters can be presented, with an instruction for the patient to covertly generate a word (or words), which begins with each letter. If during the instruction period before the fMR imaging the patient has difficulty generating words from a letter, the patient can

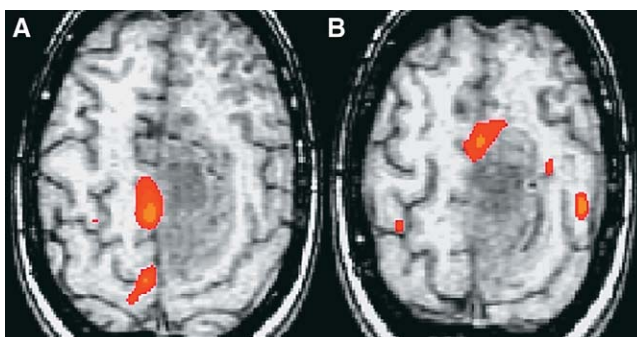


Fig. 10. Comparison of medial superior frontal gyrus fMRI responses during performance of (A) a foot movement motor task and (B) a word generation task in a patient with a left frontal meningioma. In (A) activation is evident in the right SMA and in (B) in the left pre-SMA. The meningioma likely distorts the superior frontal gyrus and displaces the activation. The patient has a risk for postoperative aphasia if the left SMA or pre-SMA is damaged.

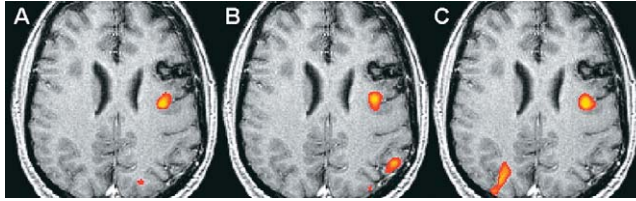


Fig. 11. fMRI responses for three different language paradigms in a patient with a left frontal lobe lesion. In (A) word generation from synonyms; in (B) word generation from a given alphabet letter; and in (C) text reading was performed by the patient. The frontal lobe activation has the same location in all three tasks, lending a high degree of confidence to this language region mapping.

be instructed to covertly generate the next letter of the alphabet in sequence. A simple text reading paradigm has also been successful, consisting of 10 blocks (eight seconds each) of a visually presented short descriptive paragraph alternating with blocks of incomprehensible letter strings, alternating with blocks of blank screen or fixation. The patient is instructed to observe the presentation during the entire scan and concentrate on reading and comprehending the blocks of descriptive text. Post-processing of this paradigm design can yield separate contrasts for text reading versus letter strings, or text reading versus rest. The text reading versus letter string contrast controls for the effects of the visual presentation, whereas text reading versus rest can yield a robust contrast for fMRI imaging mapping of visual processing and receptive language.

Cognitive paradigms

Beyond the capabilities of mapping sensory and language function, fMRI imaging has been applied extensively in neuropsychiatric applica-

tions to explore the neuroanatomic organization of cognitive processes. Clinically, cognitive fMRI imaging paradigms have been applied toward the assessment of patient populations including schizophrenia, dementia, autism, depression, and traumatic brain injury [40–42]. While most of these studies have examined population effects, some cognitive paradigms may be used to study individual patients referred for presurgical mapping. As stated in the introduction, a presurgical fMRI imaging program might include a “menu” of paradigm options, each of which can demonstrate responses in an expected pattern of regional functional activation. The advantage of various paradigms would be mapping multiple activation sites in proximity to a lesion, thus providing the neurosurgeon with an assessment of surrounding eloquent cortices. For example, a patient with a lesion in the right frontal lobe might perform one or two language paradigms to establish hemispheric dominance for language, a sensorimotor paradigm to localize central sulcus, and a cognitive paradigm that is expected to involve right prefrontal functionality.

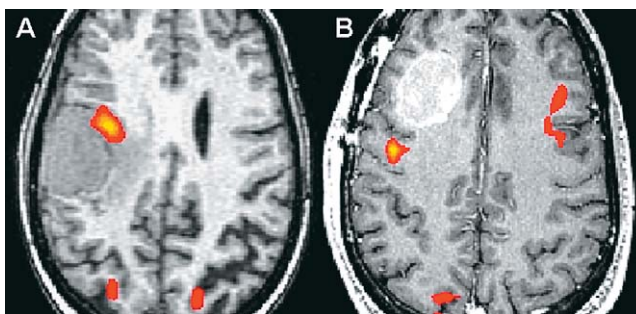


Fig. 12. fMRI responses to lesions during performance of a visual organization task in a patient with a right parietal meningioma (A); and a patient with a right frontal oligodendroglioma (B). The activation has close proximity to the lesion in the right frontal lobe. In (B), the location of the activation is displaced posteriorly from its normal location.

Two examples of cognitive paradigms for right frontal lobe involvement that are used at the author's facility are a visual organization task, and an arithmetic task. For the former, the Hooper Visual Organization Task [43], a commonly applied neuropsychiatric test of visual spatial ability, has been adapted to use in the MRI scanner [44]. Patients are visually presented with a line drawing depicting a simple object, which has been cut into 2 to 4 pieces and rearranged in a puzzle-like fashion, followed by a single word presentation. The patients are instructed to covertly name the fractured line drawing during each picture presentation, and then decide whether the word presentation matches the preceding picture. This task typically evokes fMR imaging responses in bilateral dorsolateral prefrontal lobes, bilateral superior parietal lobules, and visual association cortices (Fig. 12). In the arithmetic paradigm, a set of simple arithmetic equations and numeric answers are presented in each task block, and the patient is instructed to indicate whether the answer is correct for each presentation. This paradigm typically demonstrates a bilateral dorsolateral prefrontal lobe fMR imaging response (Fig. 13), and bilateral parietal lobes. These tasks may be useful for identifying right hemisphere eloquent cortices.

Memory function is another important concern for preoperative mapping, especially for patients with refractory epilepsy being considered for temporal lobectomy [45]. The broad category of memory function encompasses many aspects, several of which have been the focus of fMR imaging research: working memory [46] and long-term memory [47], semantic [48] and episodic memory [49], memory encoding and retrieval [50],

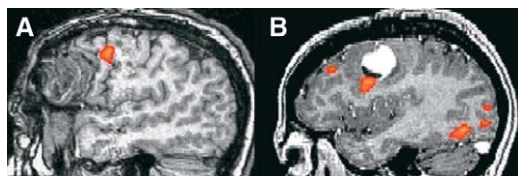


Fig. 13. Sagittal images illustrating right hemisphere fMRI responses during performance of an arithmetic computation paradigm in (A) a patient with a right frontal AVM and (B) a patient with a right frontal oligodendroglioma. Mapping was requested to determine the risk for postoperative deficit. Activation in both cases has close proximity to the lesion in the right frontal lobe. Resection was modified to avoid injury to the eloquent brain regions.

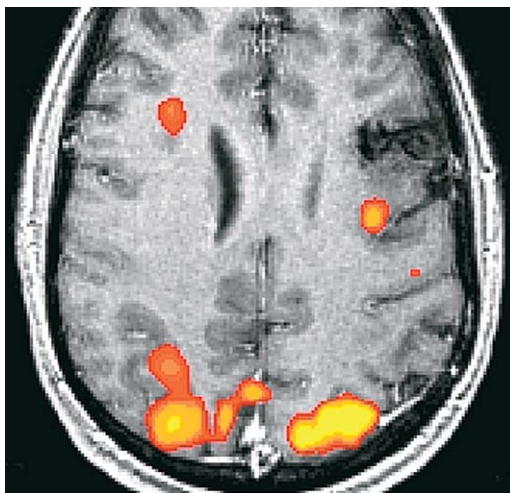


Fig. 14. fMRI responses during performance of a spatial working memory paradigm in a patient with a left frontal lesion and seizures (same patient as in Fig. 11). Bilateral frontal and superior parietal lobe activation is seen at this slice location, with the left frontal lobe response located just posterior to the lesion.

and recognition memory [51]. To date, many of these fMR imaging memory studies have reported population-level statistics, not the level of reliable individual mapping required for preoperative assessments. A potential confound for memory related paradigms is the associated non-memory specific responses for attentional load [52].

While paradigms for fMR imaging assessment of memory function continue to be investigated, some paradigms have been applied toward preoperative assessments of surgical candidates. A visual-spatial working memory paradigm has demonstrated a robust pattern of bilateral frontal and bilateral superior parietal responses (Fig. 14). This paradigm consists of visual presentation of seven blocks of an alphabet letter grid containing five letters, followed by six seconds of fixation on a blank screen with cross hairs, followed by presentation of a single letter. The patient is instructed to memorize the letters and their positions during the initial presentation, and then respond whether the single letter is a positional match. These blocks alternate with an easier task consisting of a single letter presentation followed six seconds later by another single letter presentation, with the same instruction for responding whether the single letters match. Activation, demonstrating possible memory-related brain activity, is identified by post-processing comparing

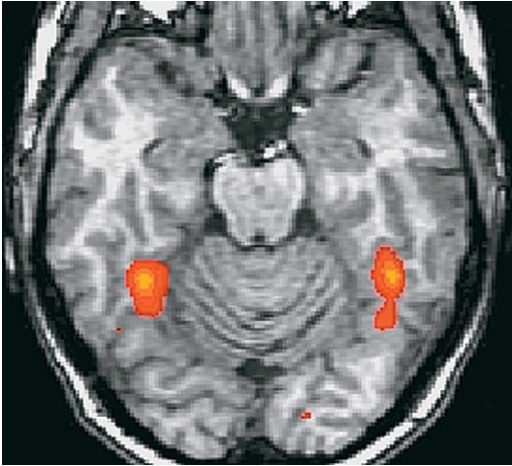


Fig. 15. fMRI responses during performance of a face memory paradigm in a neurology patient referred for episodes of prosopagnosia. Activation is detected bilaterally in the fusiform gyri.

signal intensity in multiple letter presentations versus single letters.

Another memory paradigm, which can be used to evaluate functionality in the posterior mesial temporal lobes involves a face memory task. In this paradigm, a face is presented which the patient is instructed to memorize, followed in brief succession by two more face images. The patient is instructed to indicate which of the two faces is a match for the first. Additional faces, followed by test faces, are presented repeatedly during each of the task periods. Activation is identified in the fusiform gyrus bilaterally in normal subjects (Fig. 15). The fusiform gyri responses are presumably related to both visual processing and working memory of the face images [53].

Research continues toward the application of fMR imaging memory paradigms in the pre-operative assessment of memory function in the medial temporal lobes for epilepsy patients being assessed for temporal lobectomy. In patients with sclerosis or with other cause for dysfunction in the mesial temporal lobe, activation is hypothetically diminished in the hippocampus and fusiform gyrus. One potential application of fMR imaging is to replace the memory portion of the Wada test. Recent reports show promise for fMR imaging as a possible replacement of the more invasive Wada test of memory, but full concurrence has not yet been achieved [54]. An fMR imaging paradigm incorporating the encoding of various image types

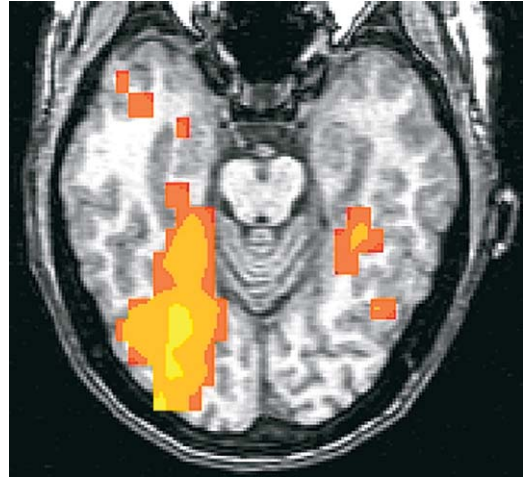


Fig. 16. fMRI activation during performance of a novel versus. familiar images paradigm in an epilepsy patient. In this patient with left mesial temporal sclerosis, activation is demonstrated in the right fusiform gyrus and hippocampus. Activation is diminished in the left mesial temporal lobe.

was reported to be in agreement with eight of nine Wada patient assessments for memory lateralization [55]. A paradigm based on a contrast of memory-related responses to over-learned familiar images and novel images has shown promise [56]. This paradigm has demonstrated symmetric results in control subjects and asymmetric mesial temporal lobe responses in epilepsy patients (Fig. 16), but results have not been 100% consistent. As of this writing, fMR imaging assessment of memory lateralization and localization appear complementary to the Wada memory test as a predictor of surgical risk to memory.

Interpretation

With the paradigms used in presurgical planning, the location and the size of the activated region depend on many factors, including the amount of effort expended by the patient, the sensitivity of the scanner to the BOLD effect, the noise and signal in the acquisition and the threshold chosen for displaying the activation. The precision of the activation is also less than finite. Activation on two successive iterations of the paradigm overlap substantially, but only about half of the voxels activated in one iteration are also activated in the next iteration. Therefore the distance between activation and lesion cannot

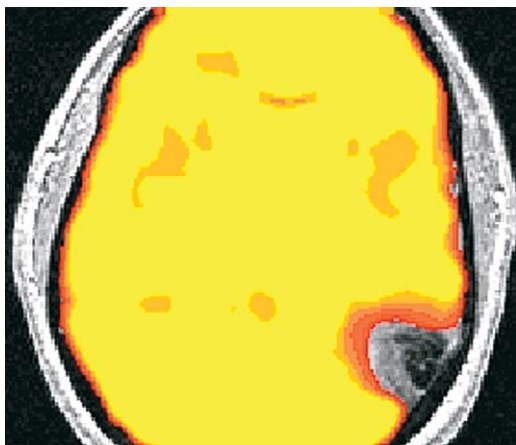


Fig. 17. A map of signal intensity (red coloration) superimposed on an anatomic image showing loss of signal in the left posterior temporal region secondary to blood products in a cavernous hemangiomas. The lack of signal implies a failure to detect any BOLD effect present in that region. A study that is negative for activation in that region does not then imply a lack of neuronal function in that region.

be measured with millimeter accuracy. Mapping with intraoperative stimulation mapping has a similar degree of imprecision and inaccuracy because the electric current used to stimulate the cortical surface may spread up to 1 cm through the cerebral cortex. For intraoperative electrical stimulation or fMR imaging, a distance of more than 1 cm between the edge of lesion and the activated regions suggests a low risk for new postoperative deficit whereas a distance less than 1 cm implies a significant risk [57]. The goal of fMRI interpretation is generally to identify the gyrus in which the activation is located and then to determine the relationship of this gyrus to the lesion.

Activation is generally taken to indicate the presence of eloquent cortex, that is cerebral cortex in which neurologic activity for clinically observable actions take place. Activation usually suggests the location of brain which if injured will result in a neurologic deficit. While activation generally implies eloquent brain, exceptions do occur. Some regions of activation may represent cerebral functioning that takes place simultaneously with the task but not indispensable for the task. Some areas of activation may represent functional connectivity, regions of brain that share pathways with the eloquent region. Some areas of activation may represent artifacts. There-

fore injury to a region of brain with activation may not in every case result in a neurologic deficit. In the case of the SMA, injury to this region in the mesial superior frontal gyrus may result in a neurologic deficit or may not, depending on the state of organization in the SMA [58]. Activation does not in every case predict a region necessary for normal neurologic function.

The absence of activation where it is anticipated must be interpreted with caution. Absence of activation may signify the absence of functional brain in that area, but it may also be explained by a technical failure. One example is a region with magnetic susceptibility effects in which the detection of the BOLD effect is impaired. Anatomic images should be inspected carefully to identify possible causes for technical failure, such as metallic clips, blood products, or other source for susceptibility effects. Some institutions generate signal intensity maps (Fig. 17) for each fMRI examination to measure the homogeneity of the magnetic field. The absence of signal in these maps indicates the insensitivity of the acquisition to the BOLD effect in that region. Activation may be missed because of reduced sensitivity caused by magnetic field inhomogeneities (eg, in the mesial temporal lobes because of the adjacent sphenoid sinuses), to insufficient signal to noise ratio (eg, in a patient who does not remain immobile during the acquisition), or to technical choices (eg, choice of a higher than optimal threshold). T2*-weighted scan parameters used in the acquisition of fMR images are inherently sensitive to susceptibility-induced signal losses [59], such as may occur near sinuses, a cavernous angioma, or site of a previous resection. These regions of susceptibility-induced signal losses may mask underlying cortical responses. Activation may also be reduced or obscured in the proximity of a large vascular malformation or malignant tumor. Vascular malformation with shunting may alter the BOLD effect locally [61]. Functionally intact eloquent cortex adjacent to a glioblastoma has been shown to display no activation [60]. Absence of activation must be interpreted cautiously. In a patient evaluated for language laterality, the absence of activation in the usual location of Broca's area in left frontal lobe does not imply that surgical resection of that lobe will leave no deficit. The presence of activation in the homologous region in the right frontal lobe suggests mixed or right hemispheric language dominance, but does not exclude the possibility of language function in the left hemisphere that is masked by a nearby lesion or

susceptibility effect. The effects and depth of anesthesia may also inversely affect the BOLD response [61].

fMR imaging is not a direct measure of neuronal activity, but instead depends on statistical analysis to identify areas with a hemodynamic response secondary to neuronal activity. The BOLD effect depends on the linkage between neuronal activity and blood flow. Inappropriate statistical analysis or post-processing techniques may lead to spurious false positives, lack of identified fMR imaging response, or misregistration of activation maps.

References

- [1] Ogawa S, Tark DW, Menon R, et al. Intrinsic signal changes accompanying sensory stimulation: functional brain mapping with magnetic resonance imaging. *Proc Natl Acad Sci USA* 1992;87:9860–72.
- [2] Bandettini PA, Jesmanowicz AJ, Wong EC, Hyde JS. Processing strategies for time-course data sets in functional MRI of the human brain. *Magn Reson Med* 1993;30:161–73.
- [3] Friston KJ, Holmes AP, Worsley KJ, et al. Statistical parametric maps in functional imaging: A general linear approach. *Hum Brain Mapp* 1995;2:189–210.
- [4] Cox RW. AFNI Software for analysis and visualization of functional magnetic resonance neuroimages. *Comput Biomed Res* 1996;29:162–73.
- [5] Atlas SW, Howard RS 2nd, Maldjian J, et al. Functional magnetic resonance imaging of regional brain activity in patients with intracerebral gliomas: findings and implications for clinical management. *Neurosurgery* 1996;38(2):329–38.
- [6] Schlosser MJ, McCarthy G, Fulbright RK, et al. Cerebral vascular malformation adjacent to sensorimotor and visual cortex. Functional magnetic resonance imaging studies before and after therapeutic intervention. *Stroke* 1997;28:1130–7.
- [7] Fitzgerald DB, Cospgrove GR, Ronner S, et al. Location of language in the cortex: a comparison between functional MR imaging and electrocortical stimulation. *Am J Neuroradiol* 1997;18(8):1529–39.
- [8] Schulder M, Maldjian JA, Liu WC, et al. Functional image-guided surgery of intracranial tumors located in or near the sensorimotor cortex. *J Neurosurg* 1998;89(3):412–8.
- [9] Brannen JH, Badie B, Moritz CH, et al. Reliability of fMRI of Word-Generation Tasks for Mapping Broca's Area. *Am J Neuroradiol* 2001;22:1711–8.
- [10] Krings T, Schreckenberger M, Rohde V, et al. Metabolic and electrophysiological validation of functional MRI. *J Neurol Neurosurg Psychiatry* 2001;71(6):762–71.
- [11] Liu TT, Frank LR, Wong EC, Buxton RB. Detection power, estimation efficiency, and predictability in event-related fMRI. *Neuroimage* 2001;13:759–73.
- [12] Birn RM, Cox RW, Bandettini PA. Detection versus estimation in event-related fMRI: choosing the optimal stimulus timing. *Neuroimage* 2002;15(1):252–64.
- [13] Price CJ, Friston KJ. Scanning patients with tasks they can perform. *Hum Brain Mapp* 1999;8:102–8.
- [14] Rao SM, Binder JR, Bandettini PA, et al. Functional magnetic resonance imaging of complex human movements. *Neurology* 1993;43(11):2311–8.
- [15] Roux FE, Ranjeva JP, Boulanouar K, et al. Motor functional MRI for presurgical evaluation of cerebral tumors. *Stereotact Funct Neurosurg* 1997;68(1–4 Pt 1):106–11.
- [16] Moritz CH, Meyerand ME, Cordes D, Haughton VM. Functional MR imaging activation after finger tapping has a shorter duration in the basal ganglia than in the sensorimotor cortex. *Am J Neuroradiol* 2000;21(7):1228–34.
- [17] Chung GH, Han YM, Kim CS. Functional MRI of the supplementary motor area: comparison of motor and sensory tasks. *J Comput Assist Tomogr* 2000;24(4):521–5.
- [18] Hammeke TA, Yetkin FZ, Mueller WM, et al. Functional magnetic resonance imaging of somatosensory stimulation. *Neurosurgery* 1994;35(4):677–81.
- [19] Yetkin FZ, Mueller WM, Hammeke TA, et al. Functional magnetic resonance imaging mapping of the sensorimotor cortex with tactile stimulation. *Neurosurgery* 1995;36(5):921–5.
- [20] Yetkin FZ, Haughton VM, Cox RW, et al. Effect of motion outside the field of view on functional MR. *Am J Neuroradiology* 1996;17(6):1005–9.
- [21] Moritz CH, Rowley HA, Haughton VM, Swartz KR, Jones J, Badie B. Functional MR imaging assessment of a non-responsive brain injured patient. *Magn Reson Imaging* 2001;19(8):1129–32.
- [22] Binder JR, Rao SM, Hammeke TA, Frost JA, Bandettini PA, Hyde JS. Effects of stimulus rate on signal response during functional magnetic resonance imaging of auditory cortex. *Brain Res Cogn Brain Res* 1994;2(1):31–8.
- [23] Millen SJ, Haughton VM, Yetkin Z. Functional magnetic resonance imaging of the central auditory pathway following speech and pure-tone stimuli. *Laryngoscope* 1995;105(12 Pt 1):1305–10.
- [24] Alsop DC, Detre JA, D'Esposito M, et al. Functional activation during an auditory comprehension task in patients with temporal lobe lesions. *Neuroimage* 1996;4(1):55–9.
- [25] Wilke M, Holland SK, Ball WS Jr. Language Processing during Natural Sleep in a 6-Year-Old Boy, as Assessed with Functional MR Imaging. *Am J Neuroradiol* 2003;24:42–4.
- [26] DeYoe EA, Bandettini P, Neitz J, Miller D, Winans P. Functional magnetic resonance imaging (fMRI)

- of the human brain. *J Neurosci Methods* 1994; 54(2):171–87.
- [27] Binder JR, Swanson SJ, Hammeke TA, et al. Determination of language dominance using functional MRI: A comparison with the Wada test. *Neurology* 1996;46(4):978–84.
- [28] Lehericy S, Cohen L, Bazin B, et al. Functional MR evaluation of temporal and frontal language dominance compared with the Wada test. *Neurology* 2000;54(8):1625–33.
- [29] Rutten GJ, Ramsey NF, Van Rijen PC, Alpherts WC, Van Veelan CW. FMRI-determined language lateralization in patients with unilateral or mixed language dominance according to the Wada test. *Neuroimage* 2002;17(1):447–60.
- [30] Gaillard WD, Balsame L, Xu B, et al. Language dominance in partial epilepsy patients identified with an fMRI reading task. *Neurology* 2002;59: 256–65.
- [31] Cuenod CA, Bookheimer SY, Hertz-Pannier L, Zeffiro TA, Theodore WH, Le Bihan D. Functional MRI during word generation, using conventional equipment: a potential tool for language localization in the clinical environment. *Neurology* 1995; 45:1821–7.
- [32] Ojemann JG, Buckner RL, Akbudak E, et al. Functional MRI studies of word-stem completion: reliability across laboratories and comparison to blood flow imaging with PET. *Hum Brain Mapp* 1998;6:203–15.
- [33] Carpenter PA, Just MA, Keller TA, Eddy WF, Thulborn KR. Time course of fMRI-activation in language and spatial networks during sentence comprehension. *Neuroimage* 1999;10(2):216–24.
- [34] Lurito JT, Kareken DA, Lowe MJ, Chen SH, Mathews VP. Comparison of rhyming and word generation with FMRI. *Hum Brain Mapp* 2000; 10(3):99–106.
- [35] Baciú M, Kahane P, Minotti L, et al. Functional MRI assessment of the hemispheric predominance for language in epileptic patients using a simple rhyme detection task. *Epileptic Disord* 2001;3(3): 117–24.
- [36] Brockway JP. Two functional magnetic resonance imaging f(MRI) tasks that may replace the gold standard, Wada testing, for language lateralization while giving additional localization information. *Brain & Cognition* 2000;43(1–3):57–9.
- [37] Ramsey NF, Sommer IE, Rutten GJ, Kahn RS. Combined analysis of language tasks in fMRI improves assessment of hemispheric dominance for language functions in individual subjects. *Neuroimage* 2001;13(4):719–33.
- [38] Maldjian JA, Laurienti PJ, Driskill L, Burdette JH. Multiple reproducibility indices for evaluation of cognitive functional MR imaging paradigms. *Am J Neuroradiology* 2002;23(6):1030–7.
- [39] Nelson L, Lapsiwala S, Haughton VM, et al. Preoperative mapping of the supplementary motor area in patients harboring tumors in the medial frontal lobe. *J Neurosurg* 2002;97(5):1108–14.
- [40] Beauregard M, Leroux JM, Bergman S, et al. The functional neuroanatomy of major depression: an fMRI study using an emotional activation paradigm. *Neuroreport* 1998;9(14):3253–8.
- [41] Muller RA, Pierce K, Ambrose JB, Allen G, Courchesne E. Atypical patterns of cerebral motor activation in autism: a functional magnetic resonance study. *Biol Psychiatry* 2001;49(8):665–76.
- [42] Wishart HA, Saykin AJ, McAllister TW. Functional magnetic resonance imaging: Emerging clinical applications. *Curr Psychiatry Rep* 2002;4(5):338–45.
- [43] Hooper HE. The Hooper Visual Organization Test manual. Los Angeles: Western Psychological Services; 1958.
- [44] Moritz CH, McMillan KM, Rogers BP, Haughton VM, Johnson SC, Meyerand ME. Functional MRI Neuroanatomic Correlates of the Hooper Visual Organization Task. *Proc. Int. Soc. for Magn. Reson. in Med. (ISMRM)* Toronto, Canada, 2003.
- [45] Detre JA, Maccotta L, King D, et al. Functional MRI lateralization of memory in temporal lobe epilepsy. *Neurology* 1998;50(4):926–32.
- [46] Casey BJ, Cohen JD, O’Craven K, et al. Reproducibility of fMRI results across four institutions using a spatial working memory task. *Neuroimage* 1998;8(3):249–61.
- [47] Ryan L, Nadel L, Keil K, et al. Hippocampal complex and retrieval of recent and very remote autobiographical memories: evidence from functional magnetic resonance imaging in neurologically intact people. *Hippocampus* 2001;11(6):707–14.
- [48] Saykin AJ, Flashman LA, Frutiger SA, et al. Neuroanatomic substrates of semantic memory impairment in Alzheimer’s disease: patterns of functional MRI activation. *J Int Neuropsychol Soc* 1999;5(5):377–92.
- [49] Cabeza R, Dolcos F, Graham R, Nyberg L. Similarities and differences in the neural correlates of episodic memory retrieval and working memory. *Neuroimage* 2002;16(2):317–30.
- [50] Mottaghy FM, Shah NJ, Krause BJ, et al. Neuronal correlates of encoding and retrieval in episodic memory during a paired-word association learning task: a functional magnetic resonance imaging study. *Exp Brain Res* 1999;128(3):332–42.
- [51] Stark CE, Squire LR. FMRI activity in the medial temporal lobe during recognition memory as a function of study-test interval. *Hippocampus* 2000; 10(3):329–37.
- [52] Jansma JM, Ramsey NF, Coppola R, Kahn RS. Specific versus nonspecific brain activity in a parametric N-back task. *Neuroimage* 2000;12(6):688–97.
- [53] Druzgal TJ, D’Esposito M. Activity in fusiform face area modulated as a function of working memory load. *Brain Res Cogn Brain Res* 2001;10(3):355–64.
- [54] Baxendale S. The role of functional MRI in the presurgical investigation of temporal lobe epilepsy

- patients: a clinical perspective and review. *J Clin Exp Neuropsychol* 2002;24(5):664–76.
- [55] Golby AJ, Poldrack RA, Illes J, Chen D, Desmond JE, Gabrieli JD. Memory lateralization in medial temporal lobe epilepsy assessed by functional MRI. *Epilepsia* 2002;43(8):855–63.
- [56] Moritz CH, Johnson SJ, Meyerand ME. Variable-length block memory encoding paradigm demonstrates individual subject hippocampal fMRI response. *Proc. Int. Soc. for Magn. Reson. in Med. (ISMRM) Honolulu, HI, 2002.*
- [57] Yetkin FZ, Mueller WM, Morris GL, et al. Functional MR activation correlated with intra-operative cortical mapping. *AJNR Am J Neuro-radiol* 1997;18(7):1311–5.
- [58] Sailor J, Meyerand ME, Moritz CH, et al. Supplementary motor area activation in patients with frontal lobe tumors and arteriovenous malformations (in press *AJNR*).
- [59] Cordes D, Turski PA, Sorenson JA. Compensation of susceptibility-induced signal loss in echo-planar imaging for functional applications. *Magn Reson Imaging* 2000;18(9):1055–68.
- [60] Holodny AI, Schulder M, Liu WC, Wolko J, Maldjian JA, Kalnin AJ. The effect of brain tumors on BOLD functional MR imaging activation in the adjacent motor cortex: implications for image-guided neurosurgery. *Am J Neuroradiology* 2000; 21(8):1415–22.
- [61] Lehericy S, Biondi A, Sourour N, et al. Arteriovenous brain malformations: is functional MR imaging reliable for studying language reorganization in patients? Initial observations. *Radiology* 2002;223(3):672–82.
- [62] Antognini JF, Buonocore MH, Disbrow EA, Carstens E. Isoflurane anesthesia blunts cerebral responses to noxious and innocuous stimuli: a fMRI study. *Life Sci* 1997;61(24):PL 349–54.



MR myelography of the spine and MR peripheral nerve imaging

Jeffrey A. Stone, MD

Department of Radiology, Medical College of Georgia, 1120 15th Street, Augusta, GA, 30912, USA

MR myelography

Contrast-enhanced myelography has long been a standard diagnostic procedure to evaluate degenerative spine disease in patients with symptoms suggestive of spinal cord and nerve root compression. Injection of intra-theal contrast enhances evaluation of compressive effects on nerve roots and thecal sac and allows evaluation of bony pathology and its effect on these neural structures. The disadvantages of contrast-enhanced myelography include expense, risks related to lumbar or cervical puncture, and ionizing radiation.

MR myelography (MRM) has slowly evolved into a useful diagnostic tool that has advantages of being noninvasive, does not use ionizing radiation, and can be obtained simultaneously during routine spine MR imaging. MRM allows evaluation of the nerve root sheath and unlike contrast-enhanced myelography, is not dependent on spine curvature, gravity effects or size of the thecal sac. Its disadvantages include increased motion susceptibility, the inability to image in the upright or symptomatic position and the dependence on technical settings that can greatly vary depending on the manufacture of the MR imaging unit.

Henning et al [1] initially described the use of MRM in 1986 using rapid acquisition with relaxation enhancement (RARE). In 1992, Krudy [2] described a heavily T2-weighted fast spin-echo pulse sequence with fat presaturation that provided excellent contrast and resolution in the lumbar region with minimal artifact from para-

vertebral vessels. Scan time was approximately 6.5 minutes but this technique was suboptimal for imaging the cervical and thoracic region because of poor spinal cord definition and cerebral spinal fluid (CSF) flow artifact. Also in 1992, Vandyke et al [3] described a three-dimensional (3D) fast imaging with steady state precession (FISP) sequence that produced high signal intensity from the CSF by maintaining constant phase at the radiofrequency pulse in the presence of CSF motion. Two separate 2.5-minute acquisitions were obtained, one with the RF pulses of the same phase and the other with alternating phases. The maximum signal between the two acquisitions was taken on a pixel-by-pixel basis and a localized region of interest was created by removing surrounding high signal from fat. These were displayed as two-dimensional (2D) and reformatted three-dimensional (3D) cross-sectional images. This technique resulted in a short imaging time, five minutes in total, and provided images with uniform, high signal intensity CSF. The need for post-processing at a workstation however, was a disadvantage with these techniques and in our experience; the image quality has been less optimal often degraded by patient motion and juxta-theal venous structures (Fig. 1).

MRM images using heavily T2-weighted images with fat-suppression are susceptible to artifact because of the hyperintense signal of juxta-theal venous structures. This signal can be suppressed by administration of intravenous gadopentetate dimeglumine (0.15 mmol/kg) as a negative contrast agent during turbo short tau inversion recovery (STIR) MRM, and gadolinium also improves the signal-to-noise ratio of adjacent CSF containing structures [4]. This technique has the obvious

E-mail address: jstone@mail.mcg.edu

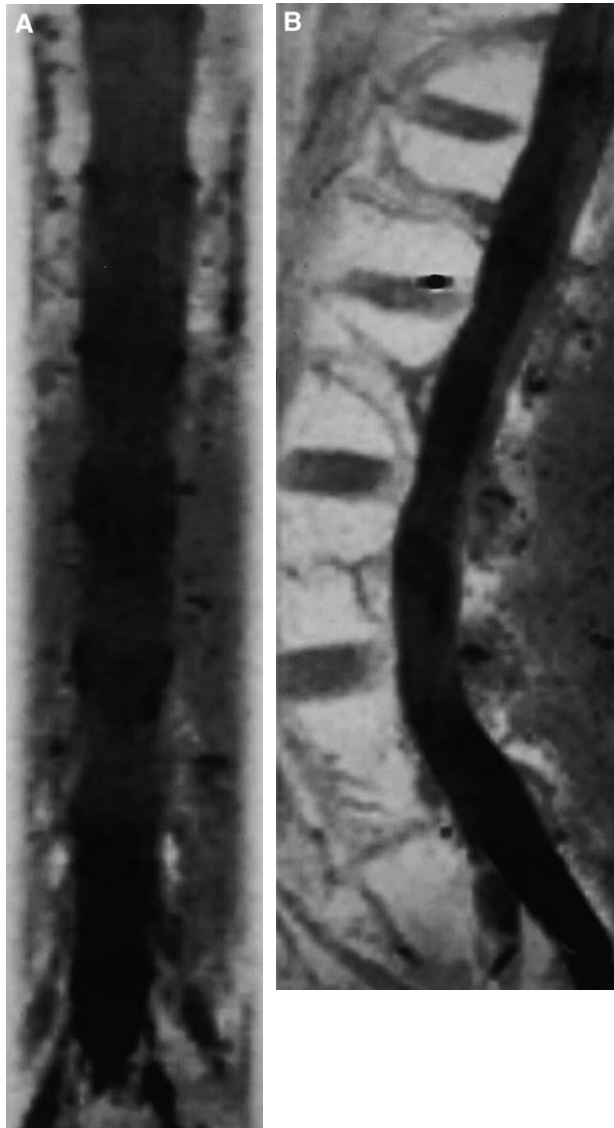


Fig. 1. Normal MRM using 3D FISP technique. Anterior (A) and lateral (B) maximum intensity images produced at the MR workstation show the thecal sac without compressive deformity. Left (C) and right (D) oblique images show a large portion of the respective left and right nerve root sleeves particularly at lower lumbar levels. The vertebral bodies are faintly visualized on the lateral and oblique images using this technique.

disadvantage of increased time and expense. A shorter scan time with high resolution and contrast however, is the ultimate solution for MRM to be a useful add-on to standard spine MR imaging.

MRM reached a new height in 1997 using echo-planar imaging to rapidly acquire MRM images. Damaerel et al [5] described a technique derived from a RARE sequence, single-shot turbo spin-echo (SS-TSE) that allowed image acquisi-

tion in 2 seconds per image (coronal, sagittal, and oblique views) and alleviated the need for post-processing at a workstation. The parameters used by Damaerel et al were an effective TE, 850 milliseconds; echo train length 160; TR, 11.5 milliseconds; matrix, 160×256 ; number of acquisitions, one; field of view, 125×200 mm; slice thickness, 20 mm; and acquisition time 1.8 seconds.

The authors have since modified the technique used by Damaerel to increase resolution while only

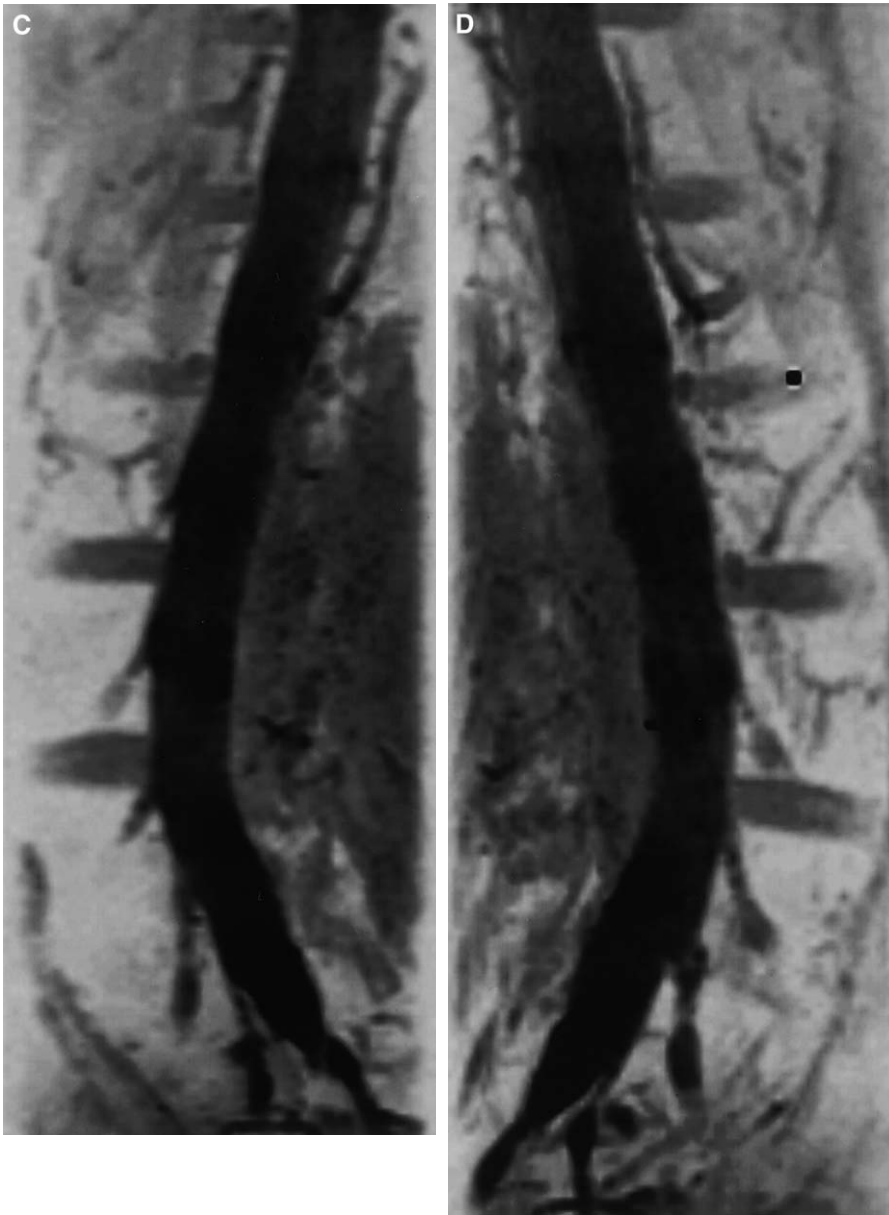


Fig. 1 (continued)

increasing scan time to 8 seconds per view (TE, 199.5 milliseconds; TR, 8000 milliseconds; matrix, 256×256 ; number of acquisitions, one; field of view, 200×200 mm; slice thickness, 20 mm; acquisition time 8 seconds; presaturation fat pulse) [6] (Fig. 2). This technique uses a fat-suppression pulse and thus eliminates bony landmarks. It is therefore important to mark a reference level using the workstation before filming (see Fig. 2). It also is

useful to invert the image contrast using reverse mode so that CSF appears black on a white background. The authors have found that this technique results in excellent resolution in the cervical and lumbar spine and is not significantly degraded by cerebrospinal fluid (CSF) flow or paraspinal vessel artifacts (Figs. 3, 4). Based on the authors' clinical experience, we believe that this technique accurately depicts the nerve root sleeves

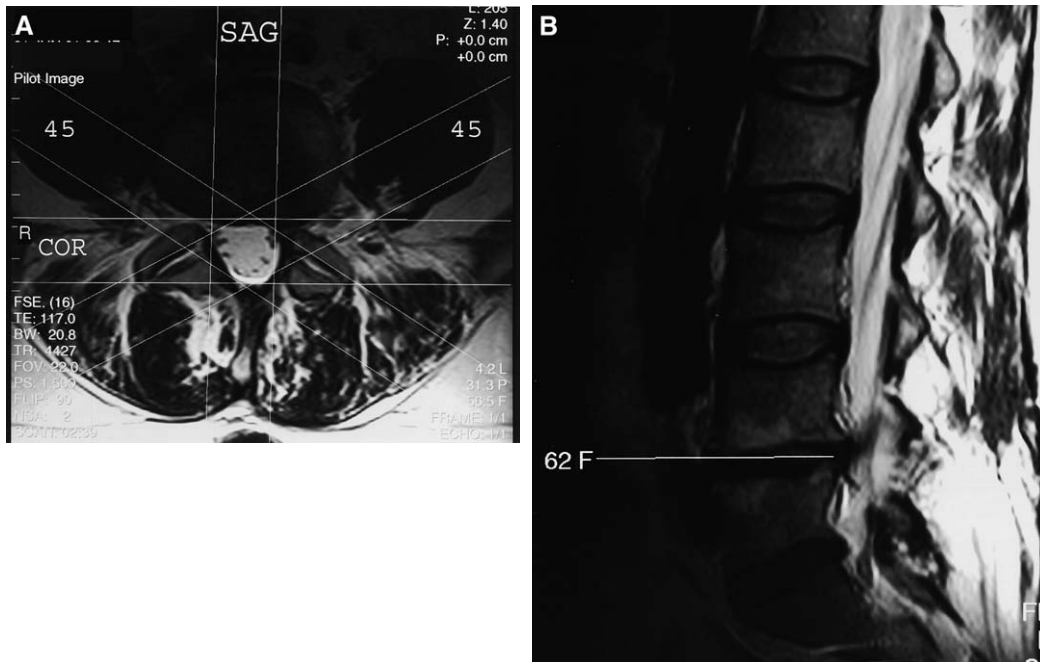


Fig. 2. A 62-year-old female patient evaluated for low back pain using our echo-planar RARE technique (A) Axial T2-weighted image is used for localization. Sagittal (SAG), coronal (COR) and bilateral 45° oblique (45) planes oriented with the neural foramen are obtained. (B) Sagittal T2-weighted image shows L4-5 and L5-S1 disc desiccation and a small disc or osteophyte complex at L4-5. A localizing mark (62F) has been placed at the level of abnormality for reference on the MRM images. (C–F) Anterior (C), lateral (D), left (E) and right (F) oblique images better demonstrate the CSF filled thecal sac, nerve roots within the thecal sac and nerve root sheath complex. Minimal compressive effect is seen at L4-5 on the lateral image and the nerve roots are well preserved on the oblique images.

and compressive effects on the thecal sac, spinal cord, and nerve roots.

Karantanas et al [7] compared the SS-TSE technique to 3D-turbo spin echo (3D-TSE) MRM and routine T2-turbo spin-echo (T2-TSE) MR imaging. They concluded there was no significant difference in measuring the AP diameter of the spinal canal between the three techniques and no significant difference in evaluating signal-to-noise ratio (SNR) of the spinal cord between the SS-TSE and 3D-TSE techniques, but both were better for SNR of the cord than T2-TSE. SS-TSE also was better than either 3D-TSE or T2-TSE for SNR of CSF, contrast-to-noise ratio between CSF and spinal cord, and relative contrast between CSF and spinal cord.

Several investigators have evaluated the accuracy of MRM compared with conventional contrast-enhanced myelography for lumbar spine imaging. A distinct advantage of MRM is the ability to evaluate nerve root sheaths. Kuroki et al [8] used a 3D fast spin-echo technique to show that MRM was equivalent to contrast-enhanced

myelography in evaluating the lower lumbosacral nerve roots. Eberhardt et al [9] evaluated 3D-FISP MRM technique and conventional contrast-enhanced myelography in an effort to compare differences in evaluating normal anatomy and pathologic states. The lengths of individual spinal nerve roots from the L1 to S3 level were compared in 50 asymptomatic patients. The sensitivity for evaluation of the L4 through S1 nerve roots was comparable but 3D-FISP MRM better delineated the L1 to L3, S2, and S3 nerve roots than contrast-enhanced myelography. MRM and contrast-enhanced myelography were also compared with findings at surgery in 80 patients presenting with radicular symptoms. The sensitivity for detecting nerve root compression caused by spinal stenosis was significantly higher for 3D-FISP MRM than contrast-enhanced myelography, particularly in patients with severe stenosis. There was no significant difference in the ability to detect disc herniation or post-operative scar tissue, and both techniques showed 80% to 90% sensitivity.

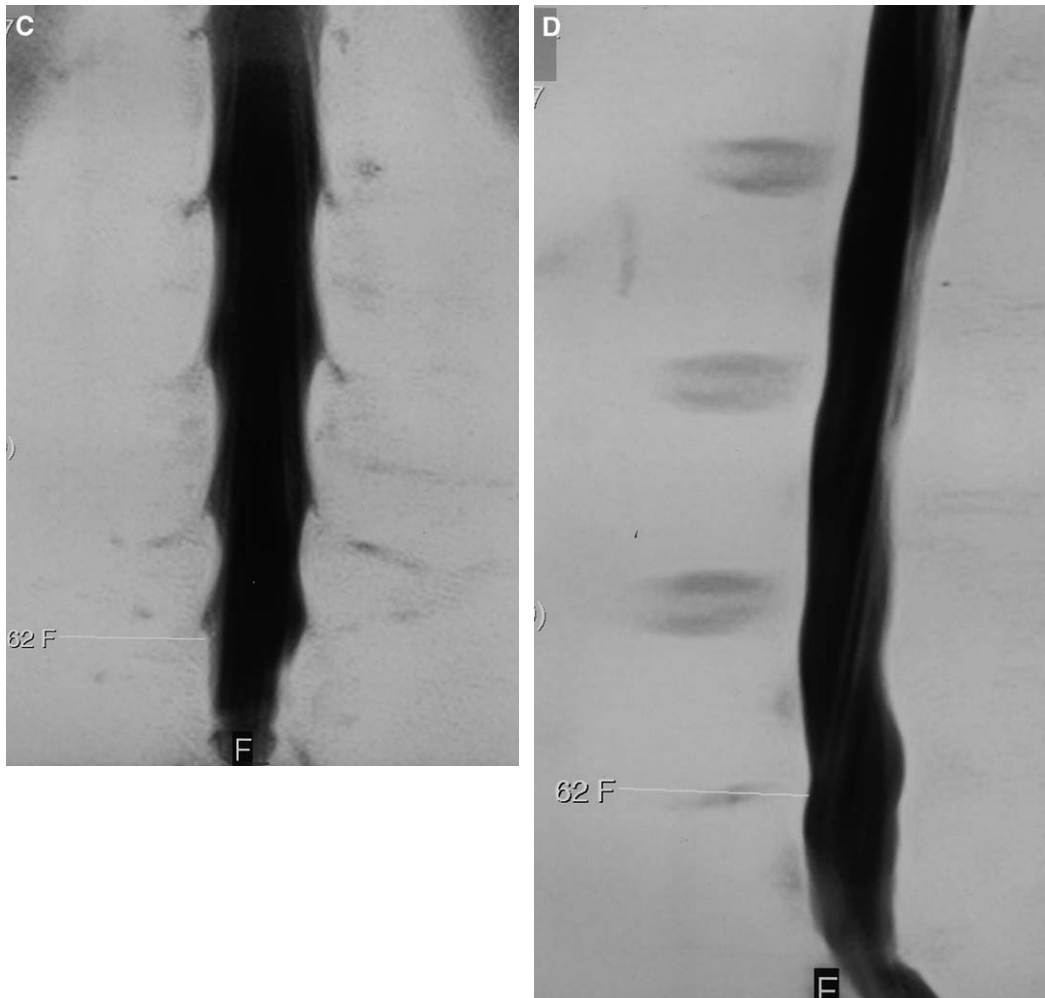


Fig. 2 (continued)

Ramsbacher et al [10] prospectively evaluated 41 patients with lumbar radicular symptoms using conventional contrast myelography and compared it to MRM. They used a heavily T2*-weighted 3-D gradient echo sequence (4 min scan time) and 3D maximum intensity projections (MIP). MRM and contrast myelography had identical sensitivity and specificity in 35 cases of thecal sac indentation with nerve root sheath amputation and 6 cases of spinal stenosis. These results were confirmed at surgery in 38 patients.

The dorsal root ganglion is believed to play a significant role in the mechanism of low back or sciatic pain [11]. Animal studies suggest that dorsal root ganglion edema caused by compression produces nerve root pain [12]. Imaging of the dorsal root ganglion is possible with MRM using

heavily T2-weighted images with fat suppression that enhances signal intensity of CSF and the dorsal root ganglion with subtraction of background signal. Yohichi et al [13] blindly evaluated the dorsal root ganglion on MRM images in 83 patients with monoradicular symptoms. Indentation and swelling of the ganglion was assessed and a “dorsal root ganglion ratio” was quantitatively expressed as a ratio of the dorsal root ganglion width on the involved side to that of the contralateral side, and these were compared with 83 random control uninvolved levels. The dorsal root ganglion ratio was significantly higher at involved levels and in patients with lateral disc herniations. There was a moderate correlation between the dorsal root ganglion ratio and leg pain, gait, and motor symptoms. Indentation of

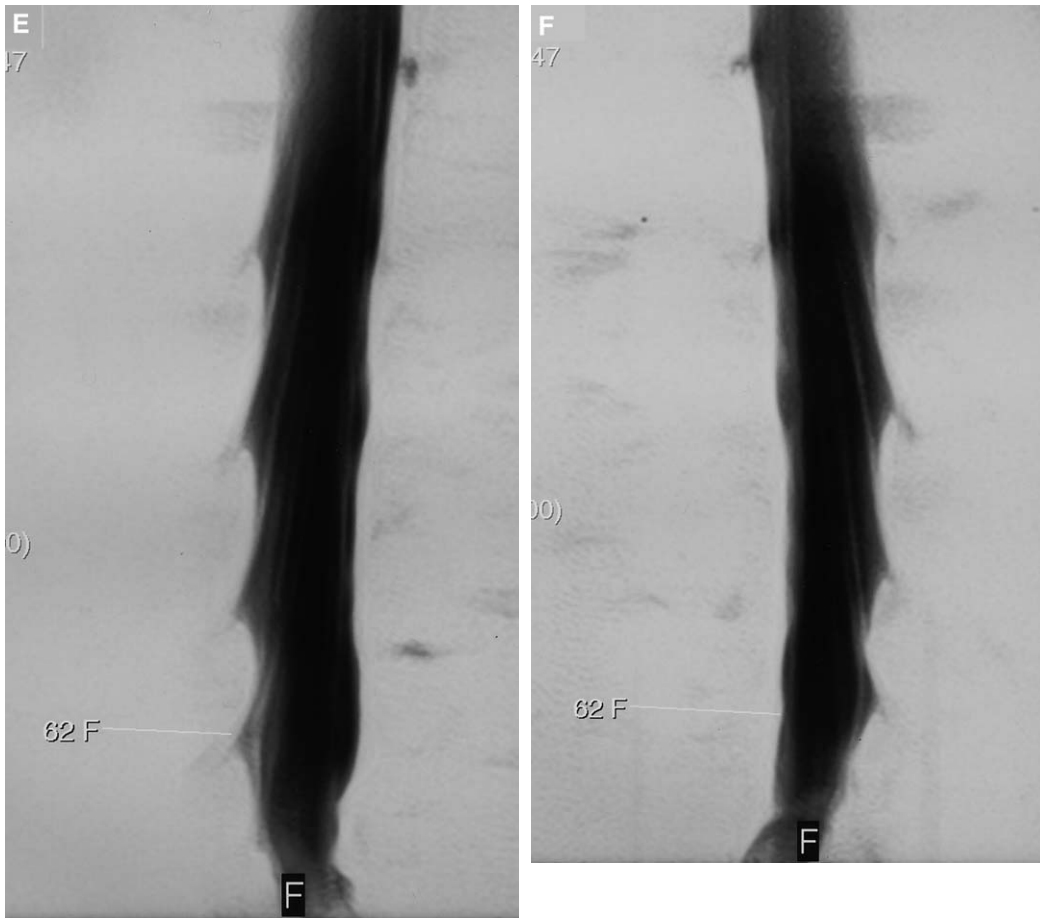


Fig. 2 (continued)

the dorsal root ganglion was also significantly higher at involved nerve roots, in older patients and in patients with a worse leg pain score, based on the Japan Orthopedic Association scoring system. Twenty-three patients were re-imaged at one year following treatment (19 patients underwent surgery and 6 managed conservatively) that had good or excellent clinical results and the dorsal root ganglion ratio had significantly decreased. Careful evaluation of the dorsal nerve root ganglion and correlation with clinical symptoms can potentially determine the spinal level responsible for radicular symptoms and predict those patients most likely to benefit from intervention.

MRM may also be used in the evaluation of conjoined nerve roots, nerve root avulsion, arachnoid adhesions, pseudomeningoceles, syrinx,

gomyelia, perineural, and arachnoid cysts (Fig. 5). MRM also has successfully been used for evaluation of proximal brachial plexus injuries and can detect small meningoceles with avulsed or intact nerve roots, partial or complete radicular avulsions without disruption of the thecal sac, dural sleeve abnormalities and dural scars [14,15]. When compared with conventional cervical myelography and CT myelography, 3D constructive interference in the steady state (CISS) MRM shows 89% sensitivity, 95% specificity, and 92% diagnostic accuracy for detection of traumatic brachial plexus injuries [15].

The future evaluation of CSF leak and CSF flow dynamics may eventually be possible using intrathecal gadolinium enhanced MRM and cisternography. Zeng et al [16] demonstrated the feasibility and safety of using low dose intra-

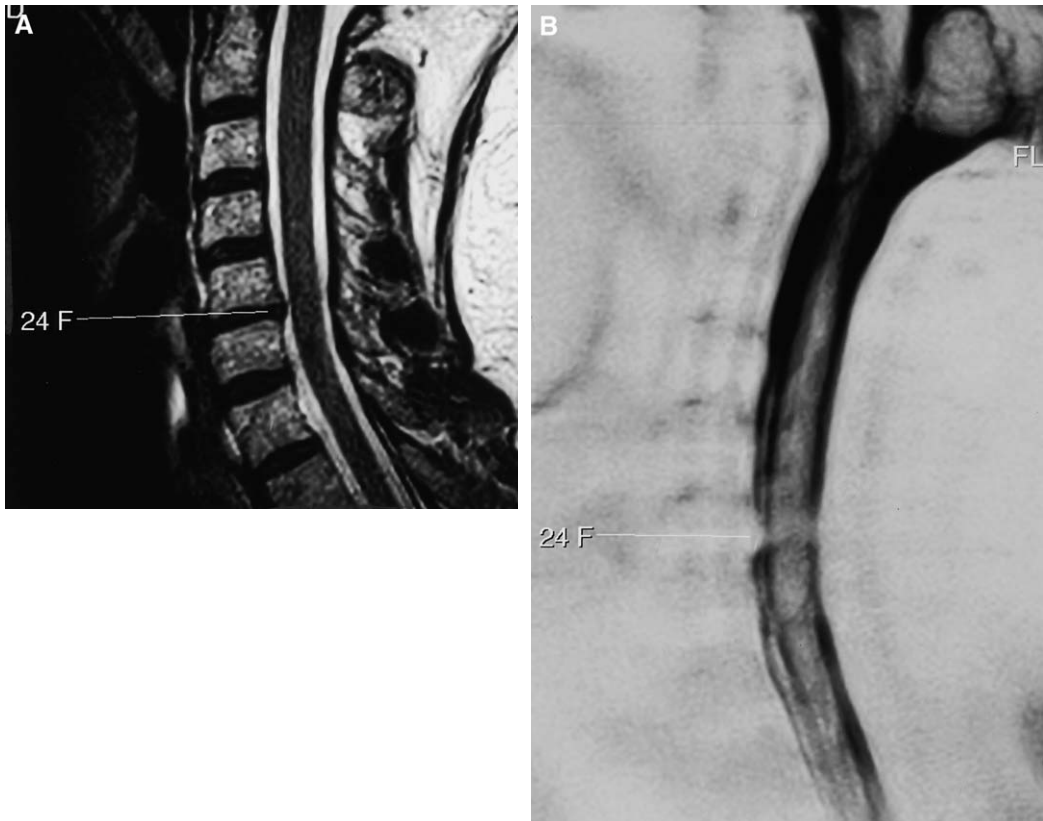


Fig. 3. A 24-year-old female patient with bilateral radiculopathy greater in the right arm. (A) Sagittal T2-weighted image at midline shows a small disc herniation (24F) at the C5-6 level. (B) Sagittal MRM image also at midline shows mild compression of the anterior thecal sac with no deformity of the spinal cord. (C) Right oblique MRM image shows decreased "myelographic effect" at the level of compression and amputation of the right C6 nerve root (black arrow). (D) Left oblique MRM image shows the inferior aspect of the left C6 nerve root contains CSF signal (black arrow) whereas there is blunting of the superior nerve root sleeve. Given the findings and failure of conventional therapy, a C5-6 anterior cervical discectomy and fusion was performed with relief of her symptoms. The asymmetry of the MRM nerve root compression may account for her asymmetric symptoms.

thecal gadolinium (gadopentetate dimeglumine) in 11 patients. A single dose of either 0.2 mL, 0.5 mL, or 1.0 mL of gadolinium (500 mmol/l) was injected by way of lumbar puncture after baseline MR imaging. The normal hypointensity of subarachnoid space on T1-weighted images was reversed to hyperintensity, particularly with lower doses (0.2 mL and 0.5 mL), but areas of hypointensity were seen in dependent portions of the thecal sac with a higher dose (1.0 mL). The normal hyperintensity on T2-weighted images was reversed to hypointensity after the 0.5 mL and 1.0 mL doses but not after the 0.2 mL dose. Six patients were monitored with pre- and post-imaging CSF analysis and five patients with

12-lead electroencephalography. No significant abnormality was detected during a 24-hour observation period following the procedure. No neurologic sequelae were seen in any of the 11 patients during 9 to 15 month follow-up. MR imaging at 1 year follow-up in 3 patients showed no gross morphologic or MR signal changes compared with initial baseline MR studies. Jinkins et al [17] further illustrated the use of intra-thecal gadolinium for the detection of CSF leaks by using it in conjunction with MR cisternography. While this method has the obvious disadvantage of requiring lumbar puncture and intra-thecal use of gadolinium and it is not approved in many countries, it warrants further

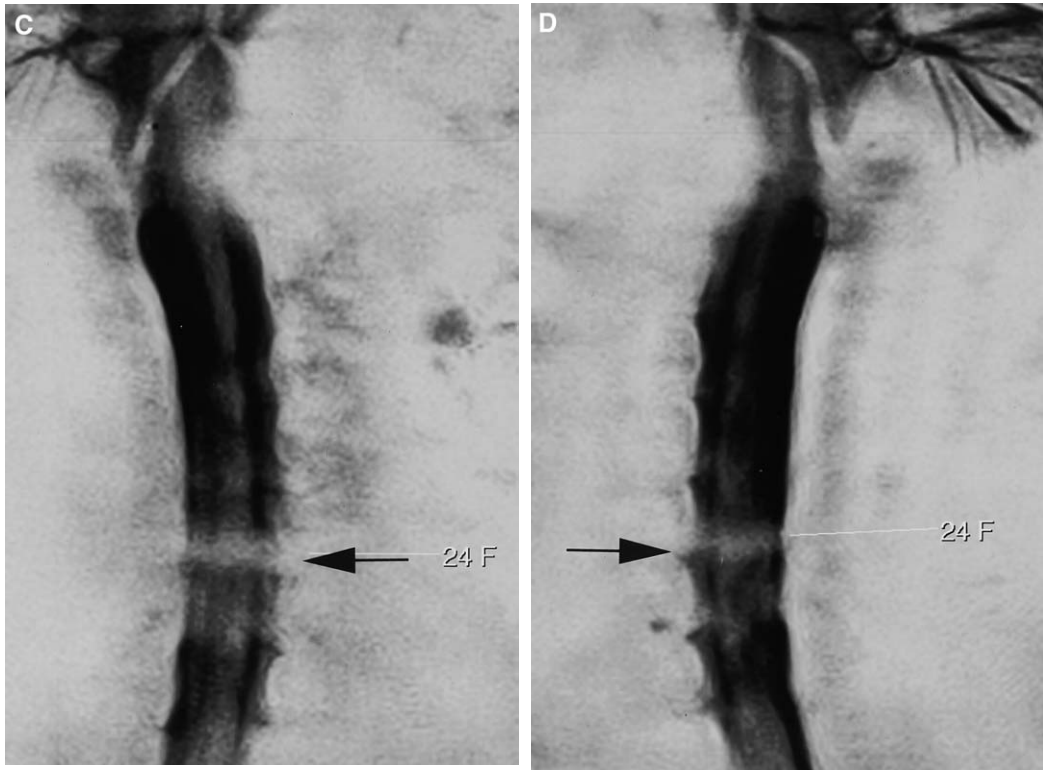


Fig. 3 (continued)

investigation and also has potential for evaluation of CSF flow dynamics.

MR peripheral nerve imaging

Radicular symptoms are common and involve both the upper and lower extremities. The majority of patients with radiculopathy have abnormalities localized to the cervical and lumbar spine and routine MR imaging studies of the spine suffice. There is a subgroup of patients however, with neurogenic symptoms referable to peripheral nerve pathology, most notably the lumbosacral plexus; sciatic nerve; and brachial plexus. Electrodiagnostic studies, such as electromyography (EMG) is useful to localize the level of a peripheral nerve lesion but does not provide information as to the etiology of the lesion. Ultrasonography, computed tomography, and standard MR imaging techniques have been used to evaluate these patients but have limited capacity and accuracy in detecting pathologic lesions. MR peripheral nerve imaging (MRPNI) using phase array coils and fast

imaging technique is a sensitive diagnostic tool that allows high definition imaging of the extra-spinal neural structures and improved detection of intraneural and extraneural pathology.

The brachial and lumbosacral plexus are formed by multiple ventral rami of spinal nerves. The C5 through T1 spinal nerves form the brachial plexus as roots that subsequently form the trunks, divisions, cords, and branches. The lumbosacral plexus is composed of two separate plexus. The lumbar plexus is formed by L1 through L3 spinal nerves and the sacral plexus from L4 through S4 spinal nerves. Both the lumbar and sacral plexus divide into anterior and posterior branches. The posterior branches of the lumbar plexus are located within the psoas muscle and the sacral plexus is anterior to the piriformis muscle. The sciatic nerve is formed by the tibial portion from the anterior branch of the sacral plexus and the peroneal portion from the posterior branch. The sciatic nerve courses through the greater sciatic foramen of the pelvis accompanied by the piriformis muscle and gluteal

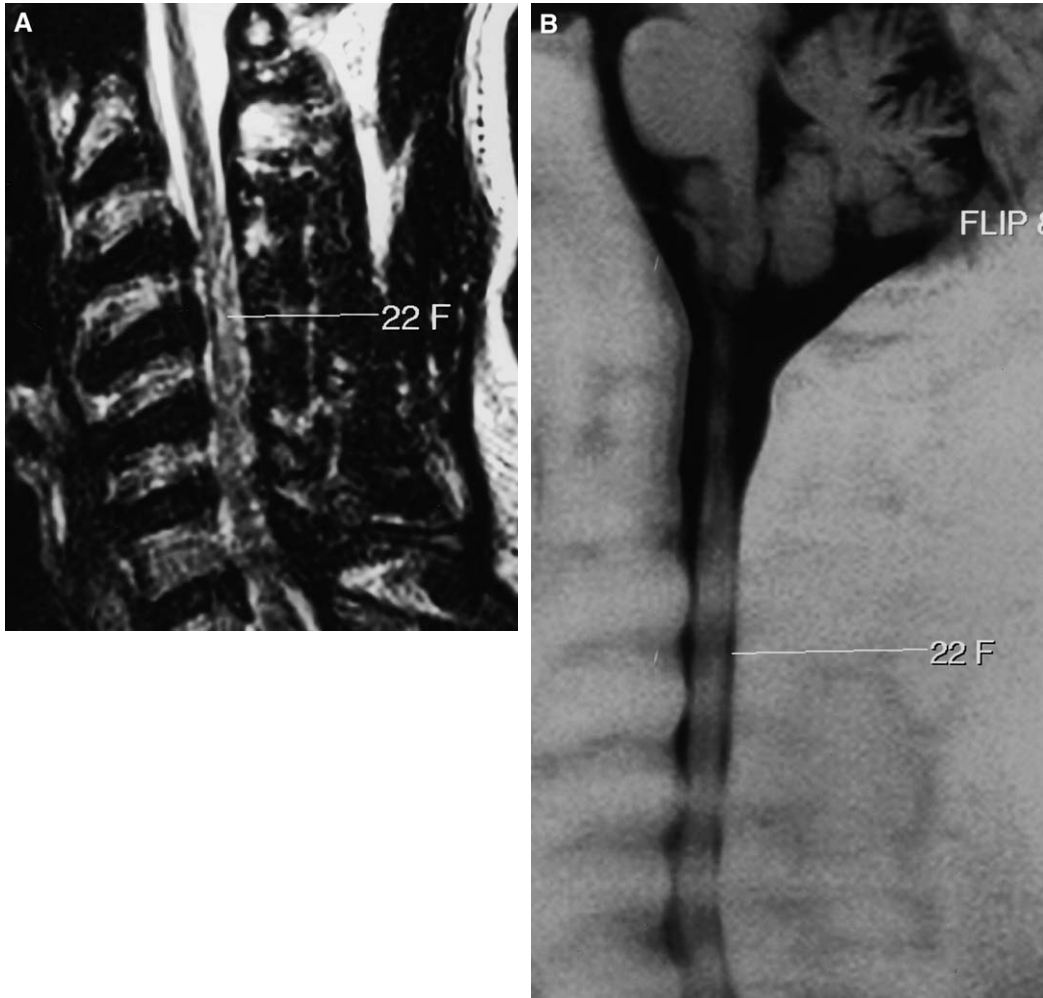


Fig. 4. A 52-year-old female patient with myelopathy. (A) Sagittal T2-weighted image shows multi-level spondylolysis of the cervical spine with increased spinal cord signal at the C4-5 level (22F). The degree of spinal cord compression at lower cervical levels is often difficult to ascertain on routine T2-weighted images in these patients with advanced hypertrophic change. (B) Sagittal MRM image better demonstrates the degree of spinal canal stenosis and spinal cord compression at multiple cervical levels.

vessels and nerves. The sciatic nerve divides into tibial and peroneal nerves in the lower thigh region.

Peripheral nerves are composed of several fascicles interspersed with adipose and fibrous connective tissue contained as a structural unit by the epineurium. Each fascicle is surrounded by perineurium and the nerve axons that compose the fascicle are surrounded by loose connective tissue called endoneurium. The tightly adherent cells of the perineurium isolate the endoneurial fluid from the surrounding extracellular space, and when intact, act as a barrier to the spread of

disease [18]. Axoplasmic fluid is also present within the axons. The intrinsic contrast properties of adipose tissue and both endoneurial and axoplasmic fluid allow distinct MR imaging of peripheral nerves. The individual fascicles of larger nerves are visualized as smooth, uniform, soft tissue structures isointense to muscle on T1-weighted MR images and are well delineated by interspersed epineurial adipose tissue. Fascicles appear as high signal intensity dot-like structures on T2-weighted images that generally show less intense signal than adjacent blood vessels and mild to moderate hyperintense signal compared to



Fig. 5. A 45-year-old male patient with prior traumatic thoracic spine injury and syringomyelia. (A) Sagittal T2-weighted image shows a focal area of syringomyelia within the lower thoracic spinal cord (*white arrow*). (B) Sagittal MRM image takes advantage of the CSF signal with the syringomyelia cavity (*black arrow*) and also shows the extent of the lesion. MRM is particularly useful for small CSF containing lesions such as nerve root avulsions, pseudomeningoceles and CSF leaks.

adjacent muscle. The nerve fascicles are separated by low-signal intensity on T2-weighted images because of interspersed connective tissue and fat-suppressed adipose tissue.

Typical MRPN protocols use high-resolution spin-echo T1-weighted images to show anatomic detail and fat-suppressed T2-weighted or STIR images to detect abnormal nerve signal intensity (Figs. 6, 7) [19]. STIR images are preferable to provide uniform and consistent fat suppression with excellent T2 contrast [18]. STIR imaging however, has a low SNR and is sensitive to blood-flow artifacts. Flow saturation pulses are useful to attenuate these phase-shift artifacts [18].

Gadolinium enhanced fat-suppressed T1-weighted images are typically reserved for patients with neoplasm, suspected infection, and post-surgical evaluation.

MR imaging of the peripheral nerves is time consuming and motion sensitive. It is therefore useful to limit MR imaging to the most likely region of nerve pathology. This may be deduced based on clinical presentation and electrodiagnostic testing (EMG and nerve conduction velocity studies). Lesions also may be clinically localized based on pain distribution, palpable mass, and motor or sensory deficits [19]. Patient sedation is routinely used during image acquisition and

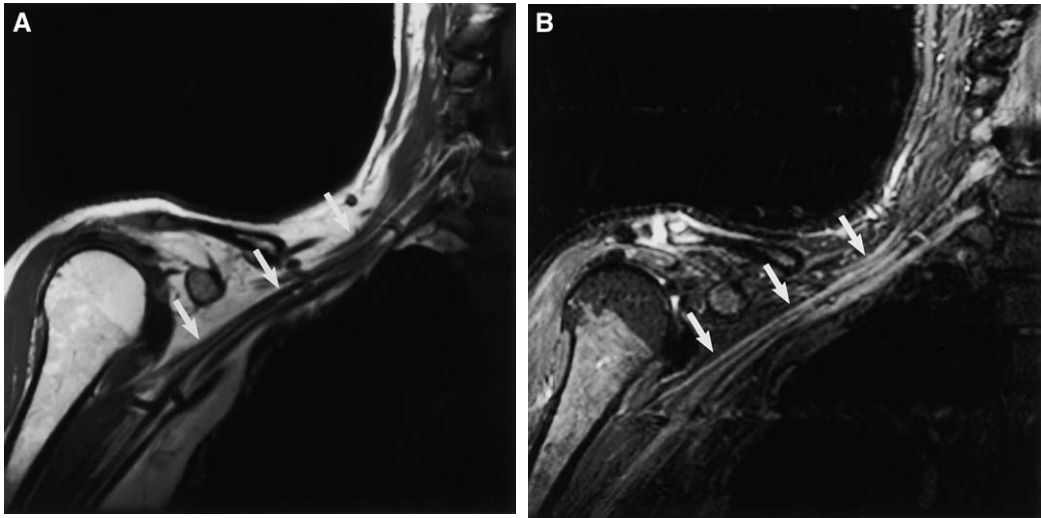


Fig. 6. Normal brachial plexus. (A) Oblique coronal T1-weighted image (to maximize long axis of brachial plexus) of the lower brachial plexus shows the brachial plexus isointense to muscle extending from the trunks to cords (*white arrows*) as well as the proximal roots of C8 and T1. (B) Oblique coronal STIR images (same plane as A) show the normal brachial plexus (*white arrows*) with signal higher than muscle but less than vascular structures in the neck. (From Moore KR. Spine Image Archive. Salt Lake City (UT): Advanced Medical Imaging; Accessed June 2003; with permission.)

occasional patients may require more than one imaging session.

The use of phase array coils allows a composite image to be performed from multiple receive-only surface coils. This allows anatomically detailed

images with high SNR and a small field of view. High-resolution matrices are used to improve in-plane spatial resolution. Most phase array coils are shapeable to fit the curves of the extremity being imaged [18]. Moore et al [19] have indicated

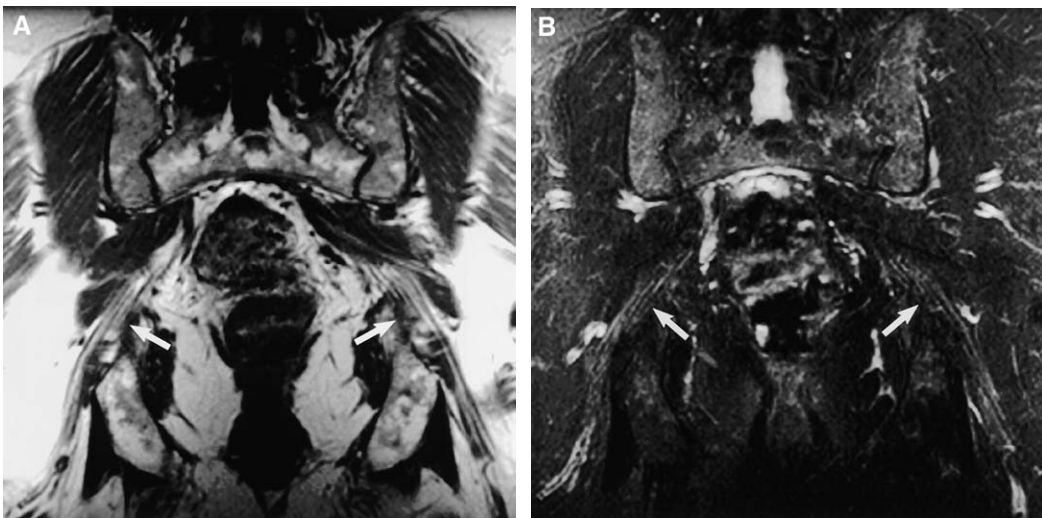


Fig. 7. Normal sciatic nerve. (A) Coronal T1-weighted image oriented to long axis of sciatic nerve as it courses through the greater sciatic foramen (*arrows*). Nerve fascicles are isointense to muscle and surrounded by high signal of adipose tissue within the epineurial space. (B) Coronal T2-weighted FSE image with fat saturation obtained in same plane as shown in A. Fascicles appear bright in signal intensity but remain less intense than adjacent blood vessels. (From Moore KR. Spine Image Archive. Salt Lake City (UT): Advanced Medical Imaging; Accessed June 2003; with permission.)

that a standard wrap-around thoracic phase array coil placed over the pelvis or thighs works well for imaging the lumbosacral plexus and sciatic nerve, whereas pelvic phase-array coils are generally limited to imaging the lumbosacral plexus. Images are best obtained parallel and perpendicular to the nerve of interest. The field of view is dependent on the size of the body part being imaged but is in the range of 18 to 26 cm when imaging the brachial or lumbosacral plexus and 12 to 16 cm when imaging the sciatic nerve. A 256×256 or 512×256 matrix size is usually adequate for imaging these regions. Contiguous 4 to 7 mm thick images are used for imaging parallel to the nerve course and perpendicular to the nerve in the brachial plexus or lumbosacral plexus. A 50% to 100% gap (2–4 mm) may however, be used for imaging perpendicular (cross-sectional) to the sciatic nerve course, particularly when a specific anatomic region is difficult to ascertain based on clinical information and a large region of imaging is necessary.

Peripheral nerve injuries are divided into two basic groups based on the mechanism of injury: traumatic axonal disruption caused by a crush injury or transection and compressive neuropathy secondary to neoplasm, entrapment, or non-disruptive trauma [20]. Both mechanisms increase permeability of endothelial junctions of the endoneurium and allow an influx of free water into the endoneurial space. This may account for increased signal on T2-weighted or STIR images often approaching that of adjacent blood vessels. The nerve often becomes enlarged and fascicular architecture may be distorted. It is important to image the muscle groups supplied by the nerve of interest because secondary denervation changes may be seen. Early denervated muscle has normal size and initially shows increased signal intensity on T2-weighted images. Chronic denervation leads to muscle atrophy and therefore decreased size and adipose tissue infiltration. This is best evaluated on T1-weighted images of the affected muscle groups.

Many pathologic conditions can be identified on MRPNI. Compressive neuropathy may be caused by intrinsic or extrinsic compression of a peripheral nerve. Extrinsic compression is seen in entrapment syndromes and occurs in locations where the nerve has an intimate association with bone, muscle, or vascular structures. The lower trunk of the brachial plexus is prone to compression at the insertion site of the anterior scalene muscle on the first rib or at the crossing point of

a cervical rib [18]. The sciatic nerve is compressed at the greater sciatic foramen by the piriformis muscle and the lateral femoral cutaneous nerve at the attachment of the inguinal ligament to the anterior superior iliac spine [18]. Vascular entrapment is often caused by aneurysm formation or can be the result of hematoma.

Intrinsic compression is often caused by tumors and may be caused by primary neural tumors such as neuroma, neurofibroma, and schwannoma (Figs. 8, 9). Intrinsic compression also results from metastases, lymphoma, or direct extension of a non-neural primary tumor as seen with breast carcinoma and the brachial plexus (Fig. 10). Granulomatous infiltration as seen in sarcoidosis may also present as an intrinsically compressive mass as can postradiation scar tissue [19]. Postradiation injury however, is frequently seen as diffuse nerve swelling with T2-hyperintensity conforming to the field of radiation. Hypertrophic neuropathy may mimic a primary nerve tumor, such as schwannoma [19].

In the absence of a mass lesion or nerve enlargement, it is imperative to scrutinize for abnormal nerve signal as acute nerve injury (intermittent trauma or ischemia) may alter nerve physiology without altering nerve morphology. Animal models have shown that acute nerve compression can cause transient alterations in axonal transportation without Wallerian degeneration or detectable morphologic changes [21–23]. Axonal transportation occurs at varying rates of speed, is bidirectional, and moves axonal water and many substances such as neurotransmitters, enzymes, and cytoskeleton proteins along the axon to and from the cell body. Disruption of axonal transport can lead to inhibited axoplasm water flow and thus lead to localized or diffuse increase in axoplasm water content.

Based on this model, Gupta et al [24] produced compression injury to the sciatic nerve of rats to produce altered neural function without morphologic injury. MR imaging was performed at 24 hours and again between 24 to 96 hours after surgery. The opposite sciatic nerve was exposed but not compressed to serve as an internal control. Signal intensity was measured on T2-weighted images of background muscle (to correct for signal intensity variations within the field of view), compressed nerve, and normal nerve at multiple locations and histologic evaluation was performed to exclude morphologic changes. There was no significant difference in the nerve or muscle signal intensity ratio at different locations of the control

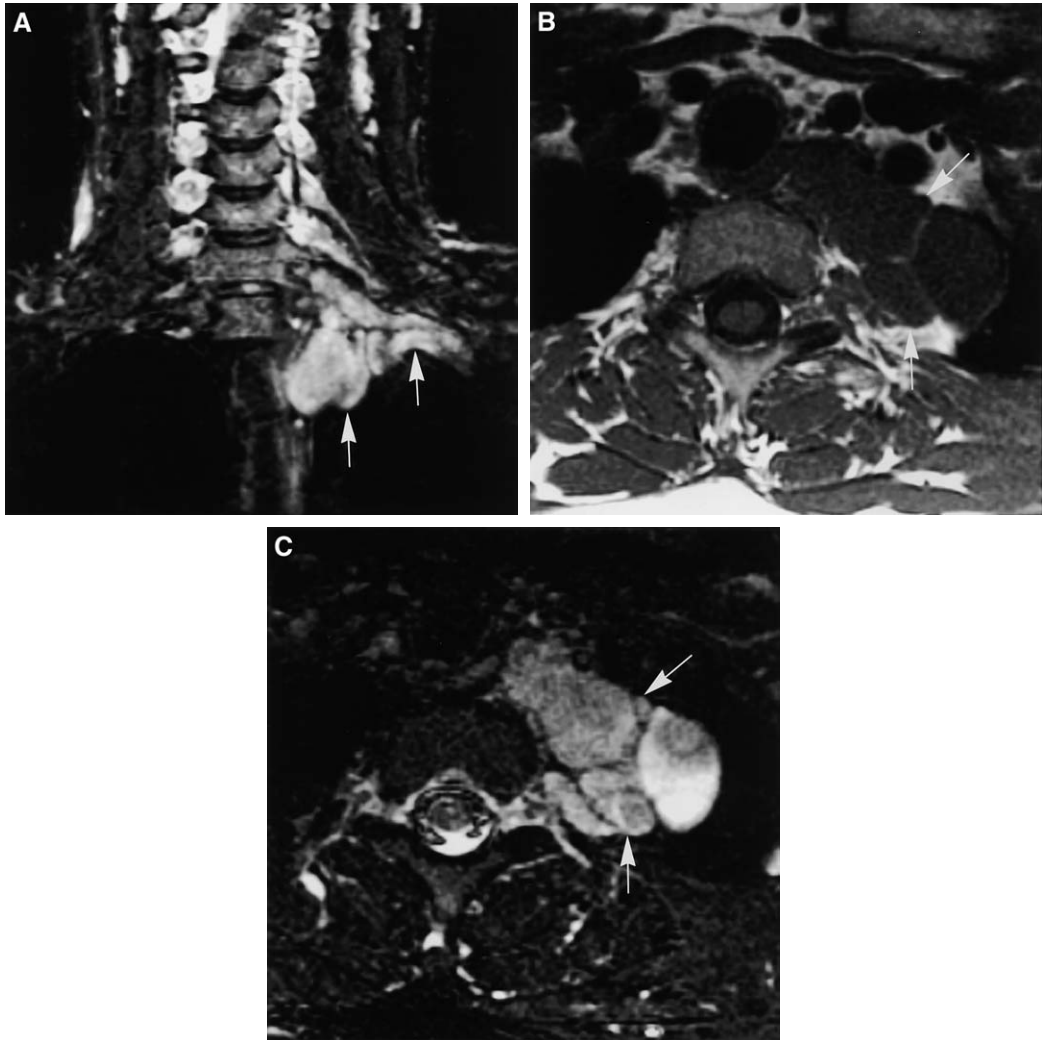


Fig. 8. Neurofibroma of brachial plexus. (A) Coronal T2-weighted FSE image with fat suppression shows a hyperintense mass in the left paraspinal region with extension along the C8 and T1 nerve roots and proximal inferior trunk (arrows). Axial T1-weighted (B) and T2-weighted FSE with fat saturation (C) images further show the mass to be multi-lobulated with heterogeneous signal on T2-weighted images. (From Moore KR. Spine Image Archive. Salt Lake City (UT): Advanced Medical Imaging; Accessed June 2003; with permission.)

sciatic nerve but there was statistically significant increased signal intensity in the compressed nerve both at the level of injury and distal to the level of injury. There was, however, no significant difference in signal intensity between normal nerve and nerve proximal to the level of injury on the compressed side. Given the distribution of abnormal signal in the compressed nerve, it is likely that ischemic effects play a role in the mechanism of this type of injury. It is also possible that disruption of axoplasm transport leads to a greater accumulation of water at the point of injured

nerve resulting in greater accumulation of axonal water distal to the injury. Application to human subjects may allow identification of an injured nerve segment in the absence of a morphologic abnormality that results from intermittent compression as is seen in several entrapment syndromes.

A correlation between abnormal high signal on T2-weighted MR imaging of human nerves and abnormal clinical and electrodiagnostic studies has been shown in a limited number of patients [25,26]. Quantitative image analysis of nerve

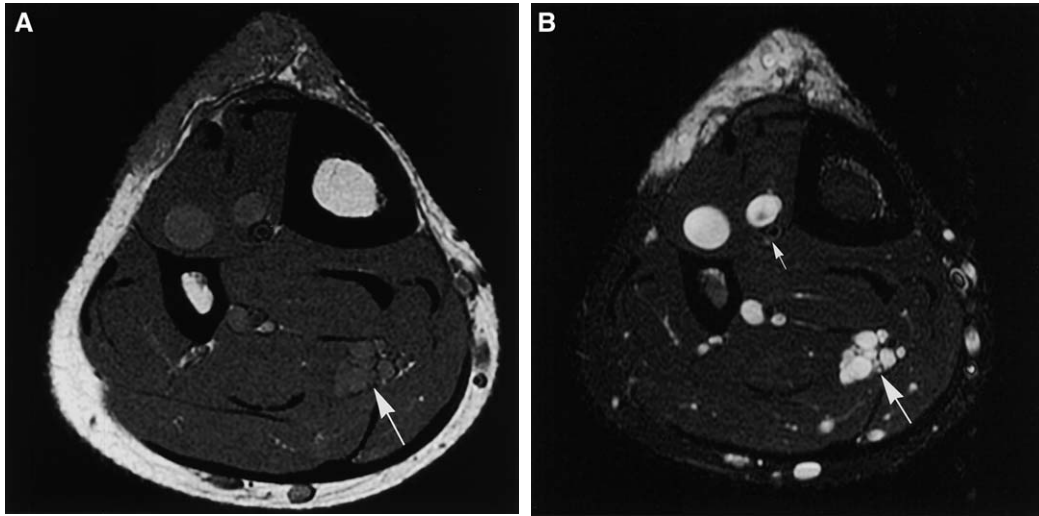


Fig. 9. Neurofibroma of tibial nerve. (A) Axial T1-weighted image shows a soft tissue lesion (*arrow*) with signal similar to adjacent vessels and higher in signal than adjacent muscle. (B) Axial STIR image at same level as A shows that the lesion signal intensity (*long white arrow*) increases similar to that of adjacent blood vessels compared with the normal deep peroneal nerve (*short white arrow*). (From Moore KR. Spine Image Archive. Salt Lake City (UT): Advanced Medical Imaging; Accessed June 2003; with permission.)



Fig. 10. Non-Hodgkin's Lymphoma. Coronal T2-weighted FSE image with fat suppression shows abnormally thickened lumbar nerve roots with extension into the lumbar plexus (*arrows*) tracking medial to the right psoas muscle. The abnormal plexus shows moderate abnormally increased signal intensity. This was secondary to lymphomatous involvement of the neural axis. (From Moore KR. Spine Image Archive. Salt Lake City (UT): Advanced Medical Imaging; Accessed June 2003; with permission.)

signal has further potential for evaluating patients with radicular symptoms and multilevel disc or spondylotic disease [26]. Detection of abnormal increased cervical nerve root signal on T2-weighted images caused by proximal compression may select patients and cervical levels most likely to benefit from decompression surgery. Larger human case studies however, will be necessary before global application is acceptable.

Peripheral nerve recovery from trauma also may be followed with MRPNI. Severe injury to a peripheral nerve may result in axonal disruption whereas the Schwann cells and endoneurium remain intact, resulting in Wallerian degeneration [20]. Wallerian degeneration results in an increase in nerve water content (25% increase in water content by day 15 post-injury) believed to result from a decrease in membrane bound water and an associated increase in extracellular water [27]. This leads to prolongation of the T1 and T2 relaxation times on MR imaging. The intact endoneurium however, permits axonal regeneration and potential restoration of nerve function. Using a rat sciatic nerve crush model, Cudlip et al [28] have shown that quantitative assessment of nerve signal may confirm acute nerve injury and that a return toward normal signal correlates with functional improvement. Increased T2 signal peaks at 14 days after the injury, as does maximal functional deficit as measured by walking-track analysis. T2

signal decreases proportionally to functional recovery over time with near-normal signal and return of normal function at 70 days post-injury.

Dailey et al [29] reported a case of a young man with traumatic laceration of the peroneal branch of the sciatic nerve. Despite surgical anastomosis, follow-up electrodiagnostic tests showed no re-innervation and T2-weighted MRPNI showed persistent increased signal at and distal to the level of injury. The scarred segment was subsequently excised and a sural nerve graft was used across the gap. MRPNI showed progressive normalization of the distal nerve signal as function returned by clinical exam and EMG. While experience in this clinical setting is limited and the exact time course of human nerve regeneration and corresponding MR signal intensity change needs further study, preliminary evidence suggests that MRPNI may be a useful monitoring tool for nerve recovery.

Summary

MRM is a useful imaging technique that can be incorporated into routine spine MR imaging protocols without a significant increase in imaging time or patient discomfort. When combined with high quality, sequential (no inter-slice gap), axial images of the spine, the authors have found that it decreases the surgeon's need for conventional contrast enhanced myelography by showing the etiology of compression and degree of compressive effect, particularly in cases of degenerative spine disease. In select cases where greater bone detail is desired, an unenhanced CT is often sufficient.

MRPNI also is a useful imaging technique that is primarily used in the evaluation of patients with radicular symptoms not explained by spine MR imaging findings. Selective MRPNI is performed based on clinical and electrodiagnostic results to evaluate extra-spinal causes of peripheral neuropathy. It is easily performed using phase array coils and is primarily used to detect traumatic axonal disruption and compressive neuropathy.

References

- [1] Henning J, Friedburg H, Stroebel B. Rapid non-tomographic approach to MR myelography without contrast agents. *J Comput Assist Tomogr* 1986;10:375–8.
- [2] Krudy AG. MR myelography using heavily T2-weighted fast spin-echo pulse sequences with fat presaturation. *AJR* 1992;159:1315–20.
- [3] VanDyke CW, Modic MT, Beale SM, Martur S, Ross JS. Technical note: 3D MR myelography. *J Comput Assist Tomogr* 1992;16(3):497–500.
- [4] Nasu K, Takano H, Ito H. Vascular suppression technique in MRI using Gd-DTPA improving image quality of MR myelography. *J Comput Assist Tomogr* 1999;23:346–50.
- [5] Demaerel P, Bosmans H, Wilms G, Aerts P, Gaens J, Goffin J, et al. Rapid lumbar spine MR myelography using rapid acquisition with relaxation enhancement. *AJR* 1997;168:377–8.
- [6] Figueroa RE, Stone JA. MR imaging of degenerative spine disease: MR myelography and imaging of the posterior spinal elements. In: Castillo M, editor. *Spinal imaging: state of the art*. Philadelphia: Hanley and Belfus Inc.; 2001. p. 105–22.
- [7] Karantanas AH, Zibis AH, Papanikolaou N. Single-shot turbo spin-echo MR myelography: comparison with 3D-turbo spin-echo MR myelography and T2-turbo spin-echo at 1T. *Comput Med Imaging Graph* 2000;24:37–42.
- [8] Kuroki H, Tajima N, Hirakawa S, Kubo S, Tabe R, Kakitsubata Y. Comparative study of MR myelography and conventional myelography in the diagnosis of lumbar spinal diseases. *J Spinal Disord* 1998;11:487–92.
- [9] Eberhardt KEW, Hollenbach HP, Tomandl B, Huk WJ. Three-dimensional MR myelography of the lumbar spine: comparative case study to X-ray myelography. *Eur Radiol* 1997;7:737–42.
- [10] Ramsbacher J, Schilling AM, Wolf KJ, Brock M. Magnetic Resonance Myelography (MRM) as a spinal examination technique. *Acta Neurochir (Wien)* 1997;139:1080–4.
- [11] Howe JF, Loeser JD, Calvin WH. Mechanosensitivity of dorsal root ganglia and chronically injured axons: a physiological basis for the radicular pain of the nerve root compression. *Pain* 1977;3:25–41.
- [12] Wienstein J. Mechanism of spinal pain: the dorsal root ganglion and its role as a pain mediator of low-back pain. *Spine* 1986;22:999–1001.
- [13] Yohichi A, Katsuhiko O, Howard A, Kohki Y. Dorsal root ganglia morphological features in patients with herniation of the nucleus pulposus: assessment using magnetic resonance myelography and clinical correlation. *Spine* 2001;26:2125–32.
- [14] Nakamura T, Yabe Y, Horiuchi Y, Takayama S. Magnetic resonance myelography in brachial plexus injury. *Journal of Bone and Joint Surgery* 1997; 79-B:764–9.
- [15] Gasparotti R, Ferraresi S, Pinelli L, Crispino M, Pavia M, Bonetti M, et al. Three-dimensional MR myelography of traumatic injuries of the brachial plexus. *Am J Neuroradiol* 1997;18:1733–42.
- [16] Zeng Q, Xiong L, Jinkins JR, Fan Z, Liu Z. Intrathecal gadolinium-enhanced MR myelography and cisternography: a pilot study in human patients. *AJR* 1999;173:1109–15.
- [17] Jinkins JR, Rudwan M, Krumina G, Tali ET. Intrathecal gadolinium enhanced MR cisternography in

- the evaluation of clinically suspected cerebrospinal fluid rhinorrhea in humans: early experience. *Radiology* 2002;222:555–9.
- [18] Maravilla KR, Bowen BC. Imaging of the peripheral nervous system: evaluation of peripheral neuropathy and plexopathy. *Am J Neuroradiol* 1998; 19:1011–23.
- [19] Moore KR, Tsuruda JS, Dailey AT. The value of MR neurography for evaluating extraspinal neuropathic leg pain: a pictorial essay. *Am J Neuroradiol* 2001;22:786–94.
- [20] Maravilla KR, Aagaard BDL, Kliot M. MR neurography: MR imaging of peripheral nerves. *MR Clinics of North America* 1998;6:179–94.
- [21] Kitao A, Hirata H, Morita A, Yoshida T, Uchida A. Transient damage to the axonal transport system without Wallerian degeneration by acute nerve compression. *Exp Neurol* 1997;147:248–55.
- [22] Dahlin LB, McLean WG. Effects of graded experimental compression on slow and fast axonal transport in rabbit vagus nerve. *J Neurol Sci* 1986;72:19–30.
- [23] Dahlin LB, Sjöstrand J, McLean WG. Graded inhibition of retrograde axonal transport by compression of rabbit vagus nerve. *J Neurol Sci* 1986; 76:221–30.
- [24] Gupta R, Villablanca PJ, Jones NF. Evaluation of an acute nerve compression injury with magnetic resonance neurography. *J Hand Surg [Am]* 2001; 26A:1093–9.
- [25] Kuntz C IV, Blake L, Britz G, Filler A, Hayes CE, Goodkin R, et al. Magnetic resonance neurography of peripheral nerve lesions in the lower extremity. *Neurosurgery* 1996;39:750–7.
- [26] Dailey AT, Tsuruda JS, Goodkin R, Haynor DR, Filler AG, Hayes CE, et al. Magnetic resonance neurography for cervical radiculopathy: a preliminary report. *Neurosurgery* 1996;38:488–92.
- [27] Jolesz FA, Polak JF, Ruenzel PW, Adams DF. Wallerian degeneration demonstrated by magnetic resonance: spectroscopic measurements on peripheral nerve. *Radiology* 1984;152:85–7.
- [28] Cudlip SA, Howe FA, Griffiths JR, Bell A. Magnetic resonance neurography of peripheral nerve following experimental crush injury, and correlation with functional deficit. *J Neurosurg* 2002;96:755–9.
- [29] Dailey AT, Tsuruda JS, Filler AG, Maravilla KR, Goodkin R, Kliot M. Magnetic resonance neurography of peripheral nerve degeneration and regeneration. *Lancet* 1997;350:1221–2.



MR angiography of the spine: update

Brian C. Bowen, PhD, MD^{a,b,c,*}, Efrat Saraf-Lavi, MD^b,
Pradip M. Pattany, PhD^{a,c}

^a*Division of Neuroradiology/MRI Center, Department of Radiology (R-308), University of Miami School of Medicine, 1115 Northwest 14th Street, Miami, FL 33136, USA*

^b*Department of Radiology, Jackson Memorial Medical Center, 1611 North West 12th Avenue, Miami, FL 33136, USA*

^c*Miami Project to Cure Paralysis, University of Miami School of Medicine, 1095 North West 14th Terrace, The Lois Pope Life Center, Miami, FL 33136, USA*

Since the publication of “MR Angiography of the Spine” in the 1998 Magnetic Resonance Imaging Clinics of North America volume entitled “New Techniques in MR Neuroimaging” [1], three important developments in noninvasive spinal vascular imaging have occurred:

- (1) Fast (dynamic, time-resolved, or first pass) three-dimensional (3D) contrast-enhanced (CE) MR angiography (MRA) has been applied to the detection of normal and abnormal spinal vessels [2–7].
- (2) Retrospective review of the results of “standard” spinal MRA studies over an 8-year period (1992–2000) has been published by each of two groups [8,9].
- (3) Helical CT angiography has been applied to the detection of the major spinal vessels in patients with thoracoabdominal occlusive vascular disease [10].

This article focuses on the first 2 developments. The emphasis, as in 1998, will be on the appearance of intradural spinal vessels on 3D CE MRA and on spin-echo MR imaging of individuals without and with vascular lesions, in comparison to the appearance of the same vessels

on digital subtraction x-ray angiography (DSA). Spinal vascular anatomy is not reviewed in this article. The reader is referred to the earlier article [1] for a complete description of the nomenclature, location, number, and sizes of the major intradural vessels:

- (1) On the cord surface—anterior spinal artery, posterolateral spinal arteries, and pial arterial plexus and the anterior median vein, posterior median vein, and coronal venous plexus.
- (2) Extending from the cord surface to the epidural space—anterior and posterior medullary arteries (also referred to as radiculomedullary and radiculo-pial arteries [11], respectively), and the anterior and posterior medullary veins (also referred to as radiculomedullary veins). Some investigators simply refer to all vessels accompanying nerve roots as “radicular” vessels [12].

Techniques: 3D contrast-enhanced MR angiography

All spinal MRA studies are now performed during or after intravenous infusion of a gadolinium-chelate contrast agent, with doses ranging from 0.1 to 0.3 mmol gadolinium per kg body weight. Primarily, two approaches to data acquisition are now used: an older, “standard” approach and a newer, “fast” approach.

Standard 3D contrast enhanced MR angiography

The first approach has been applied, with some modifications, for almost a decade [13]. This

* Corresponding author. Division of Neuroradiology/MRI Center, Department of Radiology (R-308), University of Miami School of Medicine, 1115 Northwest 14th Street, Miami, FL 33136.

E-mail address: bbowen@med.miami.edu
(B.C. Bowen).

approach uses traditional 3D time-of-flight MRA pulse sequences with TR values of 20 to 50 milliseconds and scan times on the order of 10 minutes per 3D volume. Vascular contrast is primarily caused by the relative T1 shortening of

flowing blood by gadolinium in spinal vessels rather than “time-of-flight” differences in signal intensity. Normal intradural vessels are undetectable on pre-contrast MRA acquisitions [1,14]. Despite the long scan times, a sufficient difference

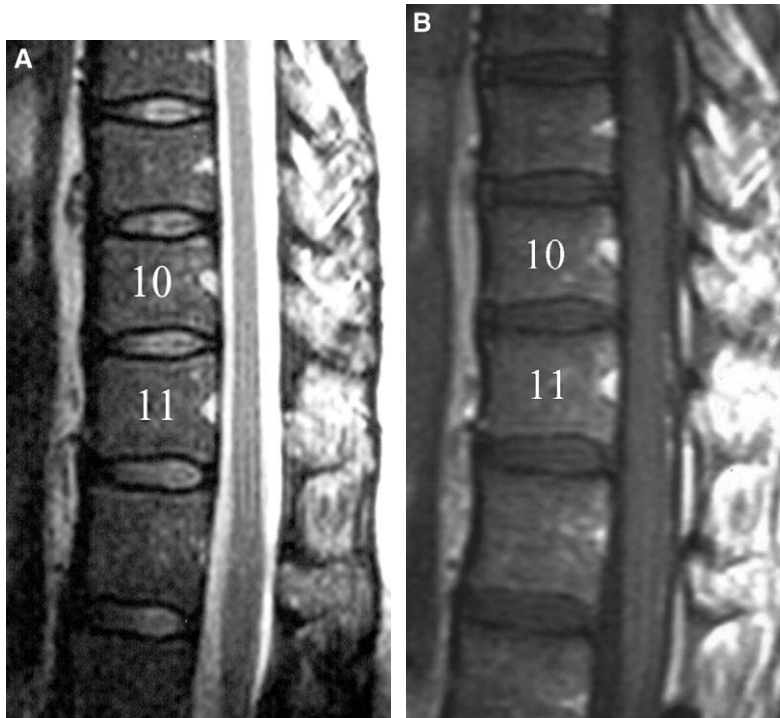


Fig. 1. MR imaging, standard 3D CE MRA, and DSA of normal intradural vessels. (A) Midsagittal T2-weighted fast-spin-echo MR image. The spinal cord is normal in size and signal intensity. No “flow voids” are detected in the subarachnoid space. The T10 and T11 vertebral bodies are identified by the numbers 10 and 11. (B) Postcontrast T1-weighted MR image. Vessel-like, serpentine enhancement is detected on the posterior surface of the cord at T11 and faintly at T12. No linear enhancement is identifiable on the anterior surface of the cord. There is no abnormal enhancement of the cord itself. (C) DSA from the same patient—left anterior oblique view at 19 seconds following injection of the left L2 lumbar artery. Only the veins are opacified. The anterior (*small open arrows*) and the larger, more tortuous posterior (*large open arrows*) median veins are shown. The two vessels have an anastomosis (*small arrowhead*) around the right side of the cord at the T10-T11 level. The left L1 medullary vein (*closed arrow*) is shown to be a posterior draining vein, based on its confluence with the posterior median vein. A “kink” (*large arrowhead*) in the anterior median vein was used as a marker for identifying this vein on 3D MRA MIP images and distinguishing it from the anterior spinal artery. The approximate locations of the T10 and T11 neural foramina are indicated by the numbers 10 and 11. (D) Standard 3D CE MRA sagittal maximum-intensity-projection (MIP) image targets the midline vessels with a volume-of-interest approximately 3 mm thick. The vessels, which correspond to the anterior and posterior median veins described in (C) are better shown than in the MR images (A) and (B). The superior portion of the posterior median vein seems to end at T10-T11, consistent with the findings in (C) and (E). (E) Coronal MIP image encompassing approximately the posterior half of the spinal canal targets the posterior median vein (*open arrows*), the left L1 great posterior medullary vein (*large arrow*), the T10 posterior draining veins (*small arrows*), and the anastomotic loop at T11 (*arrowhead*). Identification of the vessels as veins is based on a comparison between (E) and (C). The right T10 and T11 neural foramina are indicated. (F) Coronal MIP image encompassing approximately the anterior 10% to 20% of the canal targets the anterior median vein in the midline, the right T10 anterior medullary vein (*arrow*), the anastomotic loop at T10-T11 (*small arrowhead*), and the “kink” (*large arrowhead*) in the anterior median vein (compare with C). (From Bowen BC, DePrima S, Pattany PM, et al. MR angiography of normal intradural vessels of the thoracolumbar spine. Am J Neuroradiol 1996;17:483–94; with permission.)

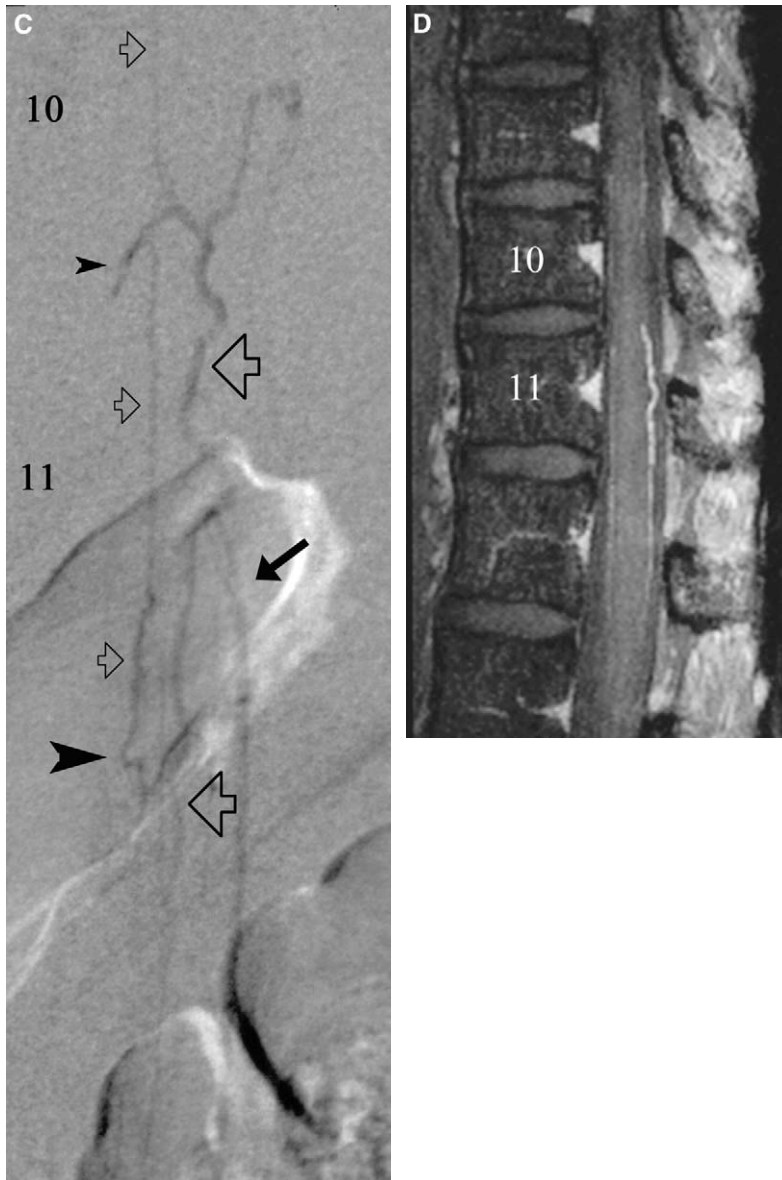


Fig. 1 (continued)

in gadolinium concentration (intravascular > extravascular) exists during the post-contrast acquisitions that the largest normal spinal vessels (principally veins) can be readily detected (Fig. 1). This approach has been referred to as “standard,” or “steady-state,” 3D CE MRA [4].

The CE MRA data are acquired at 1.0 T or 1.5 T as a single 3D slab that has sagittal (or coronal) orientation and encompasses the spinal canal in the antero-posterior (A-P) and right-left (R-L)

directions [13,14]. The pulse sequence is typically a radiofrequency (RF)-spoiled, flow-compensated, gradient-echo sequence (40–50 milliseconds/8–10 milliseconds/20° [repetition time (TR)/echo time (TE)/flip angle]) with 30 cm field-of-view (FOV), 400 (phase) × 360 (read) matrix, phase sampling ratio 0.758, and 0.8 mm slice (partition) thickness, producing an effective voxel size of approximately 0.5 mm³. Similar vascular contrast has been obtained with values of (29 milliseconds/

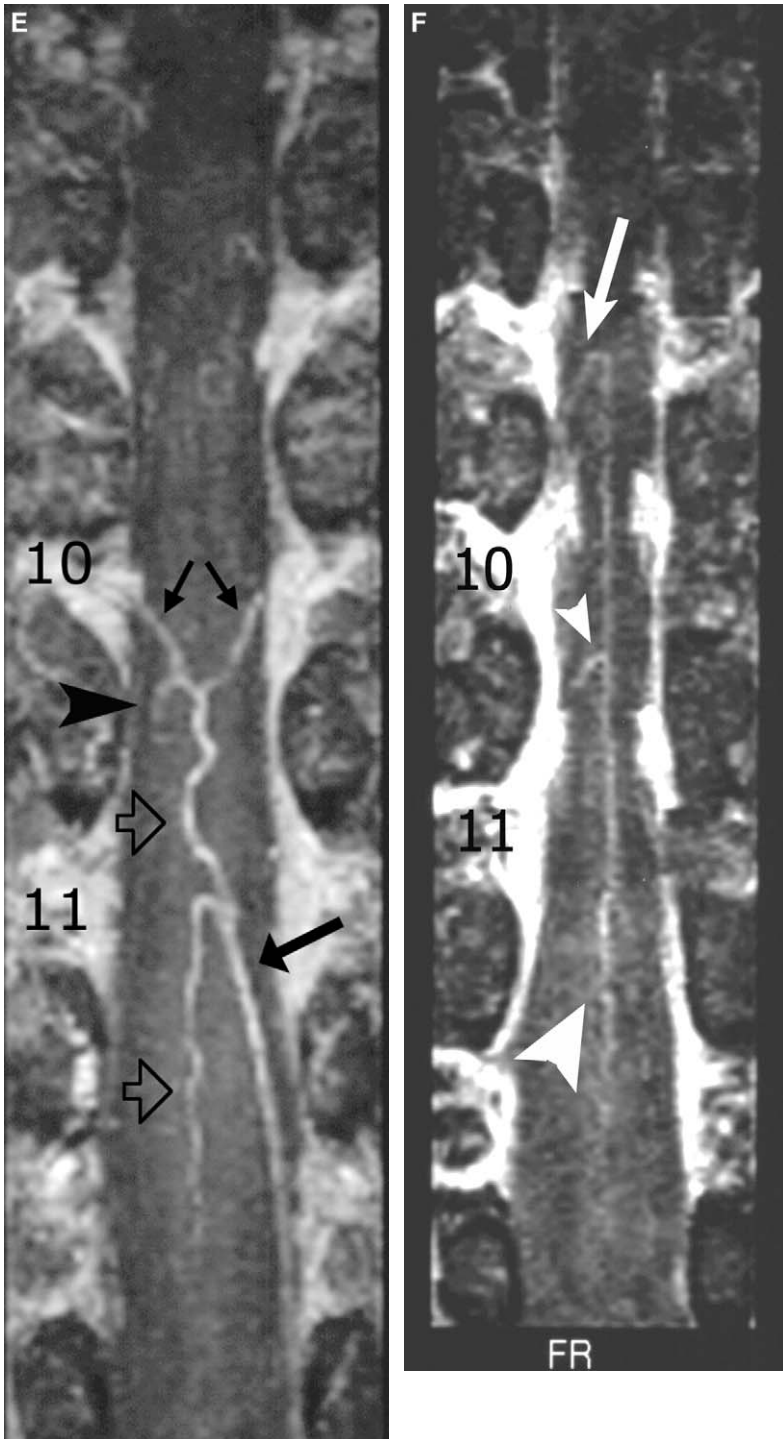


Fig. 1 (continued)

4.8 milliseconds/15°) for [TR/TE/flip angle] (B. Bowen and P. Pattany, unpublished observations, 2003). Spatial presaturation pulses are used to reduce or eliminate aliasing and motion-induced artifacts. For sagittal slab acquisitions, one presaturation zone covers the abdomen and chest anterior to the aorta and a second presaturation zone covers the cutaneous and subcutaneous tissues of the back (thoracolumbar MRA). In the neck and upper chest, the presaturation zones cover the soft tissues anterior to the airway and posterior to the spinal canal (cervicothoracic MRA).

Although less commonly used in current practice, “standard” (TR ~25–60 milliseconds) gadolinium-enhanced phase contrast (PC) MRA, with two-dimensional (2D) or 3D acquisition techniques, has been applied previously to image spinal vascular malformations, before and after treatment [8,15–17]. Small vessels with complex flow are better delineated with 3D than with 2D PC MRA when similar velocity encoding (VENC) values are used for both techniques. No reports describing the appearance of normal intradural vessels on standard PC MRA have appeared in the literature.

Fast 3D contrast enhanced MR angiography

The more recent approach uses higher performance gradient coils and rapid gradient-echo pulse sequences to achieve TR values less than 10 milliseconds and scan times less than 1 minute (as low as 5–10 seconds) per 3D volume, and incorporates various methods of k-space sampling. This approach has been referred to as “fast,” “dynamic,” “time-resolved,” or “first-pass” (bolus) 3D CE MRA [18]. Both the “standard” and the “fast” 3D CE MRA approaches are capable of displaying normal intradural vessels [4,5], and both have been applied to the study of vascular lesions of the spine or spinal cord.

With fast 3D CE MRA, the image data are acquired from a single 3D slab, with sagittal or coronal orientation, encompassing the spinal canal in A-P and R-L directions [2,3,5–7]. In most published studies, one 3D data set (“mask”) is acquired before contrast enhancement, followed by serial acquisition of three or four complete 3D data sets (phases) without interruption. An exception is the auto-triggered, elliptic-centric-ordered, first-pass 3D CE MRA technique reported by Farb and colleagues [7], in which only one 3D data set is acquired and postprocessed for vessel display. The

goal of the fast technique with multiple acquired phases is to capture predominantly arterial enhancement in the early phases and predominantly venous enhancement in later phases (Fig. 2). Temporal resolution of arterial and venous enhancement depends on the complex relationship between k space sampling method, acquisition (scan) time required for each 3D data set, and the arrival and transit times of the contrast bolus for the region of interest. Based on DSA studies, an estimate for the average length of time between optimal anterior spinal artery enhancement and optimal median vein enhancement in the thoracolumbar region is approximately 10 seconds [14].

The data acquisition and image reconstruction parameters reported for the fast technique with multiple acquired phases are typified by the values used by Binkert and colleagues [2], although shorter TR and TE values and higher spatial resolution are now attainable on commercially available whole body MR scanners. Binkert et al [2] used a 3D gradient-echo pulse sequence with the following parameters: 7 milliseconds/2.3 milliseconds/25° [TR/TE/flip angle], 28 cm FOV (3/4 phase), and 0.5 NEX. Data were acquired with 34 slices, each 2 mm thick, 192 (phase) × 256 (read) in-plane matrix size, and then increased to 57 slices with 384 × 512 matrix size by zero-fill interpolation, producing an effective voxel size of approximately 1 mm³. For the 3D CE MRA acquisition, Binkert et al [2] administered a gadolinium dose of 0.2 mmol/kg at a rate of 3 mL/second, and following the appropriate time delay, the data were acquired with sequential k-space encoding. The scan time per 3D volume was 24 seconds.

Binkert and colleagues [2] determined the appropriate delay time between intravenous injection of the contrast bolus and the initiation of the 3D MRA data acquisition using a 2 mL (1 mmol) test dose of gadolinium chelate with rapid sampling of the signal in the mid-thoracic aorta by a single slice (sagittal) 2D gradient-echo technique. Other investigators have used alternative schemes: Yamada et al [5] sampled the signal in the descending aorta in a single axial section located at the diaphragm, whereas Shigematsu et al [6] initiated the 3D acquisition at the start of the bolus injection.

Fast 3D CE MRA using elliptic centric k-space encoding seems promising because the sampling of peripheral lines of k space, after the central lines (responsible for vessel signal and contrast) have been acquired, improves spatial resolution (vessel detail) [4,7,19,20]. Farb and

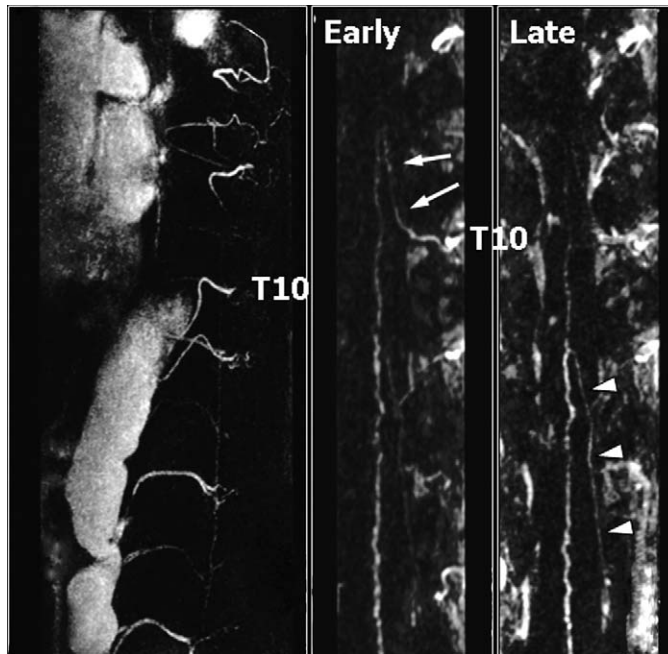


Fig. 2. Fast 3D contrast-enhanced MRA of the artery of Adamkiewicz and the great anterior medullary vein in a 72-year-old woman with an aneurysm of the descending aorta. The left frame of the figure demonstrates 3 MIP views of the aorta with the lower half of the frame showing the lateral view and the origin and proximal portion of the left T10 intercostal artery. The middle frame is a coronal MIP image from the “early phase” 3D MRA volume acquisition. This MIP image, which is targeted to the spinal canal, shows the artery of Adamkiewicz (*arrows*) originating from the left T10 intercostal artery in the neural foramen and ascending to join a midline vessel in the canal. The right frame is a coronal, targeted MIP image from the “late phase” 3D volume acquisition. This image shows a left anterior medullary vessel (*arrowheads*), which extends from the midline vessel on the cord to the left L1 neural foramen. The medullary vessel is more intense on the “late phase” image, and therefore represents a left L1 anterior medullary vein. The midline vessel on the cord surface represents the incompletely resolved anterior spinal artery and the anterior median vein. The level of the T10 neural foramina is labeled for the “early” and “late” phase MIP images. (*From Yamada N, Takamiya M, Kuribayashi S, et al. MRA of the Adamkiewicz artery: a preoperative study for thoracic aortic aneurysm. J Comput Assist Tomogr 2000;24:362–68; with permission.*)

colleagues [7] reported sequence parameters of 6.2 milliseconds/1.5 milliseconds/30° [TR/TE/flip angle], 36×27 cm FOV (3/4 phase), 352×352 matrix, 70 sections, each 1.2 mm thick, achieving voxel dimensions of 1×1×1.2 mm without zero-filling techniques. Scan time, though, was approximately 2 minutes per 3D volume—approximately five times the scan time of Binkert et al [2] and other investigators noted previously, and 10 times the estimated time difference between optimal arterial and venous opacification on DSA. Thus, despite careful synchronization of the initiation of 3D data sampling and the “first pass” arrival of the contrast bolus, temporal separation of arterial and venous signal changes with the elliptic centric ordering 3D CE MRA technique is difficult [4,7].

Postprocessing

For the standard and fast 3D CE MRA techniques, targeted, maximum intensity projection (MIP) images of the spinal vessels are produced from subsets of the source image data (subvolumes) by manual selection of a region-of-interest (ROI). Based on our experience we recommend the following approach to display intradural vessels detected on sagittal source images with the standard CE MRA method: (1) generate four or five coronal MIP images (each from a ROI thickness equal to approximately one-fourth of the spinal canal AP diameter) progressing from the posterior to the anterior margin of the canal; (2) generate four or five sagittal MIP images in a similar fashion, progressing from the right side

to the left side of the canal; (3) for the coronal and sagittal subvolumes that best display the vessels, modify the thickness or angulation of the ROI, and repeat the MIP until the greatest length and intensity of the intradural vessels on the posterior

or anterior surface of the cord are achieved (Fig. 3). The ROIs that are drawn for the coronal MIPs usually have curved anterior and posterior margins because the spine characteristically has anterior-posterior curvature. In some cases, multiplanar



Fig. 3. Left T12 dural AVF. All three reviewers in the study by Saraf-Lavi and colleagues thought that a fistula was present based on the MR imaging (true positive result, *A* and *B*) and based on MR imaging plus standard 3D contrast-enhanced MRA (true positive result, *A–E*) findings. (*A*) T2-weighted fast-spin-echo MR image shows hyperintense cord from T9 to the conus tip and serpentine flow voids, consistent with enlarged intradural vessels, posterior to the cord from T6 to T10 (note serrated appearance of the posterior margin of the cord). (*B*) Postcontrast T1-weighted MR image shows patchy enhancement within the cord from T9 to the conus tip. (*C*) MR angiography sagittal MIP image demonstrates marked tortuosity and length of a posterior perimedullary, intradural vessel, corresponding to the posterior median vein. (*D*, *E*) The coronal MIP images are targeted to the posterior half of the thoracic spinal canal in (*D*) and to the more anterior portion of the canal in (*E*) which demonstrates an enlarged, tortuous vessel (*arrow*) extending toward the left T12 foramen. The vessel corresponds to the left T12 anterior medullary vein. The left pedicle of T12 is labeled. (*F*) DSA posteroanterior view, following injection of the dorsal ramus of the left T12 intercostal artery, shows the fistula (*arrowhead*) and draining medullary vein (*arrow*). (From Saraf-Lavi E, Bowen BC, Quencer RM, et al. Detection of spinal dural arteriovenous fistula with MR imaging and angiography: sensitivity, specificity, and prediction of vertebral level. *Am J Neuroradiol* 2002;23:858–67; with permission.)

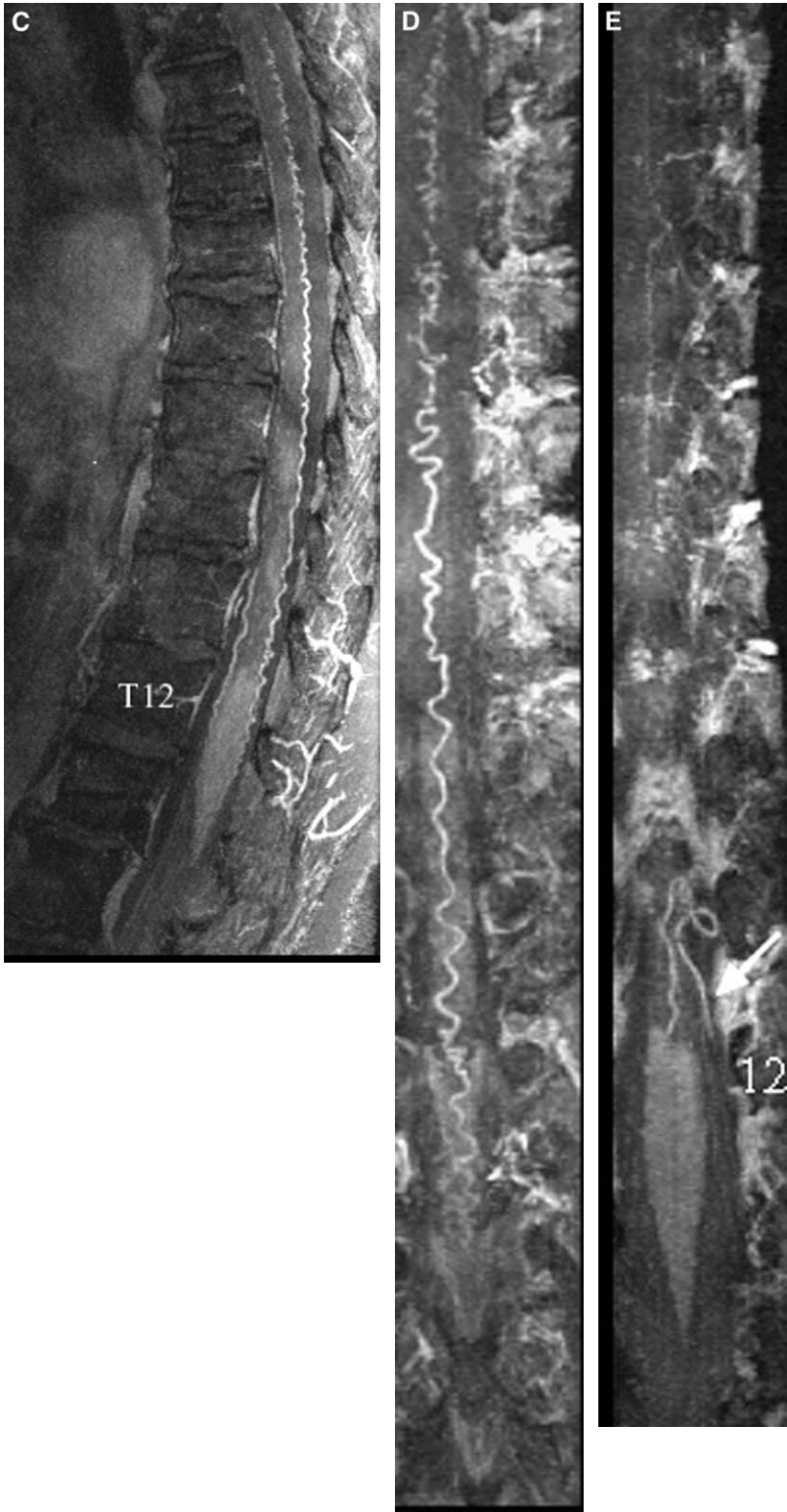


Fig. 3 (continued)



Fig. 3 (continued)

reformatting before application of the MIP algorithm improves the display of vessels. Unfortunately, not all scanner manufacturers offer MIP algorithms that have the range of capabilities described above. When the MIP options are limited, the multiplanar reformatted sections may provide the best display of intradural vessels. Although gadolinium enhancement of a mass or the cord itself in pathologic conditions can potentially obscure or mimic the enhancement within spinal vessels on CE MRA, this shortcoming has rarely occurred in our experience [13].

Appearance of spinal intradural vessels on MR imaging and MR angiography

Normal vessels

Only the largest intradural vessels, measuring approximately 1 mm in diameter, are displayed on the sagittal and coronal MIP images. Standard CE 3D MRA of the thoracolumbar region demonstrates vessels that correspond to the major intradural veins (see Fig. 1). The venous anatomy is better displayed on CE MRA sagittal MIP images (see Fig. 1D) than on postcontrast T1-weighted sagittal images (see Fig. 1B). The tortuosity of normal anterior and posterior median veins is variable, but usually not extreme. Occasionally, the tortuosity (as measured in turns

per vertebral segment) of either of these veins may be marked and extend over several vertebral levels so that the appearance mimics that observed in patients with vascular malformations [9]. The appearance of the posterior median vein on CE MRA and the appearance of the “filling defect” produced by the vein on supine thoracic myelography are similar [21].

The major intradural arteries, including the artery of Adamkiewicz, are shown poorly, or not at all, on MIP images from standard 3D CE MRA [14]. Presumably, veins are preferentially shown because of their greater diameter and hemodynamics (lack of pulsatile flow and hairpin turns). With the standard CE technique, normal veins and arteries cannot be distinguished *de novo* except by anatomic differences in vessel location, of which the most distinctive finding is the presence of a large vein (posterior median vein), and no large artery, in the midline of the posterior surface of the cord.

The “fast” contrast-enhanced technique offers the possibility of distinguishing between the largest intradural arteries and veins by temporally resolving the arterial and venous phases of the contrast bolus. As discussed earlier, though, adequate temporal resolution is difficult because 3D-volume acquisition times of about 10 to 15 seconds may be necessary for a clear distinction between arteries and veins [5,14]. Using a “fast” technique with 3D-volume acquisition times of 34 to 45 seconds, Yamada and colleagues [5] have shown that vessels larger than 0.5 mm diameter may be detected and that the artery of Adamkiewicz can be distinguished from the great medullary vein (see Fig. 2). Distinguishing between the two vessels is tedious, however, since identification of the artery is contingent on tracking its course from the dorsal branch of the intercostal or lumbar artery to its junction with the anterior spinal artery on the cord surface. A similar approach has been used to identify the artery of Adamkiewicz on contrast-enhanced, multi-detector row, helical CT angiography (CTA) [10].

Yamada and colleagues [5] tracked the artery of Adamkiewicz on targeted MIP images constructed from double oblique, multiplanar reformatted (MPR) images that were derived from the original 3D source images. To improve arterial contrast, pre-injection “mask” source images were subtracted from the contrast-enhanced, early-phase source images. The primary criterion which was used to distinguish major arteries (eg, artery of Adamkiewicz and the anterior spinal artery)

from major veins (eg, anterior median vein and great medullary vein) was that arteries should exhibit an early-phase signal intensity that was equal to or greater than the late-phase signal intensity (see Fig. 2). This criterion may be difficult to verify for the midline vessels on the anterior surface of the cord where a prominent anterior median vein, for example, courses adjacent to, and is not spatially resolved from, the anterior spinal artery. Because of the proximity of the two vessels, the late-phase venous enhancement may obscure the declining enhancement in the anterior spinal artery and may exceed the early-phase enhancement, suggesting that only a midline vein is present [4].

Using the detailed postprocessing steps and the criterion described earlier, Yamada and colleagues [5] were able to identify the artery of Adamkiewicz in 69% of patients who underwent MR angiography before surgical or endovascular stent-graft repair of thoracic and abdominal aortic aneurysms. The anterior spinal artery caudal to the junction with the artery of Adamkiewicz was identified in only 50% of the patients, while the anterior spinal artery cranial to the junction was never identified. The great anterior medullary vein was reportedly identified in 65% of patients; however, the investigators presented no targeted, midsagittal MIP images or source images to document that the vein displayed on coronal MIP images (see Fig. 2) was in fact the anterior, and not the posterior, medullary vein.

Regarding detection of the artery of Adamkiewicz, CTA may be more sensitive than MRA. Takase and colleagues [10] have reported that the artery was clearly visualized in 63 of 70 patients (90%) who underwent helical CTA for evaluation of presumptive thoracoabdominal vascular disease. Although this detection rate exceeds that of Yamada et al, no direct comparisons between MRA and CTA in the same patient population have been reported. Furthermore, Takase's study is limited by a lack of DSA documentation of the identity of intradural arteries as distinct from veins.

Detection of normal intradural vessels using PC MRA techniques has been disappointing. For 2D PC angiography, Mascalchi et al [16] found that modulus images failed to show the largest intradural vessels in normal volunteers. The anterior epidural venous plexus and basivertebral veins were demonstrated and appeared as single longitudinal and multiple transverse, well-defined stripes behind and within the vertebral bodies on

sagittal, low VENC acquisitions. Similarly, 3D PC angiography has not been shown to detect normal intradural vessels, or differentiate between arteries and veins. With PC techniques, the distinction between arteries and veins is likely to be difficult because of the overlap of velocities and the presence of bidirectional flow in the anterior spinal artery and the major coronal veins [11].

Abnormal vessels

Morphologic and flow-related differences on MR imaging between intradural vessels in normal controls and the vessels in patients with dural arteriovenous fistula (DAVF) have been examined retrospectively by Saraf-Lavi and colleagues [9] in the first part of a recently published study. They showed that two features of intradural vessels in patients were abnormal and that these features were strongly associated with the presence of fistula. First, visibility of flow voids on T2-weighted images was greater, and could be recognized by the significantly increased percentage of patients (compared with controls) with flow voids extending for a distance of at least three vertebral segments (Fig. 4). Second, serpentine enhancement on postcontrast T1-weighted images was greater, and also was manifested as a significantly increased percentage of patients with this enhancement extending for a distance of at least three vertebral segments (see Fig. 4).

Also, in the first part of their study, Saraf-Lavi and colleagues [9] evaluated morphologic and flow-related differences detected on standard 3D CE MRA for the same subject groups (Fig. 5). Features displayed on the MIP images, such as the length, tortuosity, and size (qualitatively) of the dominant intradural, perimedullary vessel, yielded significantly increased mean values for the group of patients with dural AVF compared with the control group. In future studies, these features could be used as criteria for determining the presence of DAVF prospectively.

Vascular malformations

The classification scheme of Anson and Spetzler [22] continues to be used in recent articles on MR angiography of the spine. This scheme recognizes 4 types of spinal vascular malformations:

Type I—dural arteriovenous fistula (AVF), with single (IA) or multiple (IB) feeding arteries

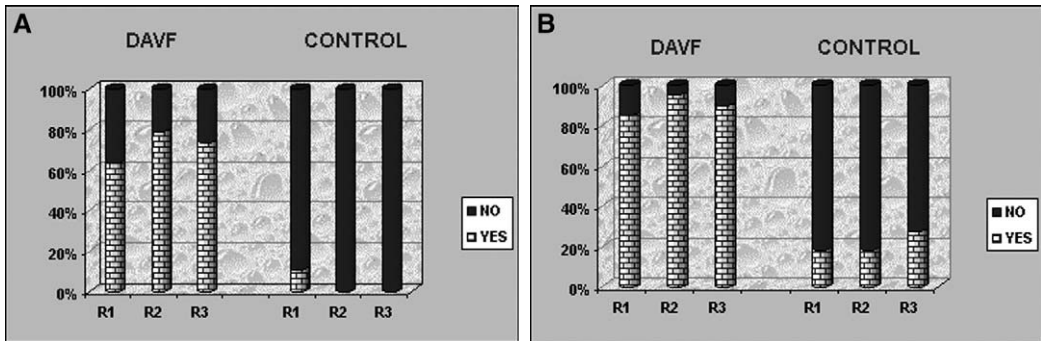


Fig. 4. Detection of intradural vessels on conventional MR imaging of patients with proven dural arteriovenous fistula (DAVF group, $n = 20$) and control individuals with normal DSA studies (control group, $n = 11$). For each graph, the ordinate (y-axis) indicates the percentage of subjects with (YES) and without (NO) the specified finding in each subject group (DAVF or control). R1, R2, and R3 refer to the group assignment of each subject. (A) Intravascular “flow voids” extending over at least three contiguous vertebral segments in the intradural space on T2-weighted MR images. (B) Serpentine enhancement extending over at least three contiguous vertebral segments in the intradural space on contrast-enhanced T1-weighted MR images. (From Saraf-Lavi E, Bowen BC, Quencer RM, et al. Detection of spinal dural arteriovenous fistula with MR imaging and angiography: sensitivity, specificity, and prediction of vertebral level. *Am J Neuroradiol* 2002;23:858–67; with permission.)

Type II—intramedullary, glomus-type arteriovenous malformation (AVM)

Type III—juvenile-type AVM, which has intramedullary, extra-medullary, and sometimes extradural components

Type IV—perimedullary (intradural, extramedullary) AVF

Epidural or paraspinal AVMs, metameric vascular malformations (eg, Cobb’s syndrome),

or cavernous malformations are not specifically included in this scheme.

Dural arteriovenous fistula

The most common of the four types of vascular malformation in the Anson-Spetzler classification is the dural AVF, which is an acquired lesion. Dural AVF consists of a vascular nidus or shunt which is located on the dorsal aspect of the nerve root sleeve at the neural foramen [23]. The fistula is

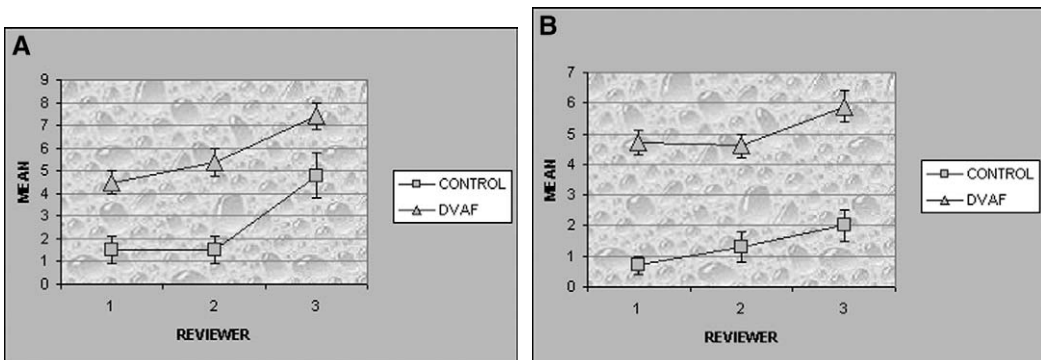


Fig. 5. Detection of intradural vessels on standard 3D contrast-enhanced MRA. Same subject groups and reviewers as in Fig. 4. For each graph, the error bars indicate the standard error of the mean. (A) Mean tortuosity of the dominant intradural vessel on MIP images. The ordinate (y-axis) has units of “turns per vertebral segment” (B) Mean length of the dominant intradural vessel on MIP images. The ordinate (y-axis) has units of “vertebral segments”. (From Saraf-Lavi E, Bowen BC, Quencer RM, et al. Detection of spinal dural arteriovenous fistula with MR imaging and angiography: sensitivity, specificity, and prediction of vertebral level. *Am J Neuroradiol* 2002;23:858–67, with permission.)

supplied by the dural branch of the radicular–medullary–dural artery (reviewed in reference [1]). The nidus is drained intradurally by retrograde flow through the medullary vein, resulting in venous hypertension and engorgement of the predominantly longitudinally oriented veins on the cord surface (coronal venous plexus) and the intraparenchymal radially oriented veins [24,25].

Several MR imaging features of the spinal cord have been reported to occur in association with dural AVF: hypointensity on T1-weighted images and hyperintensity on T2-weighted images involving the central region of the cord and extending over several levels; scalloping of the cord contours on sagittal images caused by enlarged intradural vessels, variable enlargement

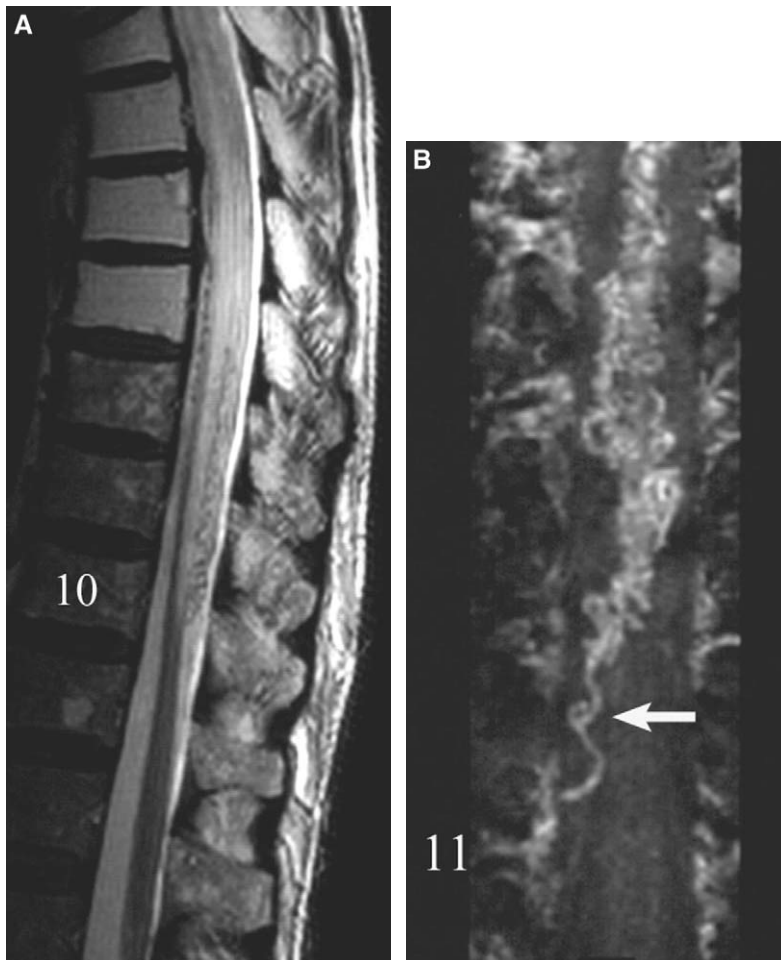


Fig. 6. Dural arteriovenous fistula at T12 in a 68-year-old man with a 3-year history of progressive myelopathy. His symptoms began approximately 6 months after radiotherapy and surgical excision of a carcinoma of the right lung apex. His progressive neurological deficits were initially attributed to radiation myelitis of the upper thoracic cord. (A) Midsagittal T2-weighted fast-spin-echo MR image shows hyperintense cord from T4 to T10 and serpentine flow voids, consistent with enlarged intradural vessels, posterior to the cord from T8 to T10. (B) Standard 3D contrast-enhanced MRA coronal MIP image (targeted to posterior half of the spinal canal) demonstrates an enlarged, tortuous vessel (arrow) extending from the right T11 foramen to the posterior cord surface, where numerous, convoluted vessels are seen. The right T11 vessel corresponds to the posterior medullary vein. (C) DSA posteroanterior view, following injection of the right T11 posterior intercostal artery, demonstrates a fistula in the region of the neural foramen with drainage into the canal by way of the medullary vein (arrow). (From Bowen BC, Pattany PM. Vascular anatomy and disorders of the lumbar spine and spinal cord. Magn Reson Imaging Clin N Am 1999;7:555–71, with permission.)

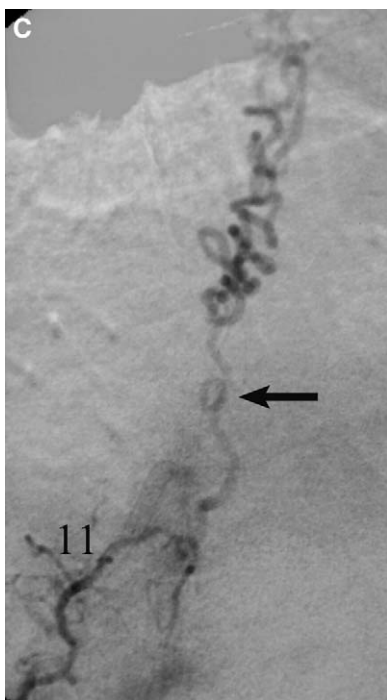


Fig. 6 (continued)

of the cord; and patchy or diffuse enhancement of the cord on postcontrast T1-weighted images (Figs. 3, 6) [9,26–29]. The frequency with which each of these changes is observed is variable. Hyperintensity within the center of the cord on T2- or T2*-weighted images has been reported as the most consistently observed abnormal cord finding [30]; however, it is not specific and may be seen in patients with inflammation/infection, neoplasm, trauma, or arterial ischemia. Cord enhancement also is nonspecific. Hurst and Grossman [31] have recently reported frequent detection of a hypointense rim or anulus in the periphery of the cord on T2-weighted fast-spin-echo images and have proposed this feature as a reliable sign of the venous hypertension associated with dural AVF.

The spinal cord imaging findings described above typically occur in conjunction with the evidence for abnormal vessels that was described by Saraf-Lavi and colleagues [9]: (1) “flow voids” in the extramedullary, intradural space, and (2) serpentine postcontrast enhancement. This evidence of abnormal vessels is crucial when constructing a differential diagnosis, yet such evidence is not always detectable because of blood

flow properties and spin-echo pulse sequence parameters [32] or it may be confused with or masked by cerebral spinal fluid (CSF) pulsation artifacts [13,27,29,30]. Thus, in early investigations, and even today, some authors contend that a negative MR imaging study does not rule out dural AVF [33].

The addition of MRA to the routine MR imaging study improves visibility of intradural vessels, and thus may increase the sensitivity and specificity with which dural AVF (or other vascular lesion) is detected. As discussed above (Abnormal vessels section), standard 3D CE MRA enables determination of parameters, such as mean length, mean tortuosity, and mean size (qualitatively) of the dominant intradural perimedullary vessel, that are significantly increased when DAVF is present and could be used as additional diagnostic criteria, supplementing the two MR imaging features of abnormal vessels.

In the second part of their investigation, Saraf-Lavi et al [9] presented three neuroradiologists with conventional spinal MR images from control individuals ($n = 11$) and from patients with proven dural AVF ($n = 20$). One week later, the reviewers were presented with the conventional MR images plus 3D CE MRA images (MRI + MRA) for the same subjects. In each review session, the sets of images for the controls and patients were presented in a blinded, randomized format. The reviewers, who had different degrees of experience in interpreting spinal MR studies, were asked to indicate whether or not a dural AVF was present based on MR imaging alone (first session), and later based on MRI + MRA (second session). Each reviewer’s answers were based on his or her general subjective impression derived from the MR findings for abnormal intradural vessels. Specific quantitative and semi-quantitative criteria, such as threshold values for tortuosity and length of the dominant vessel, that were determined from the first part of the investigation, were not applied in this second part, but certainly merit testing in subsequent studies.

For each reviewer, there was no significant difference in sensitivity and specificity for the detection of fistula by MR imaging versus MRI + MRA (Table 1). When reviewers with different degrees of experience were compared, however, the more experienced neuroradiologist R2 achieved a significantly higher sensitivity (100%) than the less experienced neuroradiologist R3 (80%) for MRI + MRA, but not for MRI alone. Thus, when standard 3D CE MRA is added to conventional MR imaging of the spine, sensitivity

Table 1

Detection of the presence of dural arteriovenous fistula by MR imaging alone (MRI) and by combined MR imaging plus MR angiography (MRI + MRA)

Reviewer	Sensitivity		Specificity		Accuracy	
	MRI	MRI + MRA	MRI	MRI + MRA	MRI	MRI + MRA
R1	85%	85%	91%	82%	87%	84%
R2	90%	100%	82%	82%	87%	94%
R3	85%	80%	100%	82%	90%	81%

From Saraf-Lavi E, Bowen BC, Quencer RM, et al. Detection of spinal dural arteriovenous fistula with MR imaging and angiography: sensitivity, specificity, and prediction of vertebral level. AJNR Am J Neuroradiol 2002;23:858–67, with permission.

in the detection of dural AVF may be improved for the experienced reviewer.

As shown in Figs. 3 and 6, the dominant intradural vessels detected by standard 3D CE MRA in patients with dural AVF represent engorged veins of the coronal venous plexus, especially the anterior and posterior median veins. Delineation of a dominant, tortuous medullary vein, and thus identification of the corresponding neural foramen, potentially enable the reviewer to predict the level of a suspected fistula. In an early, non-blinded study, Bowen [13] identified the dominant vein and corresponding fistula level on standard 3D CE MRA in 67% (6 of 9) of the reported cases. In their

blinded study, Saraf-Lavi et al [9] assessed the accuracy of MR imaging versus MRI + MRA in detecting the vertebral level of the fistula. On average, the percentage of true positive subjects in whom the correct fistula level was predicted increased from 15% for MR imaging alone to 50% for the combined study (MRI + MRA), and the correct level plus or minus one level was predicted in 73% for the combined study. The improvement in predicting the correct level from MRI + MRA rather than MR imaging alone is illustrated in Fig. 7, where the levels estimated from MRI + MRA cluster around the horizontal line representing the correct levels in the true-positive cases. Note that in some cases, no level

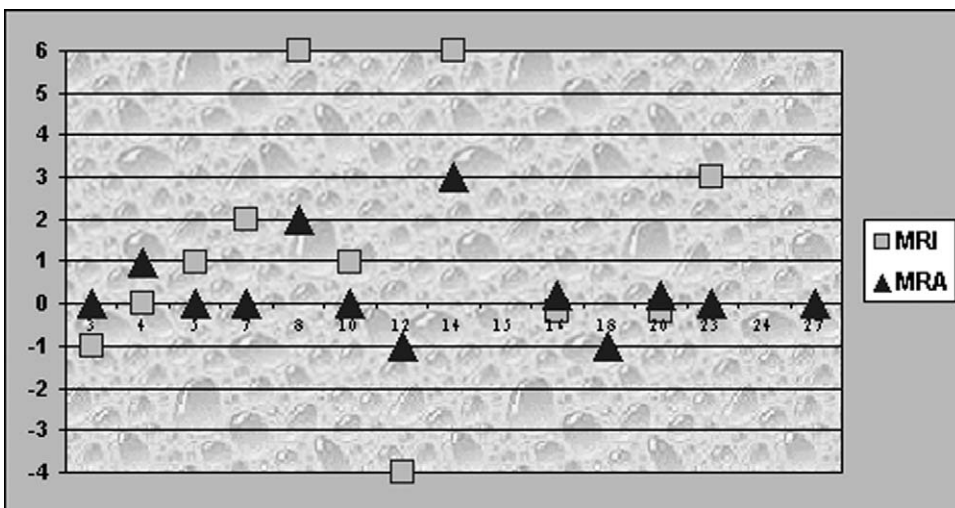


Fig. 7. Estimation of vertebral level of DAVF by one reviewer (out of three reviewers total) based on MR imaging findings alone (squares, MR imaging) versus MR imaging plus MR angiography findings (triangles, MRA). Numbers on the y-axis refer to the deviation (in vertebral segments, cranial “+” or caudal “-”) of the estimate from the correct level of the fistula, indicated by “0”. Numbers on the x-axis are the case numbers assigned to the subjects with documented DAVF. The absence of a square or triangle for a case indicates that the reviewer did not suspect fistula (false negative), or that fistula was suspected but the level was indeterminate. (From Saraf-Lavi E, Bowen BC, Quencer RM, et al. Detection of spinal dural arteriovenous fistula with MR imaging and angiography: sensitivity, specificity, and prediction of vertebral level. Am J Neuroradiol 2002;23:858–67, with permission.)

could be estimated from the MR imaging, whereas the correct level or an adjacent one could be estimated from the MRI + MRA.

The investigators concluded that the principal benefit of standard 3D CE MRA was not improved detection of the presence of fistula but rather improved localization of the vertebral level of the fistula compared with MR imaging alone. These benefits of MRA obviate the need for supine myelography [34] in the diagnostic work-up of patients with suspected spinal vascular malformation. In addition, the ability to predict the fistula level plus or minus one level noninvasively can potentially expedite the subsequent invasive DSA examination by directing the angiographer to certain spinal levels initially.

The fast 3D CE MRA technique does not seem to improve the detection of draining intradural veins of dural AVFs compared with the standard 3D technique, although no direct comparison of techniques on a case-by-case basis has been done. The fast 3D method may be advantageous since it can display the AV shunt (Fig. 8), which is not typically seen with the standard 3D method because of diffuse epidural enhancement (Figs. 3, 6). The AV shunt was detected in two of three cases of dural AVF by Binkert and colleagues [2] and prospectively in eight of nine cases by Farb et al [7]. In the latter study, several patients underwent fast 3D MRA on more than one occasion to localize the fistula site. The number of 3D MRA examinations required to confidently identify the site before DSA was as follows: one MRA in four patients, two MRAs in three patients, three MRAs in one patient.

While the level of the fistula can often be determined from the course of the draining vein only, the display of the fistulous communication provides added confidence in diagnosis and localization. Both coronal and sagittal (or axial [2,7]) targeted MIP images are useful and should be obtained to determine whether the fistula drains initially to the anterior or the posterior surface of the cord. Detection of the feeding artery or arteries to a fistula potentially also provides added confidence in diagnosis. Using the auto-triggered, elliptic centric ordered 3D MRA technique, Farb and colleagues [7] were able to demonstrate the feeding artery at the level of the fistula in eight of their nine cases. In three of the eight identified cases, there were additional feeding arteries, but these additional feeders were demonstrated by MRA in only one case.

Because the standard and fast 3D techniques do not have the temporal resolution of DSA, more of the enlarged intradural veins are often demonstrated on the MIP images than on individual frames of the DSA filming sequence [13]. Also, the delayed frames of DSA studies are often degraded by contrast dilution and patient motion, so that the visibility of the anterior or posterior median vein on DSA is inferior to MRA. By augmenting the display of intradural veins, CE MRA complements the catheter DSA study, which has unparalleled sensitivity in demonstrating normal spinal arteries and the feeding arteries of vascular malformations.

Most of the papers evaluating the application of standard gadolinium-enhanced PC MRA to the detection of spinal dural AVF were published before 1998 [15–17]. Using 2D PC MRA, Mascalchi and colleagues [16] observed vascular abnormalities in five out of six patients with dural AVF, but the investigators were able to identify the level of the draining medullary vein (and hence the vertebral level of the fistula) on modulus images in only two of the six patients. Similarly, Provenzale et al [15] demonstrated enlarged midline intradural veins in a patient with dural AVF using 3D PC angiography (VENC = 25 cm/second), but were unable to show the site of the fistula. Mascalchi et al [17] reported improved detection of fistula location when 2D phase images were acquired in addition to 2D and 3D modulus images. No articles describing improvements in these PC MRA techniques applied to spinal vascular lesions have appeared in the radiology literature since 1998, although Mascalchi et al [8] recently published a retrospective review of their previous experience with 34 post-treatment patients.

Intramedullary arteriovenous malformation

Several early MR studies [32,35,36] reported sensitive detection of intramedullary AVMs with routine spin-echo MR imaging. The findings included intramedullary low signal with surrounding normal cord tissue, focal cord enlargement at the location of the nidus, and serpentine signal voids within the subarachnoid space in the region of the nidus. Improvements in MR scanner hardware and software, and the application of new pulse sequences such as STIR (short tau, or short TI, inversion recovery), have resulted in greater sensitivity in detecting intramedullary lesions, such as glomus AVM and the presence of edema or hemorrhage.



Fig. 8. Fast 3D contrast-enhanced MR angiography of a left T11 dural arteriovenous fistula. (A) The coronal MIP image demonstrates marked tortuosity of the posterior median vein and the left T11 posterior medullary vein (arrow) draining the fistula (arrowhead). (B) The axial targeted MIP image shows the fistula (arrowhead) in the left neural foramen draining to the posterior surface of the cord. (C) DSA (posteroanterior view), following injection of the left T11 intercostal artery, shows the fistula (arrowhead) and draining medullary vein (arrow). (From Binkert CA, Kollias SS, Valavanis A. Spinal cord vascular disease: characterization with fast three-dimensional contrast-enhanced MR angiography. *Am J Neuroradiol* 1999;20:1785–93, with permission.)

The evaluation of AVMs using standard gadolinium-enhanced PC MRA techniques were reported by Mascalchi and colleagues in their series that included patients with AVMs and patients with dural AVFs [16,17]. Detection of the feeding arteries of AVMs was limited with 2D PC MRA [16], but improved when 2D and 3D PC modulus images, and 2D phase images, were acquired and then reviewed together [17]. Mascalchi and colleagues were more successful in characterizing “high flow” lesions, such as AVMs, than “low flow” lesions, such as dural AVFs.

The fast 3D CE MRA technique seems to provide better delineation of the nidus and draining veins of an AVM (Fig. 9), and the draining

medullary vein of a dural AVF (see Fig. 8), than PC techniques. Binkert and colleagues [2] used the fast MRA technique to prospectively characterize and categorize 12 vascular lesions: 6 spinal cord AVMs, 3 spinal dural AVFs, and 3 spinal or paraspinal tumors. Except for one of the dural AVFs, all of the vascular lesions were correctly characterized. For the intramedullary AVMs, the level of the main arterial feeder was identified in all six cases. Mascalchi and colleagues [3] have questioned whether the fast 3D CE MRA method improves the visibility of the feeding arteries of AVMs compared with PC techniques. They found that the combined PC techniques were superior; however, their fast 3D CE MRA technique differed from that used by Binkert et al [2] in

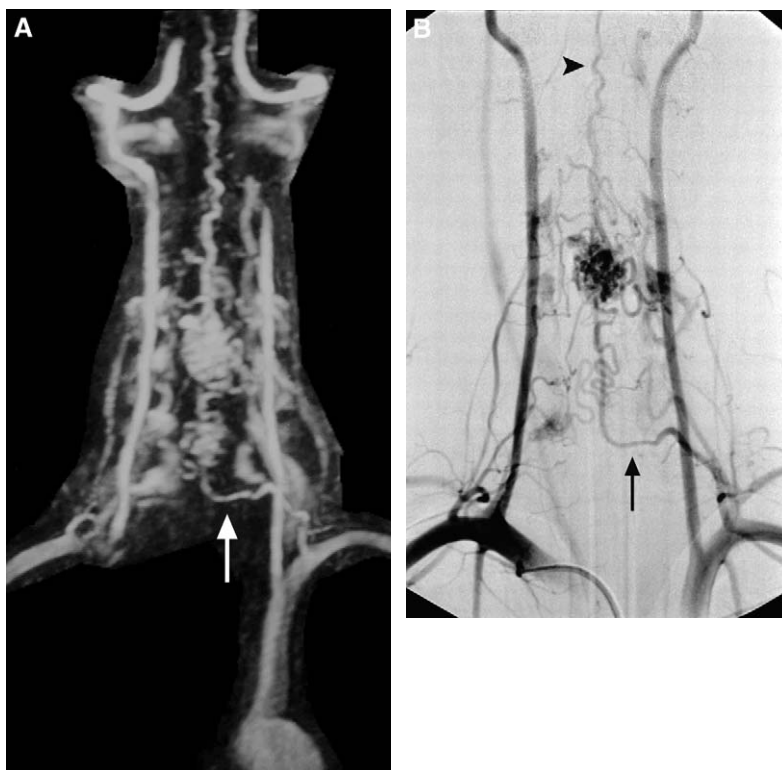


Fig. 9. Fast contrast-enhanced MR angiography of a cervical spinal cord AVM. (A, B). Coronal MIP image (A) is compared with an anteroposterior DSA image (B). The MIP image shows the main arterial feeder (arrow), which originates from the left costocervical trunk. The AVM drains primarily into an enlarged posterior median vein (arrowhead). (From Binkert CA, Kollias SS, Valavanis A. Spinal cord vascular disease: characterization with fast three-dimensional contrast-enhanced MR angiography. *Am J Neuroradiol* 1999;20:1785–93, with permission.)

several ways, including the time of initiation of 3D data acquisition relative to the passage of the contrast bolus.

There are no published series of spinal cord AVMs evaluated with the standard 3D CE MRA technique. In our experience, the draining veins, and often the nidus, are well shown; however, the feeding artery or arteries are inapparent or indistinguishable from draining veins [37]. When compared with Binkert's results, it appears that the feeding arteries are better detected and identified with the fast 3D CE MRA. This assertion should be viewed cautiously, though, because the feeding arteries and draining veins of intramedullary AVMs are not temporally resolved in any of the fast 3D CE techniques published to date [2,3]. Thus, "identification" of feeding arteries de novo requires tracking of the vessel or vessels of interest on MIP images from a known parent artery (see Fig. 9).

Posttreatment vascular malformations

The MR angiographic findings in patients with treated spinal vascular malformations, primarily AVFs, have been described [8,13,38,39]. Treatment of dural AVF is either surgical or endovascular using embolic agents [22,40–42], whereas treatment of intramedullary AVM often requires a combined approach [41]. Surgical treatment of dural AVF usually involves interruption of the draining intradural vein, with or without removal of the dural nidus, depending on the pattern of venous drainage [40]. There is no resection or "stripping" of the engorged coronal venous plexus.

In early [13] and more recent [39] articles, Bowen and colleagues showed that standard 3D CE MRA obtained 2 to 4 months after successful surgical treatment of dural AVF typically detected one or a few non-enlarged, minimally serpentine vessels along the cord (Fig. 10). The pattern was consistent with residual flow in normal anterior or

posterior median veins. The abnormal medullary vein draining the fistula preoperatively was no longer seen. In some patients, MR imaging revealed a decrease in hyperintensity on T2-weighted images and cord enhancement on postcontrast T1-weighted images, depending on the extent of pre-treatment signal abnormalities.

In one case [13], MRA performed at 1 and 5 months after attempted embolization of a dural AVF with polyvinylalcohol microspheres, showed no change in the appearance of the enlarged medullary vein draining the fistula, compared with the pretreatment MR study. Residual or recurrent fistula was found at surgery and treated, after which the enlarged medullary vein was no longer observed on MRA or DSA. In cases where dural AVF was successfully embolized with “glue” (n-butyl 2-cyanoacrylate, NBCA), the post-treatment 3D CE MRA revealed a lack of flow in the draining medullary vein, consistent with occlusion, which was confirmed by DSA. These preliminary results suggest that 3D CE MRA may be able to accurately detect evidence of

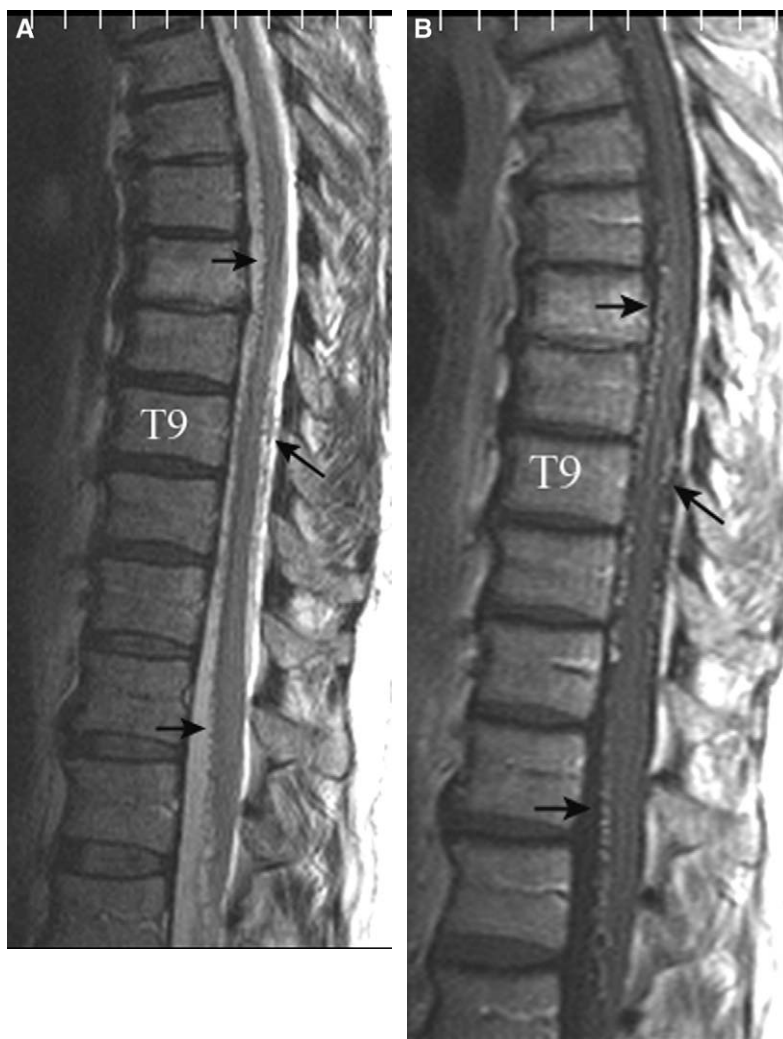
both unsuccessful and successful treatment of dural AVF.

Mascalchi and colleagues [8] studied 34 patients with spinal vascular malformations (30 dural AVFs, 2 intramedullary AVMs, and 2 perimedullary AVFs) who underwent MR imaging and MRA before and after endovascular or surgical treatment. The cases were accumulated over an 8-year period, and MRA consisted of PC techniques only (early cases) and PC techniques combined with a fast 3D CE method [3] (later cases). MRA was found to be more sensitive than conventional MR imaging in depicting residual or recurrent flow in peri- or intramedullary vessels, and hence patency of the vascular malformation. Studies testing whether MRA can substitute, at least partially, for DSA in the posttreatment evaluation of spinal vascular malformations have not been published.

Epidural arteriovenous malformation

Bowen and Pattany [43] have reported a case of proven epidural AVM (L2 level) with intra-

Fig. 10. MR imaging and standard 3D contrast-enhanced MRA of a left T9 dural arteriovenous fistula (DAVF) before (A–F) and 2 months after (H–I) surgical interruption of the fistula. (A) Midsagittal, T2-weighted fast-spin-echo MR image shows normal cord size and minimally increased cord signal at T8. Intravascular flow voids (arrows) produce a hypointense, serrated appearance along the anterior surface of the cord from T6 to L2 and along the posterior surface of the cord from T9 to T10. (B) Postcontrast T1-weighted MR image shows a scalloped cord contour with enhancing serpentine vessels (arrows) corresponding to the flow voids observed in (A). Questionable cord parenchymal enhancement is also noted at T8. (C) Standard 3D CE MRA sagittal MIP image demonstrates an enlarged serpentine vessel (open arrows) on the anterior surface of the cord. Also shown is an incompletely resolved network of vessels (closed arrow) on the posterior surface from T8–T9 to T11–T12. (D, E) Coronal MIP images targeted to the anterior (D) and posterior (E) portions of the spinal canal. In D, the midline tortuous vessel corresponds to an enlarged anterior median vein. No dominant anterior medullary vein is detected. Thus, drainage to the cord from a DAVF is likely to be through a posterior medullary vein. In E, a cluster of tortuous, enlarged intradural vessels, corresponding to the coronal venous plexus, is detected between T8 and T11. A vessel (black arrow overlying left T9 pedicle) extends to the prominently enhancing left T9 neural foramen. No other forminal level has this combination of findings, suggesting that the fistula is located at T9 and drainage to the cord is through the left T9 posterior medullary vein. F, G. DSA lateral (F) and posteroanterior (G) views following contrast injection of the left T9 intercostal artery. In F, several enlarged, convoluted veins located posteriorly (closed arrows), and a single enlarged vein located anteriorly (open arrows) are opacified. The approximate location of the T9 vertebral body is indicated. In G, the left T9 DAVF (arrowhead) and the draining posterior medullary vein are shown. The early draining veins of the posterior coronal venous plexus are also opacified. Note the similarities between C and F and between E and G. (H) Midsagittal, T2-weighted fast-spin-echo MR image shows laminectomy defects at T9 and T10 and ferromagnetic artifact (arrow) resulting from surgical treatment of the DAVF. Cord size and signal intensity are normal, and the flow voids detected preoperatively in A are no longer well demonstrated. (I) Postcontrast T1-weighted MR image shows minimal linear or serpentine enhancement anterior (open arrow) and posterior to the cord compared with B. Ferromagnetic artifact (arrow) displayed in H is again observed. (J) Standard 3D CE MRA sagittal MIP image demonstrates a decrease in size and tortuosity of the anterior median vein (open white arrows) and a marked decrease in visibility of the posteriorly located intradural veins (open black arrowheads) compared with the pretreatment image C. Ferromagnetic artifact (closed black arrow) and enhancing scar in the surgical bed are detected on the MIP image. (K) Coronal MIP image targeted to the posterior portion of the spinal canal reveals minimal enhancement from residual small vessels and scarring, and the ferromagnetic artifact (arrow) on the left at T9. No abnormally enlarged left T9 medullary vein or posterior coronal venous plexus is detected. Compare with the corresponding pretreatment image E. (From Lee TT, Gromelski EB, Bowen BC, Green BA. Diagnostic and surgical management of spinal dural arteriovenous fistulas. *Neurosurgery* 1998;43:242–7, with permission.)



dural venous drainage. The findings with respect to cord signal changes and enhancement on MR imaging and the findings associated with abnormal intradural vessels on MR imaging and standard 3D CE MRA were indistinguishable from those described above for dural AVF. An additional finding, which may favor an epidural AVM rather than dural AVF, was the large size of the markedly enhancing region around the epidural nidus. On postcontrast T1-weighted images and on MIP images, this region was larger than that observed at the adjacent and contralateral vertebral levels, and extended from the paraspinous region lateral to the L2 foramen to the epidural space, with indentation of the thecal sac. Thus, the epidural space in the region of the neural foramen corresponding to an abnormal medullary vein

should be scrutinized for evidence of enhancement that is more conspicuous than seen in cases of dural AVF. Differentiation of epidural AVM from dural AVF may still be difficult, because in some cases of dural AVF intradural and epidural venous drainage are present [40].

Vascular tumors

Hemangioblastoma, hemangiopericytoma (formerly included under the term “angioblastic meningioma” which is now considered obsolete), and paraganglioma are neoplasms that are likely to produce abnormal MR findings because of increased flow in intradural vessels. Bowen and Pattany [1] presented the findings for a case of hemangiopericytoma in the 1998 Magnetic

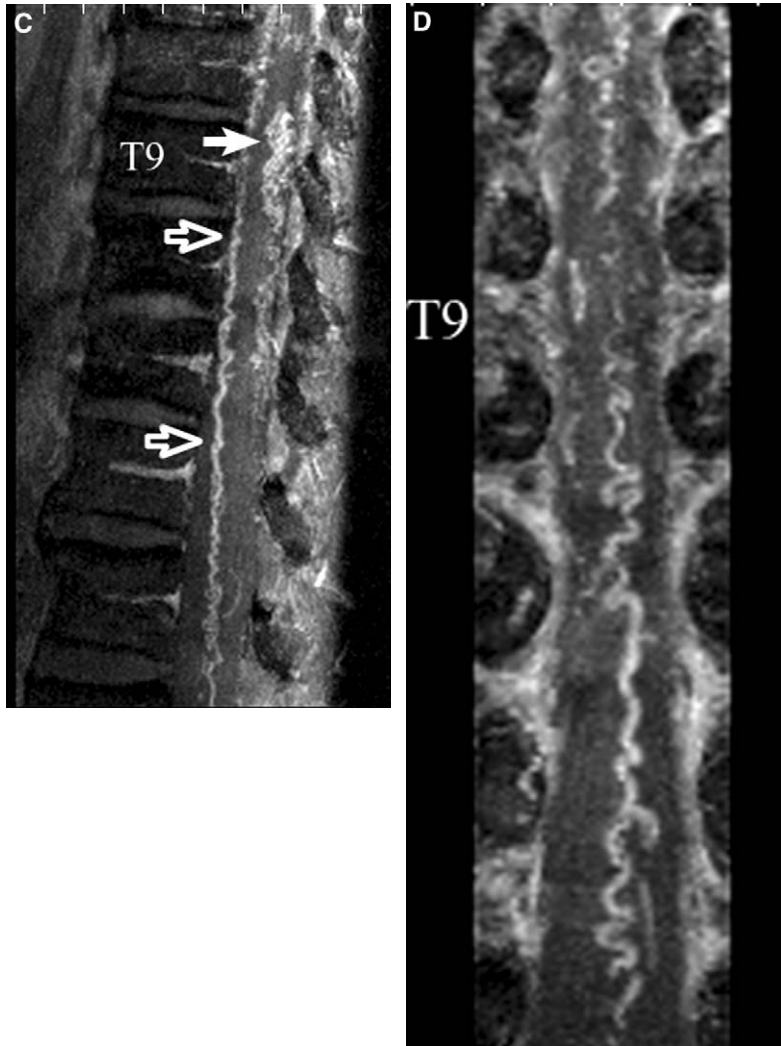


Fig. 10 (continued)

Resonance Imaging Clinics of North America volume on “New Techniques in MR Neuroimaging”, and they had previously published an example of paraganglioma [44]. More recently, these investigators reported three cases of intramedullary hemangioblastoma (two thoracic and one cervical) on standard 3D CE MRA [4,45,46]. Standard 3D CE MRA was used (1) to establish that hypointense foci on MR images represent blood flow within normal-sized or enlarged intradural (intra- or extramedullary) vessels and (2) to elucidate the relationship of the vessels, usually veins, to the tumor mass. Better characterization of the arterial supply seems to be possible with the fast 3D CE MRA technique. Binkert and colleagues [2] were

able to identify the arterial supply to a lower thoracic cord hemangioblastoma from the left T11 intercostal artery through the artery of Adamkiewicz and anterior spinal artery. Enlarged veins of the coronal venous plexus, though, dominated the MIP images and partially obscured the intradural course of the artery of Adamkiewicz. In a few cases of vertebral, paraspinal or presacral vascular lesions (eg, symptomatic vertebral body hemangioma), the fast 3D CE MRA technique has been used successfully to rule out potential involvement of the intradural vasculature [2].

The recognition of abnormal intradural vessels in association with an intrapinal mass favors the presence of a vascular tumor over a less vascular

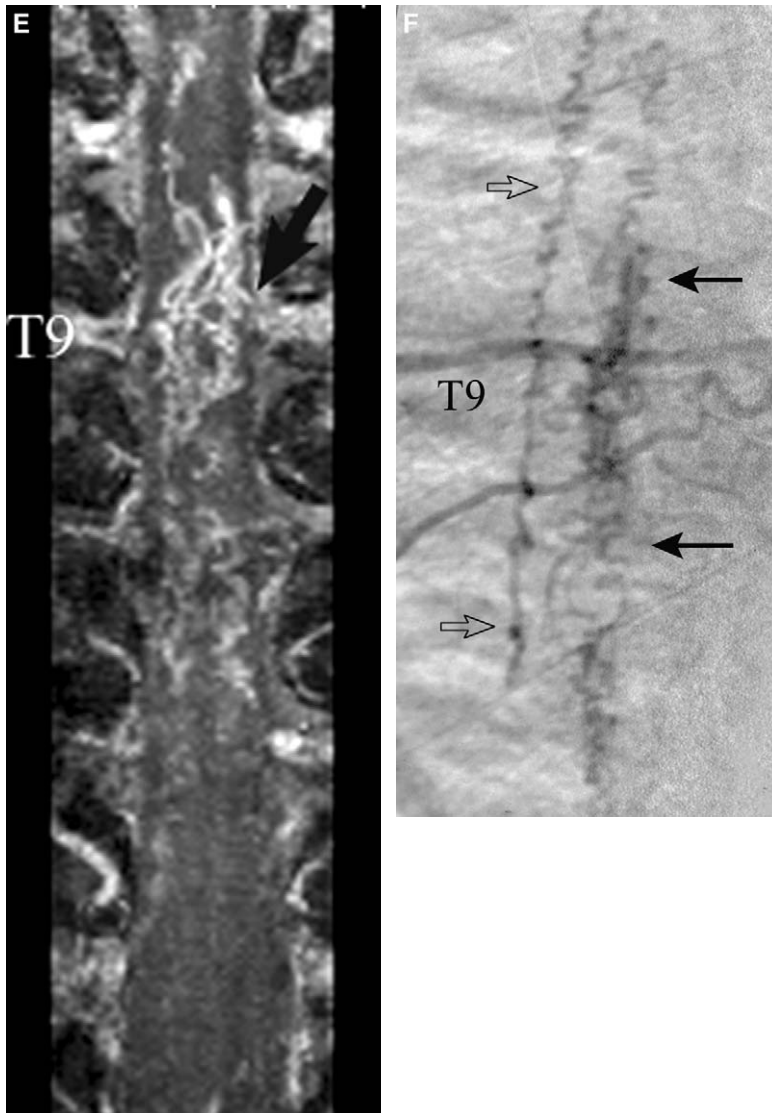


Fig. 10 (continued)

intramedullary (astrocytoma, ependymoma) or extramedullary (schwannoma or neurofibroma, ependymoma of the filum terminale) neoplasm and typically influences subsequent evaluation and treatment. Vascular tumors often require catheter angiography pre-operatively to define blood supply and drainage and to determine whether pre-operative embolization is warranted.

Vascular occlusive disease

The diagnosis of spinal cord infarction caused by arterial occlusion is primarily made on clinical

grounds and is often difficult to verify by conventional angiography. Blood is supplied to the cord by the sulcal branches of the anterior spinal artery and by radial perforating branches of the pial arterial plexus on the cord surface [1]. The anterior spinal artery supplies approximately the anterior two-thirds of the cord and most of the central gray matter. Hypoperfusion in this vascular distribution, as may occur from pathologic changes in the descending aorta (aneurysm, thrombosis, dissection) or from small vessel vasculitides, can result in cord infarction. When an infarction results from compromise of a

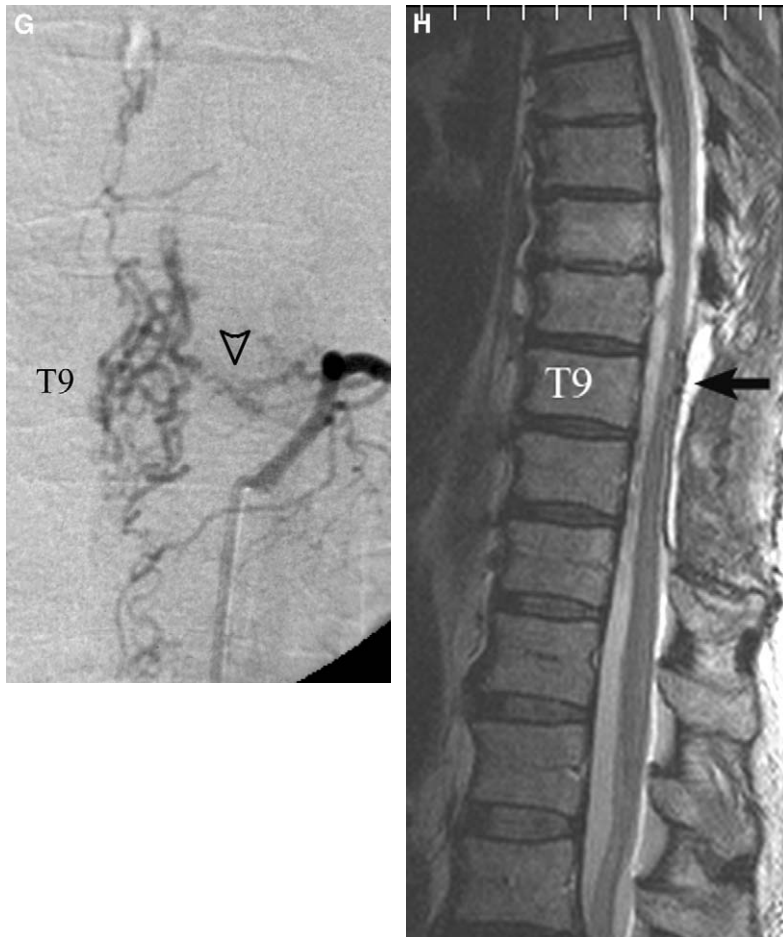


Fig. 10 (continued)

segmental artery, the branches that supply the ipsilateral half of the vertebral body may be affected also. Vertebral body infarct is best detected on sagittal images, usually appearing as a triangular area of increased signal near the endplate or deep medullary portion of the vertebral body [47]. The role of MRA in the diagnosis of cord infarction has not yet been determined. Yamada and colleagues [5] evaluated a series of patients before surgical or endovascular stent-graft repair of thoraco-abdominal aortic aneurysms. The patients had no history of cord infarction, yet the artery of Adamkiewicz was identified in only 69% of the patients. This apparently low sensitivity (correlative DSA was not done in all cases) for detecting the dominant arterial supply to the thoracolumbar cord, combined with the known difficulty in demonstrating arterial occlusion on DSA in patients with

clinical evidence of cord infarction, suggests that current 3D CE MRA techniques are likely to have little if any impact on the diagnosis of cord infarction.

Venous infarction is a feature of the clinicopathologic entity called “subacute necrotizing myelopathy” (SNM), which is characterized by coagulative necrosis involving both gray and white matter, thickened leptomeninges with inflammatory cell infiltrates, normal arteries, and enlarged, tortuous veins within the cord parenchyma and on its surface [48]. Some investigators [49] consider SNM equivalent to the Foix-Alajouanine syndrome, which represents the end stage of chronically elevated venous pressure distal to a spinal dural AVF [50]. Other investigators [48] argue that SNM encompasses a broader spectrum of disease, including thrombophlebitis. MR imaging findings reported for SNM include diffuse hypointensity on

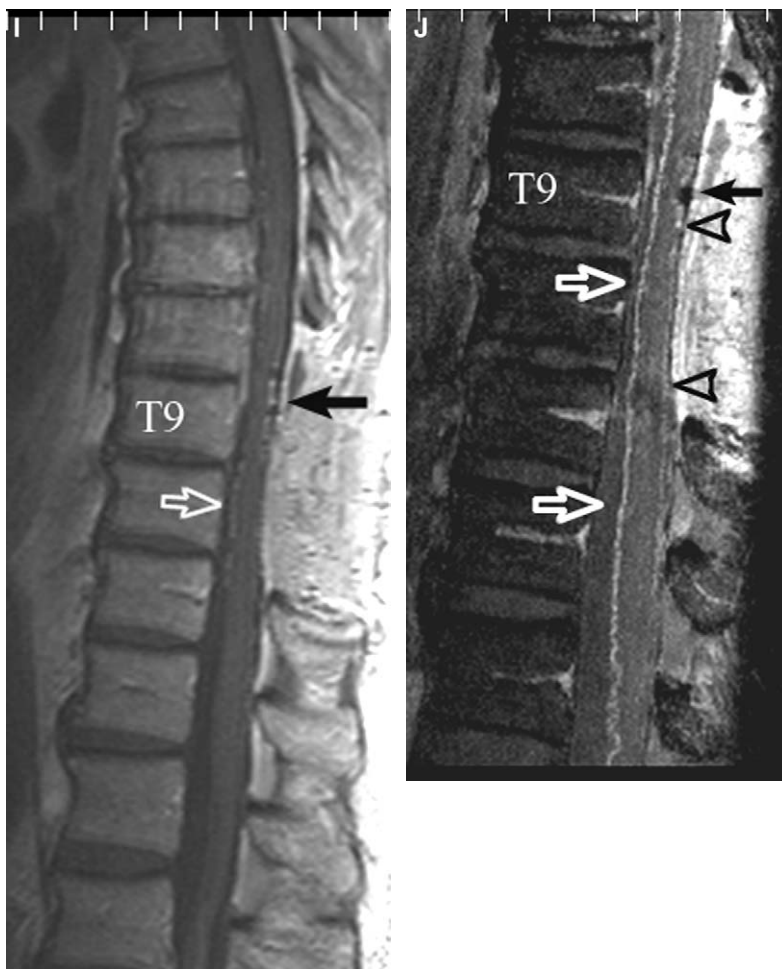


Fig. 10 (continued)

T1-weighted images and hyperintensity on T2-weighted images, cord enlargement, and dilated vessels (veins) on the cord surface. The role of 3D CE MRA in discriminating between potentially different etiologies for SNM has not yet been defined.

Summary

The role of MRA, as an adjunct to conventional MR imaging of the spine and spinal cord, is evolving. The older MRA methods that have been applied to spinal vascular imaging include 2D and 3D phase contrast techniques and a derivative of 3D time-of-flight techniques with data acquired for about several minutes after gadolinium contrast injection (standard 3D CE MRA). Newer 3D gradient-echo techniques, which allow the acqui-

sition of each volume of data in tens of seconds as a contrast bolus traverses the region of interest (fast 3D CE MRA), offer the possibility of temporally resolving intradural arteries and veins. The appearance of normal and abnormal intradural vessels, primarily veins, on the standard 3D CE MRA method has been described for the thoracolumbar region. Normal intradural arteries have been more difficult to detect, although preliminary results with the fast 3D CE MRA method, are promising [5]. Only by establishing the MRA appearance of normal arteries and veins, can one begin to define “abnormal” with greater confidence (presuming that the variability in the appearance of normal vessels is not so great as to preclude differentiation). In striving for this goal, MRA has already encountered competition from CT angiography [10].



Fig. 10 (continued)

In the characterization of spinal vascular lesions, the value of MRA has been demonstrated most convincingly for dural AVF. This lesion is more accurately localized and more sensitively detected (by neuroradiologists and others experienced in spine imaging) with combined MR imaging and standard 3D CE MRA than with MR imaging alone [9]. Preliminary results suggest that sensitivity and specificity may be further improved if fast 3D CE MRA is combined with conventional MR imaging [2,7]. Although less well documented, the value of MRA in characterizing other lesions, such as AVMs and vascular tumors, has been reported in recent publications [3,4,8,37,45]. In the future, the role of MRA will depend on technical advances, such as parallel acquisition techniques and possibly implantable RF coils, which permit improved detection of, and differentiation between, intradural arteries and veins. With these improvements, MRA may play an expanded role in the characterization of spinal vascular abnormalities, encompassing trauma and degenerative spine disease and vascular malformations and tumors.

References

- [1] Bowen BC, Pattany PM. MR angiography of the spine. *Magn Reson Imaging Clin N Am* 1998;6:165–78.
- [2] Binkert CA, Kollias SS, Valavanis A. Spinal cord vascular disease: characterization with fast three-dimensional contrast-enhanced MR angiography. *Am J Neuroradiol* 1999;20:1785–93.
- [3] Mascalchi M, Cosottini M, Ferrito G, Quilici N, Bartolozzi C, Villari N. Contrast-enhanced time-resolved MR angiography of spinal vascular malformations. *J Comput Assist Tomogr* 1999;23:341–5.
- [4] Bowen BC, Pattany PM. Contrast-enhanced MR angiography of spinal vessels. *Magn Reson Imaging Clin N Am* 2000;8:597–614.
- [5] Yamada N, Takamiya M, Kuribayashi S, et al. MRA of the Adamkiewicz artery: a preoperative study for thoracic aortic aneurysm. *J Comput Assist Tomogr* 2000;24:362–8.
- [6] Shigematsu Y, Korogi Y, Yoshizumi K, et al. Three cases of spinal dural AVF: evaluation with first-pass, gadolinium-enhanced, three-dimensional MR angiography. *J Magn Reson Imaging* 2000;12:949–52.
- [7] Farb RI, Kim JK, Willinsky RA, et al. Spinal dural arteriovenous fistula localization with a technique of first-pass gadolinium-enhanced MR angiography: initial experience. *Radiology* 2002;222:843–50.
- [8] Mascalchi M, Ferrito G, Quilici N, et al. Spinal vascular malformations: MR angiography after treatment. *Radiology* 2001;219:346–53.
- [9] Saraf-Lavi E, Bowen BC, Quencer RM, et al. Detection of spinal dural arteriovenous fistula with MR imaging and angiography: Sensitivity, specificity, and prediction of vertebral level. *Am J Neuroradiol* 2002;23:858–67.
- [10] Takase K, Sawamura Y, Igarashi K, et al. Demonstration of the artery of Adamkiewicz at multi-detector row helical CT. *Radiology* 2002;223:39–45.
- [11] Lasjaunias P, Berenstein A. Functional vascular anatomy of the brain, spinal cord, and spine. In: Lasjaunias P, Berenstein A, editors. *Surgical Neuroangiography*, vol 3. New York: Springer-Verlag; 1987. p. 15–87.
- [12] Thron AK. *Vascular anatomy of the spinal cord: neuroradiological investigations and clinical syndromes*. New York: Springer-Verlag; 1988.
- [13] Bowen BC, Fraser K, Kochan JP, et al. Spinal dural arteriovenous fistulas: evaluation with magnetic resonance angiography. *Am J Neuroradiol* 1995;16:2029–43.
- [14] Bowen BC, DePrima S, Pattany PM, et al. MR angiography of normal intradural vessels of the thoracolumbar spine. *Am J Neuroradiol* 1996;17:483–94.
- [15] Provenzale JM, Tien RD, Felsberg GJ, et al. Spinal dural arteriovenous fistula: demonstration using phase contrast MRA. *J Comput Assist Tomogr* 1994;18:811–4.
- [16] Mascalchi M, Bianchi MC, Quilici N, et al. MR angiography of spinal vascular malformations. *Am J Neuroradiol* 1995;16:289–98.
- [17] Mascalchi M, Quilici N, Ferrito G, et al. Identification of the feeding arteries of spinal vascular lesions via phase-contrast MR angiography with three-dimensional acquisition and phase display. *Am J Neuroradiol* 1997;18:351–8.
- [18] Bowen BC, Saigal G, Ruiz A. *Neuroimaging: CT/MRI vascular imaging*. In: Bradley WG, Daroff RB, Fenichel GM, Marsden CD, editors. *Neurology in clinical practice*. 4th edition. New York: Butterworth-Heinemann; 2003, in press.
- [19] Huston 3rd J, Fain SB, Riederer SJ, Wilman AH, Bernstein MA, Busse RF. Carotid arteries: maximizing arterial to venous contrast in fluoroscopically triggered contrast enhanced MR angiography with elliptic centric view ordering. *Radiology* 1999;211:265–73.
- [20] Foo TK, Ho VB, Choyke PL. Contrast-enhanced carotid MR angiography. *Imaging principles and physics*. *Neuroimaging Clin N Am* 1999;9:263–4.
- [21] Gulliver D, Noakes J. Myelographic correlations of vascular anatomy of the spinal cord. *Australas Radiol* 1988;32:65–72.
- [22] Anson JA, Spetzler RF. Spinal dural arteriovenous malformations. In: Awad IA, Barrow DL, editors. *Dural arteriovenous malformations*. Park Ridge (IL): American Association of Neurological Surgeons; 1993. p. 175–93.
- [23] McCutcheon IE, Doppman JL, Oldfield EH. Microvascular anatomy of dural arteriovenous

- abnormalities of the spine: a microangiographic study. *J Neurosurg* 1996;84:215–20.
- [24] Kendall HE, Logue V. Spinal epidural angiomatous malformations draining into intrathecal veins. *Neuroradiology* 1977;13:181–9.
- [25] Rosenblum B, Oldfield EH, Doppman JL, DiChiro G. Spinal arteriovenous malformations: a comparison of dural arteriovenous fistulas and intradural AVMs in 81 patients. *J Neurosurg* 1987;67:795–2.
- [26] Masaryk TJ, Ross JR, Modic MT, et al. Radiculomeningeal vascular malformations of the spine: MR imaging. *Radiology* 1987;164:845–9.
- [27] Minami S, Sagoh T, Nishimura K, et al. Spinal arteriovenous malformation: MR imaging. *Radiology* 1988;169:109–15.
- [28] Dormont D, Gelbert F, Assouline E, et al. MR imaging of spinal arteriovenous malformations at 0.5T: study of 34 cases. *Am J Neuroradiol* 1988;9:833–8.
- [29] Terwey B, Becker H, Thron AK, et al. Gadolinium-DTPA enhanced MR imaging of spinal dural arteriovenous fistulas. *J Comput Assist Tomogr* 1989;13:30–7.
- [30] Gilbertson JR, Miller GM, Goldman MS, et al. Spinal dural arteriovenous fistulas: MR and myelographic findings. *Am J Neuroradiol* 1995;16:2049–57.
- [31] Hurst RW, Grossman RI. Peripheral spinal cord hypointensity on T2-weighted MR images: a reliable imaging sign of venous hypertensive myelopathy. *Am J Neuroradiol* 2000;21:781–6.
- [32] Doppmann JL, DiChiro G, Dwyer AJ, et al. Magnetic resonance imaging of spinal arteriovenous malformations. *J Neurosurg* 1987;66:830–4.
- [33] Rosenblum DS, Myers SJ. Dural spinal cord arteriovenous malformation. *Arch Phys Med Rehab* 1991;72:233–6.
- [34] Gulliver D, Noakes J. Myelographic differentiation of spinal cord arteriovenous malformations from the normal population. *Australas Radiol* 1988;32:57–64.
- [35] Dormont D, Gelbert F, Assouline E, et al. MR imaging of spinal arteriovenous malformations at 0.5T: study of 34 cases. *Am J Neuroradiol* 1988;9:833–8.
- [36] Minami S, Sagoh T, Nishimura K, et al. Spinal arteriovenous malformation: MR imaging. *Radiology* 1988;169:109–15.
- [37] Bowen BC. MRI evaluation of spinal vascular malformations. Online CME course published under the auspices of the Foundation of the American Society of Neuroradiology. Available at: <http://www.asnr.org>. Accessed October 2002
- [38] Gelbert F, Guichard J-P, Mourier KL, et al. Phase-contrast MR angiography of vascular malformations of the spinal cord at 0.5T. *J Mag Reson Imag* 1992;2:631–6.
- [39] Lee TT, Gromelski EB, Bowen BC, Green BA. Diagnostic and surgical management of spinal dural arteriovenous fistulas. *Neurosurgery* 1998;43:242–7.
- [40] Afshar JK, Doppman JL, Oldfield EH. Surgical interruption of intradural draining vein as curative treatment of spinal dural arteriovenous fistulas. *J Neurosurg* 1995;82:196–200.
- [41] Berenstein A, Lasjaunias P. *Surgical Neuroangiography: Endovascular treatment of spine and spinal cord lesions*, vol 5. New York: Springer-Verlag; 1992.
- [42] Meisel HJ, Lasjaunias P, Brock M. Modern management of spinal and spinal cord vascular lesions. *Minim Invasive Neurosurg* 1995;38:138–45.
- [43] Bowen BC, Pattany PM. Vascular anatomy and disorders of the lumbar spine and spinal cord. *Magn Reson Imaging Clin N Am* 1999;7:555–71.
- [44] Bowen BC, Pattany PM. Spine MR angiography. *Clin Neurosci* 1997;4:165–73.
- [45] Bowen BC, Latchaw RE. Magnetic resonance Angiography of the spinal cord. In: Alexander E III, Maciunas RJ, editors. *Advanced neurosurgical navigation*. New York: Thieme Medical Publishers; 1999. p. 49–60.
- [46] Bowen BC, Saraf-Lavi E. Imaging of spinal vascular lesions. In: Latchaw RE, Kucharczyk J, Moseley ME, editors. *Advanced imaging and image-guided therapy of the nervous system*. Philadelphia: Mosby; 2003, in press.
- [47] Haddad MC, Al-Thagafi MYA, Djurberg H. MRI of spinal cord and vertebral body infarction in the anterior spinal artery syndrome. *Neuroradiology* 1996;38:161–2.
- [48] Mirich DR, Kucharczyk W, Keller MA, et al. Subacute necrotizing myelopathy: MR imaging in four pathologically proved cases. *Am J Neuroradiol* 1992;12:1077–83.
- [49] Enzmann DR. Vascular diseases. In: Enzmann DR, LaPaz RL, Rubin JB, editors. *Magnetic resonance of the spine*. Baltimore: Mosby Company; 1990. p. 510–39.
- [50] Criscuolo GR, Oldfield EH, Doppman JL. Reversible acute and subacute myelopathy in patients with dural arteriovenous fistulas. *J Neurosurg* 1989;70:354–9.



MR angiography of the extracranial circulation

Valerie Jewells, DO*, Mauricio Castillo, MD

Section of Neuroradiology, University of North Carolina, School of Medicine, Chapel Hill, NC 27599, USA

The goal of MR angiography (MRA) of the carotid arteries is not only to replace the more invasive conventional catheter angiography (XRA) but also to provide information not available with the latter method. Time-of-flight (TOF) MRA and black blood techniques have been studied extensively but lately have been surpassed in quality and diagnostic information by contrast-enhanced MRA. There are, however, techniques such as sonography (US), particularly with the addition of power color Doppler and more recently computed tomography angiography (CTA), that offer reliable high quality information, comparable to that obtained with MRA. MR imaging may be used to provide information regarding the intrinsic characteristics of an atherosclerotic plaque and thus offers possible prognostic implications. The role of plaque-stabilizing therapy may also in the future be assessed with high-resolution MR imaging of the carotid arteries. With the availability of perfusion MR imaging, evaluation of the effects of carotid artery disease on the intracranial circulation can also be observed. In this article, the authors review the role of different MRA techniques (with emphasis on contrast enhanced MRA) in the evaluation of carotid artery stenoses, evaluation of plaques and dissections.

MRA with regards to carotid artery atherosclerotic disease

Cerebral infarctions distal to ipsilateral internal carotid artery (ICA) atherosclerotic nar-

rowing cause 20% to 30% of strokes [1–4]. The risk of stroke increases with the severity of stenosis and is likely caused by embolic material arising in plaques [5–8]. Plaque assessment with XRA according to the North American symptomatic carotid endarterectomy trial (NASCET) revealed that patients with very severe stenosis (80%–99%) and with irregular plaques have a high risk of stroke [9,10]. Additionally, in a study by Rothwell et al [11], irregular plaques on XRA were more likely to have macroscopic ulceration and thrombus at surgery than were smooth plaques. The frequency of cerebral micro-emboli and the prevalence of emboli from a plaque surface will decrease over time after a symptomatic event because of healing of the plaque rupture [12,13]. The degree of the stenosis and plaque morphology, are predictors for stroke risk for 2 years if medical treatment rather than surgical treatment is implemented [11]. Therefore, since the degree of stenosis and plaque morphology affect the probability for strokes, both need to be addressed by diagnostic imaging.

MRA evaluation of the extracranial carotid arteries

Wagle et al [14] evaluated the extracranial carotid arteries in 1989 with 2D Fourier transform, and 3D Fourier transform imaging. Also in 1989, spoiled gradient echo imaging with TOF techniques for carotid artery evaluation was used [15]. Later, a comparison of non-contrast 2D TOF MRA to XRA was performed with good intra-observer agreement, particularly with respect to severe stenoses [16]. Another study comparing non-contrast 2D TOF MRA of the carotid artery bifurcations in 200 patients found that MRA agreed with XRA in 114 of 119 arteries with mild stenosis (0% to 29%), 15 of 21 arteries with

* Corresponding author.

E-mail address: valerie_jewells@med.unc.edu
(V. Jewells).

moderate stenosis (30% to 69%), and 41 of 45 arteries with severe stenosis (70% to 99%). Seventeen occluded arteries were also accurately diagnosed with MRA [17]. Furst et al [18], however stated that non-contrast MRA was not capable of differentiating true occlusion of an ICA from a pseudo-occlusion, although 3D MRA imaging improved visualization of the bifurcations [19]. Multislab 3D acquisition when introduced, also allowed for better depiction of carotid artery stenoses when it was compared with direct sagittal MRA [20]. In a study by Patel et al [21], 176 carotid arteries were studied for severe stenosis (70% to 99%) with 2D and 3D TOF non-contrast MRA. This study revealed that 3D imaging was significantly more accurate than 2D imaging when compared with XRA and sonography US [21]. Despite these advances, a review of the literature by Kallmes et al [22] in 1996 stated that the specificity of MRA, according to his calculations ranged from 18% to 100% for carotid artery stenosis and, therefore claimed that its true specificity remains unknown.

Some investigators have studied the evaluation of the carotid arteries with US and MRA in combination as a replacement for carotid XRA and concluded that XRA is indicated if a disagreement in regards to stenosis measurements between MRA and US exists [23]. A study by El-Saden et al [24], stated that MRA and US could replace XRA if the studies were in agreement (100% sensitivity and 91% specificity with an accuracy rate of 94%), and concluded that agreement with MRA and US meant that further evaluation with XRA was unnecessary. In this study, the statistical analysis revealed high sensitivities and specificities when using 3D TOF MRA (100% sensitivity and 91% specificity with an accuracy rate of 94%), but flow gaps resulted in inaccurate MRA examinations necessitating XRA in some patients. (Figs. 1, 2) Other authors were able to accurately differentiate carotid occlusions from high-grade stenoses (90%–99%) [25]. Still, others found that both US and 2D TOF MRA without contrast or 3D MRA overestimated carotid stenotic lesions when compared with XRA [26]. This latter study was plagued by flow voids that limit the interpretation of the MRA examinations. When a study of flow voids and their significance was undertaken by Nederkoorn et al [27], it was found that flow voids in non-contrast 3D TOF examinations had a positive predictive value for severe stenosis of 84.3%, but that even mild stenosis (0% to 49%) could demonstrate flow voids (2.9%) (Fig. 3).

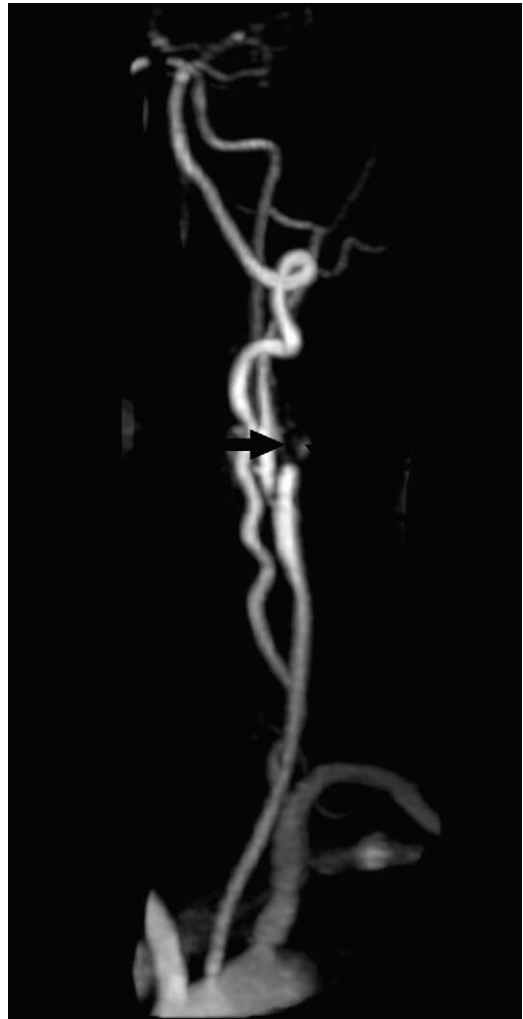


Fig. 1. MRA of occluded ICA. Oblique view of 2D TOF MRA demonstrating complete occlusion (*arrow*) of the proximal left ICA just distal to the bifurcation and also a focal stenosis of the proximal external carotid artery.

An extensive study of XRA demonstrated that it is not without limitations either. In a study by Anderson et al [28], XRA missed a partially thrombosed aneurysm seen on US and 2D and 3D MRA. Recent studies reveal the shortcomings of conventional XRA when compared with MRA and rotational XRA. XRA has also been shown to be inaccurate for evaluation of the degree of stenosis and has a tendency to underestimate stenosis because of the eccentric configuration of plaques [29–31].

Since MRA demonstrates inconsistencies with regards to estimations of arterial stenosis when

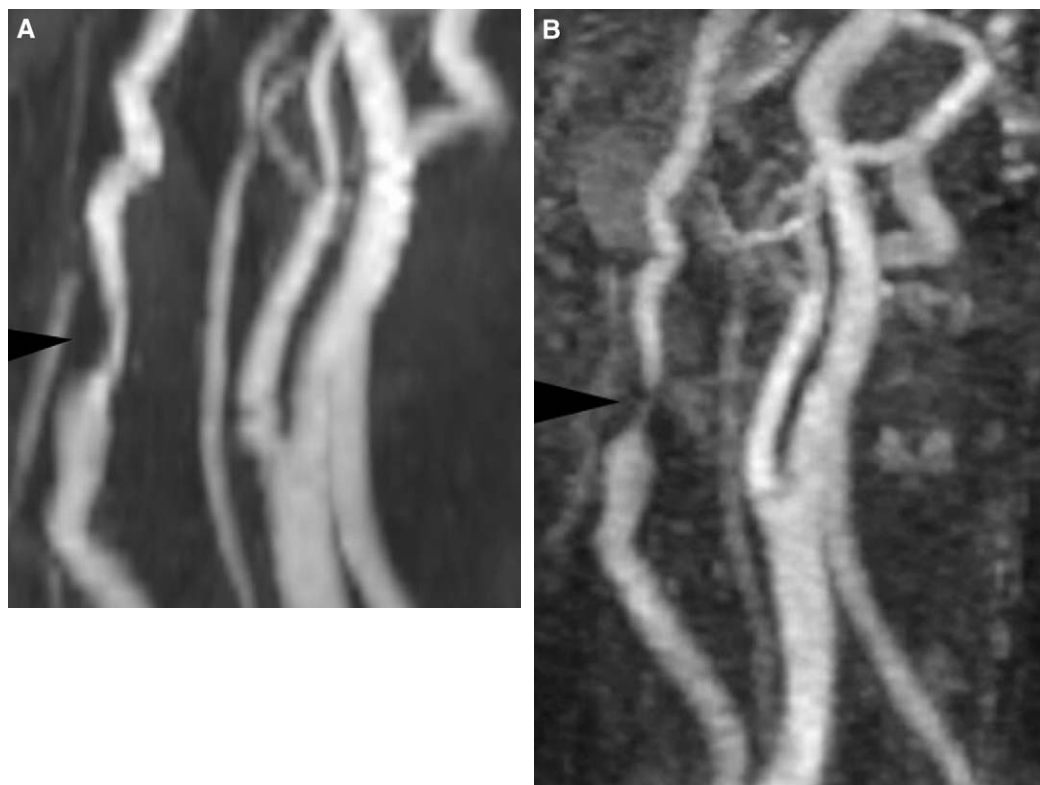


Fig. 2. Differences in degree of stenosis with varying MRA techniques. (A) Oblique view of 2D TOF MRA demonstrating a focal smooth stenosis (*arrowhead*) of the right vertebral artery. (B) Corresponding 3D TOF MRA shows that the stenosis appears to be more severe than on A.

compared with XRA, contrast-enhanced MRA may be implemented to improve evaluation, specificity, and sensitivity. Limits with regard to the visualization of the vessels, particularly the region of the origin of the great vessels (caused by motion artifacts), and the distal carotid and vertebral arteries segments remain even with contrast-enhanced MRA. These limitations may result in poor surgical outcomes [32,33]. Another problem encountered with contrast-enhanced MRA examinations is that of adequately imaging the contrast bolus at its peak enhancement. This requires shorter acquisition times, and to help remedy the examination length problems and associated motion artifacts, contrast bolus tracking techniques with a modified keyhole scheme or elliptical centric k-space ordering can be used to optimize the visibility of the contrast bolus on MRA [34,35]. Central sampling of the k-space is another method of data acquisition that has shown improved temporal resolution and also allows for improved spatial resolution by reducing

voxel size. To obtain a smaller voxel size, it is necessary to acquire the center of k-space during the peak concentration of contrast delivered by way of a power injector during breath holding [36]. Using a smaller voxel size ($0.95 \times 0.76 \times 0.82$ mm versus $1.3 \times 1.29 \times 1.25$ mm) for coronal imaging with a test bolus helps delineate the arterial lumen, but wrap-around artifacts and signal fall-off at the origin of the great vessels occur, limiting study quality [37]. These high-resolution images do not always allow enough time for the examination to be performed during a single breath hold. Saturation bands used over the dural venous sinuses reduce venous contamination. Using phantoms, Melhem et al [38] showed that the greater the stenosis, the larger percentage of sampling of k-space needed to accurately demonstrate it. A study by Serfaty et al [39] used fluoroscopic triggering and demonstrated a 94% sensitivity and a 85% specificity with 3D TOF post-contrast MRA for stenosis evaluation when compared with XRA. When combined with

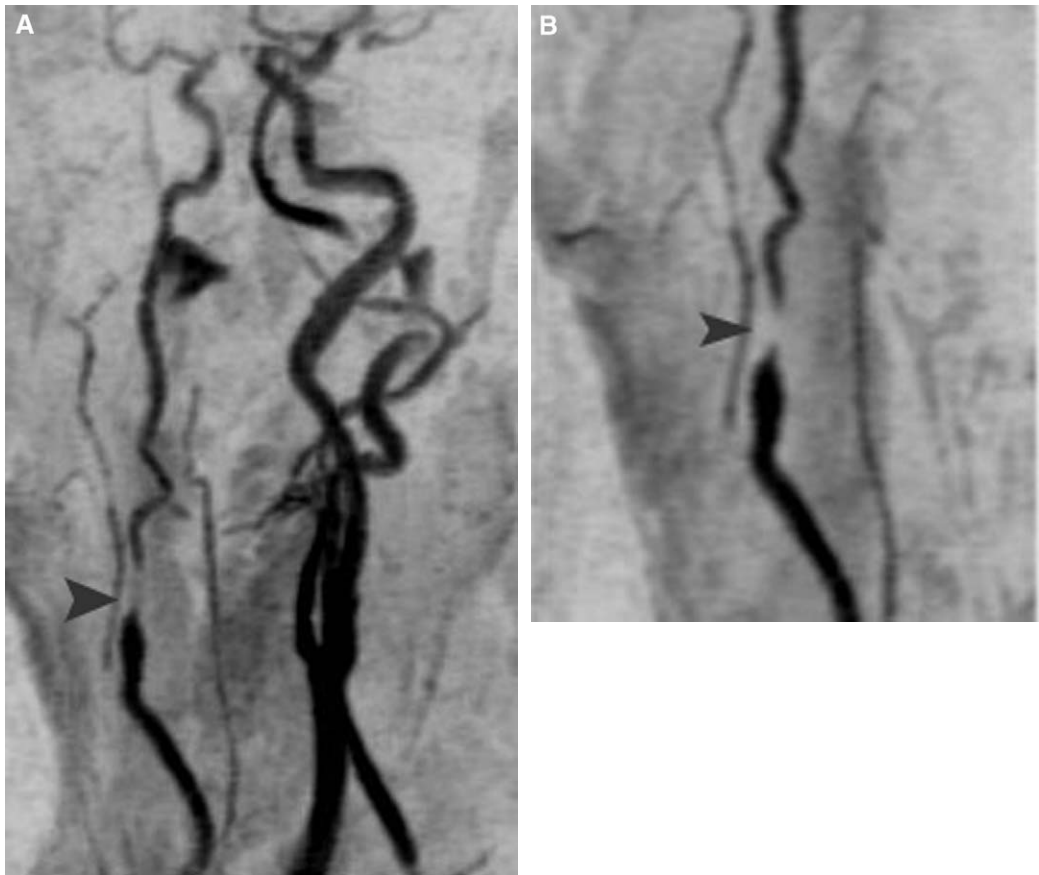


Fig. 3. Flow gaps with varying MRA techniques. (A) Oblique view from a 3D TOF post-contrast coronal MRA demonstrates a vertebral artery flow gap (*arrowhead*) because of stenosis. (B) Similar findings are seen on the corresponding non-contrast 2D TOF MRA. Both techniques are not able to show the angiographic “string sign”.

US, the sensitivity and specificity increased to 100% for evaluation of stenosis of 70% to 99%. This obviated the need for XRA in 61% of patients when MRA was used alone or in 74% of cases when MRA and US were used together. Other investigators also used fluoroscopic triggering to improve examination quality to obtain optimum vessel enhancement and some have reported sensitivities of 88.9% and specificities of 58.1% using the maximum intensity projection (MIP) images, and sensitivities of 83.3% and specificities of 97% using elliptic-centric post-contrast images [40–42]. These investigators also used venous suppression techniques. An accuracy level of 87.6% was attained and with the addition of reformatted transverse images an accuracy of 92.8% was possible. Evaluation of plaques revealed a 58.1% specificity for irregularity or

ulceration [43]. Addition of the first-pass method to fluoroscopic triggering improved the examinations, but quality limitations caused by failure of triggering still occurred. In these cases, the second phase of acquisition yielded sufficient image quality. However, in a study by Akoi et al [43], the axial-based source images still suffered from ring artifacts, low-resolution and low soft-tissue visualization. Adding a 1 minute second-phase acquisition in a different plane (axial) after first pass contrast-enhanced MRA improved these short falls and lengthened acquisition only slightly.

The next improvement came from better software and hardware for sensitivity encoding (SENSE) MRA. Sensitivity encoding is a new method that improves performance and has been used to study the carotid arteries without fluoroscopic triggering by Golay et al [44] and with

fluoroscopic triggering by Jewells et al [45]. The study by Jewells et al demonstrated a 100% sensitivity and specificity using 3D TOF post-contrast MRA images when compared with XRA for stenosis evaluation, even in the presence of a long string sign seen in 22 carotids (Fig. 4). This method of evaluation uses multiple receiver coils in parallel to encode the location of pixels within a patient in reference to the coils. The coils register the location of each pixel on the reference scan and use the data to reduce misregistration artifacts by placing the pixels back in the right location when they have been displaced or “wrapped around”. This method also allows for a reduction in scan time by one half resulting in motion artifact reduction [46]. Therefore, scanning time is short enough that three examinations can be obtained during a single breath-hold 3D TOF post contrast MRA. SENSE MRA has also been used to study the abdominal vasculature and to reduce artifacts in echo-planar imaging [47,48]. A recent study by Borish et al [49], using a time-resolved technique without bolus-timing, yielded

less favorable results demonstrating that this technique is best used in conjunction with bolus timing.

CTA carotid artery evaluation

A discussion of carotid MRA is not complete without commenting about carotid artery CTA. In a study by Link et al [50], there was an agreement of stenosis classification in 82% of moderate stenoses and in 90% of severe stenoses, but limited evaluation of mild stenosis with an agreement of only 59%. Accuracy in the evaluation of occlusion was 100%. Other investigators have experienced different results with CTA demonstrating its poor ability to distinguish between moderate (50%–69%) stenosis (sensitivity = 65%) and severe (70%–99%) stenosis (sensitivity = 73%) (Fig. 5). These limitations are most likely secondary to artifacts from calcific and eccentric plaques.

The addition of shaded surface display (SSD) to CTA, and evaluation of the source images in



Fig. 4. SENSE (parallel imaging) technique for MRA. (A) Lateral digital subtraction view from a catheter angiogram demonstrates a significant post-bulbar ICA stenosis. (B) Lateral view from a SENSE encoded post-contrast 3D TOF MRA image with central k-space acquisition, breath hold and fluoroscopic triggering. The stenosis is well seen and also notice the excellent demonstration of all arterial branches.

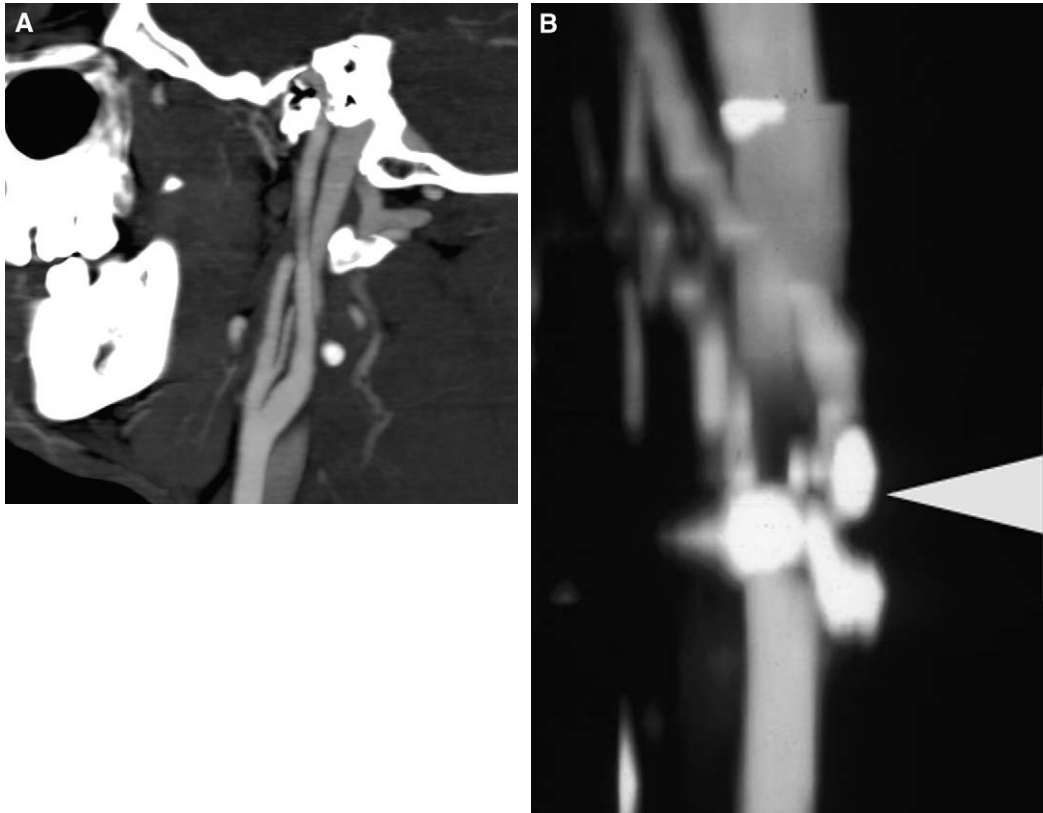


Fig. 5. CTA of the carotid arteries. (A) Lateral maximum intensity CTA image of a normal carotid artery bifurcation. There is some venous contamination because bolus-tracking was not employed but it does not affect the visualization of the arteries. (B) Older (*note step artifact*) oblique maximum intensity CTA image of the carotid artery bifurcation shows a calcific plaque that prevents visualization of the lumen.

carotid artery stenoses, improved its accuracy when compared with XRA in a study by Papp et al [51]. The source images alone tended to underestimate the stenoses. Another study by Marcus et al [52] revealed an 83% agreement between XRA and SSD CTA images. Dix et al [53] demonstrated that optimum parameters for carotid stenosis evaluation with CTA should include MIP and SSD axial magnified images with the level set halfway between luminal density and vessel wall density for greatest accuracy. This study demonstrated less than a 1% average difference in stenosis measurements by CTA when compared with the average caliper measurements in phantoms. Leclerc et al [54] documented similar results using SSD and MIP images. Axial images classified stenosis correctly in 95% of instances. Similarly, volume-rendering display yielded a sensitivity of 92% and a specificity of 96%. These results are similar to those seen using SSD CTA

imaging alone [53]. Other investigators have not found such promising results because of plaque eccentricity and the resultant non-circular lumens (a similar problem to that seen with XRA). In a study by Porche et al [55] using CTA, incorrect measurement of stenoses was found in 18 of 100 patients with non-circular lumens. This resulted in 2 out of 12 patients being diagnosed with moderate stenosis by CTA when it was severe stenosis, or 16% of patients not being selected properly for surgery. Inaccurate stenosis measurements were also seen with CTA when phantoms were evaluated using helical scanning with orientations parallel to, and at 45° oblique and perpendicular angles to the z-axis [56]. This problem worsened with increasing slice thickness and increasing length of stenosis. A recent study by Lev et al [57] comparing total occlusion versus near-total or hairline residual lumen (>90%–99% stenosis) with CTA and XRA revealed promising results

with accuracy rates of 95% and 85%, but did not compare these results to 3D post-contrast MRA.

Plaque evaluation

It has been shown that ulcerated plaques are more likely to produce emboli caused by a combination of slowly swirling blood within them allowing platelet aggregates to form, and intermittent Bernoulli effects, which then pull these platelet aggregates into the flowing blood creating emboli [56]. Plaque destabilization secondary to infiltration by macrophages and T-cells appears to be related to the presence of procoagulant protein tissue factor (TF). TF has been found to be present more frequently in patients who have cerebral microembolism (symptomatic patients more than in asymptomatic ones) [58]. Another important plasma indicator of plaque instability is oxidized low density lipoprotein [59]. Therefore, laboratory analysis and analysis of plaque morphology are important for evaluation of risk of embolic events.

US may depict plaque morphology, which correlates with symptomatology. The degree of plaque irregularity is not significant with regards to symptomatology [60]. In that study, plaques were characterized as Type I (hypo-echoic: equal brightness to blood), Type 2 (iso-echoic: brightness equal to periadventitia), and Type III (hyper-echoic: brightness greater than periadventitia). The hypoechoic areas within a plaque correlate with lipids and hemorrhage. The isoechoic areas correlate with fibrosis and the hyperechoic areas may also be consistent with hemorrhage [61]. There is a correlation between plaque heterogeneity and future rate of ipsilateral strokes in the presence of associated carotid artery stenosis, as well as a correlation between plaque heterogeneity and severity of stenosis [62,63]. Limitations of plaque assessment also exist with intravascular US as shown by Miskolczi et al [64] in a study of 140 carotid arteries that accurately depicted plaque ulcerations, but small mural thrombus was misinterpreted as plaque. Comparison of MRA with XRA according to Anderson et al [65] resulted in a similar assessment of carotid bifurcation stenosis, but MRA allowed for better direct visualization of the plaque than did US and therefore, the authors believe MRA could replace XRA for evaluation of carotid artery stenosis. A study by Nederkoorn et al [66] yielded similar findings when a comparison of US with contrast-enhanced MRA and XRA was performed. Both

US and MRA were accurate examinations but MRA performed better for plaque analysis.

CTA is also useful for the evaluation of plaque morphology. CT evaluation of carotid plaques in a study by Oliver et al [67] revealed a correlation between plaque appearance on CT and their histology. A plaque appearing patchy or homogeneous on CT, had a necrotic lipid core at histology and often hemorrhage. Fifteen out of 16 plaques that were of lower density than muscle on CT had a lipid core. Fibrous plaques had soft tissue density equal to muscle in six out of seven instances. CT also demonstrated high-density calcifications better than histology, but fair to poor for visualization of ulceration, an important predictor of plaque instability [67]. Lack of plaque ulceration identification is problematic since it is known that soft-plaques and ulceration in particular predict embolic potential. In a study evaluating plaque morphology by Randoux et al [68], visualization of plaque irregularities was good with CTA, but XRA and MRA demonstrated ulceration better than CTA (Fig. 6). Other authors have shown that CTA was not accurate for evaluation of plaque composition and that ulceration prediction was only moderate compared with histologic analysis [69,70]. Plaque evaluation with MRI is a developing technique (Fig. 7). Hatsukami et al [71] evaluated atherosclerotic plaques for instability using gradient-echo-recalled



Fig. 6. Plaque ulceration on MRA. Slightly oblique 3D TOF post-contrast MRA shows a small ulcerated plaque (arrow) in the posterior wall of the ICA.

imaging with multiple overlapping thin section acquisitions. Using spin echo techniques, the same investigators, demonstrated a sensitivity of 81% and a specificity of 90% in 18 patients who underwent endarterectomies. The three spin echo sequences used were 3D TOF T1 double inversion recovery, intermediate signal and T2-weighted images at 3 to 5 mm for optimal voxel sizes, and acceptable signal-to-noise ratios. Black-blood technique also aids the process by suppressing the signal from flowing blood with resultant increased vessel conspicuity.

Evaluation of plaque morphology in endarterectomy specimens using MRI may require 3D imaging for sufficient resolution to identify the cartilaginous cap, necrotic core and calcifications [72,73]. Callahan et al [74], and Connors et al [75] investigated the use 3-Tesla units in the evaluation of plaque morphology and found a high correlation with histology. The work is still ongoing, but the images are capable of demonstrating lipid cores, hemorrhage, plaque ulceration, plaque rupture and inflammation, and plaque calcification. A T2 imaging classification scheme for atherosclerotic plaques has been adapted for MRI with a Type 0 meaning no intimal thickening, a Type I-II being a thin plaque with less than 10% stenosis and no calcification, and a Type III plaque having with small lipid cores and no calcification. Type IV-V plaques are divided into a, b, and c. A type IV-Va has a large lipid core with a fibrous cap and small calcifications. A type Vb has a lipid core or

fibrotic tissue with large calcifications, a type Vc is a fibrous plaque with no lipid core, and a type Vb-Vic is a plaque containing hemorrhage or thrombosis [75]. Several new methods for plaque evaluation are currently under investigation, including the use of gadolinium derivatives for plaque volume evaluation and of iron oxide particles to evaluate macrophage density [76]. CT imaging with liposomal iohexol and positron emission tomography imaging with 18 fluoro-deoxyglucose are also ongoing research projects [77].

Prediction of brain hemodynamics with conventional and perfusion MRI: added decision-making factors for surgery

The blood supply to the brain is affected by stenoses in the carotid arteries and by the burden of disease involving the intracranial vasculature. Therefore, evaluation of the intracranial vasculature along with the carotid vasculature is probably warranted in most patients with vascular disease. Mean transit time (MTT) may be affected by severe occlusive disease of the carotid arteries without changes in cerebral blood volume (CBV). In ischemic tissue there is prolonged MTT and higher signal intensity than in adjacent normal tissue which is proportional to the degree of severity of proximal vessel disease [78]. Regional MTT maps are the best indicator of relative oligemia and ischemia caused by reduction of cerebral blood flow (CBF). Normal CBV maps

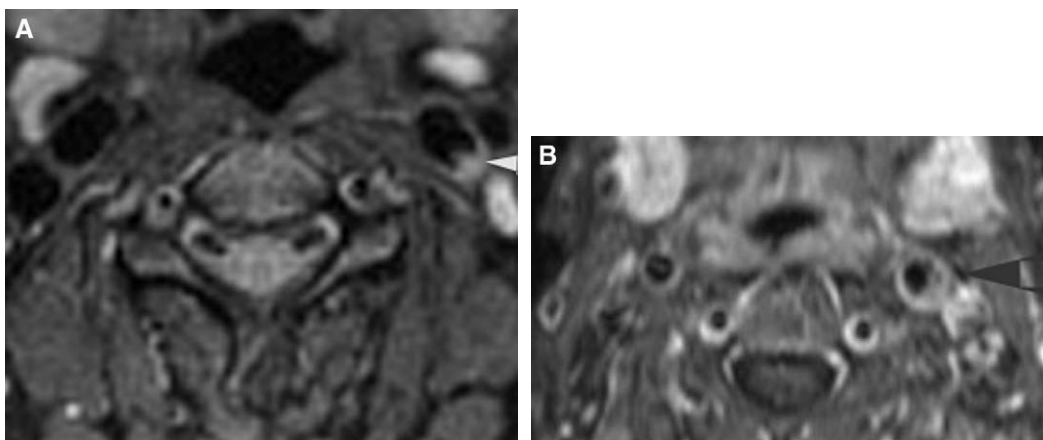


Fig. 7. Plaque characteristics on MR imaging. (A) Axial fat suppressed T2 weighted image shows thick, bright, and somewhat irregular atherosclerotic plaque (*arrowhead*) in the posterior wall of the left ICA. (B) In a different patient, axial post contrast T1 weighted image with fat suppression shows a thick plaque (*arrowhead*) with enhancement and areas of no enhancement suggesting the presence of intra-plaque fibrous tissues, fat or calcifications.

despite MTT abnormalities indicate the circulatory systems' ability to compensate for hypoperfusion, in particular in the gray matter, where the regional CBV may be increased with significant carotid stenosis. This phenomenon may be explained by perfusion of gray matter by way of pial collaterals and not just macro-circulatory compensation by way of the internal carotid and external carotid (by way of the superior ophthalmic artery) arteries. Abnormal T2 signal in the area of hypoperfusion has also been reported with internal carotid artery occlusive disease before the development of major neurologic deficits or infarction [79]. Therefore, brain imaging with perfusion and MRA may be warranted for evaluation of individuals with significant carotid stenosis to determine the true severity of their disease.

MRA of the neck for arterial dissections

Evaluation of the post-traumatic carotid and vertebral arteries is becoming more common as clinicians and radiologists realize the potential of these vessels to be injured. Most commonly, injury to these vessels results in dissection, although occlusions and pseudoaneurysms also occur [80]. Pseudoaneurysms remain unchanged in 46% of patients, disappear with 36%, and decrease in size in 18%. Resolution occurs more commonly with vertebral artery aneurysms than it does with internal carotid artery aneurysms [81]. The injuries are often related to fractures or subluxations of the spine, facial bones, and skull base,

and are most frequently secondary to motor vehicle accidents [82–86]. The patient may demonstrate cerebral infarction (up to 20% of infarcts in young individuals), or there may be face, neck, occipital pain, vertigo, cranial nerve III symptoms, or visual symptoms, although some patients are asymptomatic [82–88]. Dissections may heal spontaneously and the type of healing depends on the length of the dissection. A normal appearing vessel after healing may be seen after a 2-mm long dissection. A stenotic vessel after healing of a 6-mm long dissection, pseudoaneurysm formation after a 4- to 6-mm long dissection or an occluded vessel after a 8-mm long dissection [89].

On MRI, vertebral and carotid artery dissections have an eccentric signal void with surrounding semilunar, oval, or circumferential area of increased T1 signal (hematoma) [90–93] (Fig. 8). This finding may also be the result of normal laminar flow on gradient echo images and thus, the use of fat suppression T1 images may help differentiate mural hematoma from surrounding tissues [82,92,94,95]. Differentiation of mural from luminal thrombus is best done with gradient echo images through the stenotic arterial segment perpendicular to the length of the vessel [93]. In a study of 20 vertebral artery dissections evaluated by MRI, XRA, and US, MRA was able to identify a double lumen, intimal flap or mural hematoma with stenosis or aneurysmal dilatation consistent with dissection, or irregular stenosis or string sign as suggestive of dissection (sensitivity: 94%, specificity: 29% for dissections) [96]. XRA was 100% sensitive and 35% specific.

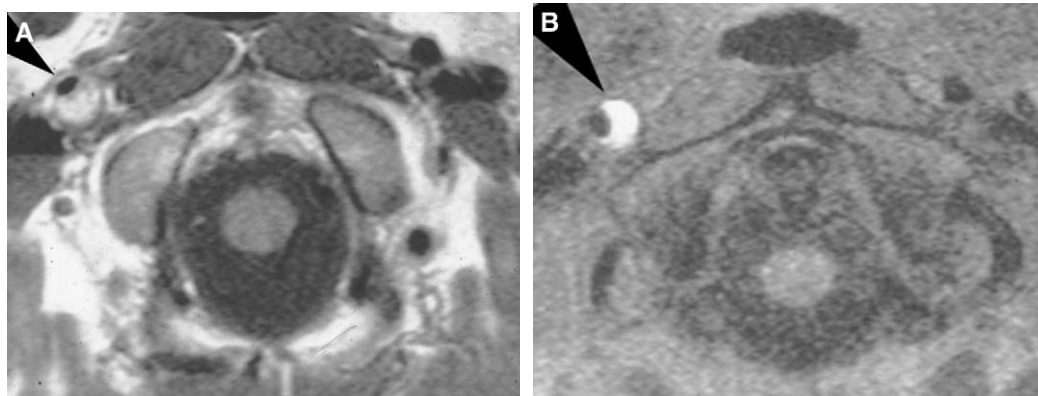


Fig. 8. Vertebral artery dissections. (A) Axial T1 weighted image shows dissection of the right internal carotid artery (arrowhead) with diminished central lumen and bright mural clot. (B) In the same patient, the dissected artery (arrowhead) is better seen on a T1 weighted, fat suppressed image.

Combining MRA with XRA increased the specificity to 50%. The sensitivity of US was 79% but US lacked specificity. Follow-up MRI demonstrated recanalization of vessels in 63% of patients, persistent occlusion in 31%, and a dissecting aneurysm in one patient.

CTA was used for the diagnosis of dissections of the internal carotid artery [97] by Leclerc et al [97]. They evaluated 16 patients with 18 dissections and found that CTA demonstrated 100% specificity and 100% sensitivity for stenotic dissections. Using enlargement of the dissected artery as a criterion for the diagnosis of occlusive dissection, they achieved 100% specificity and sensitivity. CTA has also been used for follow-up evaluation of ICA dissections over time to assess changes seen on XRA between 7 and 26 months [98]. CTA is deemed to be a good method for initial evaluation of cervical dissection and for follow up. CTA is easily added to screening spine CT in patients with cervical spine fractures obviating the need for MRA, and at least according to the previously cited study it seems to be accurate.

References

- [1] Harrison MJG, Marshall J. Prognostic significance of severity of carotid atheroma in early manifestations of cerebrovascular disease. *Stroke* 1982; 13:567–9.
- [2] Thiele BL, Young JV, Chikos PM, Hirsh JH, Strandness DE. Correlation of arteriographic findings and symptoms in cerebrovascular disease. *Neurology* 1980;30:1041–6.
- [3] Ricci S, Flamini FO, Celani MG, Marini M, Antonini D, Bartolini S, et al. Prevalence of internal carotid artery stenosis in subjects older than 49 years: a population study. *Cerebrovasc Dis* 1991; 1:16–9.
- [4] Jose MO, Touboul PJ, Mas JL, Laplane D, Bousser MG. Prevalence of asymptomatic internal carotid artery stenosis. *Neuroepidemiology* 1987;6: 150–2.
- [5] European Carotid Surgery Trialists' Collaborative Group. MRC European Carotid Surgery Trial: interim results for symptomatic patients with severe (70–99%) or with mild (0–29%) carotid stenosis. *Lancet* 1991;337:1235–43.
- [6] Chambers BR, Norris NW. Outcome in patients with asymptomatic neck bruits. *N Engl J Med* 1986;315:860–5.
- [7] Fisher CM. Observations of the fundus oculi in transient monocular blindness. *Neurology* 1959;9: 333–47.
- [8] Siebler M, Kleinschmidt A, Sitzer M, Steinmetz H, Freund HJ. Cerebral microembolism in symptomatic and asymptomatic high-grade internal carotid artery stenosis. *Neurology* 1994;44:615–8.
- [9] Streifler JY, Eliaziv M, Fox AJ, Benavente OR, Hachinski VC, Ferguson GG, et al. North American Symptomatic Carotid Endarterectomy Trial. Angiographic detection of carotid plaque ulceration: comparison with surgical observations in a multicenter study. *Stroke* 1994;25:1130–2.
- [10] Eliaziv M, Streifler JY, Fox AJ, Hachinski VC, Ferguson GG, Barnett. North American symptomatic carotid endarterectomy trial: significance of plaque ulceration in symptomatic patients with high-grade carotid stenosis. *Stroke* 1994;25:304–8.
- [11] Rothwell PM, Gibon R, Warlow CP. Interrelation between plaque surface morphology and degree of stenosis on carotid angiograms, and the risk of ischemic stroke in patients with symptomatic carotid stenosis. *Stroke* 2000;31:615–30.
- [12] Siebler M, Sitzer M, Rose G, Bendfeldt D, Steinmetz H. Silent cerebral embolism caused by Neurologically symptomatic high-grade stenosis. *Brain* 1993; 116:1005–15.
- [13] Forteza AM, Babikian VL, Hyde C, Winter M, Pochay V. Effect of time, and cerebrovascular symptoms on the prevalence of microembolic signals in patients with cervical carotid stenosis. *Stroke* 1996;27:687–90.
- [14] Wagle WA, Doumoulin CI, Souza SP, Cline HE. 3D FT MR angiography of carotid and basilar arteries. *Am J Neuroradiology* 1989;10:911–9.
- [15] Keller PJ, Drayer BP, Fram EK, Williams KD, Dumoulin CL, Souza SP. MR angiography with two dimensional acquisition and three-dimensional display. Work in progress. *Radiology* 1989;173: 527–32.
- [16] Litt AW, Eidelman EM, Pinto RS, Riles TS, McLachlan SJ, Schwartzberg S, et al. Diagnosis of carotid artery stenosis: comparison of 2DFT time-of-flight MR angiography with contrast angiography in 50 patients. *Am J Neuroradiology* 1991; 12:149–54.
- [17] Laster RF, Acker JD, Halford 3rd HH, Nauert TC. Assessment of MR angiography versus arteriography for evaluation of cervical carotid bifurcation disease. *Am J Neuroradiology* 1993;14:681–8.
- [18] Furst G, Saleh A, Wenserski F, Malms J, Cohen M, Aulich A, et al. Reliability and validity of non-invasive imaging of internal carotid artery pseudo-occlusion. *Stroke* 1999;30:1444–9.
- [19] Robison RO, Blatter DD, Parker DL, Hou P, Collins JS, Barney WW. Fat suppression in combination with multiple overlapping thin-slab 3-D acquisition MR angiography: proposed technique for improved vessel visualization. *Am J Neuroradiology* 1992;13:1429–34.
- [20] Li W, Kramer J, Kleeffeld J, Edelman RR. MR angiography of the extra-cranial carotid arteries using a two-slab oblique 3-D acquisition. *Am J Neuroradiology* 1992;13:1423–8.

- [21] Patel MR, Klufas BA, Kim D, Edelman RR, Kent KC. MR angiography of the carotid bifurcation: artifacts and limitations. *Am J Roentgenol* 1994; 162:1431–7.
- [22] Kallmes DF, Omary RA, Dix JE, Evans AJ, Hillman BJ. Specificity of MR angiography as a confirmatory test of carotid artery stenosis. *Am J Neuroradiology* 1996;17:1501–6.
- [23] Nederkoorn PJ, Kappelle LJ, Van Der Graaf Y, Humink MG, Eikelboom BC, Mali WP. Duplex ultrasound, MR Angiography, and Conventional angiography in Carotid artery disease: interpretation of separate test results and their combinations. *Stroke* 2001;32:335b.
- [24] El-Saden SM, Grant EG, Hathout GM, Zimmerman PT, Cohen SN, Baker JD. Imaging of the internal carotid artery: the dilemma of total versus near total occlusion. *Radiology* 2001;221:301–8.
- [25] Patel MR, Kuntz KM, Klufas RA, Kim D, Kramer J, Polak JF, et al. Preoperative assessment of the carotid bifurcation: Can magnetic resonance angiography and duplex ultrasonography replace contrast angiography? *Stroke* 1995;26:1753–8.
- [26] Mittl RL Jr, Broderick M, Carpenter JP, Goldberg HI, Listerud J, Mishkin HD, et al. Blinded-reader comparison of magnetic resonance angiography and duplex ultrasonography for carotid artery bifurcation stenosis. *Stroke* 1994;25:4–10.
- [27] Nederkoorn PJ, van der Graaf Y, Eikelboom BC, van der Lugt Aad, Bartels LW, Mali W. Time-of-flight MR angiography of carotid artery stenosis: does a flow void represent severe stenosis? *Am J Neuroradiology* 2002;23:1779–84.
- [28] Anderson CM, Saloner D, Lee RE, Griswold VJ, Shapeero LG, Rapp JH, et al. Assessment of carotid artery stenosis by MR Angiography: comparison with x-ray angiography and color-coded Doppler ultrasound. *Am J Neuroradiology* 1992; 13:989–1003.
- [29] Pan XM, Salopner D, Reilly LM, Bowersox JC, Murray SP, Anderson CM, et al. Assessment of carotid artery stenosis by ultrasonography, conventional angiography, and magnetic resonance angiography: correlation with ex vivo measurement of plaque stenosis. *J Vasc Surg* 1995;21:82–8.
- [30] Elgersma OE, Wust AF, Buijs PC, van Der Graaf Y, Eikerboom BC, Mali WP. Multidirectional depiction of internal carotid arterial three-dimensional time-of-flight MR angiography versus rotational conventional digital subtraction angiography. *Radiology* 2000;216:511–6.
- [31] Wutke R, Lang W, Fellner C, Janka R, Denzel C, Lell M, et al. High-resolution, contrast-enhanced magnetic resonance angiography with elliptical centric k-space ordering of supra-aortic arteries compared with selective X-ray angiography. *Stroke* 2002;33:1522–34.
- [32] Krinsky G, Maya M, Rofsky N, Lebowitz J, Nelson PK, Ambrosino M, et al. Gadolinium-enhanced 3D MRA of the aortic arch vessels in the detection of atherosclerotic cerebrovascular occlusive disease. *J Comput Assist Tomogr* 1998;206:167–78.
- [33] Leclerc X, Martinat P, Godefroy O, Lucas C, Giboreau F, Ares GS, et al. Contrast-enhanced three-dimensional with steady state (FISP) MR angiography of supraortic vessels: preliminary study. *Am J Neuroradiology* 1998;19:1405–13.
- [34] Melham ER, Caruthers SD, Faddoul SG, Tello R, Jara H. Use of three-dimensional MR angiography for tracking a contrast bolus in the carotid artery. *Am J Neuroradiology* 1999;20:263–6.
- [35] Wutke R, Lang W, Fellner C, Janka R, Denzel C, Lell M, et al. High-resolution, contrast-enhanced magnetic resonance angiography with elliptical centric k-space ordering of supra-aortic arteries compared with selective x-ray angiography. *Stroke* 2002;33:1522–34.
- [36] Kopka L, Vossenhilf R, Rodenwaldt J, Grabbe E. Differences in injection rates on contrast-enhanced breath-hold three-dimensional MR angiography. *Am J Roentgenol* 1998;170:345–8.
- [37] Leclerc X, Nicol L, Gauvrit JY, Le Thuc V, Leys D, Pruvo JP. Contrast-enhanced MR angiography of supraortic vessels: the effect of voxel size on image quality. *Am J Neuroradiology* 2000;21: 1021–7.
- [38] Melhem ER, Serfaty JM, Jones L, Itoh R, Kuszyk BS, Martin JB, et al. Contrast-enhanced MR angiography: The effects on k-space truncation on luminal representation in a carotid artery phantom model. *Am J Neuroradiology* 2000;21:1028–31.
- [39] Serfaty JM, Chirossel P, Chevallier JM, Ecochard R, Froment JC, Douek PC. Accuracy of three-dimensional gadolinium enhanced MR angiography in the assessment of extracranial carotid artery disease. *Am J Roentgenol* 2000;175:455–63.
- [40] Riederer SJ, Bernstein MA, Breen JF, Busse RF, Ehman RL, Fain SB, et al. Three-dimensional contrast-enhanced MR angiography with real-time fluoroscopic triggering: design specifications and technical reliability in 330 patient studies. *Radiology* 2000;215:584–93.
- [41] Huston 3rd J, Fain SB, Wald JT, Luetmer PH, Rydberg CH, Covarrubias DJ, et al. Carotid artery: elliptical centric contrast-enhanced MR angiography compared with conventional angiography. *Radiology* 2001;218:138–43.
- [42] Huston 3rd J, Fain SB, Riederer SJ, Wilman AH, Bernstein MA, Busse RF. Carotid arteries: Maximizing arterial to venous contrast in fluoroscopically triggered contrast-enhanced MR angiography with elliptical centric view ordering. *Radiology* 1999; 211:265–73.
- [43] Aoki S, Nakajima H, Kumagai H, Araki T. Dynamic contrast-enhanced MR angiography and MR imaging of the carotid artery: High-resolution sequences in different acquisition planes. *Am J Neuroradiology* 2002;21:381–5.

- [44] Golay X, Brown SJ, Itoh R, Malhem ER. Time-resolved contrast-enhanced carotid MR angiography using sensitivity encoding (SENSE). *Am J Neuro-radiology* 2001;22:1615–19.
- [45] Jewells VJ, Eastwood JE, Provenzale J. Time-resolved sensory-encoded (SENSE) postcontrast MR angiography: comparison with catheter angiography and 2D TOF MR angiography. ASNR, 40th meeting, June 2002. Vancouver, BC.
- [46] Pruessman KP, Weiger M, Scheidegger MB, Boesinger P. SENSE: sensitivity encoding for fast MRI. *Magn Reson Med* 1999;42:952–62.) and (Weiger M, Pruessman KP, Boesinger P. 2D SENSE for faster 3D MRI. *MAGMA* 2002;14(1):9–10.
- [47] Weiger M, Pruessman KP, Kassner A, Roditi G, Lawton T, Reid A, et al. Contrast-enhanced 3D MRA using SENSE. *J Mag Res Imag* 2000;12:671–7.
- [48] Bammer R, Keeling SL, Augustin M, Pruessman KP, Wolf R, Stollberger R, et al. Improved diffusion-weighted single-shot echo-planar imaging (EPI) in stroke using sensitivity encoding (SENSE). *Magn Reson Med* 2001;46(3):548–54.
- [49] Borish I, Horn M, Butz B, Zorger N, Draganski B, Hoelscher T, et al. Peroperative evaluation of carotid artery stenosis: Comparison of contrast-enhanced MR angiography and duplex sonography with digital subtraction angiography. *Am J Neuro-radiology* 2003;24:1117–22.
- [50] Link J, Brossman J, Grabener M, Mueller-Huelsbeck S, Steffens JC, Brinkmann G, et al. Spiral CT angiography and selective digital subtraction angiography of internal carotid artery stenosis. *Am J Neuroradiology* 1996;17:89–94.
- [51] Papp Z, Patel M, Ashtari M, Takahashi M, Goldstein J, Maguire W, et al. Carotid artery stenosis: optimization of CT angiography with a combination of shaded surface display and source images. *Am J Neuroradiology* 1997;18:759–63.
- [52] Marcus CD, Ladam-Marcus V, Bigot JL, Clement C, Baehrel B, Menanteau B. Carotid arterial stenosis: Evaluation at CT angiography with the Volume-rendering technique. *Radiology* 1999;211:775–80.
- [53] Dix JE, Evans AJ, Kallmes DF, Sobel AH, Phillips CD. Accuracy and precision of CT angiography in a model of carotid artery bifurcation stenosis. *Am J Neuroradiology* 1997;18:409–15.
- [54] Leclerc X, Godefroy O, Pruvo JP, Leys D. Computed tomographic angiography for the evaluation of carotid artery stenosis. *Stroke* 1995;26:1577–81.
- [55] Porshe C, Walker L, Mendelow D, Birchall D. Evaluation of cross-sectional luminal morphology in carotid atherosclerotic disease by use of spiral CT angiography. *Stroke* 2001;32:2511–5.
- [56] Wise SW, Hopper KD, Ten Have T, Schwartz T. Measuring carotid artery stenosis using CT angiography: the dilemma of artifactual lumen eccentricity. *Am J Neuroradiology* 1998;170:919–23.
- [57] Lev MH, Romero J, Goodman D, Goodman D, Bagga R, Young Kwon Kim H, et al. Total occlusion versus hairline residual lumen of the internal carotid arteries: accuracy of single section helical CT angiography. *Am J Neuroradiology* 2003;24:1123–9.
- [58] Imbesi SG, Kerber CW. Why do ulcerated atherosclerotic carotid artery plaques embolize? A flow dynamics study. *Am J Neuroradiology* 1998;19:761–6.
- [59] Jander S, Sitzer M, Wendt A, Schroeter M, Buchkremer M, Siebler M, et al. Expression of tissue factor in high-grade carotid artery stenosis: association with plaque destabilization. *Stroke* 2001;32:850–4.
- [60] Hishi K, Itabe H, Uno M, Kitazato K, Horiguchi H, Shinno K, et al. Oxidized LDL in carotid plaques and plasma associates with plaque instability. *Arterioscler Thromb Vasc Biol* 2002;22:1649.
- [61] Tegos TJ, Kalomiris KJ, Sabetai MM, Kalodiki E, Nicolaides AN. Significance of sonographic tissue and surface characteristics of carotid plaques. *Am J Neuroradiology* 2001;22:1605–12.
- [62] Tegos TJ, Sohail M, Sabetai M, Robless P, Akbar N, Pare G, et al. Echomorphologic and histopathologic characteristics of unstable carotid plaques. *Am J Neuroradiology* 2000;21:1937–44.
- [63] Aburahma AF, Thiele SP, Wulu JT Jr. Prospective controlled study of the natural history of asymptomatic 60% to 69% carotid stenosis according to ultrasonic plaque morphology. *J Vasc Surg* 2002;36(3):437–42.
- [64] AbuRahma AF, Wulu JT Jr, Crotty B. Carotid plaque ultrasonic heterogeneity and severity of stenosis. *Stroke* 2002;33:1772–5.
- [65] Miskolczi L, Guterman LR, Flaherty JD, Hopkins LN. Depiction of carotid plaque ulceration and other plaque-related disorders by intravascular sonography: a flow chamber study. *Am J Neuro-radiology* 1996;17:1881–90.
- [66] Anderson CM, Saloner D, Lee RE, Griswold VJ, Shapeero LG, Rapp JH, et al. Assessment of carotid artery stenosis by MR angiography: comparison with x-ray angiography and color-coded Doppler ultrasound. *Am J Neuroradiology* 1992;13:989–1003.
- [67] Nederkoorn PJ, Kappelle LJ, Van Der Graff Y, Humink MG, Eikelboom BC, Mali WP. Duplex ultrasound, MR angiography, and conventional angiography in carotid artery disease: interpretation of separate test results and their combinations. *Stroke* 2001;32:335b.
- [68] Oliver TB, Lammie GA, Wright AR, Wardlaw J, Patel SG, Peek R, et al. Atherosclerotic plaque at the carotid bifurcation: CT angiographic appearance with histopathologic correlation. *Am J Neuroradiology* 1999;20:897–901.
- [69] Randoux B, Marro B, Koskas F, Duyme M, Sahel M, Zouaoui A, et al. Carotid artery stenosis: Prospective comparison of CT, three-dimensional gadolinium-enhanced MR, and conventional angiography. *Radiology* 2001;220:179–85.

- [70] Walker LJ, Ismail A, Meekin W, Lambert D, Mendelow AD, Birchall D. Computed tomography angiography for the evaluation of carotid atherosclerotic plaque: correlation with histopathology of endarterectomy specimens. *Stroke* 2002;33:977–981.
- [71] Hatsukami TS, Ross R, Polissar NL, Yuan C. Visualization of fibrous cap thickness and rupture in human atherosclerotic plaque in vivo with high resolution magnetic resonance imaging. *Circulation* 2000;102:959–64.
- [72] Finn JP, Edelman R. Black-blood and segmented k-space magnetic resonance angiography. *Magn Reson Imaging Clin N Am* 1993;1:349–57.
- [73] Coombs BD, Rapp JH, Ursell PC, Reilly LM, Saloner D. Structure of plaque at carotid bifurcation: high-resolution MRI with histological correlation. *Stroke* 2001;32:2516–21.
- [74] Callahan A. Cervical carotid atherosclerosis: The plaque. ASNR 41st annual meeting, Thursday May 1, 2003, Washington, DC.
- [75] Connors JJ. Cervical carotid atherosclerosis: two completely different disease—Who should be treated? ASNR 41st annual meeting, Thursday May 1, 2003, Washington, DC.
- [76] Serfaty JM, Chaabane L, Tabib A, Chevallier JM, Briguet A, Douek PC. Atherosclerotic plaques: classification and characterization with T2 weighted high-spatial-resolution MR imaging—an in vitro study. *Radiology* 2001;219:403–10.
- [77] Ruehm SG, Carot C, Vogt P, Kolb S, Debatin JF. Magnetic resonance imaging of atherosclerotic plaque with small superparamagnetic particles of iron oxide in hyperlipidemic rats. *Circulation* 2001;103:415–22.
- [78] Kereikas DJ. The Emperor's clothes: in search of the vulnerable plaque. *Circulation* 2003;107:2076.
- [79] Madedda M, Yuh WTD, Ueda T, Maley JE, Crosby DL, Zhu MW, et al. Severe occlusive carotid artery disease: hemodynamic assessment by MR perfusion imaging in symptomatic patients. *Am J Neuroradiology* 1999;10:43–51.
- [80] Yamauchi H, Fukuyama H, Yamaguchi S, Miyoshi T, Kimura J, Konishi J. High-intensity area in the deep white matter indicating hemodynamic compromise in internal carotid artery occlusive disorders. *Arch Neurol* 1991;48:1067–71.
- [81] Weller SJ, Rossitch E Jr, Malek AM. Detection of vertebral artery injury after cervical spine trauma using magnetic resonance angiography. *J Trauma* 1999;46(4):660–6.
- [82] Touze E, Randoux B, Meary E, Arquizan C, Meder JF, Mas JL. Aneurysmal forms of cervical artery dissection: associated factors and outcome. *Stroke* 2001;32:418–23.
- [83] Friedman D, Flander A, Thomas C, Millar W. Vertebral artery injury after acute cervical spine trauma: rate of occurrence as detected by MR angiography and assessment of clinical consequences. *Am J Neuroradiology* 1995;164:443–7.
- [84] Crum B, Mokri B, Fulbham J. Spinal manifestations of vertebral artery dissection. *Neurology* 2000;55:304–6.
- [85] Biffi WL, Moore EE, Elliot JP, Ray C, Offner PJ, et al. The devastating potential of blunt vertebral arterial injuries. *Ann Surg* 2000;231:672–81.
- [86] Weller SJ, Rossitch E Jr, Malek AM. Detection of vertebral artery injury after cervical spine trauma using magnetic resonance angiography. *J Trauma* 1999;46(4):660–6.
- [87] Freidman D, Flanders A, Thomas C, Millar W. Vertebral artery injury after acute cervical spine trauma: rate of occurrence as detected by MR angiography and assessment of clinical consequences. *Am J Neuroradiology* 1995;164(2):443–7.
- [88] Blunt SB, Galton C. Cervical carotid or vertebral artery dissection: An underdiagnosed cause of stroke in the young, editorial. *BMJ* 1997;314:234.
- [89] Carillo EH, Osborne DL, Spain DA, et al. Blunt carotid artery injuries: difficulties with the diagnosis prior to neurologic event. *J Trauma* 1999;46:1120–5.
- [90] Okamoto T, Miyachi S, Negoro M, Otsuka G, Suzuki O, Keino H, et al. Experimental model of dissecting aneurysms. *Am J Neuroradiology* 2002;23:577–84.
- [91] Tobias JA. MRI of intracranial vascular disease with emphasis at low and intermediate field strengths. In: Pomeraz SJ, editor. *Cranio-cervical Magnetic Resonance Imaging*. Philadelphia: WB Saunders; 1989. p. 315–50.
- [92] Goldberg HI, Grossman R, Gomori J, et al. Cervical internal carotid artery dissecting hemorrhage: diagnosis using MRI. *Radiology* 1986;158:157–61.
- [93] Zuber M, Meary E, Meder JF, et al. Magnetic resonance imaging and dynamic CT scan in cervical artery dissections. *Stroke* 1994;25:576–81.
- [94] Iwama T, Andoh T, Sakai N, et al. Dissecting and fusiform aneurysms of vertro-basilar systems: MR imaging. *Neuroradiology* 1990;32:272–9.
- [95] Pacini R, Simon J, Ketonen L, et al. Chemical-shift imaging of a spontaneous internal carotid artery dissection: case report. *Am J Neuroradiology* 1991;12:360–2.
- [96] Auer A, Schmidauer C, Waldenberger P, Aichner F. Magnetic resonance angiographic and clinical features of extracranial vertebral dissection. *J Neurol Neurosurg Psychiatry* 1998;64:474–81.
- [97] Leclerc X, Godefroy O, Salhi A, Lucas C, Leys D, Pruvo JP. Helical CT for diagnosis of extracranial internal carotid artery dissection. *Stroke* 1996;27:461–6.
- [98] Leclerc X, Lucas C, Godefroy O, Tessa H, Martinat P, Leys D, et al. Helical CT for the follow-up of cervical internal carotid artery dissections. *Am J Neuroradiology* 1998;19:831–7.



Contrast-enhanced MR angiography of the intracranial circulation

Chul-Ho Sohn, MD^{a,b}, Robert J Sevick, MD^c,
Richard Frayne, PhD^{d,*}

^a*Department of Radiology, Keimyung University School of Medicine, Daegu, Korea*

^b*Department of Radiology, University of Calgary, Calgary, AB, Canada*

^c*Departments of Radiology, Clinical Neurosciences, and Cell Biology and Anatomy,
University of Calgary, Calgary, AB, Canada*

^d*Departments of Radiology, and Clinical Neurosciences, University of Calgary, Calgary, AB, Canada*

MR angiography (MRA) is a powerful, non-invasive diagnostic imaging technique for examining normal and abnormal blood vessels. Initially, MRA approaches were developed that took advantages of naturally occurring vascular-stationary background tissue contrast mechanisms. These MRA techniques visualized the vasculature by using either inflow effects (a class of techniques known as time-of-flight [TOF] imaging) or by encoding blood velocity into the phase of the MR signal (phase contrast [PC] imaging) [1,2]. Over approximately 15 years these techniques have dramatically improved. Today, TOF MRA in particular, can routinely provide satisfactory images of the intracranial vasculature including rotational projection images [3]. In some medical

centers, the TOF MR angiographic technique has replaced conventional digital subtraction angiography (DSA) for screening for intracranial vascular disease [4–7]. PC MRA is less frequently used for the assessment of the intracranial circulation, but nevertheless, can provide important information about flow directionality, for example in assessing venous thrombosis [8] or in areas with retrograde blood flow [9]. Despite their success, both TOF and PC MRA have a number of limitations, such as decreased sensitivity to slow and disturbed flow [10].

A third class of MR angiographic techniques, which has been aggressively developed and evaluated only over the last decade, requires the injection of MR contrast agents [11,12]. These contrast-enhanced MRA (CE MRA) techniques use the T1-relaxation-shortening effects associated with paramagnetic MR contrast agents [13] to improve vascular signal and minimize artifact because of slow and disturbed flows. To date, nearly all major arterial systems have been imaged reliably with CE MRA [1,14,15]. Those most commonly assessed include the extra-cranial carotid arteries [16], the thoracic-abdominal aorta [17] and its major arterial branches, [18], and the peripheral arteries [19,20].

CE MRA also has been used to study intracranial vascular diseases. The authors have used a variety of CE MRA approaches to evaluate intracranial artery occlusions in acute ischemic stroke, and for the assessment of cerebral aneurysms and venous malformations. In this

Operational funds were provided by the Alberta Foundation for Health Research, the Alberta Heritage Foundation for Medical Research (AHFMR), the Calgary Health Region through the Partners-in-Health fundraising campaign, the Canadian Institutes for Health Research (CIHR), the Heart and Stroke Foundation of Canada (HSFC), and the University of Calgary. CS is funded by Keimyung University School of Medicine, Daegu, Korea. All authors are also with the Seaman Family MR Research Centre, Foothills Medical Centre, Calgary Health Region, Calgary, Alberta, Canada.

* Corresponding author. MR Research Centre, Foothills Medical Centre, 1403-29th Street, NW, Calgary, AB T2N 2T9, Canada.

E-mail address: rfrayne@ucalgary.ca (R. Frayne).

article, the authors review (1) the utility of CE techniques on the imaging of intracranial cerebrovascular diseases, and (2) the advantages and limitations of commonly used CE MRA techniques for intracranial vessel imaging. This is followed by a discussion of the clinical applications of intracranial CE MRA.

When should one use contrast enhancement for MR angiography?

Flow-dependent acquisition techniques, such as TOF and PC MRA, are in extensive clinical use today. One of the main advantages of non-CE MRA (NCE MRA) procedures is that they are noninvasive and rely only on endogenous mechanisms to provide image contrast between flowing blood and background tissue. These classes have many advantages and disadvantages.

Advantages of non-contrast-enhanced MRA techniques

TOF MRA is based on the signal difference resulting between saturated spins in the stationary

background tissue and unsaturated (ie, fully magnetized) spins in flowing blood. T1-weighted imaging sequences are used in TOF MRA to maximize the signal from blood while minimizing the signal from the background tissue (Fig. 1A, B) [21,22]. Ideally, the acquired slices are perpendicular to the direction of blood flow and are acquired sequentially in the direction opposite to the flow. This acquisition geometry ensures that fully magnetized spins in the blood enter the excited slice. In addition, specialized saturation pulses can be applied ahead of the advancing acquired slice to suppress unwanted venous or arterial blood [23]. In a region with rapid blood flow and with a vessel that is mainly perpendicular to the acquired slice, excellent angiograms can be obtained.

The 2D TOF technique is robust, fast, and often adequate for screening, but has a slice thickness > 1.5 mm that makes stenosis measurement difficult. The 3D TOF technique acquires signal from a slab of tissue, and thus has better signal-to-noise (SNR) compared with the 2D TOF approach [24]. By phase encoding in the slice-select direction, the excited slab can be subdivided

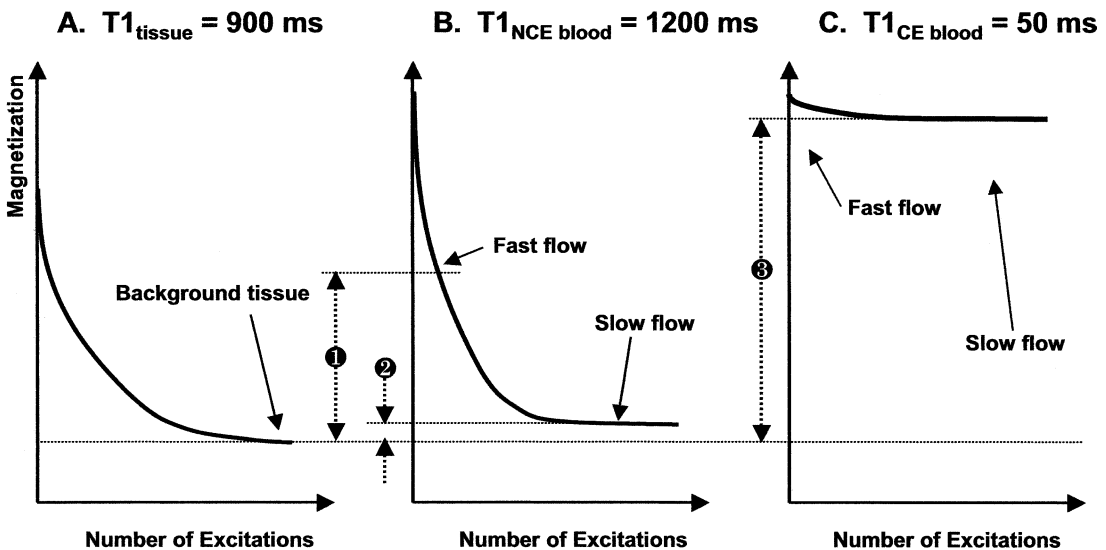


Fig. 1. Saturation effect: MR magnetization (or signal) as a function of the number of excitation pulses (which equals slice thickness/tissue velocity). (A) Stationary background brain parenchymal tissue with a T1 relaxation time of 900 milliseconds, (B) for flowing blood (T1 = 1200 milliseconds), and (C) flowing blood containing MR contrast agent (T1 \approx 50 milliseconds, see text). The image contrast between the blood and the background tissue is a complex function of the excitation parameters (flip angle and repetition time), the T1 relaxation time and velocity. Difference 1 shows a large image contrast between fast moving non-contrast-enhanced blood and background, whereas difference 2 shows a small image contrast since the slow moving blood is saturated. The introduction of MR contrast into the blood increases the image contrast and also removes the influence of blood velocity (Difference 3).

into many partitions, each 1 mm or less in thickness. Thus 3D TOF has higher SNR and better spatial resolution compared with 2D TOF. The principal disadvantage to 3D TOF is the progressive saturation of blood as it flows through the excited volume. 3D TOF examinations are also longer and are therefore more sensitive to patient motion. Multiple overlapping thin slab acquisition (MOTSA) [25] is a hybrid approach that acquires a series of thin-slab 3D acquisitions to achieve high spatial resolution, good SNR, and decreased sensitivity to slow flow saturation.

PC MRA is another approach that generates image contrast between flowing and stationary tissues by encoding velocity into the phase of the acquired MR signal. PC techniques also are useful in eliminating signal from high-intensity stationary material such as blood products, which on TOF imaging can also appear hyperintense because of their very short T1 values. An important feature of PC MRA is that the image contrast mechanism is nearly uncoupled from the acquisition geometry. Unlike TOF, PC MRA can acquire angiograms in slices or slabs with an arbitrary orientation relative to the direction or directions of blood flow. This is an important feature given the variety of flow directions encountered when imaging the intracranial vasculature. While signal saturation effects are greatly diminished in PC MRA, the decreased signal from saturation does, however, cause a decrease in SNR [26]. Another advantage of PC over TOF MRA is that it is able to acquire directional flow information.

Disadvantages of non-contrast-enhanced MRA techniques

NCE MRA techniques have several technical and clinical disadvantages. Depending on the technique, these disadvantages [27] can include long examination times (typically many minutes), poor or non-visualization of flow dynamics, sensitivity to pulsatile flow artifacts, and dependence on blood moving perpendicular to the acquired slice. This last disadvantage causes progressive saturation of flowing blood and is the major limitation of the TOF technique. Saturation of the blood is particularly pronounced when the mean blood flow is slow (ie, venous flow, patients with low cardiac output, impaired arterial flow, and high-resistance distal arteries), when the imaging slice or plane is parallel to the vessels, when the vessels are not unidirectional, or when the acquisition volume

is large (such as with 3D acquisitions) [28]. Saturation effects are increased when short repetition times (TR) are used because there is not enough time for recovery of the magnetization. Intra-voxel dephasing is another cause of signal loss and occurs when a large distribution of velocities occurs within an image pixel. The effects of intra-voxel dephasing are exacerbated by using large pixels, fast or disturbed flow, or long echo times (TE) [29].

In clinical practice, NCE MRA can suffer from inadequate visualization of arteries with slow or complex flow, particularly in areas of vascular pathology (Fig. 2). PC MRA, unlike TOF MRA, is able to acquire directional flow information. The major drawbacks of PC methods are their lengthy acquisition times and the need to match the velocity sensitivity to the anticipated flow conditions a priori. Inappropriate settings can lead to aliasing effects in which flow directionality is incorrectly displayed or to reduced sensitivity [21]. The SNR of PC MRA also is indirectly sensitive to the effects of signal loss because of slow or disturbed flow.

Contrast-enhanced MR angiography

CE MRA is a more invasive class of MRA techniques that requires the intravenous injection of a MR contrast agent. Chelated gadolinium (Gd) ions [30] are commonly used paramagnetic substances that shorten the longitudinal relaxation time (T1) of the blood. Unlike iodinated X-ray agents, commercially available MR contrast agents do not have clinically detectable nephrotoxicity, even at the high doses ($>0.1 \text{ mmol kg}^{-1}$) sometimes required for CE MRA [31]. These agents also have a low incidence of allergic reactions [32]. Notwithstanding the need for a venous administration, an excellent safety profile is associated with CE MRA. MR contrast agents do not cross the intact blood-brain barrier. For intracranial imaging this property is advantageous in that cerebral enhancement is essentially confined to the intravascular space during data acquisition.

In CE MRA, MR contrast agents are used to counter the saturation and intra-voxel dephasing effects found in 3D TOF and to a lesser degree in PC MRA. When imaged with a short-TR, T1-weighted imaging technique (similar to TOF), the addition of the contrast agent greatly increases the signal from blood (Fig. 1C) and thus greatly reduces the detrimental effects of signal loss

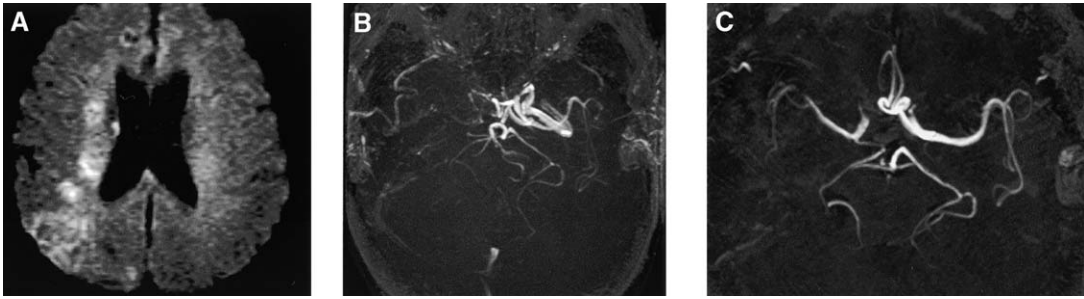


Fig. 2. A 65-year-old man who presented with a 2.7-h history of neurological symptoms. On diffusion weighted MR imaging (DWI) (A), acute ischemic changes are evident in a watershed distribution in the right hemisphere. NCE 3D TOF MRA (B) shows apparent total occlusion of right internal carotid artery and questionable faint signal intensity in the right M1. Twenty minutes after the NCE 3D TOF examination, post-contrast 3D TOF MRA (C) shows a focal narrowing of the distal M1 and decreased blood flow in the right MCA and PCA caused by occlusion of right ICA.

resulting from slow and disturbed flows. The presence of contrast in the blood makes CE MRA essentially flow independent, provided that sufficient contrast arrives in the vessels of interest. The short echo time (TE) typically used for CE MRA sequences further minimizes signal loss by decreasing intra-voxel dephasing. Motion artifacts are also less evident because of the short acquisition time. Finally, the use of the coronal, sagittal, or oblique acquisition geometries enables flexibility in imaging blood vessels, and can provide angiographic images similar to those obtained with conventional catheter angiography.

Because CE MRA is less sensitive to blood velocity or the direction of blood flow, the technique is more likely to accurately reflect the severity and length of a stenosis, or other vascular pathologies. Because of the degree of artifact reduction, CE MRA has led to improved diagnostic accuracy and, most importantly, increased diagnostic confidence. These developments are important when imaging intracranial diseases. For example, in stroke patients (discussed later in this study), it is important to distinguish between vessels that are occluded and those that have only slow flow, because the prognosis and potential therapies are different for these two conditions.

In general the T1-shortening associated with MR contrast agents can be used to substantially reduce the saturation of blood signal associated with NCE MR angiographic techniques. CE-MR angiographic techniques commonly used short TR (<10 milliseconds) and TE (<2 milliseconds) gradient-recalled echo sequences. CE MRA has three principle variants, which differ in acquisition time and the pharmacologic distribution of contrast agent during the image acquisition: (1)

post-contrast CE MRA, (2) dynamic CE MRA, and (3) time-resolved CE MRA.

Post-contrast CE MRA

This technique is performed during the steady-state phase after the contrast injection when it is uniformly distributed throughout the intravascular and extravascular spaces. Because the elimination of MR contrast agents by way of the kidney is slow, the intravascular contrast concentration remains uniform for about 20 minutes after injection [33]. Intracranially, contrast remains intravascular provided the blood-brain barrier is not compromised. This steady-state contrast agent concentration in blood lowers the T1 relaxation of blood from approximately 1200 ms to between 200 milliseconds and 400 milliseconds [33]. Superb vascular enhanced images with minimal artifacts [33] can be acquired during this interval. In post-contrast TOF, an important consideration is determining the optimal flip angle that maximizes the vascular signal. For example in acute stroke imaging, the authors increased the flip angle and TR (flip angle of 35° and TR of 32 milliseconds) to maximize vessel signal intensity on post-contrast TOF while suppressing background signal (non-CE MRA, conventional 3D TOF acquisition: flip angle = 15°, TR = 24 milliseconds) [34].

The dosage of administered MR contrast directly effects visualization of intracranial vessels. In the authors' acute stroke protocol, 20 mL (10 mmol) of gadopentetate dimeglumine (Magnevist; Berlex, Wayne, New Jersey) is injected for dynamic susceptibility contrast perfusion-weighted imaging (PWI) 3 to 5 minutes before the

post-contrast CE MRA acquisition. Jung et al [35] studied the optimal dose of gadopentetate dimeglumine for post-contrast CE MRA in intracranial vascular disease. They reported that 5 mL to 10 mL volumes (2.5 mmol to 5 mmol) of contrast agent aided in (1) differentiating true stenoses in large arteries from areas of artifactual narrowing and (2) in depicting small AVMs with slow flow. Tartaro et al [36] reported that after injection of a double-dose (0.2 mmol kg^{-1}) of MR contrast, the signal-to-noise ratio (SNR) for small arteries and veins increased, while the SNR for larger arteries decreased.

Dynamic contrast-enhanced MRA

MR hardware and software capabilities have undergone significant evolution in the past decade. Fast gradients (up to 50 mT m^{-1}) coupled with real-time imaging now allow the acquisition of temporally synchronized 3D gradient-recalled echo images that are suitable for CE MRA. The two primary issues in dynamic CE MRA are: (1) detection of contrast arrival and (2) efficient acquisition of the appropriate MR data.

Dynamic CE MRA techniques are based on acquiring images during the first pass of the contrast agent so that ideally only signal from blood in the arterial system is enhanced. For best image quality there should be no background or venous enhancement. Ideally, data should be acquired while the arterial MR contrast agent concentration is high and constant. This is not easily achieved because of uncertainty in contrast arrival in the vessels of interest and the short optimal interval between the arterial and venous enhancement phases (Fig. 3). Typically the intracranial arteriovenous circulation time is between 2.5 seconds and 6 seconds [37]. Several techniques have been devised to ensure that data is acquired during the arterial contrast concentration phase.

The uncertainty in the transit time of contrast agent from the injection site to the brain vary significantly from patient-to-patient, and depending on factors such as cardiovascular output and presence of vascular pathology. Several strategies are currently employed to determine the time of contrast arrival, including detection of a test bolus injection before the CE MRA acquisition, automated triggering, and fluoroscopic imaging to detect bolus arrival followed by manually triggering [38] of the acquisition (Fig. 4).

The first strategy, imaging a test bolus of contrast is a simple yet effective method that

rapidly acquires a series of images during the passage of a small injection of contrast (ie, a “test” bolus of typically between 5% and 10% of the total injected volume). This method (Fig. 4A) acquires a series of 2D T1-weighted images during the passage of the test bolus, and from these data calculates the contrast arrival time. This strategy is straightforward and does not require special hardware and software, yet reduces the major sources of patient-to-patient variability. The automated trigger and fluoroscopic monitoring approaches (Fig. 4B) do not use an early “test” injection since they sense the arrival of the full contrast injection in or near the vessel-of-interest. To accomplish this task, however, these approaches require additional hardware capabilities. Automated triggering is a strategy that determines the arrival of contrast in the vessels of interest, [39,40], by following the MR signal in a small tracker volume placed in or near the vessel-of-interest. When the detected signal level in the tracker volume exceeds a predetermined threshold, the acquisition of the CE MRA volume is triggered. Fluoroscopic triggering, is the most advanced strategy for bolus detection that uses a series of rapid 2D images to determine contrast arrival [41]. The operator views these images and commences the CE MRA volume once the contrast agent arrives. Both the automated triggered and fluoroscopic approaches require a small delay (~ 1 second or more) to switch from detection mode to acquisition of CE MRA data. Nevertheless, automated and fluoroscopic triggering are the preferred and most robust strategies for determining contrast arrival.

The second issue in dynamic CE MRA is the short recirculation time in the intracranial circulation (Fig. 3) [37]. Acquiring the data before the arterial peak is reached reduces the SNR and produces artifacts [42,43]. Conversely, delayed acquisition, in addition to reduced SNR and increased artifacts, results in venous enhancement which further complicates image interpretation [42,43]. A variety of centric-encoding approaches have been suggested to collect data during the short arterial-venous interval. Centric approaches ensure that the central portions of k-space are collected immediately to minimize the possibility of venous contamination. k-space is a mathematical formalism that describes the method of collecting MR data. The center of k-space contains information about large structures (ie, low spatial frequencies) whereas the periphery of k-space describes the edges of the image (ie, high spatial frequency).

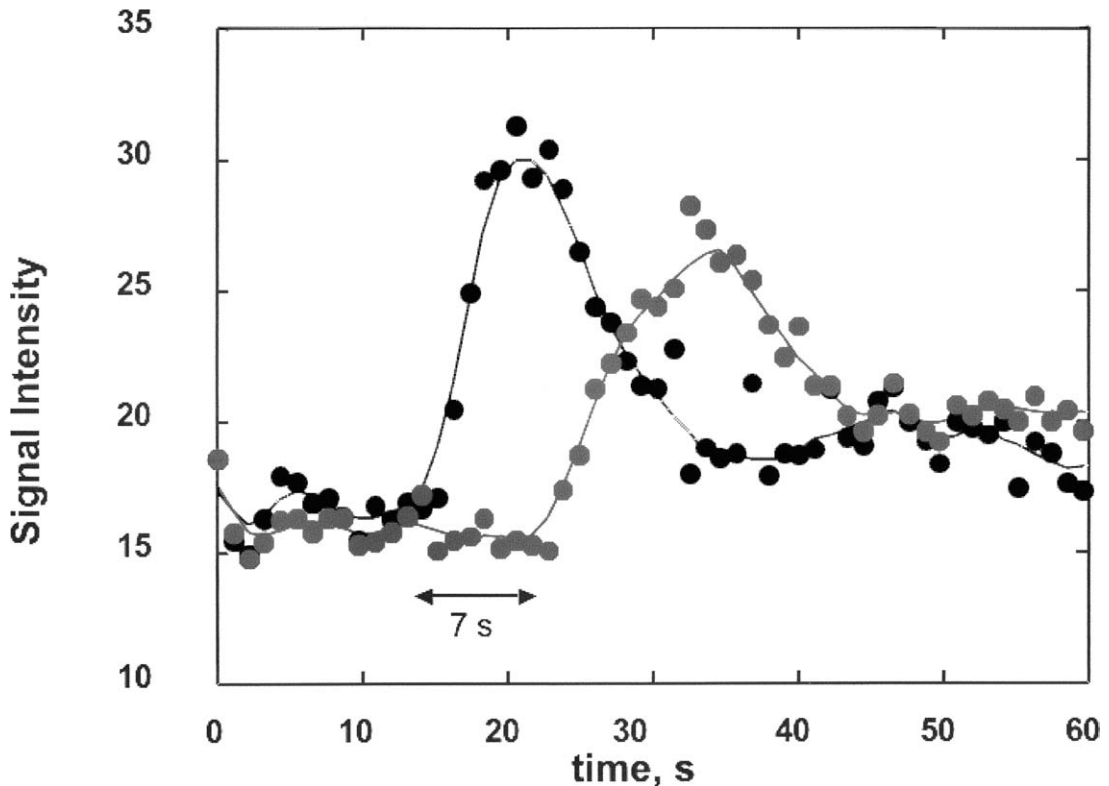


Fig. 3. MR imaging signal versus time for an injection of a 4-mL test bolus of MR contrast agent. Curves are plotted for the extra-cranial arterial (*black*) and venous (*gray*) circulation. The two unknowns are (1) the arrival of contrast in the arterial system (~13 seconds after intravenous injection in this example) and (2) the delay between the arterial and venous passage of the agent (7 seconds in the extracranial circulation). Intracranially, the arterio-venous delay will be even shorter. In dynamic CE MRA approaches, a timing technique (see text) is necessary to ensure data acquisition begins at the appropriate time. Data must be collected using a centric phase-encoding approach to ensure arterial imaging. Time-resolved approaches collect data throughout the contrast injection and do not require explicit synchronization.

The most appropriate approach for dynamic CE MRA is the elliptical-centric phase-encoding order proposed by Wilman et al [44]. Elliptical-centric phase encoding acquires phase encodings in order of increasing distance from the center of k-space. A high degree of venous suppression can be achieved with a data acquisition time several times longer than the arterial-venous interval [45].

Time-resolved approaches to CE MRA

Time-resolved techniques are another approach to performing CE MRA that acquired images during the passage of contrast (Fig. 4C). Unlike dynamic CE MRA techniques that must first explicitly determine contrast arrival (Fig. 4A or 4B), time-resolved techniques collect images before, during, and after the arterial contrast phase. These approaches offer the possibility of

observing flow dynamics, although to accomplish this requires an inherent trade-off between spatial and temporal resolution. Both 2D (single slice) and 3D (volume) implementations have been used.

Two-dimensional time-resolved conventional and projection-imaging techniques [46–49] achieve sub-second resolution, but have drawbacks: (1) only one or a few relatively thick slices can be obtained; (2) small vessels may be obscured because of low spatial resolution; and (3) vessel overlap cannot be eliminated in the projections. Time-resolved 2D CE MRA techniques in intracranial vessels require trade-offs between spatial resolution, acquisition time, and image contrast, according to the clinical applications.

With time-resolved 3D CE MRA sequences, early, mid, and late arterio-venous phases of the intracranial circulation can be portrayed.

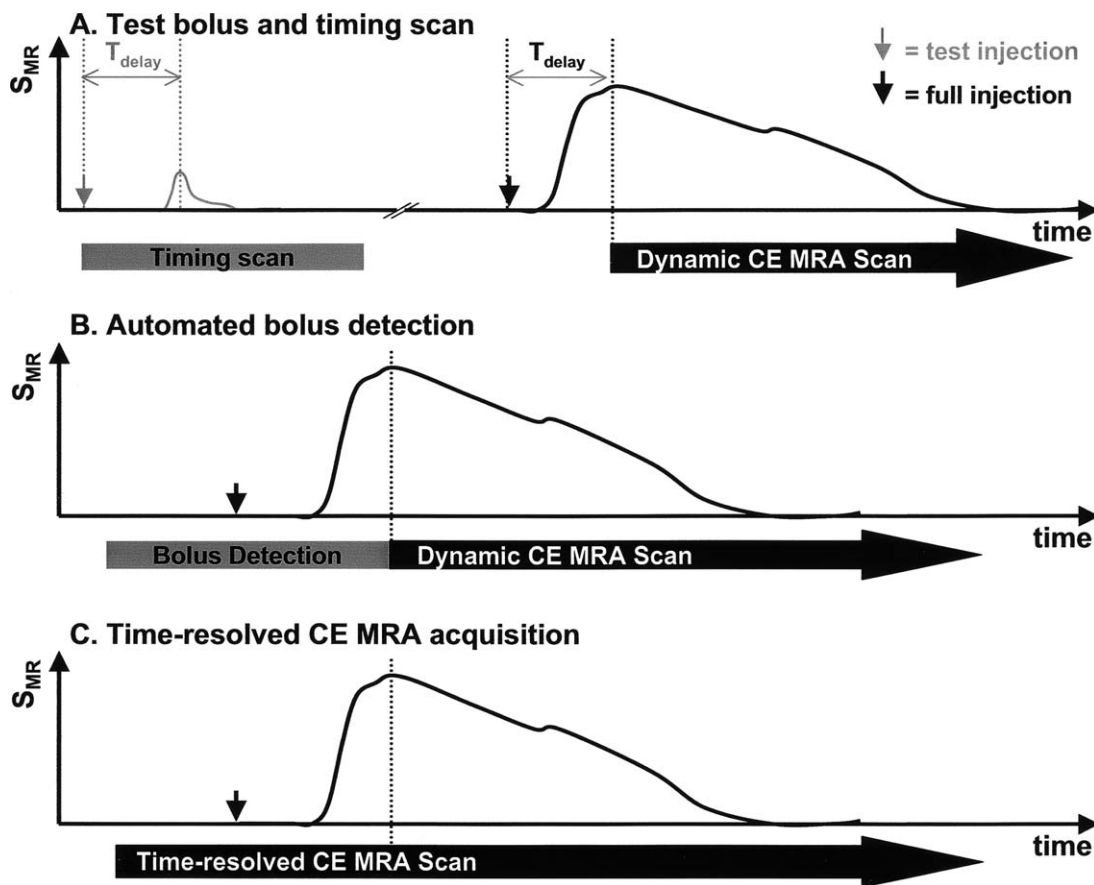


Fig. 4. Approaches to synchronizing CE MRA. (A) Injection of a small test-bolus during acquisition of timing scan. The delay between injection and peak arterial enhancement (T_{delay}) is used to coordinate a dynamic CE MRA acquisition. (B) Use of an automated system for detecting the arrival of the contrast agent. Once the contrast agent is detected in or near the vessel-of-interest, the dynamic CE MRA acquisition is initiated. There are two primary methods for detecting contrast arrival: monitoring of the signal from a small tracker volume [39,40] and fluoroscopic 2D imaging [41] (see text). (C) Time-resolved CE MRA does not require explicit synchronization to the contrast bolus because it collects a series of images through the arterial and venous phases of the contrast agent [14,16,50].

Time-resolved CE MRA offers the possibility of observing contrast dynamics by periodically updating all or portions of k-space [50]. One technique, time-resolved imaging of contrast kinetics (TRICKS) [50], updates the center of k-space more frequently than the periphery of the k-space. In this way TRICKS consistently captures an arterial-only time frame, free of venous overlay even in regions of rapid venous return [51].

Clinical applications

Ischemic stroke

Ischemic stroke results from occlusion of the extra- and intra-cranial arteries and can be

broadly classified as thrombotic, embolic, or lacunar. Mohr et al [52] evaluated 694 patients who were hospitalized for stroke and found that 53% had large vessel thrombosis and 31% had cerebral emboli. Thrombotic ischemic infarction is the result of thrombosis of a specific vessel, most frequently caused by atherosclerosis. Embolic ischemic infarctions are often abrupt and catastrophic, with the severity of symptoms often peaking at the ictus. The clinical signs and symptoms relate to the specific affected vascular territory. The most common source of emboli is atherosclerotic alterations at or proximal to the internal carotid. In about 25% of patients, emboli arise because of cardiac disease.

MR has been demonstrated to have an important role in acute ischemic stroke, particularly the use of diffusion-weighted (DWI) and perfusion-weighted (PWI) imaging [53,54]. MRA has an important role in acute cerebral ischemia (<3 hours). Ischemic stroke symptoms are because of decreased cerebral blood flow, which is normally attributable to a blocked or partial blocked vessel. In many patients a major vessel, such as the internal carotid, anterior cerebral, middle cerebral, or posterior cerebral artery (ICA, ACA, MCA, PCA), is involved. These vessels are visible on TOF, so in principle NCE MRA should be useful in detection of vascular change associated with ischemic stroke. Because the blood-to-background image contrast is dependent on flow in TOF and PC MRA and because flow is reduced in ischemic stroke, these techniques suffer signal loss secondary to saturation effects and dephasing, resulting in signal degradation near pathology.

In the authors' experience, they have observed that non-contrast enhanced and post-contrast 3D TOF, individually and in combination, have important roles in acute stroke management. They have found that 3D TOF acquired 5 minutes after

the injection of 20 mL of contrast (post PWI) to have clinical utility [34]. The authors' post-contrast 3D TOF acquisition is focused on visualization of the circle of Willis and is used in conjunction with noncontrast 3D TOF images to assess flow in the distal ICA, ACA, MCA and PCA. Specifically, the authors observed that 66% of vessel segments that appear abnormal on NCE 3D TOF MRA had a changed appearance on the post-contrast TOF. In most cases (94% of the changes) the post-contrast TOF indicated improved blood flow in the questioned segment. Of the vessels initially graded as occluded, 21% were subsequently found to be patent (see Fig. 2; Fig. 5). This may significantly alter treatment decisions. Other groups [35,49] also have confirmed the accuracy of this technique for intracranial angiography. Kucinski et al [55] have reported that the degree of collateral circulation was an independent radiological predictor of favorable outcome after thrombolysis in acute ischemic stroke. Collateral flow is often slow and post-contrast TOF is often a good predictor of the presence of leptomeningeal collateral flow in patients with occlusion of major proximal arteries (Fig. 6). Unlike dynamic and

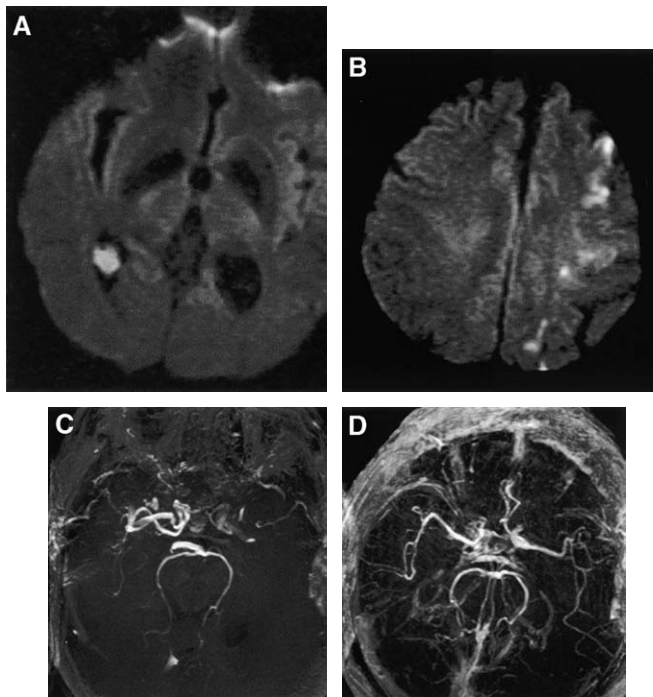


Fig. 5. A 70-year-old man who presented with a 2.1-h history of right hemiplegia and aphasia. Diffusion weighted images (A, B) show left hemisphere watershed ischemic lesions. NCE 3D TOF-MRA (C) shows complete occlusion of the left MCA. Nineteen minutes after the conventional 3D TOF MRA, a post-contrast 3D TOF MRA examination (D) showed no evidence of occlusions. There is flow asymmetry, with flow in the right MCA being greater than in the left.

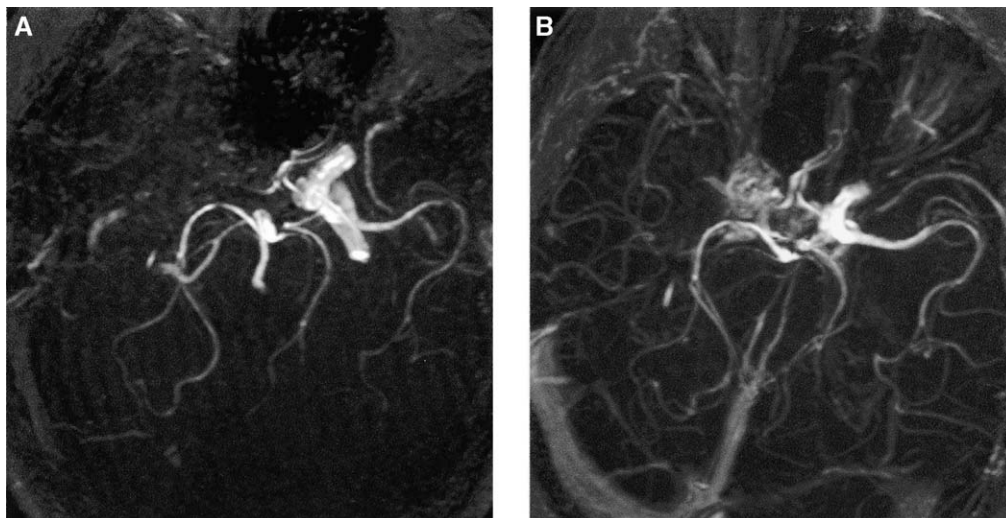


Fig. 6. A 64-year-old man who presented with a 2.8-hour history of weakness of left face, arm, and leg. Diffusion weighted images were normal. NCE 3D TOF MRA (A) shows completed occlusion of right internal carotid artery. Thirty minutes later, post-contrast 3D TOF MRA examination (B) showed occlusion of the right internal carotid artery and MCA, and also shows distal MCA branches that are filled via collateral vessels.

time-resolved approaches, acquisition after contrast administration can potentially be adversely affected by enhancement of tissue and venous structures, however the authors have found with proper placement of the acquired 3D slab, this is not a significant problem. Overall, the authors found post-contrast 3D TOF to be a critical part of their acute stroke imaging protocol.

Aneurysms

The accepted standard for identification of intracranial aneurysms is intra-arterial digital subtraction angiography (IA DSA). The diagnostic cerebral angiogram procedure has an overall neurologic complication rate of 1.3% and a permanent neurologic complication rate of 0.5% [56]. Many factors modify this risk, so that neurologic complications were significantly more common in patients 55 years of age or older (1.8%), in patients with cardiovascular disease (2.3%), and when fluoroscopic times were 10 minutes or longer (1.9%) [52]. For these reasons, 3D TOF is considered as an alternative approach to conventional angiography. In an early study, Ross et al [57] demonstrated that conventional 3D TOF had a combined sensitivity of 95% and specificity of 100% compared with intra-arterial angiography. Atlas et al [58] reported that MRA had a 95% sensitivity, an 88% specificity, a 95% positive predictive value, and an 89% negative predictive value for the presence of at least one

aneurysm in patients with one or more aneurysms larger than 3 mm. They also reported a low sensitivity (72%) for aneurysms less than 3 mm and a low sensitivity (41%) for morphologic features suggestive of rupture. Further, they showed that post processing and source image review were useful when evaluating the shape of aneurysm [59]. While these results were encouraging, conventional 3D TOF was found to underestimate size and poorly visualize the sac and neck of giant and fusiform aneurysms [57].

Post-contrast 3D TOF has been shown to improve the detection of aneurysms and depiction of surrounding vascular anatomy [12,33]. In dynamic CE MRA studies, Isoda et al [60] reported that CE MRA resulted in clear images of lateral saccular aneurysm models, compared with 3D TOF MRA. Metens et al [61] assessed the clinical utility and accuracy of dynamic CE MRA in the detection of unruptured intracranial aneurysms. In this study, the dynamic CE MRA technique depicted all 23 aneurysms detected in 17 patients with IA DSA (aneurysm ranged from 2 mm to 21 mm). One false-positive result was reported (overall sensitivity and specificity of 100% and 94%, respectively). The authors have compared NCE and dynamic CE 3D MRA for the detection of ruptured intracranial aneurysms. In this study, the reviewer is unblinded to the CT findings and, thus, knew the location of aneurysms. Both NCE and dynamic CE MRA

techniques failed to depict one aneurysm in the series of 21 ruptured aneurysms confirmed by conventional angiography (sensitivity 95%, specificity 100%, see Fig. 7). Depiction of aneurysm sac with dynamic CE MRA was better than conventional 3D TOF MRA (Fig. 8).

Jager et al [62] have reported that dynamic CE MRA provided better delineation of the giant aneurysms compared with conventional and post-contrast 3D TOF. They also stated that delineation of entering vessels, aneurysm sacs, and exiting vessels on dynamic CE MRA images was comparable to conventional angiography. Boulin et al [63] assessed comparison of post-contrast 3D TOF and DSA in the follow-up of intracranial aneurysms treated with detachable platinum coils. The sensitivity and specificity of this study were 72% and 98% for depicting an aneurysm remnant, respectively. In this series, only small aneurysm neck remnants (less than 3 mm) were

not visualized by CE MRA. Therefore, these authors indicated that MR angiography is probably a good noninvasive tool for the follow-up of intracranial aneurysms treated by using coils.

Vascular malformations

Arterio-venous malformations (AVMs) are non-neoplastic vascular abnormalities that are often incidentally discovered. AVMs are an important cause of nontraumatic intracranial hemorrhage in adults and children. Symptoms may reflect perfusion changes implicit in such modification of the blood flow (ie, lack of perfusion to adjacent brain parenchyma), or the inability of the vessel to sustain the altered hemodynamics (mechanical rupture). Surgery, radiosurgery, or intravascular embolization are possible therapies, each of which are suited to specific types, locations and hemodynamic properties of AVMs. The visualization of the venous

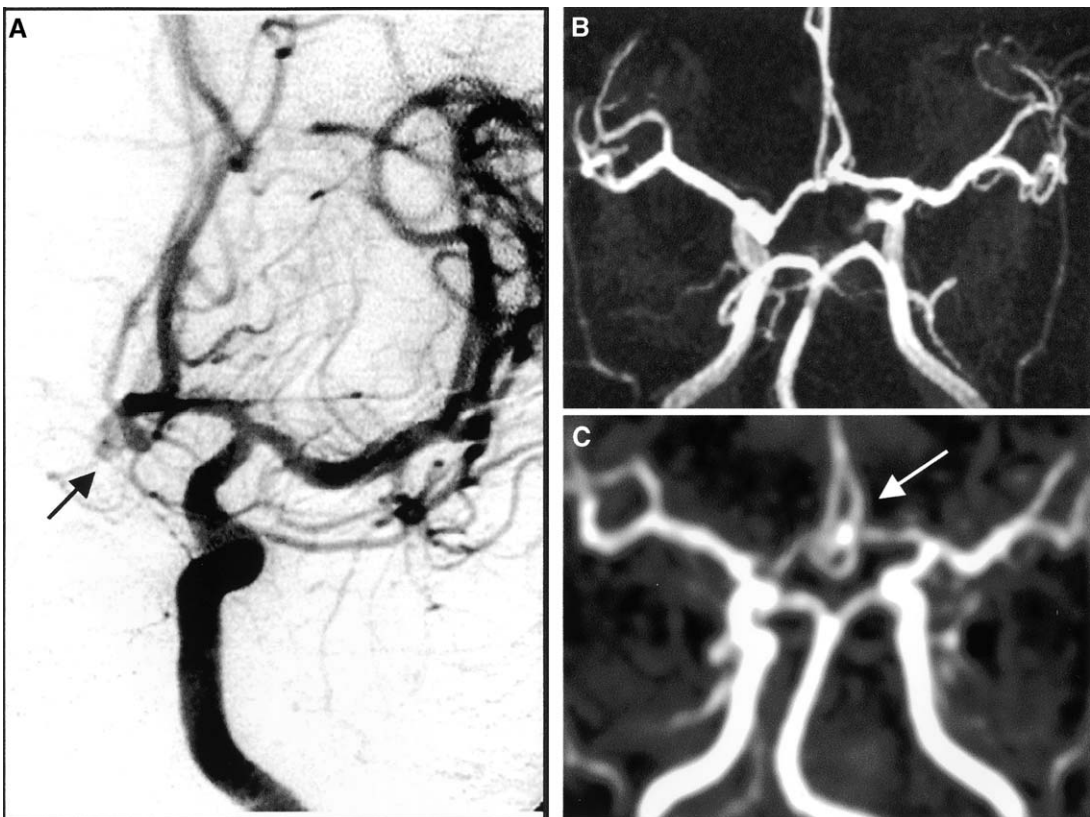


Fig. 7. A 33-year-old man presenting with subarachnoid hemorrhage secondary to rupture of a left anterior communicating artery (A-comm) aneurysm. Right oblique angiogram view (A) confirmed ruptured left A-comm aneurysm (black arrow). On MIP image through a NCE 3D TOF MRA data set (B), the A-comm aneurysm is not visualized. The aneurysm sac (white arrow) is well visualized by CE-MRA (C).

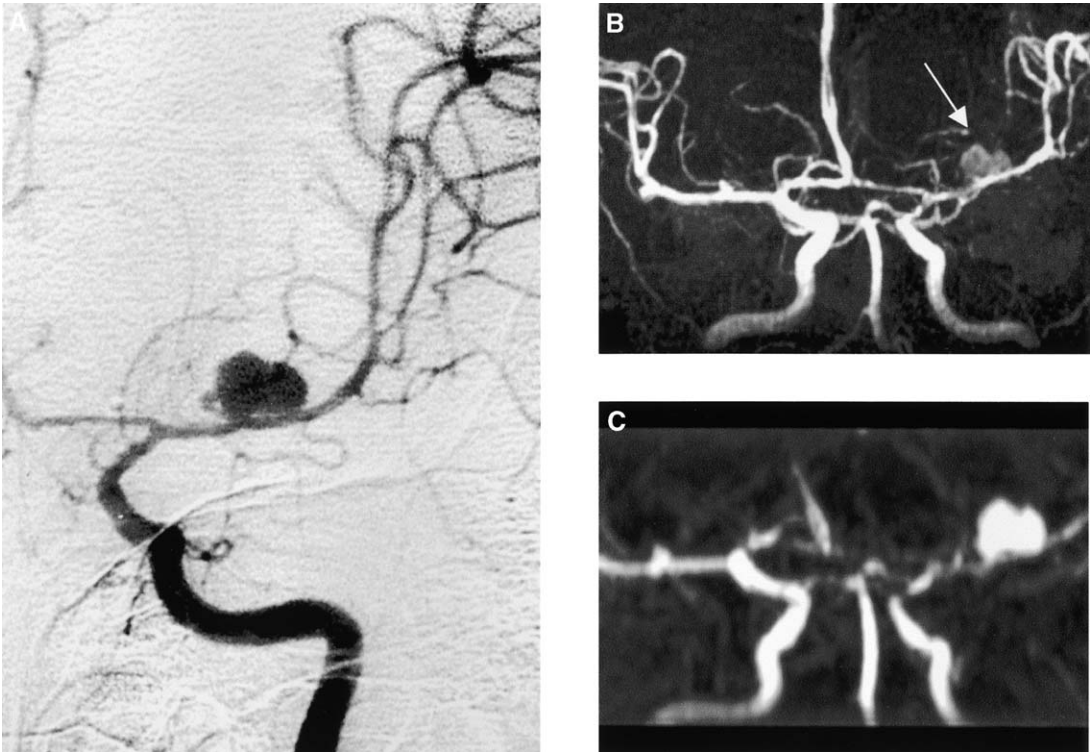


Fig. 8. A 41-year-old man presenting with subarachnoid hemorrhage secondary to rupture of left middle cerebral artery (MCA) bifurcation aneurysm. In Towne's projection (IA-DSA) (A), a large lobulated aneurysm sac is visualized at the bifurcation of the left MCA. A 3D TOF MRA projection image (B) shows the aneurysm sac (arrow), but the dynamic CE-MRA projection image more clearly demonstrates the shape of the aneurysm sac (C).

drainage of AVMs is important for the pre-operative estimation of the bleeding risk, and for the exact definition of the target volume in radiosurgery. Conventional angiography is still the gold standard technique for detection and characterization of an AVM. Although flow through AVMs is elevated, NCE MRA is poorly suited to detailing the features of these lesions, as 3D TOF or PC tend to be limited to the feeding arteries while the draining veins and the nidus are inadequately visualized. A further major drawback to NCE MRA study of AVMs is the lack of temporal selectivity and of dynamic information.

The use of time-resolved CE MRA to study AVMs has proved most encouraging (Fig. 9) because by using time-resolved imaging during a bolus injection of MR contrast, information about the complex hemodynamics of vascular malformations may be obtained [48,64,65]. A sensitivity of 95% for nidus detection with time-resolved CE MRA is comparable or slightly superior to that of conventional 3D TOF MRA

[48]. Dynamic CE MRA has been employed as a less invasive, dynamic angiographic tool for screening and follow-up of AVMs after radiosurgery or embolization [66–68]. Fast dynamic 3D CE MRA has been found to be superior to conventional TOF MRA in the assessment of vascular architecture of the cerebral AVMs. An acquisition time of 9 seconds was sufficient to differentiate feeding arteries, the AVM nidus, and the venous drainage patterns [69]. Nevertheless, this technique has several limitations. First, the spatial resolution is still low compared with DSA. Second, the acquisition time of 9 seconds is too long to clearly differentiate between arteries and veins. In some images, a mild venous overlay was observed on the CE MRA projection images, and dynamic information was not obtained. While time-resolved and dynamic CE MRA may provide a useful initial diagnostic test, in all patients selective and superselective conventional angiography remains necessary to make rational therapeutic decisions.

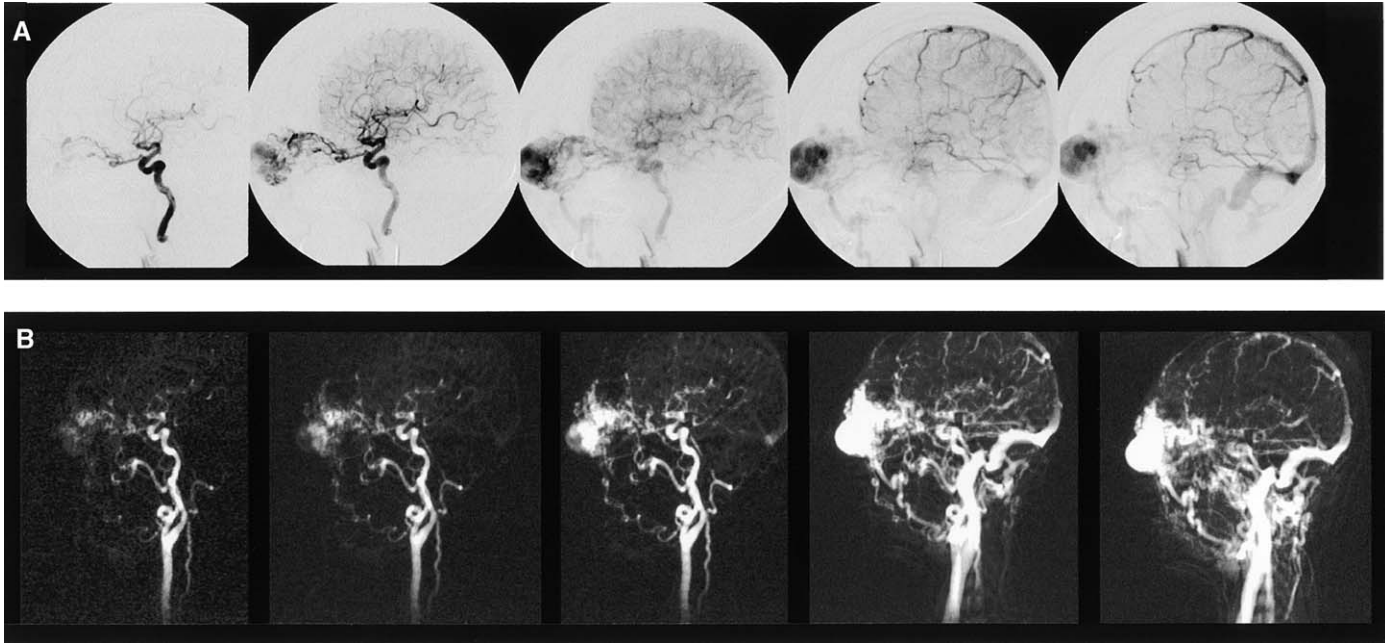


Fig. 9. A 59-year-old woman with a large pulsating right facial mass. Intra-arterial DSA (A) shows the complex dynamics of this lesion. Time-resolved CE MRA (B) provides similar hemodynamic information in this facial AVM. (Courtesy of Tae-Sub Chung, MD, Seoul, Korea).

Dural arterial-venous malformations (DAVMs, or arterio-venous fistulae) are vascular malformations that have a different clinical presentation, natural history, imaging features, and therapy from parenchymal AVMs of the brain. The natural history and clinical symptomatology of DAVMs is variable and to a large extent dependent on the location of the lesion and its venous drainage pathways [70]. Diagnosis of DAVMs is difficult by CT and conventional MR imaging techniques. Post-contrast TOF MRA may allow visualization of abnormal arterial pedicles and static venous anatomy, but only time-resolved projection MRA enables dynamic assessment of the vascular malformations [71].

Moyamoya disease

Moyamoya disease is characterized by severe stenosis or occlusion of the internal carotid artery bifurcation followed by progressive internal carotid artery occlusions and development of basal (parenchymal) collateral vessels from perforators, leptomeningeal collateral vessels from the posterior cerebral artery, and transdural collateral vessels from the external carotid artery. Conventional 3D TOF already plays an important role in diagnosing moyamoya disease, and in following disease progression [72]. Time-resolved CE MRA techniques can also be applied to moyamoya disease. In addition to identifying stenoses, time-resolved technique can also evaluate hemodynamics in the brain.

Summary

NCE MRA can provide the authors with useful diagnostic information in patients suffering from intracranial vascular disease, often leading to improved or altered treatment decisions. Most centers have used 3D TOF for evaluation of stroke—the most common cerebral vascular disease. Because of slow and disturbed flow, conventional 3D TOF MRA tends to overestimate stenotic lesions and occluded arteries and this can confound neurovascular assessment in stroke patients. Post contrast 3D TOF techniques provide a more robust and more specific method for imaging the intracranial circulation that overcomes the drawbacks of conventional 3D TOF. In the setting of acute ischemic stroke, the authors have found that the combination of conventional and CE 3D TOF MRA improves their overall diagnostic ability. Dynamic and time-resolved CE MRA techniques have evolved rapidly. Time-

resolved CE MRA, in particular, is emerging as a useful technique for imaging dynamic vascular pathologies such as AVMs. Unfortunately, time-resolved MRA of the intracranial circulation provides images with low spatial resolution and is currently limited to subsecond frame rate 2D acquisitions, and less than 2 seconds frame rates for 3D acquisitions. Nevertheless, like in other vascular regions, CE MRA represents a milestone for non-invasive intracranial vascular imaging. The continuing development of CE MRA techniques and of new contrast agents will lessen the need for intra-arterial angiography in the future.

Acknowledgments

The authors thank the Canada Foundation for Innovation for providing funding for a whole-body 3.0 T MR scanner in many of these studies, they also thank Tae-Sub Chung, MD and Mohammad Sabati, MSc, for their assistance in preparing this article.

References

- [1] Laub GA. Time-of-flight method of MR angiography. *Magn Reson Imaging Clin N Am* 1995;3: 391–8.
- [2] Dumoulin CL. Phase contrast MR angiography techniques. *Magn Reson Imaging Clin N Am* 1995; 3:399–411.
- [3] Adams WM, Laitt RD, Jackson A. The role of MR angiography in the pretreatment assessment of intracranial aneurysms: a comparative study. *Am J Neuroradiol* 2000;21:1618–28.
- [4] Huston J, Rufenacht DA, Ehman RL, Wiebers. Intracranial aneurysms and vascular malformations: comparison of time-of-flight and phase-contrast MR angiography. *Radiology* 1991;181: 721–30.
- [5] Stock KW, Radue EW, Jacob AL, Bao X-S, Steinbrich W. Intracranial arteries: Prospective blinded comparative study of MR angiography and DSA in 50 patients. *Radiology* 1995;195:451–6.
- [6] Wilms G, Bosmans H, Demaerel PH, Marchal G. Magnetic resonance angiography of the intracranial vessels. *Eur J Radiol* 2001;38:10–8.
- [7] Summers PE, Jarosz JM, Markus H. MR Angiography in cerebrovascular disease. *Clin Radiol* 2001; 56:437–56.
- [8] Tsuruda JS, Shimakawa A, Pelc NJ, Saloner D. Dural sinus occlusion: Evaluation with phase-sensitive gradient-echo MR imaging. *Am J Neuroradiol* 1991;12:481–8.
- [9] Drutman J, Gyorke A, Davis WL, Turski PA. Evaluation of subclavian steal with two-dimensional phase-contrast and two-dimensional

- time-of-flight MR angiography. *Am J Neuroradiol* 1994;15:1642-5.
- [10] Urchuk SN, Plewes DB. Mechanisms of flow-induced signal loss in MR angiography. *J Magn Reson Imaging* 1992;2:453-62.
- [11] Prince MR, Yucel EK, Kaufman JA, Harrison DC, Geller SC. Dynamic gadolinium-enhanced three dimensional abdominal MR arteriography. *J Magn Reson Imaging* 1993;3:877-81.
- [12] Runge VM, Kirsch JE, Lee C. Contrast-enhanced MR angiography. *J Magn Reson Imaging* 1993;3: 233-39.
- [13] Runge VM, Gelblum DY. The role of gadolinium diethylenetriaminepentaacetic acid in the evaluation of the central nervous system. *Magn Reson Q* 1990;6:85-107.
- [14] Frayne R, Grist TM, Korosec FR, et al. MR angiography with three-dimensional MR digital subtraction angiography. *Top Magn Reson Imaging* 1996;8:366-88.
- [15] Prince MR, Grist TM, Debatin JF. 3D Contrast MR Angiography. 2nd edition. New York: Springer; 1999.
- [16] Willig DS, Turski PA, Frayne R, et al. Contrast-enhanced 3D MR DSA of the carotid artery bifurcation: preliminary study of comparison with unenhanced 2D and 3D time-of-flight MR angiography. *Radiology* 1998;208:447-51.
- [17] Krinsky G, Weinreb J. Gadolinium-enhanced three-dimensional MR angiography of the thoracoabdominal aorta. *Semin Ultrasound CT MR* 1996;17: 280-303.
- [18] Hany TF, Leung DA, Pfammatter T, Debatin JF. Contrast-enhanced magnetic resonance angiography of the renal arteries. Original investigation. *Invest Radiol* 1998;33:653-9.
- [19] Rofsky NM, Adelman MA. MR angiography in the evaluation of atherosclerotic peripheral vascular disease. *Radiology* 2000;214:325-38.
- [20] Swan JS, Carroll TJ, Kennell TW, et al. Time-resolved three-dimensional contrast-enhanced MR angiography of the peripheral vessels. *Radiology* 2002;225:43-52.
- [21] Saloner D. The AAPM/RSNA physics tutorial for residents. An introduction to MRangiography. *Radiographics* 1995;15:453-65.
- [22] Bosmans H, Wilms G, Dymarkowski S, Marchal G. Basic principles of MRA. *Eur J Radiol* 2001;38:2-9.
- [23] Felmlee JP, Ehman RL. Spatial presaturation: a method for suppressing flow artifacts and improving depiction of vascular anatomy in MR imaging. *Radiology* 1987;64:559-64.
- [24] Haacke EM, Tkach JA, Parrish TB. Reduction of T2* dephasing in gradient field-echo imaging. *Radiology* 1989;170:457-62.
- [25] Blatter DD, Parker DL, Ahn SS, et al. Cerebral MR angiography with multiple overlapping thin slab acquisition. II. Early clinical experience. *Radiology* 1992;83:379-89.
- [26] Pelc NJ, Bernstein MA, Shimakawa A, Glover GH. Encoding strategies for three direction phase-contrast MR imaging of flow. *J Magn Reson Imaging* 1991;1:405-13.
- [27] Pipe JG. Limits of Time-of-flight magnetic resonance angiography. *Top Magn Reson Imaging* 2001;12:163-74.
- [28] Marchal G, Michiels J, Bosmans H, Hecke PV. Contrast-enhanced MRA of the brain. *J Comput Assist Tomogr* 1992;16:25-9.
- [29] Cosottini M, Calabrese R, Puglioli M, et al. Contrast-enhanced three-dimensional MR angiography of neck vessels: does dephasing effect alter diagnostic accuracy? *Eur Radiol* 2003;13:571-81.
- [30] Runge VM, Armstrong MR, Barr RG, et al. A clinical comparison of the safety and efficacy of MultiHance (gadobenate dimeglumine) and Omniscan (Gadodiamide) in magnetic resonance imaging in patients with central nervous system pathology. *Invest Radiol* 2001;36:65-71.
- [31] Prince MR, Arnoldus C, Frisoli JK. Nephrotoxicity of high-dose gadolinium compared with iodinated contrast. *J Magn Reson Imaging* 1996;6:162-6.
- [32] Murphy KJ, Brunberg JA, Cohan RH. Adverse reactions to gadolinium contrast media: A review of 36 cases. *Am J Roentgenol* 1996;167:847-9.
- [33] Parker DL, Tsuruda JS, Goodrich KC, Alexander AL, Buswell HR. Contrast-enhanced magnetic resonance angiography of cerebral arteries. A review. *Invest Radiol* 1998;33:560-72.
- [34] Yang JJ, Hill MD, Morrish WF, et al. Comparison of pre- and postcontrast 3D time-of-flight MR angiography for the evaluation of distal intracranial branch occlusions in acute ischemic stroke. *Am J Neuroradiol* 2002;23:557-67.
- [35] Jung HW, Chang KH, Choi DS, Han MH, Han MC. Contrast-enhanced MR angiography for the diagnosis of intracranial vascular disease: Optimal dose of gadopen- tetate dimeglumine. *Am J Roentgenol* 1995;165:1251-5.
- [36] Tartaro A, Severini S, Tonni G, Magarelli N, Carriero A, Bonomo L. Magnetic resonance angiography with gadolinium (Gd-DTPA) versus baseline magnetic resonance angiography in the study of the intracranial circulation [abstract]. *Radiol Med (Torino)* 1992;84:536.
- [37] Levy RA, Maki JH. Three-dimensional contrast-enhanced MR angiography of the extracranial carotid arteries: two techniques. *Am J Neuroradiol* 1998;19:688-90.
- [38] Remonda L, Heid O, Schroth G. Carotid artery stenosis, occlusion, and pseudo-occlusion: first-pass, gadolinium-enhanced, three-dimensional MR angiography-Preliminary study. *Radiology* 1998;209:95-102.
- [39] Foo TK, Saranathan M, Prince MR, Chenevert TL. Automated detection of bolus arrival and initiation of data acquisition in fast, three-dimensional, gadolinium-enhanced MR angiography. *Radiology* 1997;203:275-80.

- [40] Prince MR, Chenevert TL, Foo TK, Lundy FJ, Ward JS, Maki JH. Contrast-enhanced abdominal MR angiography: Optimization of imaging delay time by automating the detection of contrast material arrival in the aorta. *Radiology* 1997;203:109–14.
- [41] Riederer SJ, Bernstein MA, Breen JF, et al. Three-dimensional contrast-enhanced MR angiography with real-time fluoroscopic triggering: design specifications and technical reliability in 330 patient studies. *Radiology* 2000;215:584–93.
- [42] Maki JH, Prince MR, Lundy FJ, Chenevert TL. The effects of time varying intravascular signal intensity and k-space acquisition order on three-dimensional MR angiography image quality. *J Magn Reson Imaging* 1996;6:642–51.
- [43] Mistretta CA, Grist TM, Korosec FR, et al. 3D time-resolved contrast-enhanced MR DSA: Advantages and tradeoffs. *Magn Reson Med* 1998;40:571–81.
- [44] Wilman AH, Riederer SJ, Huston J, Wald JT, Debbins JP. Arterial phase carotid and vertebral artery imaging in 3D contrast-enhanced MR angiography by combining fluoroscopic triggering with an elliptical centric acquisition order. *Magn Reson Med* 1998;40:24–35.
- [45] Kim JK, Farb RI, Wright GA. Test bolus examination in the carotid artery at dynamic gadolinium-enhanced MR angiography. *Radiology* 1998;206:283–9.
- [46] Hennig J, Scheffler K, Laubenberger J, Strecker R. Time-resolved projection after bolus injection of contrast agent. *Magn Reson Med* 1997;37:341–5.
- [47] Tsuchiya K, Katase S, Yoshino A, Hachiya J. MR digital subtraction angiography of cerebral arteriovenous malformations. *Am J Neuroradiol* 2000; 21:707–11.
- [48] Griffiths PD, Hoggard N, Warren DJ, Wilkinson ID, Anderson B, Romanowski C. Brain arteriovenous malformations: assessment with dynamic MR digital subtraction angiography. *Am J Neuroradiol* 2000;21:1892–9.
- [49] Aoki S, Yoshikawa T, Hori M, et al. MR digital subtraction angiography for the assessment of cranial arteriovenous malformations and fistulas. *Am J Roentgenol* 2000;175:451–3.
- [50] Korosec FR, Frayne R, Grist TM, Mistretta CA. Time-resolved contrast-enhanced 3D MR angiography. *Magn Reson Med* 1996;36:345–51.
- [51] Carroll TJ, Korosec FR, Petermann GM, Grist TM, Turski PA. Carotid bifurcation: evaluation of time-resolved three-dimensional contrast-enhanced MR angiography. *Radiology* 2001;220:525–32.
- [52] Mohr J, Caplan LR, Melski J. The Harvard cooperative stroke registry: a prospective registry. *Neurology* 1978;28:754–62.
- [53] Beaulieu C, de Crespigny A, Tong DC, Moseley ME, Albers GW, Marks MP. Longitudinal magnetic resonance imaging study of perfusion and diffusion in stroke: evolution of lesion volume and correlation with clinical outcome. *Ann Neurol* 1999;46:568–78.
- [54] Frayne R, Sevick RJ, Demchuk AM, et al. Clinical stroke imaging at 3 T. *ISMRM program*. 2000;1253.
- [55] Kucinski T, Koch C, Eckert B, et al. Collateral circulation is an independent radiological predictor of outcome after thrombolysis in acute ischaemic stroke. *Neuroradiology* 2003;45: 11–8.
- [56] Willinsky RA, Taylor SM, terBrugge K, Farb RI, Tomlinson G, Montanera W. Neurologic complications of cerebral angiography: Prospective Analysis of 2,899 Procedures and review of the literature. *Radiology* 2003;227:522–8.
- [57] Ross JS, Masaryk TJ, Modic MT, Ruggieri PM, Haaacke EM, Selman WR. Intracranial aneurysms: Evaluation by MR angiography. *Am J Neuroradiol* 1990;11:449–55.
- [58] Atlas SW, Sheppard L, Goldberg HI, Hurst RW, Listerud J, Flamm E. Intracranial aneurysms: Detection and characterization with MR angiography with use of an advanced postprocessing technique in a blinded-reader study. *Radiology* 1997; 203:807–14.
- [59] Nagasawa S, Deguchi J, Arai M, Tanaka H, Kawanishi M, Ohta T. Topographic anatomy of paraclinoid carotid artery aneurysms: Usefulness of MR angiographic source images. *Neuroradiology* 1997;39:341–3.
- [60] Isoda H, Takehara Y, Isogai S, et al. MRA of intracranial aneurysm models: a comparison of contrast-enhanced three-dimensional MRA with time-of-flight MRA. *J Comput Assist Tomogr* 2000; 24:308–15.
- [61] Metens T, Rio F, Balériaux D, Roger T, David P, Rodesch G. Intracranial aneurysms: Detection with gadolinium-enhanced dynamic three-dimensional MR angiography-Initial results. *Radiology* 2000; 216:39–46.
- [62] Jager HR, Ellamushi H, Moore EA, Grieve JP, Kitchen ND, Taylor WJ. Contrast-enhanced MR angiography of intracranial giant aneurysms. *AJNR Am J Neuroradiol* 2000;21:1900–7.
- [63] Boulin A, Pierot L. Follow-up of intracranial aneurysms treated with detachable coils: comparison of gadolinium-enhanced 3D time-of-flight MR angiography and digital subtraction angiography. *Radiology* 2001;219:108–13.
- [64] Mori H, Aoki S, Okubo T, et al. Two-dimensional thick-slice MR digital subtraction angiography in the assessment of small to medium-size intracranial arteriovenous malformations. *Neuroradiology* 2003;45:27–33.
- [65] Klisch J, Strecker R, Hennig J, Schumacher M. Time-resolved projection MRA: Clinical application in intracranial vascular malformations. *Neuroradiology* 2000;42:104–7.
- [66] Kauczor HU, Engenhardt R, Layer G, et al. 3D TOF MR angiography of cerebral arteriovenous malformations after radiosurgery. *J Comput Assist Tomogr* 1993;17:184–90.

- [67] Shim YW, Chung TS, Kang WS, Joo JY, Strecker R, Hennig J. Non-invasive follow-up evaluation of post-embolized AVM with time-resolved MRA: A case report. *Korean J Radiol* 2002;3:271–5.
- [68] Suzuki M, Matsui O, Kobayashi K, et al. Contrast-enhanced MRA for investigation of cerebral arteriovenous malformations. *Neuroradiology* 2003; 45:231–5.
- [69] Duran M, Schoenberg SO, Yuh WTC, et al. Cerebral arteriovenous malformations: morphologic evaluation by ultrashort 3D gadolinium-enhanced MR angiography. *Eur Radiol* 2002;12: 2957–64.
- [70] Atlas SW, Do HM. Intracranial vascular malformations and aneurysms. In: Atlas SW, Their SO, editors. *Magnetic resonance imaging of the brain and spine*. 3rd edition. Philadelphia: Saunders; 2002. p. 833–917.
- [71] Coley SC, Romanowski CA, Hodgson TJ, Griffiths PD. Dural arteriovenous fistulae: Noninvasive diagnosis with dynamic MR digital subtraction angiography. *Am J Neuroradiol* 2002;23:404–7.
- [72] Yoon HK, Shin HJ, Lee M, Byun HS, Na DG, Han BK. MR angiography of Moyamoya disease before and after encephaloduroarteriosynangiosis. *Am J Roentgenol* 2000;174:195–200.



Practical consideration for 3T imaging

Weili Lin, PhD^{a,b,*}, Hongyu An, DSc^a, Yasheng Chen, DSc^a,
Peter Nicholas, BS^b, GuiHua Zhai, BS^b, Guido Gerig, PhD^{c,d},
John Gilmore, MD^d, Elizabeth Bullitt, MD^{c,e}

^a*Department of Radiology and Neurology, University of North Carolina at Chapel Hill,
Old Infirmary Building CB#7515, Chapel Hill, NC 27599, USA*

^b*Department of Biomedical Engineering, University of North Carolina at Chapel Hill, NC, 27599, USA*

^c*Department of Computer Sciences, University of North Carolina at Chapel Hill, NC, 27599, USA*

^d*Department of Psychiatry, University of North Carolina at Chapel Hill, NC, 27599, USA*

^e*Department of Internal Medicine, University of North Carolina at Chapel Hill, NC, 27599, USA*

In the past 10 to 15 years, 1.5T has been one of the most commonly used field strengths for day-to-day clinical operations. However, recent advances in high field technology and the increased availability of high field (> 1.5T) human scanners have opened the doors for a variety of exciting improvements in clinical and research applications of MR imaging. In particular, 3T has continued to gain wide acceptance as one of the main field strengths for clinical and research studies. Therefore, in this article the authors focus on the pros and cons of 3T imaging and comparisons between results obtained at 3T and 1.5T.

The movement toward a magnetic field strength greater than that found in the widely available 1.5T clinical systems stems from the need to improve spatial resolution, to reduce data acquisition time allowing for an increase of patient throughput, and to augment susceptibility effects for functional MR imaging (fMR imaging). With the improved signal-to-noise ratio (SNR) associated with high field imaging, several attractive options are available. First, it is possible to increase spatial resolution, which may aid in the identification and diagnosis of subtle morphological changes and small lesions. Second, the improved intrinsic SNR at 3T can shorten data acquisition time, which leads to an increase of

patient throughput. Finally, and perhaps the major driving force for high field imaging, is the increased sensitivity to deoxyhemoglobin induced susceptibility effects, which in turn improves the quality of fMR imaging.

While the advantages of high field imaging are of clinical importance, the associated disadvantages need to be considered also. For example, the increased sensitivity to susceptibility effects will improve the quality of fMR imaging, yet it will cause signal loss in gradient echo images, particularly in regions where alterations of local magnetic field are present. In addition, although the local magnetic field alterations will not cause signal loss for spin echo images caused by the application of the 180-degree pulse, geometric distortions may occur, making it difficult to conduct morphologic analysis such as volumetric measurements at high fields. Furthermore, TE will most likely need to be reduced for high field imaging to minimize signal loss associated with the shortening of T2 and more importantly T2*. Consequently, a high performance gradient capability or a high bandwidth will be required. The latter causes a reduction in SNR, which can potentially offset the SNR gained by the increase of field strength. Finally, T1 becomes longer as the magnetic field strength increases, which could have substantial implications for the choice of TR to optimize tissue contrast, and for MR angiography (MRA). All of the above-mentioned competing factors that accompany high field imaging are

* Corresponding author.

E-mail address: linw@email.unc.edu (W. Lin).

likely to affect the image quality and alter the choice of imaging parameters. The authors discuss in this article the pros and cons and address practical considerations for the design of imaging protocols for high field imaging.

Signal-to-noise ratio

One of the major advantages of high field imaging is the improvement of SNR compared with 1.5T. In this section, theoretical background of MR SNR in relation to field strength is given, followed by a discussion of potential approaches for making the best use of the improved SNR.

For an imaging experiment, the MR signal (S) is directly proportional to the available equilibrium magnetization (M_0), the voxel size (V), and the resonance frequency (ω_0), which can be written as

$$S \propto \omega_0 M_0 V. \quad [1]$$

The equilibrium magnetization can be expressed as

$$M_0 \approx \rho \frac{\gamma^2 \hbar^2 B_0}{4kT}, \quad [2]$$

where ρ , γ , \hbar , B_0 , k , and T are spin density, gyromagnetic ratio (2.68×10^8 rad/T/seconds), Planck's constant, static magnetic field, Boltzmann's constant, and the absolute temperature, respectively. Therefore, Eq. [1] can be rewritten as

$$S \propto \omega_0 \rho \frac{\gamma^2 \hbar B_0}{4kT} V. \quad [3]$$

Given the well-known relationship between the resonance frequency and the static magnetic field (Larmor equation, $\omega_0 = \gamma B_0$), Eq. [3] can be further rewritten as

$$S \propto \rho \frac{\gamma^3 \hbar B_0^2}{4kT} V. \quad [4]$$

As a result, MR signal is quadratically dependent on the static magnetic field; MR signal is expected to increase by a factor of 4 at 3T with respect to images acquired at 1.5T. Unfortunately, while the signal will be four times higher at 3T when compared with images acquired at 1.5T, the noise also increases by a factor of two because of the frequency dependence of the electronic noise, resulting in a factor of 2 improvement in SNR. This 2-fold improvement in SNR can potentially have profound clinical implications for acquiring high-resolution images or shortening data

acquisition time. A representative comparison of T2-weighted images obtained from the same subject acquired from 1.5T (Figs. 1A and B) and 3T (Figs. 1C and D) is shown in Fig. 1. The imaging parameters were kept as similar as possible between the two field strengths. In addition, the total data acquisition times were 8 minutes 43 seconds and 7 minutes 30 seconds for 1.5T and 3T, respectively. It is immediately evident that the SNR is higher in images acquired at 3T when compared with that in 1.5T images, enhancing the visibility of fine details.

In light of the improved SNR at 3T, the authors discuss how the SNR gained at 3T can be used in practical imaging experiments in the following subsections.

Shortening data acquisition times

Without losing generality, SNR is roughly proportional to the square root of the total data acquisition time. Therefore, with a factor of 2 improvement, it is possible to shorten the total data acquisition time by a factor of 4 at 3T while maintaining an SNR comparable to that obtained at 1.5T. This reduction in total data acquisition time could minimize patient motion artifacts and increase patient throughput.

If the authors assume that the spatial resolution remains constant, two different approaches can be used to reduce total data acquisition time: one can reduce the number of averages (when multiple averages are used) or else decrease TR. The former approach is straightforward since it is common to average multiple acquisitions to improve SNR in clinical images. By acquiring images at 3T, it is possible to reduce the numbers of averages by a factor of 4 and thus reduce total data acquisition time by a factor of 4, while maintaining an SNR similar to that at 1.5T.

In addition to reducing the number of acquisitions averaged, it also is possible to reduce total data acquisition time by decreasing TR, since not all of the imaging protocols require multiple averages. Following the same logic as discussed previously, TR can be reduced by a factor of 4 at 3T while maintaining a similar SNR as that obtained at 1.5T. However, this approach is not commonly used for the following reasons. First, while SNR is one of the major considerations for the quality of MR images, the contrast-to-noise (CNR) is of primary importance, particularly in differentiating abnormal from normal tissues. For example, without losing generality, to obtain T1 weighted images using a spin echo sequence,

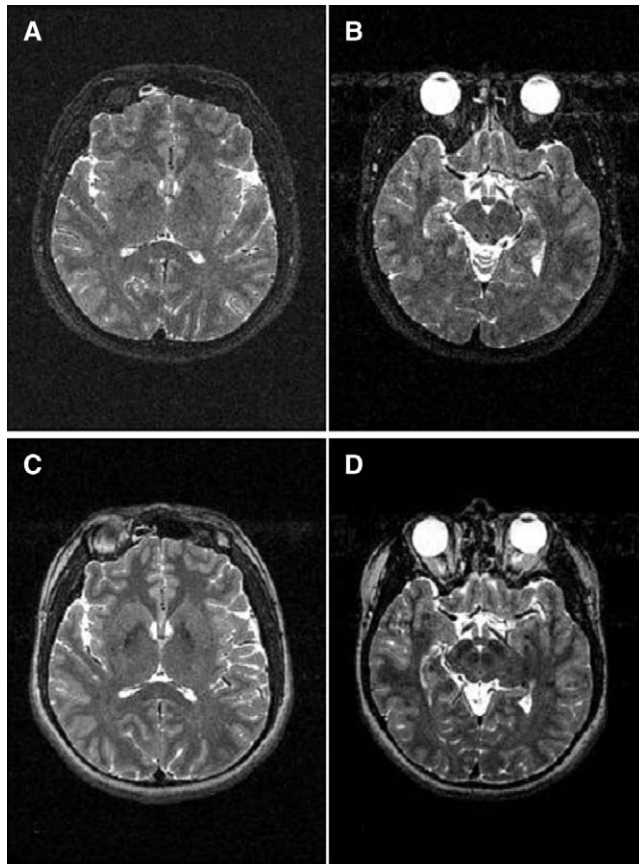


Fig. 1. T2-weighted images acquired at 1.5T (A, B) and 3T (C, D) from a subject are shown, respectively. The imaging parameters at 1.5T were as follows: TR = 9310 milliseconds; TE = 105 milliseconds; voxel size = $1 \times 1 \times 1 \text{ mm}^3$; 128 slices; and 1 average. The imaging parameters at 3T were kept as similar as possible to that used at 1.5T except for the TE = 80 milliseconds and TR = 7730 milliseconds.

an optimal TR providing the maximum contrast between two tissues of interest can be derived based on

$$TR_{\text{optimal}} = \frac{\ln(\rho_b/T1_b) - \ln(\rho_a/T1_a)}{1/T1_b - 1/T1_a}, \quad [5]$$

where the subscripts *a* and *b* indicate tissues *a* and *b*. As a result, the choice of TR is somewhat limited by the TIs of the tissues of interest, making it difficult to shorten TR without compromising tissue contrast. In addition, the anticipated increase of power deposit into the body at 3T, and the number of slices that can be acquired within one TR are likely to further limit the minimal TR that can be used. (Please see the section entitled “Specific absorption rate” [SAR] for a more detailed discussion.) Therefore, whereas TR can be reduced to decrease total data acquisition time

at 3T without unacceptable compromise of SNR, this approach is not commonly used clinically.

Improving spatial resolution

In addition to reducing total data acquisition time, the improved SNR associated with 3T can be used to improve spatial resolution while keeping the data acquisition time similar to that at 1.5T. By doing so, it is possible to reduce partial volume effects. The relation between SNR and spatial resolution can be written as [1]

$$\begin{aligned} \text{SNR}_{3D} &\propto \sqrt{\Delta x \Delta y \Delta z} \\ \text{SNR}_{2D} &\propto \text{TH} \sqrt{\Delta x \Delta y} \end{aligned} \quad [6]$$

where SNR_{2D} and SNR_{3D} correspond to SNR for 2D and 3D approaches, Δx and Δy are the voxel dimensions along the frequency and phase

encoding directions, and TH and Δz are the slice thickness for 2D and 3D acquisition approaches, respectively. Note that SNR dependence on the slice thickness differs between 2D and 3D acquisition approaches.

Given that SNR is expected to increase by a factor of 2 for images acquired at 3T compared with 1.5T, it is now possible to improve spatial resolution by a factor of 2 for both inplane directions (Eq. [6]) while maintaining the SNR expected in 1.5T images. In contrast, assuming the inplane spatial resolution remains constant, the extent to which spatial resolution can be improved along the third (slice select) direction, will depend on the acquisition approach used (2D or 3D Eq. [6]). In the case of a 2D approach, the SNR is directly proportional to the slice thickness. To maintain an identical SNR between 1.5T and 3T, the slice thickness can be reduced by a factor of 2 at 3T. In contrast, a factor of 4 reduction can be achieved with a 3D acquisition approach, without compromising SNR. Therefore, depending on the structures of interest and the imaging sequences used, one would need to consider how the improved SNR can be best used for maximizing the visibility of the relevant details.

Applications

In this section, practical examples that can benefit from the improved SNR at 3T are shown. These examples include magnetic resonance angiography, imaging of normal neonates without sedation, tissue segmentation, and diffusion tensor imaging (DTI). Unless otherwise mentioned, all images shown in the following sections were acquired from either a head-only 3T or a whole body 1.5T MR scanner (Siemens Medical Systems Inc., Erlangen, Germany).

MR angiography

Several diseases affect blood vessel morphology [2–5]. An important area of research involves the segmentation of vessels from three-dimensional (3D) image data and subsequent analysis of vessel morphology to diagnose and stage disease [6]. The author group has developed methods of segmenting vessels from 3D images and of forming connected, detailed, and clinically validated vessel trees [7–10]. Given this ability, one can then quantitatively analyze the morphology of vessel populations by many parameters to define differences between normal patients and those with suspected or known disease. At present, the

authors are particularly interested in characterizing abnormal vasculature associated with malignant tumors as seen by MRA [9,10]. This type of application, and many others, requires extraction of the smallest vessels that can be defined from MRA. It therefore would be useful to determine how the improved spatial resolution associated with 3T can be used to facilitate vascular segmentation.

A 3D time-of-flight sequence with velocity compensation along the slice select and frequency encoding directions was used to acquire images at 1.5T and 3T. The imaging parameters at 3T were as follows: 6 slabs and 40 slices per slab; TR = 35 milliseconds; TE = 3.6 milliseconds; flip angle = 18; FOV = 215 mm² with a matrix size of 256 × 512; TH = 1 mm; and a magnetization transfer contrast pulse for each TR. The imaging parameters were kept identical at 1.5T except for TR = 36 milliseconds and TE = 4.6 milliseconds.

Images obtained from both field strengths were compared by (a) examination of the images on a slice-by slice basis, (b) volume rendering (ray-casting) by maximum intensity projection, and (c) extraction of detailed vessel trees from each image set. In addition, for the slice and volume rendering comparisons, the image sets were registered using the mutual-information-based method of Rueckert et al [11]. Vessel extraction was performed by the method of Aylward et al [7]. Subsampling provided, for each vessel, an ordered set of equally spaced skeleton points at a distance of one voxel and with an associated radius at each skeleton point.

Comparison of the image pairs on a slice by slice basis demonstrated that large, bright vessels were readily appreciated on both studies. Small, dim vessels were difficult to define from background on the 1.5T MRA, however (Fig. 2).

Volume rendering of the two datasets by maximum intensity projection provided similar results. Although the brighter vessels were readily appreciated in both studies, the small, dim vessels whose image intensities were closer to background could not be well visualized in the 1.5T study (Fig. 3). In addition, it is apparent that a higher background tissue signal is observed in images acquired at 1.5T compared with 3T images. The authors attribute this elevated background to the signal from superficial fat, which is substantially reduced at high field because of the shortening of T2*.

Fig. 4 illustrates the results of vessel segmentation. The results were similar to those earlier in the discussion, with vessel extraction from the

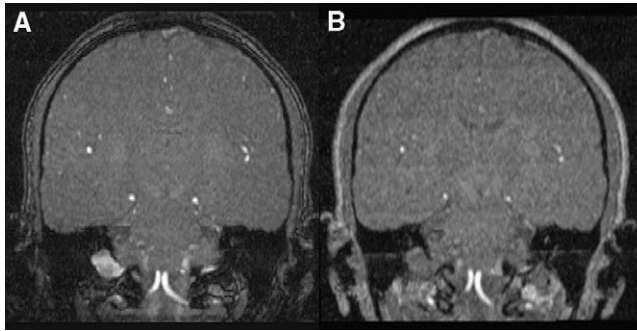


Fig. 2. Coronal sections of co-registered MRAs of the same subject obtained on a 3T scanner (A) and 1.5T scanner (B). The small vessels (arrow) easy to see in the 3T image are difficult or impossible to visualize on the 1.5T study.

1.5T study representing only the subset of large, bright vessels obtained from the 3T study. Loss of information was present in all four intracerebral circulatory groups under 1.5T imaging. The number of vessels extracted were for the 1.5T and 3T studies respectively, 32 and 48 for the anterior cerebral circulation, 25 and 40 for the left middle cerebral circulation, 27 and 42 for the right middle cerebral circulation, and 16 and 35 for the posterior cerebral circulation.

The authors expected that vessel radius might be a limiting factor, with the 3T study containing many small vessels not present in the 1.5T images. Because it could be of importance to define the limits of resolution at each magnet strength, the authors examined the average vessel radius and the smallest vessel radius present in both sets of

segmented vessels. To the authors' initial surprise, there was no obvious difference in the smallest radius between the two image segmentations. Indeed, both segmentations reported the smallest discernible vessel point to have a radius of between 0.25 and 0.3 mm. Although the 3T vessel segmentation possessed a smaller average radius, the difference in average radius between the 3T and 1.5T segmentations was small (average vessel point radius 0.83mm for 3T and 0.85 mm for 1.5T). These results are most easily explained by the noise present in the 1.5T image, making radius determination more difficult, variable, and uncertain.

The authors examined by several methods the degree of vessel detail obtainable in a single subject scanned by a 1.5T and a 3T MR magnet. All

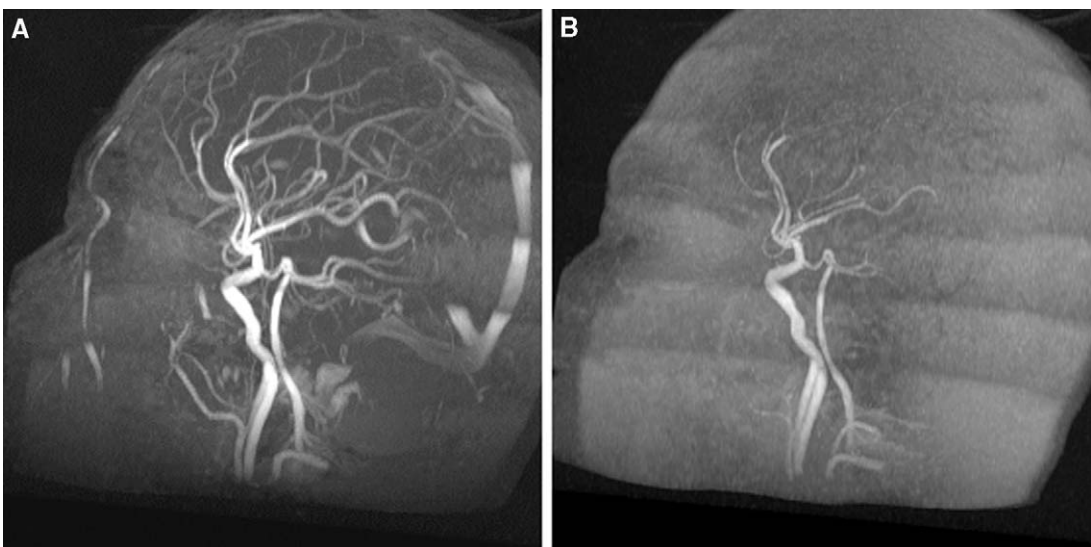


Fig. 3. Volume rendering by maximum intensity projection for MRA studies of the same subject on a 3T unit (A) and 1.5T unit (B). Small, dim vessels cannot be well seen on the 1.5T study.

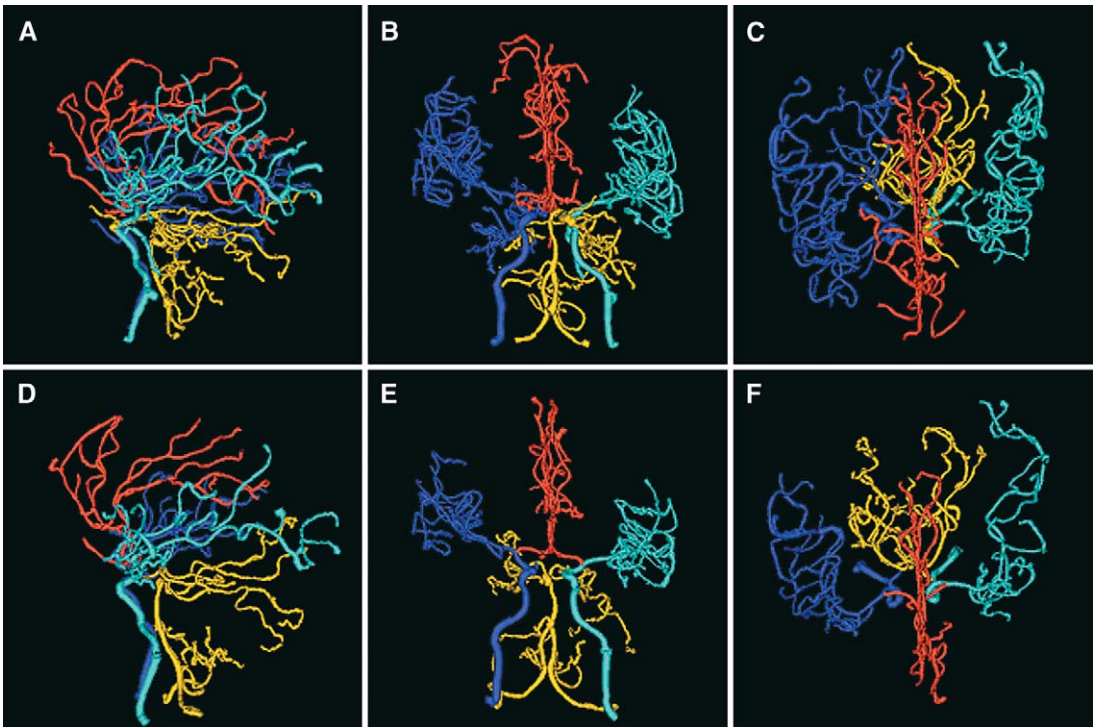


Fig. 4. Comparison of vessel extractions from 3T MRA (A–C) and 1.5T MRA (D–F). Vessels have been rotated into similar points of view for the two studies to show approximate lateral (A, D), AP (B, E), and axial (C, F) views. Anterior cerebral group (red), left middle cerebral group (cyan), right middle cerebral group (blue), and posterior circulation (gold). The 1.5T study is missing the smaller vessels, including distal branches of the anterior and middle cerebral circulations and small branches of the posterior cerebral circulation.

evaluation methods suggest that large, bright vessels are seen similarly well under both imaging protocols. However, all methods also suggest that small, dim vessels whose intensity is close to that of background can only be delineated under higher magnet strength. The smallest visualizable vessels at 3T seem to have a radius of about 0.3 mm when the voxel acquisition size is $0.4 \times 0.4 \times 1.0 \text{ mm}^3$.

Imaging of normal and healthy neonates

Motion artifacts caused by patient movement during MR acquisition have been one of the major limiting factors for MR imaging. While it is possible to minimize motion artifacts by carefully instructing subjects to remain still during data acquisition, this is obviously not applicable for neonates. Consequently, sedation is normally used for neonate imaging, making it difficult to image normal neonates. Therefore, neonate imaging thus far has been obtained from subjects who underwent MR imaging because of clinical indica-

tions and were retrospectively determined to be clinically normal. In addition to the fact that these results do not necessarily represent normal neonates because subjects were imaged for potential clinical indications, sedation was always used. With the improved SNR associated with 3T imaging, allowing rapid data acquisition, this opens a new avenue for imaging normal neonates without sedation.

The authors have recently imaged 20 full term and healthy neonates (age: 16 ± 4 days) using a head-only 3T MR scanner [12]. The imaging protocol included DTI, 3D T1 MR-RAGE, and spin-density/T2-weighted sequences. The total data acquisition time for imaging sequence was approximately 12 minutes. Excellent imaging quality was obtained from 13 of the 20 neonates. A representative set of MP-RAGE T1-weighted images is shown in Fig. 5. The spin density and T2-weighted images from the same subjects are also shown in Fig. 6. In addition, fractional anisotropy (FA) maps obtained from one neonate

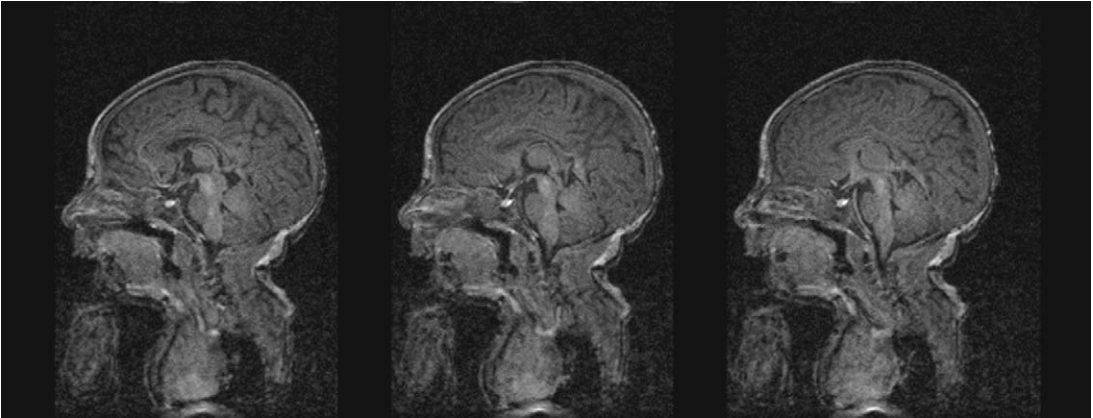


Fig. 5. Representative images obtained from a normal and healthy neonate using a 3D MP-RAGE sequence at 3T are shown. No sedation was used for this study. No clear motion artifacts are present and quality anatomical images are obtained. The imaging parameters for the MP-RAGE sequence were as follows: TR/TE/TH = 11.1 milliseconds/4.3 milliseconds/1mm, and an inplane resolution of $0.90 \times 0.90 \text{ mm}^2$. A total of 122 sagittal images were acquired to cover the entire brain and the total data acquisition time was 5 min and 34 seconds.

are shown in Fig. 7. Consistent with previously reported results, a global elevation of ADC and a reduction of FA in the major WM tracts are observed in neonates when compared with that reported in adults [13–16]. In particular, quantitative measures of FA reveal that an FA of 0.63 ± 0.06 in the major white matter tracts

(splenium of corpus callosum) and 0.10 ± 0.03 in gray matter are obtained. However, an FA of 0.20 ± 0.07 is observed for the frontal white matter despite a well-delineated gray/white contrast in T2-weighted images at the same anatomical region. This observed spatial variation of FA in white matter may suggest different degrees

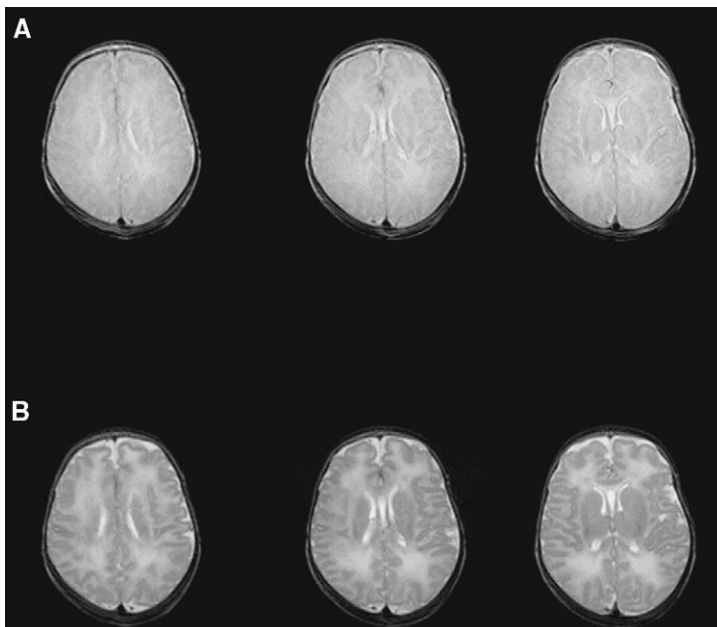


Fig. 6. High quality spin density (A) and T2-weighted (B) images were obtained from a normal and healthy neonate at 3T without sedation. In addition to the fact that the SNR is sufficient for delineating anatomical structures, no apparent motion artifacts are observed.

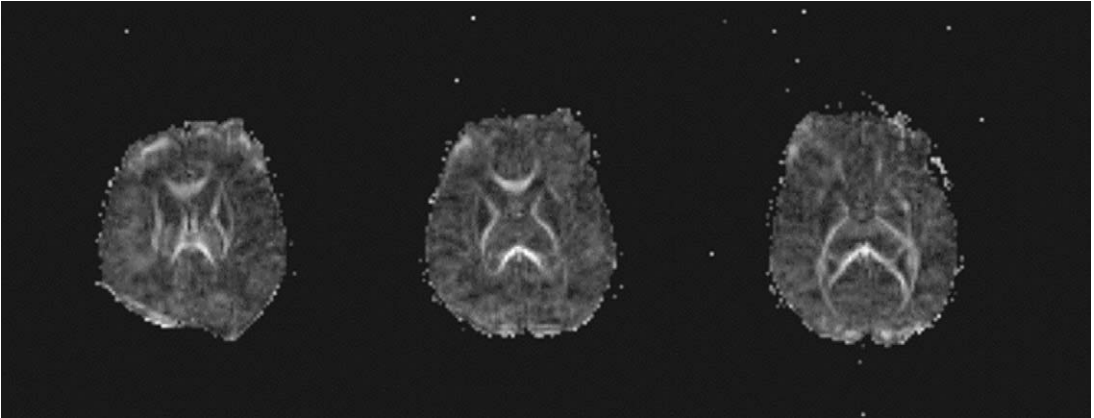


Fig. 7. Fractional anisotropy maps obtained from a normal and healthy neonate at 3T using a single shot EPI DTI sequence. The imaging parameters for the DTI sequence were as follows: TR/TE/TH = 4219 milliseconds/92.2 milliseconds/5mm, an inplane resolution of 1.72×1.72 mm, 12 averages, and 20 slices. Seven images were acquired for each slice, one without diffusion gradient ($b = 0$) while the remaining six with $b = 1000$ seconds/mm² and diffusion gradient along $\{1/\sqrt{2}, 0, 1/\sqrt{2}\}$, $\{-1/\sqrt{2}, 0, 1/\sqrt{2}\}$, $\{0, 1/\sqrt{2}, 1/\sqrt{2}\}$, $\{0, 1/\sqrt{2}, -1/\sqrt{2}\}$, $\{1/\sqrt{2}, 1/\sqrt{2}, 0\}$, $\{-1/\sqrt{2}, 1/\sqrt{2}, 0\}$ separately.

of WM maturation between the major WM tracts and the WM adjacent to the cortical gray matter rim.

The ability to image normal neonates without the need for sedation is likely to facilitate a more complete understanding of brain development in addition to establishing normative FA values of normal neonates, which should greatly facilitate differentiating abnormal from normal subjects.

Diffusion tensor imaging

DTI has recently been proven to reveal subtle microstructural alterations in white matter, which are not detectable by conventional MR imaging [17–20], and there has been extensive interest in using this new source of information for clinical purposes. However, with the application of diffusion gradients, the SNR of DTI images is much lower compared with that of conventional MR images, and thus multiple averages are normally required to obtain a sufficient SNR. This imposes constraints in a clinical setting because of magnet time limitations. Therefore, to obtain a sufficient SNR, spatial resolution is often sacrificed, making these studies more prone to partial volume effects. To determine how, potentially, partial volume effects will affect the quality of DTI images, a subject was imaged at 3T using a single shot DTI sequence. Two sets of DTI images were obtained by maintaining all imaging parameters constant except that the spatial resolution and the number of averages were varied. Images with two

different spatial resolution were obtained: $4 \times 4 \times 4$ mm³ and $2 \times 2 \times 2$ mm³ with 1 and 22 averages, respectively. The FA maps calculated from the two different resolutions are shown in Fig. 8. Regardless of the spatial resolution the FA is higher in white matter than in gray matter and the improved spatial resolution reveals (C, D) more detailed white matter structures, particularly for the peripheral white matter. In addition, fiber tracking was also performed based on the principal diffusive direction (ie, the eigenvector associated with the largest eigenvalue) of the local tensor. Volumes of interest in the splenium and genu of the corpus callosum were defined as the source regions using the FA images with a multi-planar visualization tool. The source regions were kept as similar as possible for the high- and low-resolution FA maps. The target was defined as the whole brain cortex to search for all possible trajectories originating from the two source locations. Subsequently, a fiber tracking method originally developed by Mori et al [21] was used and the resulting fiber tracts were overlaid with the $b = 0$ anatomical images to augment three-dimensional visualization.

A comparison of the fiber tracking is shown in Fig. 9 for low (A) and high-resolution (B) DTI images. In addition more fibers being visible, the fiber tracking approach is able to track the peripheral white matter with greater success in high-resolution DTI images when compared with results obtained using low-resolution DTI images.

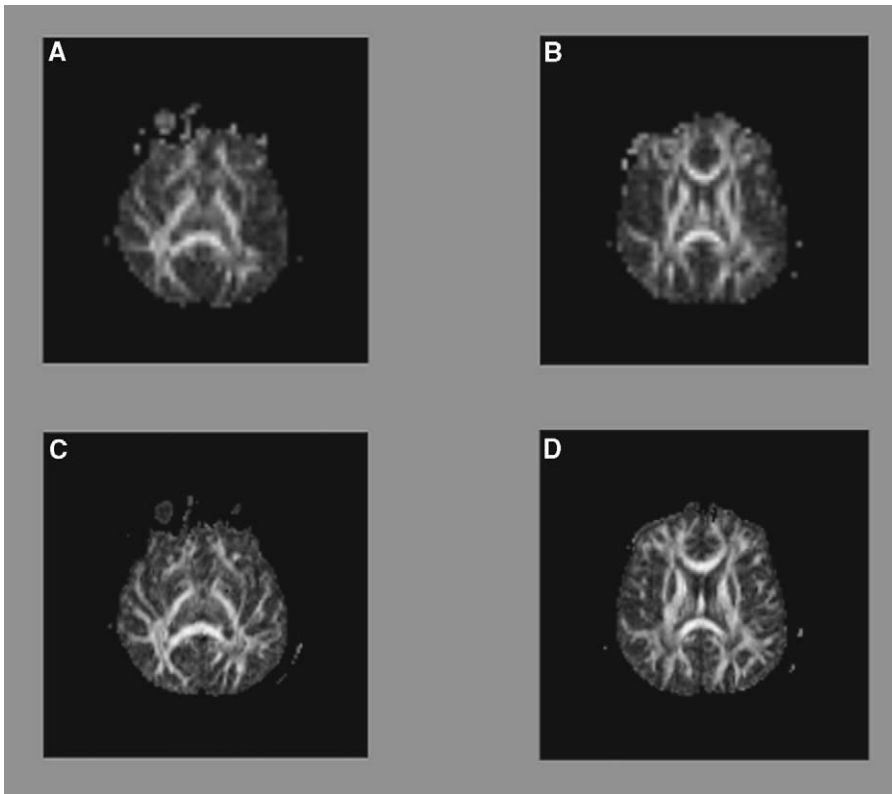


Fig. 8. FA maps obtained from a subject at 3T using two different spatial resolution, $4 \times 4 \times 4 \text{ mm}^3$ (A, B) and $2 \times 2 \times 2 \text{ mm}^3$ (C, D) are shown, respectively. It is immediately evident that the high-resolution FA maps offer more structural details of white matter tracts when compared with that in the low resolution FA maps, particularly for the peripheral white matter. The imaging parameters were as follows: TR = 6800 milliseconds; TE = 73 milliseconds; FOV = $256 \times 256 \text{ mm}^2$; and 58 slices to cover the entire brain. For the high resolution DTI images, a matrix size of 128×128 and a slice thickness of 2 mm were used while the matrix size and slice thickness were 64×64 and 4 mm, respectively, for low resolution DTI images.

These findings underscore the importance of using high-resolution DTI images for assessing FA and facilitating fiber tracking. However, as mentioned earlier in the discussion, DTI studies, require substantial averaging to offset gradient-induced reduction of SNR, which leads to substantially lengthened data acquisition time at 1.5T, making it clinically unacceptable. Nevertheless, the improved SNR associated with 3T should allow the acquisition high-resolution DTI images while maintaining a data acquisition time that is more reasonable in a clinical facility.

An additional result of fiber tracking using images obtained from a normal neonate at 3T is shown in Fig. 10. As mentioned in the previous subsection, no sedation was used for acquiring these images, yet high quality fiber tracking results can be obtained within a rather short period of

acquisition time (2 minutes and 11 seconds). This should further facilitate our ability to use DTI for the study of normal brain development.

Tissue segmentation

Tissue segmentation has been used in the study of neurodegenerative diseases such as Alzheimers [22,23] and Schizophrenia [24,25]. Because most of the studies to date have been done using images obtained at 1.5T, the ability to offer images with a higher spatial resolution or SNR at 3T could further facilitate the success of tissue segmentation. A healthy subject was imaged using MP-RAGE and T2-weighted sequences at 1.5T and 3T, respectively. The imaging parameters for MP-RAGE sequence at 1.5T were as follows: TR/TI = 1550/1100 milliseconds; TE = 4.38 milliseconds; and spatial resolution = $1 \times 1 \times 1 \text{ mm}^3$.

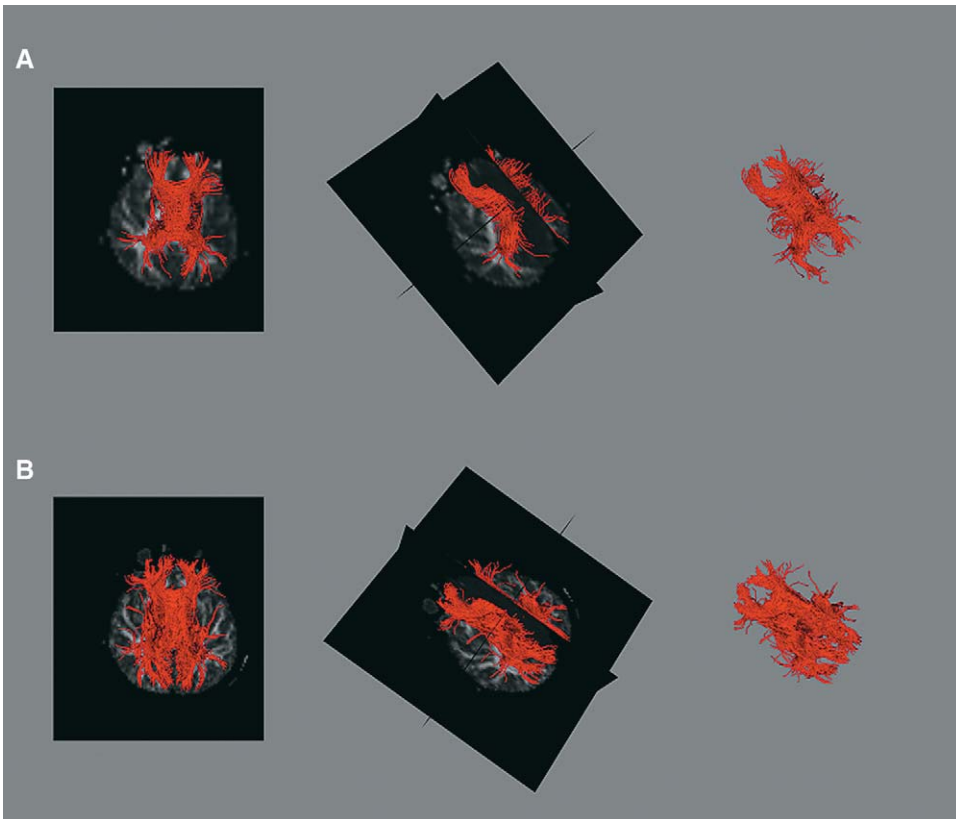


Fig. 9. Results of fiber tracking are shown using the low- (A) and high-resolution (B) DTI images as shown in Fig. 8. The tracked fibers are overlaid onto the anatomical images for the left and middle images while the corresponding fiber images without the anatomical information for the middle images are shown in the right panel. A total of 880 and 6708 fibers were tracked for the low and high-resolution images, respectively.

All of the imaging parameters remained identical except for the TR/TI = 1520/900 milliseconds at 3T. The imaging parameters for T2-weighted sequence at 1.5T were as follows: TR = 9310 milliseconds; TE = 105 milliseconds; and spatial resolution = $1 \times 1 \times 1 \text{ mm}^3$. Again, all of the imaging parameters at 3T were kept as similar as possible to that at 1.5T except for the TR = 7730 milliseconds and TE = 80 milliseconds.

Tissue segmentation of gray matter, white matter and CSF using multi-channel (T1- and T2-weighted images) was performed for images acquired at 1.5T and 3T [26,27]. It is somewhat surprising that no apparent differences are observed in tissue segmentation using images acquired at 3T (Fig. 11A) and 1.5T (Fig. 11B) as shown in Fig. 11 despite the fact that the SNR is higher in images acquired at 3T than that at 1.5T. However, on a closer inspection, it is evident that the thalamus and basal ganglia are better defined

(axial and coronal sections) and the brainstem is cleaner (sagittal and coronal sections) at 3T when compared with that obtained from 1.5T. A comparison of the volume rendering is also shown in Fig. 12. Similar to the findings shown in Fig. 11, the temporal lobe is better defined (lateral view) and there is more detail at the base (base view; center column) at 3T, although there is not much difference in the view from the front (right column).

These results are preliminary and limited by the small sample size. Nevertheless, more studies are warranted to further investigate how the improved SNR at 3T can be better used to facilitate the outcome of tissue segmentation.

Susceptibility

Perhaps one of most commonly observed artifacts associated with high field imaging is the

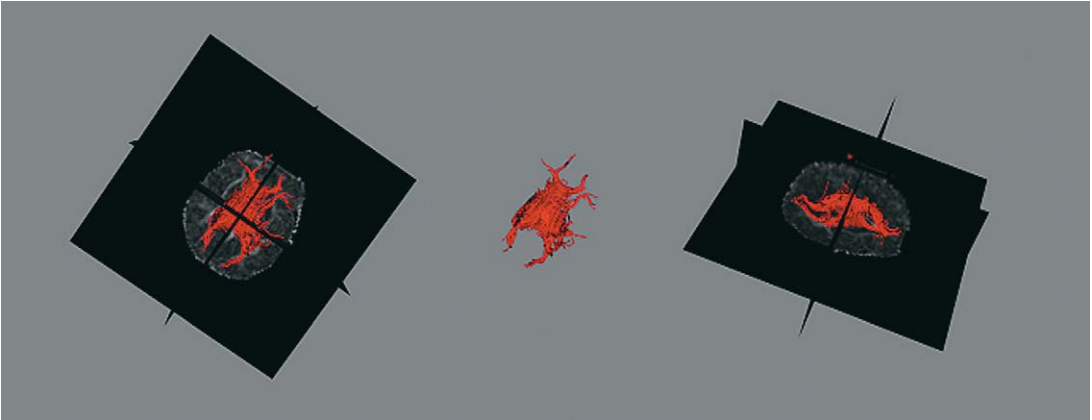


Fig. 10. Fiber tracking results obtained from a normal neonate are shown. The middle panel is the corresponding fiber images without the anatomical information as shown in the left pane. The source regions are the splenium and genu of the corpus callosum and the right and left internal capsule. Despite the fact that a rather short data acquisition time (2 minutes and 11 seconds) was used to acquire DTI images, major white matter fiber tracts are clearly visible.

increased sensitivity to susceptibility effects, which can manifest themselves in several different ways, including a shortening of T2 and T2*, signal loss, and geometric distortion. These are perhaps the most prominent shortcomings associated with high field imaging and will substantially affect the image quality. The authors first discuss the basic physics of susceptibility, followed by the concepts of signal loss induced by intravoxel

dephasing, geometric distortion, and finally how susceptibility effects can be used for fMR imaging.

Basic physics of susceptibility

Depending on the magnetic dipole moments, various materials can be grouped into three categories. In the presence of an external magnetic field, magnetic moments exhibit different magnetic properties that can be characterized as

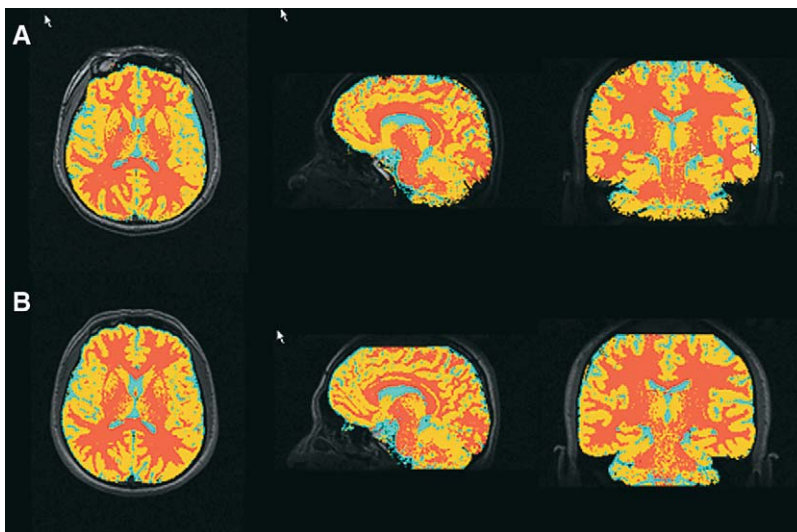


Fig. 11. Results obtained from tissue segmentation using images acquired at 3T (A) and 1.5T (B) from the same subject are shown. Although the discrepancies are subtle between the two field strengths, the thalamus and basal ganglia are better defined by the 3T (axial and coronal sections) and the brainstem is cleaner on the 3T (sagittal and coronal sections) when compared with that obtained at 1.5T.

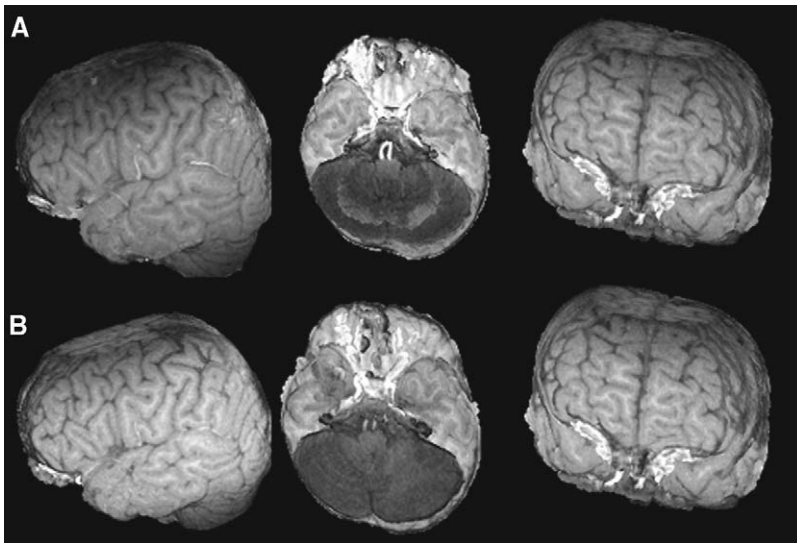


Fig. 12. Surface rendered images based on the images acquired at 3T (A) and 1.5T (B) are shown from a healthy subject. Although the differences are subtle between the two field strengths, the temporal lobe is better defined (*lateral view*) and there is more detail at the base (*base view; center column*) at 3T.

paramagnetic, diamagnetic, and ferromagnetic materials, respectively. The authors discuss all three materials in the following paragraphs.

A pair of electrons in an atom or molecule causes a cancellation of spin moments. An atom with an unpaired electron has a non-vanishing permanent magnetic moment, leading to a non-zero dipole magnetic field. This state is referred to as paramagnetism. In the absence of an external magnetic field, these moments are randomly distributed. However, in the presence of an external magnetic field, they tend to align along the direction of the external magnetic field, producing a bulk magnetic moment and a corresponding macroscopic magnetic field. In contrast, for diamagnetism, the macroscopic sum of the induced moments is roughly anti-parallel to the external magnetic field, and its associated macroscopic field weakly opposes to the external field.

The third category of materials has permanent domains of electron spin magnetic moments that produce very strong macroscopic fields independent of an external magnetic field. This property is usually referred to as ferromagnetism. These materials include iron, nickel, cobalt, gadolinium, dysprosium, and various alloys and oxides.

From the susceptibility perspective, most of the widely used contrast agents are paramagnetic, including Gadolinium diethylenetriamine

pentaacetic acid (Gd-DTPA), albumin-Gd-DTPA, Gd-DTPA-polylysine, and Dysprosium-DTPA (Dy-DTPA). They possess large magnetic moments, derived from their unpaired electrons. Among these contrast agents, Gd-DTPA has been widely used for a variety of clinical applications, including enhancing brain lesions based on contrast agents induced shortening of T1 and revealing tissue perfusion using the induced T2/T2* effects. Because these effects also depend on field strengths, instead of focusing on exogenous contrast agents, here the authors focus on the endogenous contrast agent deoxyhemoglobin, because it is perhaps more relevant to the general interests of fMR imaging while relying on similar theoretical considerations as that of exogenous contrast agents.

Blood is composed of plasma and erythrocytes (red blood cells or RBCs), various leukocytes (white blood cells), and platelets. RBCs contain either oxyhemoglobin (Hb) or deoxyhemoglobin (dHb). For deoxyhemoglobin molecules, the heme iron is in a high spin ferrous (Fe^{2+}) state characterized by four of its six outer electrons being unpaired. The unpaired electron spins have a large magnetic moment. The associated paramagnetic properties make deoxyhemoglobin behave in a manner similar to exogenous paramagnetic contrast agents [28]. In contrast, for oxygenated hemoglobin, one of the electrons is

partially transferred to an oxygen molecule and the heme iron becomes a low-spin state, exhibiting diamagnetic properties.

Effects of susceptibility on MR Images

Phase dispersion

Local magnetic field variations (ΔB) arise from the susceptibility difference ($\Delta\chi$) between two materials. Usually, $\Delta\chi$ is calculated with respect to water since water is the most abundant element in the human body. ΔB is known to be linearly proportional to the product of $\Delta\chi$ and the external magnetic field as

$$\Delta B(\vec{r}) \propto f(\vec{r}) \cdot \Delta\chi \cdot B_0, \tag{7}$$

where $f(\vec{r})$ is a spatially varying function determined by the geometry of the susceptibility source. The magnitude of $\Delta B(\vec{r})$ decreases with distance from the susceptibility source (Fig. 13).

The expected phase shift ($\phi(\vec{r}, TE)$) for an echo time (TE) is,

$$\phi(\vec{r}, TE) = \gamma \Delta B(\vec{r}) \cdot TE. \tag{8}$$

Furthermore, the MR signal can be expressed as

$$s(\vec{r}) \propto \int_v \rho(\vec{r}) e^{-i\phi(\vec{r}, TE)} d\vec{r} \tag{9}$$

$$\propto \int_v \rho(\vec{r}) e^{-i\gamma f(\vec{r}) \Delta\chi \cdot B_0 \cdot TE} d\vec{r}$$

where v is the volume of an imaging voxel.

Because of the spatially dependent term $f(\vec{r})$, spins accumulate different phases depending on their location relative to the susceptibility sources. In the case when an imaging voxel is near a susceptibility source, a severe signal reduction will occur in the presence of phase dispersion (Eq. [9]) since the MR signal is a complex sum of the magnetization within one imaging voxel. In the worst scenario, a complete signal void will occur when phase dispersion exceeds 2π . For example, in brain tissue close to the sinuses where a large ΔB is anticipated because of the large susceptibility difference between air and water, a substantial signal loss is normally seen. Fig. 14 shows images obtained from a gradient echo (Fig. 14A) and a spin echo (Fig. 14B) sequences from the same subject. A substantial signal loss is observed as expected near the sinuses (arrow) while a complete signal recovery is obtained because of the application of the 180-degree pulse when a spin echo sequence is used.

Geometric distortion

In addition to signal loss, local magnetic field variations also cause geometric distortion. Unlike signal loss that is only present in gradient echo images but not spin echo images, geometric distortion can be present in gradient echo and spin echo images. Let us look at the one-dimensional imaging equation:

$$\rho(x) = \int dk S(k) e^{j2\pi kx} \tag{10}$$

Here $\rho(x)$ and $S(k)$ correspond to MR signal in the object domain along the x direction and

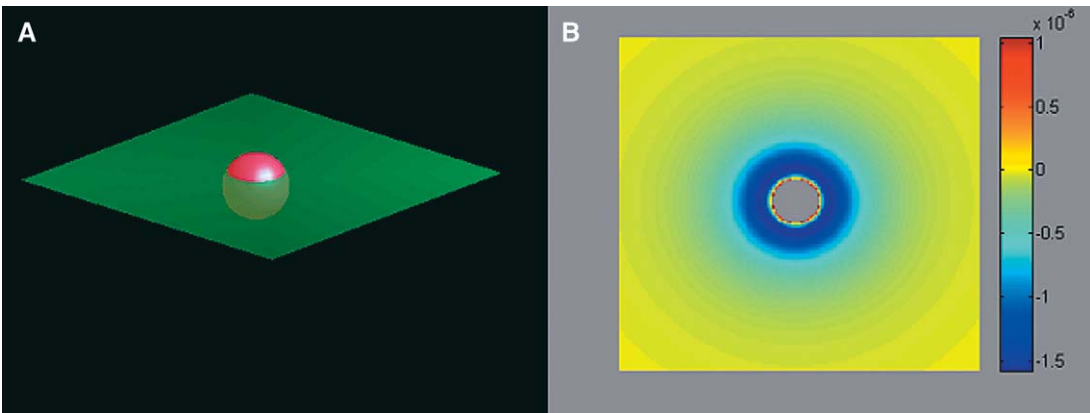


Fig. 13. A pictorial display of a spherical susceptibility source and the plane (green) where ΔB is plotted (A). The spatial magnetic field perturbation is shown (B) where “yellow” is referred to as no effects and dark blue corresponds to the largest effect. The color bar indicates the magnitude of ΔB in 10^{-6} Tesla.

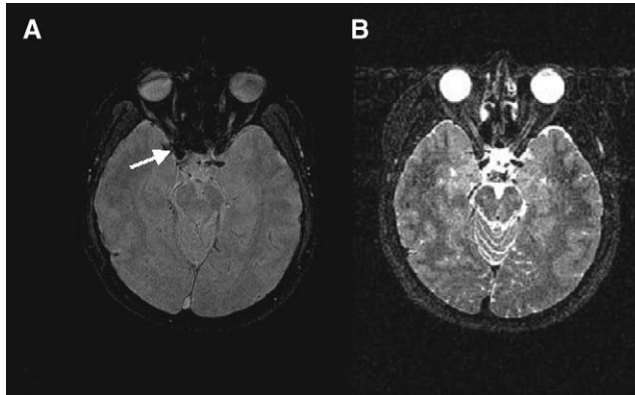


Fig. 14. Signal loss resulted from the presence of local magnetic field is seen in image acquired using a gradient echo sequence (arrow, A) while signal is recovered when a spin echo sequence is used thanks to the application of 180-degree pulses. (A, B) Both images were acquired from a head-only MR scanner and a TE of 25 milliseconds and 80 milliseconds were used for the gradient echo and spin echo sequences, respectively.

k_x -space, respectively. In addition, the expression for k is:

$$\begin{aligned} \kappa &= \varphi \int_0^t G(t') dt' \\ &= \varphi Gt \end{aligned} \quad [11]$$

where $\varphi = \gamma/2\pi$, $G(t')$ is the encoding gradient, t is the gradient on time, and a constant gradient (G) is assumed. In the case when an additional gradient such as the local (susceptibility-induced) magnetic field (G_{sus}) is present, geometric distortion may or may not be apparent, depending on the magnitude of G_{sus} with respect to G . Eq [11] can be modified to take into account the present of G_{sus} :

$$\begin{aligned} \kappa' &= \varphi t(G + G_{\text{sus}}) \\ &= \varphi tG(1 + G_{\text{sus}}/G) \\ &= \kappa(1 + G_{\text{sus}}/G). \end{aligned} \quad [12]$$

Therefore, when G_{sus} is much smaller than G , G_{sus}/G can be ignored, $\kappa' = \kappa$, and a correct spatial encoding can be obtained. In the case when G_{sus} is much greater than G , the spatial information will be encoded at κ' rather than κ , resulting in geometric distortion.

For routine clinical SE sequences where the magnitudes of the encoding gradients are normally much larger than the local magnetic field variation, geometric distortion is rarely seen. However, this problem becomes more prominent when EPI sequences are used or magnetic field is increased. For a conventional EPI sequence, a small gradient is normally used along the phase

encoding direction and thus this encoding is prone to artifacts because of local magnetic field variation. Because of the linear dependence of susceptibility-induced field perturbations on external field strength (Eq. [7]), the degree of geometric distortion will be more prominent at the 3T than 1.5T under similar experimental conditions (same phase encoding gradient magnitude and imaging parameters), particularly in regions where susceptibility artifacts are anticipated to be severe, making it difficult to cover large regions of interest without artifacts. A representative example is shown in Fig. 15. An EPI SE sequence was used to acquire images from one subject at 1.5T (Fig. 15A) and 3T (Fig. 15B). A noticeable geometric distortion is seen in the image acquired at 3T (arrows) when compared with that obtained from 1.5T.

Recently, Hunsche et al [29] compared DTI results obtained from 1.5T and 3T from the same volunteers. As anticipated, an improvement in SNR was observed for DTI images acquired at 3T. In addition, ADC and FA are statistically identical between 1.5T and 3T. However, as also seen in Fig. 15, a substantial geometric distortion is observed in images acquired from 3T, particularly at the skull base and sinuses. Their findings underscore the potential concerns for the use of high field DTI images for fiber tracking, particularly in regions where geometric distortion is anticipated.

In addition to the local magnetic field induced-geometric distortion, non-linearity of the static magnetic field can also result in geometric

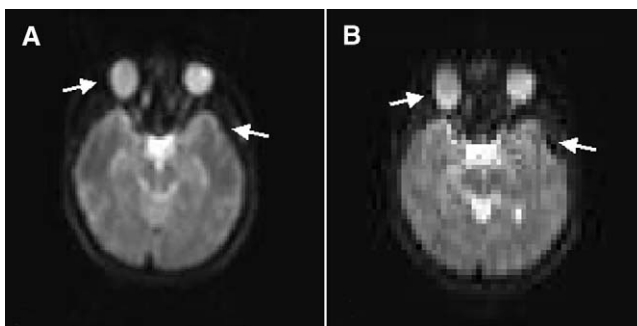


Fig. 15. Effects of geometric distortion are shown. Images were acquired at 1.5T (A) and 3T (B), respectively from a subject using an EPI SE sequence, which eliminates susceptibility induced signal loss. However, more severe geometric distortion is seen in images acquired at 3T (B, arrows) when compared with that obtained from 1.5T (A, arrows).

distortion. For example, some of the currently available 3T MR scanners have a “sweet volume” on the order of 22 cm diameter spherical volume (DSV). Therefore, as long as the imaging volume is located inside the 22 cm DSV, geometric distortion caused by the non-linear static magnetic field should be minimized. However, caution must be taken to ensure that the subject is placed within the sweet spot to minimize geometric distortion resulting from magnetic field non-linearity. Fig. 16 shows a sagittal scout image obtained from a 3T scanner. The dotted circle indicates the 22 DSV. As anticipated, no apparent geometric distortion



Fig. 16. A scout image obtained from a 3T scanner is shown. The dotted circle indicates the 22 DSV for the scanner used. Note the severe geometric distortion for regions outside the 22 DSV.

is seen for the brain while severe geometric distortion is seen immediately outside of the dotted circle.

Methods to correct susceptibility effects

As discussed in the previous two subsections, signal loss and geometric distortion induced by the presence of local magnetic field variations can potentially hamper clinical applications at 3T. Nevertheless, approaches have been proposed in an attempt to minimize susceptibility effects at high fields. Here the authors first discuss several straightforward and practical approaches.

As pointed out in Eq. 8, the phase shift is proportional to the TE used. Therefore, one of the easiest approaches to minimize signal loss and geometric distortion is to minimize TE. However, to achieve a shorter TE while maintaining a constant spatial resolution requires high gradient capability, which is limited by the gradient and the need to avoid peripheral nerve stimulation.

Another solution is to use a higher encoding gradient (either by increasing the spatial resolution or by using a higher bandwidth) to minimize signal reduction and geometric distortion [30,31]. A representative example obtained using a single shot SE EPI sequence is shown in Fig. 17. The imaging parameters were kept identical between different images except for the readout bandwidth, which was changed from 750 Hz (Fig. 17A) and 1565 Hz (Fig. 17B), to 3125 Hz (Fig. 17C). It is immediately evident that the degree of geometric distortion is substantially reduced when the highest bandwidth is used (arrows) although the SNR will be reduced by approximately a factor of 2 when compared with the image acquired using a bandwidth of 750 Hz.

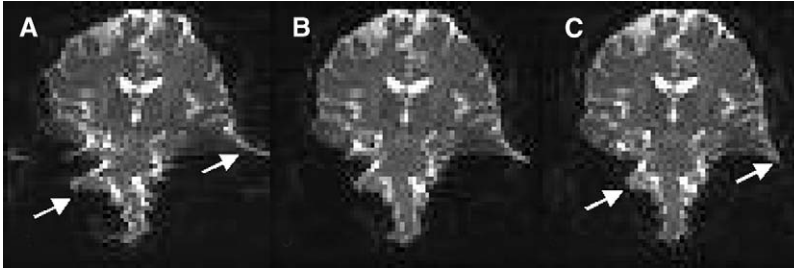


Fig. 17. A comparison of geometric distortion is shown when different gradient strengths are used by changing of bandwidth of each voxel. With an increase from 750 kHz (A), 1565 Hz (B), to 3125 Hz (C), geometric distortion is substantially reduced since a larger gradient will be needed for the increased BW without changing the FOV.

An increased spatial resolution can also be used to reduce signal loss in the presence of local magnetic field perturbations. As mentioned in the previous section, the magnitude of signal loss depends on the magnetic field variation within one voxel. Therefore, it is possible to reduce the voxel size, which in turn will minimize intravoxel dephasing (signal loss). In addition, since a higher gradient will be used to acquire high-resolution images, the ratio of G_{sus}/G (Eq. [12]) will thus be minimized, which in turn reduces geometric distortion. However, the major drawbacks of high-resolution imaging approaches are the lengthened data acquisition time and compromised SNR. Because the SNR increases by a factor of 2 at 3T with respect to 1.5T, the reduction of SNR associated with high-resolution imaging may have little effect on the overall image quality.

In addition to the above-mentioned practical approaches, more complex methods aiming to minimize signal loss and geometric distortion have also been proposed and will be discussed later. The spatial resolution along the slice select direction (z direction) for most 2D MR images is much lower than that in the readout and phase encoding directions. Therefore, susceptibility effects are usually more pronounced along the z direction since it will be more sensitive to intravoxel dephasing. To correct for the susceptibility effects along this direction, Cho et al [32] proposed to use a tailored RF pulse. Assuming the susceptibility-induced magnetic field is linear, a quadratic phase distribution along the slice select direction is used to compensate for the signal loss. Because the effectiveness of this approach has been demonstrated, this method suffers from a low SNR. Alternatively, the z shimming method [33–36] has been proposed by many investigators in an attempt to minimize signal loss along the slice

select direction. In this method, N images are acquired with N different z gradients covering positive and negative polarities. By doing so, it is possible that some of the applied z gradients will cancel out the presence of local magnetic fields and thus recover MR signal. Subsequently, either a maximum-intensity projection or a quadratic sum of the N acquired images can be used to obtain composite images where signal loss will no longer be a problem. The penalty for this approach, however, is that the total data acquisition time is N times longer without a substantial gain in SNR.

Post-processing methods can also be used to correct for signal loss and geometric distortion. In the event that magnetic field (B_0) maps are available experimentally, and assuming that background field variation is linear as a function of the spatial locations, a sinc function based on the experimentally acquired field maps can then be used to compensate for the signal loss in gradient echo images [37,38]. In addition, together with information on spatial resolution, a B_0 map can also be used to calculate the degree of shift in pixels, which correct for the geometric distortion. Because this approach seems to be effective in correcting geometric distortion, it cannot correctly determine the signal intensity of the shifted voxel. Once the signal is displaced to another voxel, unless distribution of spin density is known, this approach will not be able to estimate the correct density distribution. Alternatively, Zeng and Constable [39] proposed a novel approach for estimating the point spread function of each voxel by using additional phase encoding tables in all three directions. Subsequently, the estimated point spread function can be used to correct for geometric distortion and to estimate the correct density of each voxel. Results obtained from

phantom and human studies demonstrate the superiority of this approach when compared with that obtained using the field maps. However, this approach will substantially increase the total data acquisition time and may not be suitable in a clinical set up.

Iterative reconstruction methods can also be used to correct for signal loss induced by the presence of field inhomogeneity [40]. This method uses the experimentally measured MR signal in k -space and the field maps obtained from a separate imaging scan to iteratively derive an image without susceptibility effects. Specifically, an objective function is generated based on the difference between the experimentally acquired k -space data and the Fourier transform of the product of an image function and exponential function based on the B_0 maps. A smoothness constraint is also included to construct the objective function. The minimization of this objective function will yield an image function free from susceptibility effects. Because this approach can potentially minimize susceptibility effects, its major disadvantage is time-consuming, making it more difficult for routine clinical applications.

Finally, as mentioned in the previous section, geometric distortion is more pronounced with EPI sequences when compared with conventional imaging sequences because small gradients are used in the phase encoding direction. However, sinusoidal gradients modulated with a linear increase of gradients can be used to simultaneously sample the frequency and phase encoding directions, a technique known as spiral EPI [41]. By doing so, the presence of local magnetic field variations will no longer cause geometric distortion but rather result in blurring artifacts in the images [42]. Although the spatial resolution will suffer from the presence of local magnetic field, spiral imaging approaches may better facilitate imaging at the skull base or regions in close proximity to the sinuses.

Functional MR imaging

Functional MR imaging is perhaps one of the best examples of converting artifacts into useful physiologic information. The probable underlying biophysical mechanisms associated with blood oxygen level dependent (BOLD) contrast have been elucidated by many investigators [43–46]. Deoxyhemoglobin behaves as a paramagnetic particle. Therefore, MR signal will be altered when its concentration is changed. With the presence of external sensory or cognitive stimuli,

regional increases of cerebral blood flow are expected whereas the cerebral metabolic rate of oxygen use remains stable, resulting in a reduction of the concentration of deoxyhemoglobin. Consequently, an increase in MR signal intensity is expected in regions where brain activation occurs. Therefore, to detect signal changes caused by physiologic alterations during brain activation, a T2*-weighted or T2-weighted sequence is commonly used.

Because it is possible to localize brain functional activation using either T2*- or T2-weighted images, the underlying biophysical mechanisms differ between the two approaches. Although it is beyond the scope of this study to discuss the underlying biophysical mechanisms, the authors address briefly the pros and cons of each method. The fundamental difference between the two approaches is that T2-weighted images are more sensitive to small vessel induced signal changes by way of diffusion whereas the T2*-weighted images are sensitive to deoxyhemoglobin-induced susceptibility effects, which have been suggested to originate from vessels with a larger caliber [47–50]. Therefore, the major advantages associated with the T2-weighted imaging approach are twofold. First, it is less sensitive to susceptibility-induced signal loss, and thus may be more suitable for fMR imaging studies near the sinuses or even brain stem. Second, it has been suggested that regions of functional activation obtained from T2-weighted images are more representative of the true origin of neuronal activation [51–53]. However, the extent to which signal changes during fMR imaging using T2-weighted images is much less when compared with T2*-weighted imaging approaches. In contrast, the T2*-weighted imaging approach offers a larger percent signal change during fMR imaging than that obtained in T2-weighted images [54] although it has been suggested that regions of activation shown in T2*-weighted images may be some distance from the true neuronal activation. A comparison is shown in Fig. 18 where a visual stimulus using a flashing checkerboard (8Hz) pattern was used. Gradient echo (Fig. 18A) and spin echo single shot EPI (Fig. 18B) sequences were used on a 3T scanner to obtain functional activation maps. The results are superimposed onto the anatomical images. It is evident that a higher percent signal change and a larger number of activated pixels are observed in gradient echo EPI images (Fig. 18A) when compared with a spin echo EPI approach (Fig. 18B). Nevertheless, a more severe signal loss near the

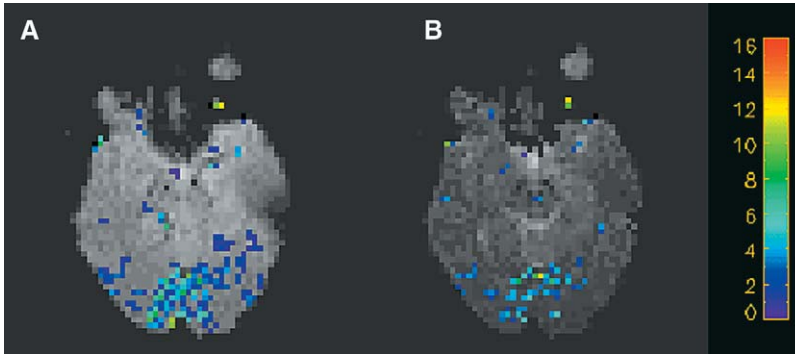


Fig. 18. Results of fMR imaging using a gradient echo EPI (A) and spin echo EPI (B) from one subject are shown. A visual stimulus using flashing checkerboard (8Hz) was used to induce brain functional activation. The color bar indicates the percent signal changes during functional activation with respect to the resting condition.

sinuses is seen in the gradient echo EPI images than the spin echo EPI images. However, because of the higher percent signal changes and the larger number of activated pixels using gradient echo EPI images, the main stream of fMR imaging studies has embraced gradient echo EPI as the method of choice to date. Therefore, the authors focus on the use of gradient echo approaches for fMR imaging.

MR signal during the resting condition can be written as

$$S(TE) = ce^{-TER2^*} \tag{13}$$

where c is a constant, including the effects of spin density, $T1$, and system related scale factors. During brain functional activation, the extent to which signal changes can be written as

$$\Delta S(TE) = c(-TE)e^{-TER2^*} \Delta R2^* \tag{14}$$

where $\Delta S(TE)$ and $\Delta R2^*$ correspond to MR signal and $R2^*$ changes between the resting and activation states. Therefore, the percent signal changes are directly proportional to TE and $\Delta R2^*$ as shown in Eq 15.

$$\frac{\Delta S(TE)}{S(TE)} = (-TE)\Delta R2^*. \tag{15}$$

Furthermore, $\Delta R2^*$ can be modeled as

$$\Delta R2^* \propto B_0 \Delta\chi \text{Hct} \Delta Y, \tag{16}$$

where B_0 is the static magnetic field, $\Delta\chi$ is the susceptibility difference between fully oxygenated and deoxygenated blood (0.18 ppm/Hct [55]), Hct

is the hematocrit, and ΔY is the changes of blood oxygenation between resting and activation conditions. Therefore, assuming the changes of the concentration of deoxyhemoglobin remain identical, the percent signal changes are expected to increase at 3T when compared with that obtained from 1.5T. Extensive results have been reported in the literature comparing fMR imaging between the widely available 1.5T and that obtained from a field strength higher than 1.5T. Nevertheless, the extent to which the increase of field strengths augment fMR imaging depends on the imaging sequences and imaging parameters used. With a conventional 2D EPI sequence, Turner et al [56] reported a percent signal change of 15.1% and 4.7% for results obtained at 4T and 1.5T, respectively at the visual cortex, indicating a 3.2-fold increase in percent signal change at 4T when compared with 1.5T. They also reported a significant increase in number of pixels of activation at 4T. However, Gati et al [57] reported smaller percentage change (1.7-fold) during functional activation as measured at the brain parenchyma when compared with results obtained from 1.5T and 4T. The observed discrepancies between the two studies are likely because of the means by which signal changes were measured. Gati et al separately measured brain parenchyma and blood vessels while a composite effect was obtained in results reported by Turner et al. Nevertheless, these findings underscore the complexity of comparing results from different field strengths and the dependence of these results on the specific image analysis procedures used.

While high field imaging seems to be advantageous for fMR imaging, particularly in augment-

ing the sensitivity to BOLD effects, several confounding factors need to be addressed. First, T1 will be increased for high field imaging, making images more sensitive to inflow effects for fMR imaging studies. In particular, 2D acquisition approaches are commonly used for fMR imaging studies. Assuming a slice thickness of 3 mm and a TR of 2 seconds are used for a typical functional MRI study, flowing spins with a velocity greater than 1.5 mm/second will be completely refreshed; slower moving spins may experience more than one rf pulse. In the event when fresh spins completely refresh an imaging voxel during one TR, the effects of inflow will not be an issue or otherwise inflow effects may also contribute to signal changes between resting and activation states, because flow is expected to increase during brain activation. This problem is likely to be more substantial at high fields since the T1 of blood will increase. Yang et al [58] used a 3D spiral multi-shot EPI approach for obtaining functional activation at 1.5T and 4T, respectively. The use of a 3D approach should greatly minimize the inflow effects during fMR imaging. They reported a smaller percent change during fMR imaging for 1.5T and 4T when compared with results reported in the literature, suggesting that inflow effects may cause an overestimate of the percent signal changes during fMR imaging, and indicating that caution should be taken in comparing percent signal changes of fMR imaging at different field strengths. Nevertheless, it has been consistently demonstrated that the percent signal changes during fMR imaging are higher as the field strength increases.

Second, as mentioned previously, the presence of local magnetic field will cause signal loss and geometric distortion, which will be more severe for high field imaging. Consequently, the regions where functional MR imaging can be confidently obtained will be limited to the anatomical regions where the magnetic field is sufficiently uniform. Several different approaches to overcome geometric distortion have been addressed previously and are applicable for functional MR imaging studies.

Finally, one of the questions remains to be addressed is what the optimal field strength is for fMR imaging if there is any. Definitive answers are yet to be seen and are dependent on the applications. Nevertheless, it has been suggested by Kruger et al [59] that the increase of physiologic noise associated with high field imaging may offset the potential advantages of conducting fMR imaging at a field strength higher than 4T. Given

the fact that high field human scanners 7T and 9.4T will be available soon, it would be of interest to make a direct comparison between the theoretical prediction and experimental results.

High resolution blood oxygen level dependent venography

To overcome the limitations of conventional MR angiography (MRA), which relies on time-of-flight (TOF) or phase contrast (PC) techniques to reveal flowing spins, Richenbach et al [60] proposed a new method that relies on BOLD contrast. This new method, high resolution BOLD venographic (HRBV) imaging [61], allows the visualization of small veins in which the flow velocity is so slow that TOF sequences would suffer from spin saturation effects, while PC images would exhibit only minimal phase shift.

The mechanisms underlying HRBV imaging can be elucidated by considering one voxel containing appreciable volumes of venous blood and brain tissue. Assuming the two compartments, namely venous blood vessel and brain tissue, are independent and have the same T2*, the equation for the signal anticipated from such a voxel can be written as:

$$S(TE) = S_0(\lambda \exp[-i\Delta\phi(TE)] + (1 - \lambda)) \times \exp[-TE/T2^*] \quad [17]$$

where S_0 is the baseline MR signal intensity, λ is the fractional volume occupied by venous blood, and $\Delta\phi(TE)$ is the phase shift of the intravascular spins, which depends linearly on echo time (TE), venous oxygenation, static field strength, and the susceptibility difference between oxygenated and deoxygenated blood. The phase shift is also dependent on the angle, θ , between the vessel axis and the main magnetic field by way of a $(\cos^2\theta - 1/3)$ term. Without losing generality, a TE can be chosen so that the phase difference ($\Delta\phi(TE)$) between the two compartments is approximately 180 degrees. In this case, the signal of the voxel will be equal to $S_0(1 - 2\lambda)$. If the authors further assume that the blood volume fraction in this voxel is 50%, the signal will be zero (Fig. 19). It is possible to choose a TE so that voxels containing appreciable volumes of venous blood and brain tissue will seem hypointense relative to the surrounding tissue.

To obtain a HRBV, a 3D sequence with velocity compensation along all three directions was used to acquire images. Phase masks were

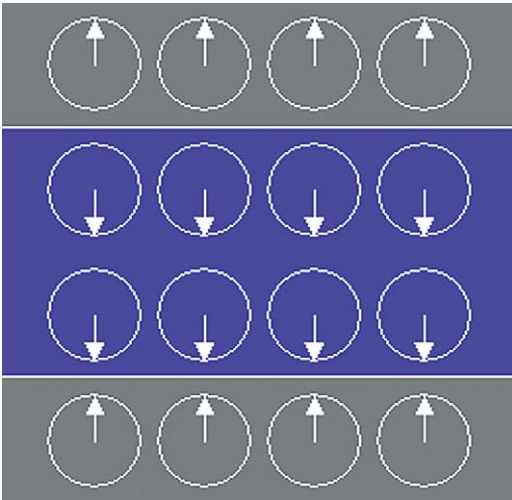


Fig. 19. A pictorial representation of a two compartment model for a voxel containing a vein (blue) and brain tissue (gray). The circles indicate the spin populations and the arrows indicate the phase angle of each spin population with arrows pointing up corresponding to 0 degree. Therefore, the overall signal of this voxel will be the vector sum of all the spin populations, which will be equal to zero in this case.

generated as proposed by Richenbach et al [60] to further improve the visibility of small venous vessels. This was done by setting all phase values between 0 to 180 degree- (π) to unity and normalizing the phase values from 0 to -180 -degree ($-\pi$) to values ranging linearly from 1 to 0 (Fig. 20). Subsequently, each magnitude image was multiplied by the corresponding phase mask four times to augment the visibility of small vessels. Finally, a minimum intensity projection (mIP) across N slices (normally 4 slices) was used to create the venogram.

A magnitude image (Fig. 20A) and its corresponding phase image (Fig. 20B) are shown in Fig. 20. Four adjacent slices were used to create mIP images as shown in Figs. 20C with and Fig. 20D without the application of phase masks. Although low intensity vascular-like structures (which are most likely intracerebral veins) are seen in Figs. 20C and D the application of the phase masks substantially improves the visibility of small venous vessels (arrow) when compared with that obtained without the phase masks.

Recently, Tong et al [62] furthermore demonstrate that HRBV also can be used to detect subtle hemorrhage in children and adolescents with diffuse axonal injury. However, in addition to

the anatomical maps of the cerebral veins that have been demonstrated in Fig. 20, the inherent sensitivity of HRBV images to blood oxygenation suggests that changes of cerebral blood oxygen saturation will likely affect the visibility of small veins in HRBV images, particularly when TE is kept as a constant. Because this hypothesis offers much intuitive appeal, such in vivo measurements are often complicated by the simultaneous change of several physiologic parameters, and to our knowledge, experimental proof of HRBV image sensitivity to venous oxygenation has not yet been presented. The authors therefore acquired HRBV images before and during experimentally induced hypercapnia in normal volunteers in an attempt to demonstrate the effect of altered cerebral blood oxygenation on HRBV images. Carbogen gas is known to be a potent vasodilator that produces significant increases in cerebral blood flow (CBF) in healthy subjects [63,64]. One consequence of the dramatic increase in CBF in the absence of a comparable increase in tissue oxygen metabolism is a decrease in the oxygen extraction fraction (OEF), and, consequently, an increase in the venous oxygenation. Thus, the authors used a well-studied gas mixture to modulate the venous oxygenation in healthy volunteers to show that a change in oxygenation of venous blood can be detected in HRBV images.

Results obtained from three subjects are shown in Fig. 21 before (upper row) and after (lower row) the onset of experimentally induced hypercapnia. The visibility of small venous vessels is substantially diminished after the onset of hypercapnia (arrows) consistently across all three subjects, suggesting that the HRBV may be useful not only for its ability to reveal small intracerebral veins, but also for its sensitivity to changes of cerebral blood oxygenation. The latter property may offer a new approach to non-invasively monitor alterations of cerebral blood oxygenation, however quantification using this approach has proven to be rather challenging.

As mentioned previously, the increase in field strength from 1.5T to 3T will improve the sensitivity to susceptibility effects such as those underlying HRBV image formation. In addition, the improved SNR at 3T should further improve the quality of HRBV images. A direct comparison of HRBV images from one subject imaged at 1.5T (Fig. 22A, B) and 3T (Fig. 22C, D) is shown in Fig. 22. Clearly, while images obtained from both field strengths exhibit small intracerebral veins, the visibility of smaller veins is greatly improved

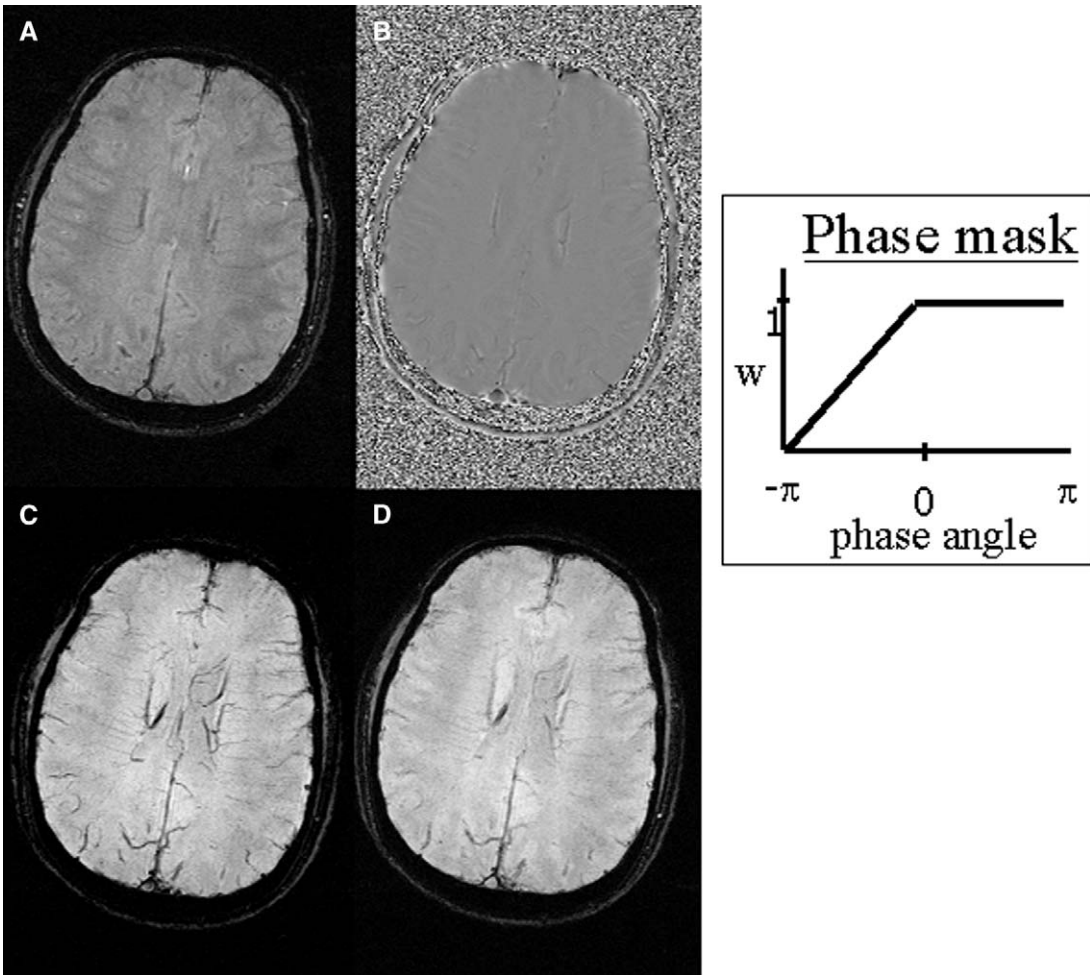


Fig. 20. A typical magnitude (A) and phase (B) images obtained using a high-resolution 3D gradient echo sequence are shown. In addition, the mIP HRBV across 4 adjacent slices with (C) and without (D) the application of the phase masks are also shown, demonstrating the improved vascular visibility with the application of phase masks. Finally, how phase masks are generated based on the phase shifts is also given.

in images obtained at 3T (arrows) compared with 1.5T.

Specific absorption rate

To excite magnetization from its equilibrium orientation (parallel to the static magnetic field) to the direction orthogonal to the direction of the static magnetic field so that MR signal can be obtained, on-resonance radiofrequency (rf) pulses will be required. The rf pulses provide the energy needed for the magnetization to change from its equilibrium state to the excited state. Consequently,

rf energy, will be deposited in the body, resulting potentially in an increase of body temperature or other harmful effects. The rate at which energy is deposited into body tissue by rf pulses during an imaging sequence is referred to as the SAR, typically specified in units of watts/kg of tissue. Obviously, it is of critical importance for the design of imaging sequences and imaging protocols to fulfill the FDA guidelines regarding SAR. Generally speaking, the energy of the radio waves increases linearly with increasing field strength (resonant frequency). At 1.5T the possibility of heating tissues is small, but one must be careful to

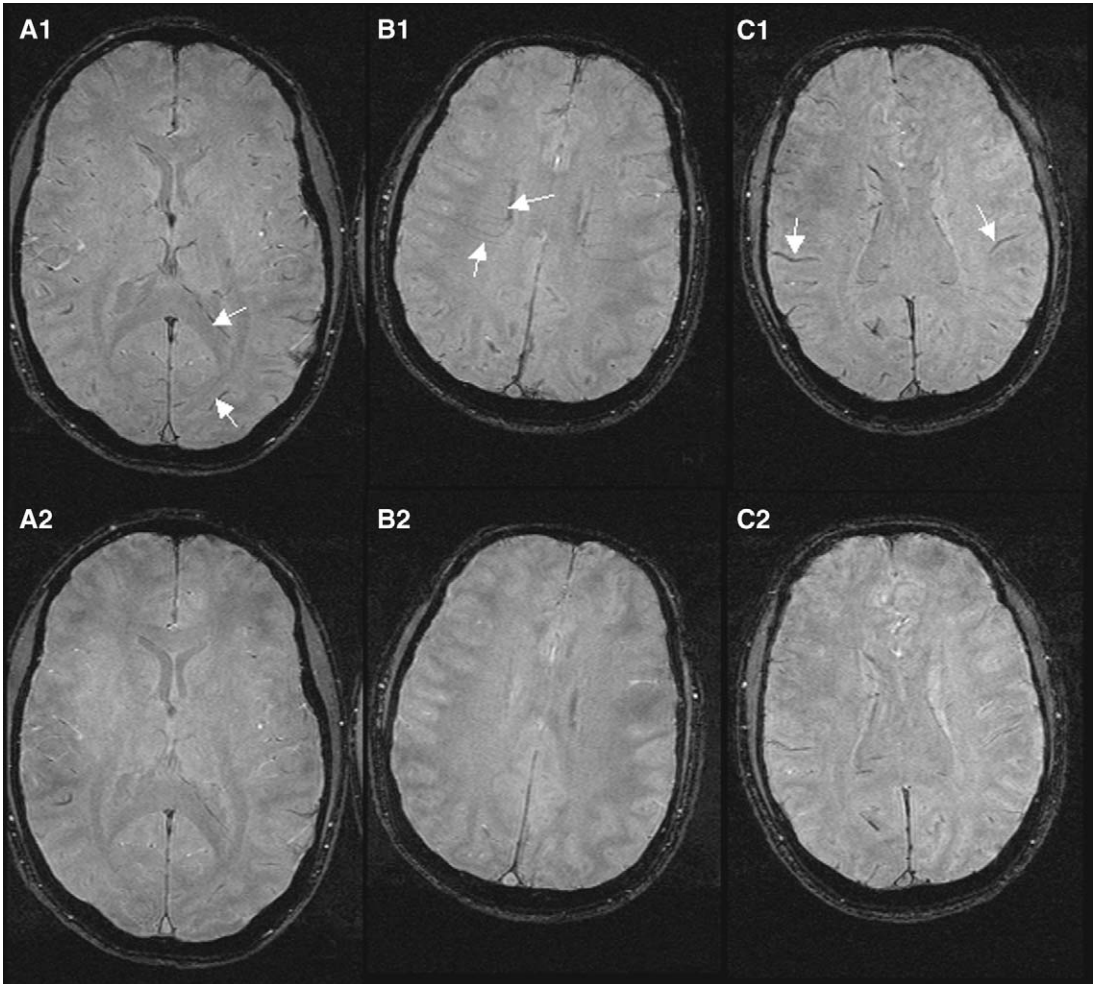


Fig. 21. A comparison of the visibility of small intracranial veins during breathing room air (*upper row*) and carbogen (*lower row*) is shown for three different subjects (*A–C*). Small intracranial veins are clearly visible (*arrows*) when subjects were breathing room air while the visibility is substantially diminished after changing the gas mixture to carbogen. This results are not surprising given the fact that carbogen will induce hypercapnia, leading to an increase of blood oxygenation in the venous vessels and thus reducing the induced-phase shifts of the venous vessels.

avoid the possibility of thermal damage to tissue at higher field. Assuming a circularly polarized coil is used for an imaging experiment, the energy deposited per unit time for a sphere with a radius of R can be rewritten as [1]

$$p = \frac{2\pi\sigma\omega^2\theta^2 R^5}{15\gamma^2\tau TR} \quad [18]$$

where σ , ω , θ , and τ , TR are the conductivity, resonance frequency, flip angle, the duration of the rf pulse, and the repetition time. It is perhaps not surprising that the energy deposit per unit

time will increase as the conductivity, resonance frequency, and flip angle increase, while an increase of TR will decrease energy deposit. In addition, note that the energy deposit is quadratically dependent on the field strength. Therefore, when the field strength increases from 1.5T to 3T, the amount of energy deposited into the body will be increased by a factor of 4, assuming an identical experimental condition.

The expected increases in SAR, imposes limitations on the number of slices that can be acquired in a given TR. In particular, fast spin-

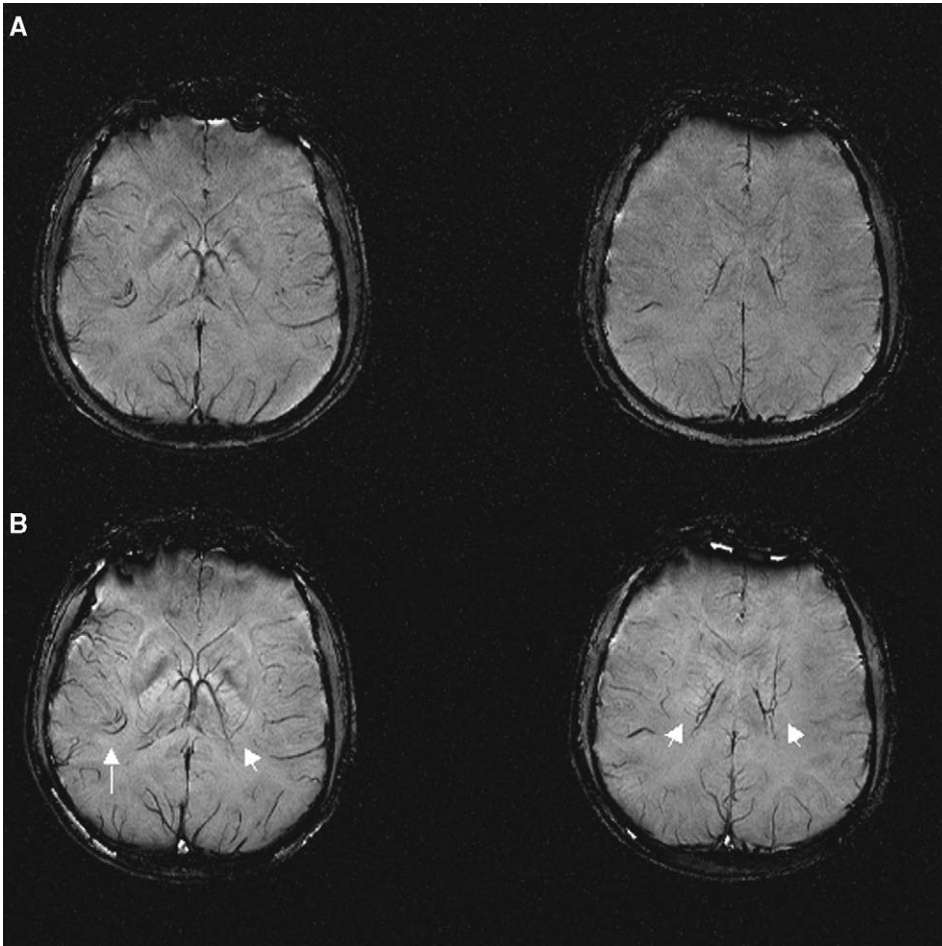


Fig. 22. A comparison of venograms obtained from the same subject at 1.5T (A) and 3T (B) is shown. It is evident that more small intracranial veins are visible (*arrows*) in results obtained from 3T when compared with that at 1.5T thanks to the increased sensitivity to BOLD effects at 3T.

echo sequences where multiple 180-degree pulses are applied within one TR are most likely to be affected by the increase of SAR, and thus the number of slices can be acquired may be reduced when compared with that obtained at 1.5T.

References

- [1] Haacke EM, Brown RW, Thompson MR, Venkatesan R. Magnetic resonance imaging: physical principles and sequence design. New York: A John Wiley and Sons; 1999.
- [2] Liem MD, Gzesh DJ, Flanders AE. MRI and angiographic diagnosis of lupus cerebral vasculitis. *Neuroradiology* 1996;38(2):134–6.
- [3] Spangler KM, et al. Arteriolar tortuosity of the white matter in aging and hypertension. A micro-radiographic study. *J Neuropathol Exp Neurol* 1994;53(1):22–6.
- [4] Jain RK. Normalizing tumor vasculature with anti-angiogenic therapy: a new paradigm for combination therapy. *Nat Med* 2001;7(9):987–9.
- [5] Alazzaz A, et al. Intracranial percutaneous transluminal angioplasty for arteriosclerotic stenosis. *Arch Neurol* 2000;57(11):1625–30.
- [6] Frangi AF, et al. Model-based quantitation of 3-D magnetic resonance angiographic images. *IEEE Trans Med Imaging* 1999;18(10):946–56.
- [7] Aylward SR, Bullitt E. Initialization, noise, singularities, and scale in height ridge traversal for tubular object centerline extraction. *IEEE Trans Med Imaging* 2002;21(2):61–75.

- [8] Bullitt E, et al. Symbolic description of intracerebral vessels segmented from magnetic resonance angiograms and evaluation by comparison with X-ray angiograms. *Med Image Anal* 2001;5(2):157–69.
- [9] Bullitt E, et al. Measuring tortuosity of the intracerebral vasculature from MRA images. *IEEE Trans Med Imaging* 2003, in press.
- [10] Bullitt E, et al. Vascular attributes and malignant brain tumors. Submitted MICCAI, 2003.
- [11] Rueckert D, et al. Nonrigid registration using free-form deformations: application to breast MR images. *IEEE Trans Med Imaging* 1999;18(8):712–21.
- [12] Zhai GH, et al. Regional differences of white matter fractional anisotropy in normal neonates but not in normal adults. *Radiology* 2003, in press.
- [13] Schmithorst VJ, et al. Correlation of white matter diffusivity and anisotropy with age during childhood and adolescence: a cross-sectional diffusion-tensor MR imaging study. *Radiology* 2002;222(1):212–8.
- [14] Neil J, et al. Normal brain in human newborns: apparent diffusion coefficient and diffusion anisotropy measured by using diffusion tensor MR imaging. *Radiology* 1998;209(1):57–66.
- [15] Mukherjee P, et al. Diffusion-tensor MR imaging of gray and white matter development during normal human brain maturation. *Am J Neuroradiol* 2002; 23(9):1445–56.
- [16] Mukherjee P, et al. Normal brain maturation during childhood: developmental trends characterized with diffusion-tensor MR imaging. *Radiology* 2001;221(2):349–58.
- [17] Basser PJ, Pierpaoli C. Microstructural and physiological features of tissues elucidated by quantitative-diffusion-tensor MRI. *J Magn Reson B* 1996; 111(3):209–19.
- [18] Arfanakis K, et al. Diffusion tensor MR imaging in diffuse axonal injury. *Am J Neuroradiol* 2002;23(5): 794–802.
- [19] Pomara N, et al. White matter abnormalities in HIV-1 infection: a diffusion tensor imaging study. *Psychiatry Res* 2001;106(1):15–24.
- [20] Taylor WD, et al. Evidence of white matter tract disruption in MRI hyperintensities. *Biol Psychiatry* 2001;50(3):179–83.
- [21] Mori S, et al. Imaging cortical association tracts in the human brain using diffusion-tensor-based axonal tracking. *Magn Reson Med* 2002;47(2): 215–23.
- [22] Slomkowski M, et al. Brain MRI hippocampal volume and prediction of clinical status in a mild cognitive impairment trial. *Neurology* 2003;60(2): 253–60.
- [23] Ward HA, et al. Hippocampal atrophy correlates with clinical features of Alzheimer disease in African Americans. *Neuroimage* 2001;14(5):1122–7.
- [24] Czobor P, et al. Neuropsychological correlates of hippocampal volumes in patients experiencing a first episode of schizophrenia. *Am J Psychiatry* 2002; 159(2):255–62.
- [25] Leserman J, et al. Reduced anterior cingulate gyrus volume correlates with executive dysfunction in men with first-episode schizophrenia. *Schizophr Res* 2000;44(1):1–10.
- [26] Szekely G, et al. Segmentation of 2-D and 3-D objects from MRI volume data using constrained elastic deformations of flexible Fourier contour and surface model. *Med Image Anal* 1996;1(1):19–34.
- [27] Kapur T, et al. Segmentation of brain tissue from magnetic resonance images. *Med Image Anal* 1996; 1(2):109–27.
- [28] Pauling L, Coryell CD. The magnetic properties and structure of hemoglobin, oxyhemoglobin and carbomonoxyhemoglobin. *Proc Natl Acad Sci USA* 1936;22:210–6.
- [29] Hunsche S, et al. Diffusion-tensor MR imaging at 1.5 and 3.0 T: initial observations. *Radiology* 2001; 221(2):550–6.
- [30] Young IR, et al. The benefits of increasing spatial resolution as a means of reducing artifacts due to field inhomogeneities. *Magn Reson Imaging* 1988; 6(5):585–90.
- [31] Haacke EM, Tkach JA, Parrish TB. Reduction of T2* dephasing in gradient field-echo imaging. *Radiology* 1989;170(2):457–62.
- [32] Cho ZH, Ro YM. Reduction of susceptibility artifact in gradient-echo imaging. *Magn Reson Med* 1992;23(1):193–200.
- [33] Frahm J, Merboldt KD, Hancike W. Direct FLASH MR imaging of magnetic field inhomogeneities by gradient compensation. *Magn Reson Med* 1988;6(4):474–80.
- [34] Yang QX, et al. Multi-gradient echo with susceptibility inhomogeneity compensation (MGESIC): demonstration of fMRI in the olfactory cortex at 3.0 T. *Magn Reson Med* 1997;37(3):331–5.
- [35] Constable RT, Spencer DD. Composite image formation in z-shimmed functional MR imaging. *Magn Reson Med* 1999;42(1):110–7.
- [36] Glover GH. 3D z-shim method for reduction of susceptibility effects in BOLD fMRI. *Magn Reson Med* 1999;42(2):290–9.
- [37] An H, Lin W. Cerebral oxygen extraction fraction and cerebral venous blood volume measurements using MRI: effects of magnetic field variation. *Magn Reson Med* 2002;47:958–66.
- [38] Cusack R, Brett M, Osswald K. An evaluation of the use of magnetic field maps to undistort echo-planar images. *Neuroimage* 2003;18(1):127–42.
- [39] Zeng H, Constable RT. Image distortion correction in EPI: comparison of field mapping with point spread function mapping. *Magn Reson Med* 2002; 48(1):137–46.
- [40] Sutton BP, Noll DC, Fessler JA. Fast, iterative, field-corrected image reconstruction for MRI. *IEEE Trans Med Imaging* 2003;22(2):178–88.
- [41] Ahn CB, Kim JH, Cho ZH. High speed spiral-scan echo planar imaging. *IEEE Transactions on Medical Imaging* 1986;5:2–7.

- [42] Noll DC, et al. Deblurring for non-2D Fourier transform magnetic resonance imaging. *Magn Reson Med* 1992;25(2):319–33.
- [43] Ogawa S, Lee TM. Magnetic resonance imaging of blood vessels at high fields: in vivo and in vitro measurements and image simulation. *Magn Reson Med* 1990;16(1):9–18.
- [44] Ogawa S, et al. Brain magnetic resonance imaging with contrast dependent on blood oxygenation. *Proc Natl Acad Sci (USA)* 1990;87(24):9868–72.
- [45] Ogawa S, Lee TM, Barrere B. The sensitivity of magnetic resonance image signals of a rat brain to changes in the cerebral venous blood oxygenation. *Magn Reson Med* 1993;29(2):205–10.
- [46] Ogawa S, et al. Oxygenation-sensitive contrast in magnetic resonance image of rodent brain at high magnetic fields. *Magn Reson Med* 1990;14(1):68–78.
- [47] Kennan RP, Zhong J, Gore JC. Intravascular susceptibility contrast mechanisms in tissues. *Magn Reson Med* 1994;31(1):9–21.
- [48] Boxerman JL, et al. MR contrast due to intravascular magnetic susceptibility perturbations. *Magn Reson Med* 1995;34(4):555–66.
- [49] Boxerman JL, et al. The intravascular contribution to fMRI signal change: Monte Carlo modeling and diffusion-weighted studies in vivo. *Magn Reson Med* 1995;34(1):4–10.
- [50] Jones RA. Origin of the signal undershoot in BOLD studies of the visual cortex. *NMR Biomed* 1999;12(5):299–308.
- [51] Hutchinson M, et al. Segmentation analysis in functional MRI: activation sensitivity and gray-matter specificity of RARE and FLASH. *J Magn Reson Imaging* 1997;7(2):361–4.
- [52] Thulborn KR, et al. High-resolution echo-planar fMRI of human visual cortex at 3.0 tesla. *NMR in Biomedicine* 1997;10:183–90.
- [53] Lee SP, et al. Diffusion-weighted spin-echo fMRI at 9.4 T: microvascular/tissue contribution to BOLD signal changes. *Magn Reson Med* 1999;42(5):919–28.
- [54] Lowe MJ, et al. Quantitative comparison of functional contrast from BOLD-weighted spin-echo and gradient-echo echoplanar imaging at 1.5 Tesla and H₂ 15O PET in the whole brain. *J Cereb Blood Flow Metab* 2000;20(9):1331–40.
- [55] Weisskoff RM, Kühne S. MRI susceptometry: image-based measurement of absolute susceptibility of MR contrast agents and human blood. *Magn Reson Med* 1992;24(2):375–83.
- [56] Turner R, et al. Functional mapping of the human visual cortex at 4 and 1.5 tesla using deoxygenation contrast EPI. *Magn Reson Med* 1993;29(2):277–9.
- [57] Gati JS, et al. Experimental determination of the BOLD field strength dependence in vessels and tissue. *Magn Reson Med* 1997;38(2):296–302.
- [58] Yang Y, et al. Comparison of 3D BOLD functional MRI with spiral acquisition at 1.5 and 4.0 T. *Neuroimage* 1999;9(4):446–51.
- [59] Kruger G, Kastrup A, Glover GH. Neuroimaging at 1.5 T and 3.0 T: comparison of oxygenation-sensitive magnetic resonance imaging. *Magn Reson Med* 2001;45(4):595–604.
- [60] Reichenbach JR, Modder U. Small vessels in the human brain: MR venography with deoxyhemoglobin as an intrinsic contrast agent. *J Comput Assist Tomogr* 1997;21(6):857–66.
- [61] Reichenbach JR, et al. High-resolution blood oxygen-level dependent MR venography (HRBV): a new technique. *Neuroradiology* 2001;43(5):364–9.
- [62] Tong KA, et al. Hemorrhagic shearing lesions in children and adolescents with posttraumatic diffuse axonal injury: improved detection and initial results. *Radiology* 2003;227:332–9.
- [63] Grubb RL Jr, et al. The effects of changes in PaCO₂ on cerebral blood volume, blood flow, and vascular mean transit time. *Stroke* 1974;5(5):630–9.
- [64] Bayerle-Eder M, et al. Hypercapnia-induced cerebral and ocular vasodilation is not altered by glibenclamide in humans. *Am J Physiol Regul Integr Comp Physiol* 2000;278(6):R1667–73.



MR microscopy of normal human brain

Girish M. Fatterpekar, MD^a, Bradley N. Delman, MD^a,
William W. Boonn, MD^{a,b}, S. Humayun Gultekin, MD^c,
Zahi A. Fayad, PhD^{a,d}, Patrick R. Hoff, MD^e,
Thomas P. Naidich, MD^{a,f,*}

^a*Department of Radiology, Box 1234, The Mount Sinai School of Medicine,
One Gustave L. Levy Place, New York, NY 10029, USA*

^b*Department of Radiology, University of Pennsylvania Hospital, Philadelphia, PA, USA*

^c*Division of Neuropathology, The Mount Sinai Medical Center, New York, NY, USA*

^d*The MRI Research Laboratory, The Mount Sinai Medical Center, New York, NY, USA*

^e*The Kastor Neurobiology of Aging Laboratories and Fishberg Research Center for Neurobiology,
The Mount Sinai Medical Center, New York, NY, USA*

^f*Department of Neurosurgery, The Mount Sinai Medical Center, New York, NY, USA*

MR imaging of formalin-fixed specimens of the brain and spinal cord at 9.4 Tesla now provides images with an in-plane resolution of 40×40 to 70×70 microns and a slice thickness of 300 to 500 microns. Such images mimic the appearance of neural tissue on light microscopy, and may properly be designated MR microscopy (MRM) [1–4]. This article reviews MRM of selected portions of the normal adult brain including: cerebral cortex (motor, sensory and association isocortex; allocortex; and juxta-allocortex), basal ganglia (caudate, putamen, and globus pallidus externa and interna), thalamus, subthalamus, metathalamus, cerebellar cortex, and roof nuclei of the fourth ventricle.

In each case, the anatomic material was obtained from cadavers of adult humans who died of unrelated causes. The imaging studies were performed on formalin-fixed samples of that material, using a Brüker 9.4T superconducting magnet with microimaging (Brüker Analytik, Rheinstetten, Germany), an 89 mm bore, a 25 mm bird cage coil, and intermediate-weighted pulse sequences (repetition time [TR] = 2400 milliseconds, echo time [TE] = 45 milliseconds, Nex = 100, section thickness 500 microns, field of view 20×20 mm, data matrix 256×256 , and antialiasing factor 1). Following scanning, each specimen was processed for light microscopy with Nissl and Luxol Fast Blue stains to display the neurons and myelin, respectively. The histologic images were then correlated with the MRM obtained at the same level to determine the histopathologic bases for the magnetic resonance appearance.

Cerebral cortex

The human cerebral cortex is divided into three major cytoarchitectural types: the six-layered neocortex, the cytoarchitecturally-distinct allocortex, and the intervening transitional periallocortex (juxta-allocortex). The neocortex (synonym: isocortex) forms most of the cerebral

Portions of this material were presented at the 87th Scientific Assembly and Annual Meeting of the Radiological Society of North America (2001), at the 39th (2001) and 40th (2002) Annual Meetings and Scientific Assemblies of the American Society of Neuroradiology, and in the American Journal of Neuroradiology 2002; 23:1313–21.

* Corresponding author. Department of Radiology, Box 1234, The Mount Sinai School of Medicine, One Gustave L. Levy Place, New York, NY 10029.

E-mail address: Thomas.naidich@mounsinai.org (T.P. Naidich).

cortex. The allocortex forms the olfactory cortex and hippocampal formation. The periallocortex forms the retrosplenial region, the anterior cingulate cortex, and the ectosplenial cortex [5–24].

The neocortex

The neocortex displays a characteristic horizontal lamination. This lamination is conceptualized as having six basic layers, with variable degrees of specialization for motor and sensory function (Fig. 1). Intermediate-weighted MR microscopy displays the laminar pattern as corresponding layers of differing signal intensities. In these images, regions with greater cell density or of more prominent myelination display lower signal intensity.

From the pial surface to the underlying white matter, the six layers of the human neocortex (Fig. 2) can be identified as:

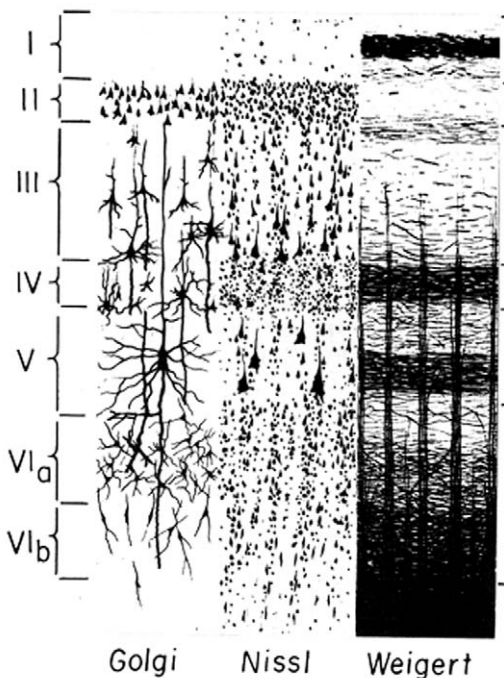


Fig. 1. Human cerebral isocortex. Diagrammatic representation of cortical lamination. Column (A, left). Golgi silver stain displays the full extent of the axons, dendrites, and cell bodies of the individual neurons; Column (B) Middle. Nissl stain displays the granular endoplasmic reticulum within the cell bodies of neurons; Column (C, Right). Weigert stain displays myelin. (From Carpenter MB, Sutin J, editors. Human neuroanatomy. Baltimore: Williams & Wilkins; 1983, with permission.)

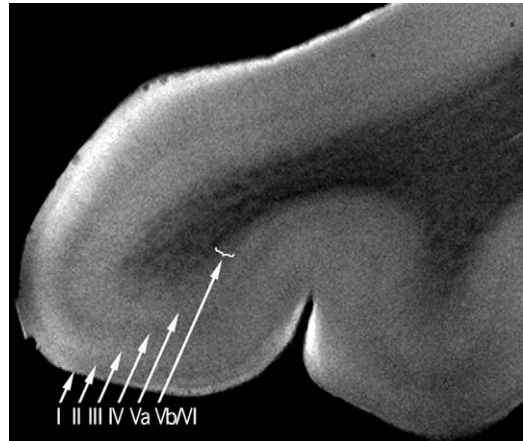


Fig. 2. Homotypical isocortex (frontal pole). The frontal polar cortex displays the characteristic six-layers of the isocortex. The signal intensity varies directly in proportion to the cell concentration and myelin distribution.

Layer I, the molecular layer (plexiform layer), is a cell-sparse layer that appears bright on IW-MRM.

Layer II, the external granular cell layer, consists primarily of closely packed granule cells, and is shown as a band of intermediate gray signal on IW-MRM.

Layer III, the external pyramidal cell layer, is composed predominantly of pyramidal cells with scattered non-pyramidal cells. Layer III is divided into sublayers IIIa (superficial), IIIb (intermediate) and IIIc (deep). On IW-MRM, layer III appears as a homogenous layer brighter than the superjacent layer II.

Layer IV, the internal granular cell layer, is the narrowest of the cellular laminae, and is composed of stellate cells and granule cells. It is subdivided into a superficial sublayer (IVa), and a deep sublayer (IVb). Layer IVb is permeated by a dense plexus of myelinated fibers designated the external band of Baillarger. The dense myelination causes Layer IVb to appear dark on MRM. Because the whole layer has a narrow caliber, however, it is difficult to differentiate IVa from IVb on IW-MRM, so layer IV appears as a sharply defined, dark gray to black band. The primary visual (calcarine) cortex contains the thickest external band of Baillarger of any cortex in the cerebrum. For that reason layer IVb of the calcarine cortex is written with a capital letter B as layer IVB. Layer IVB forms the prominent line of

Gennari, which gives the calcarine cortex its alternate name: striate cortex (Fig. 3).

Layer V, the internal pyramidal cell layer, contains both large pyramidal cells and scattered non-pyramidal cells. Like Layer IV, it is subdivided into superficial (Va) and deep portions (Vb). Layer Vb also is permeated by a plexus of myelinated fibers designated the *internal* band of Baillarger. However, the internal band of Baillarger (Layer Vb) is much thinner and forms a less densely interwoven plexus of myelinated fibers than does layer IVb. On MRM, layer Va can be distinguished as a bright band just deep to layer IV. Layer Vb appears dark, because of the presence of the myelinated internal band of Baillarger, and merges into the dark band formed by the subjacent layer VI.

Layer VI, the multiform layer (fusiform or pleomorphic layer) is composed predominantly of spindle-shaped cells with interspersed fiber bundles. On IW-MRM, it is seen as a dark gray zone that blends with the

still-darker underlying white matter at the subcortical arcuate “U” fibers.

Variations in the neuronal distribution and myelin connections within the cortex are used to define the cytoarchitecture of each cortical region [5,11]. Neocortex in which all six layers are distinct and well defined is designated homotypical cortex. Neocortex in which one or more of the layers show specialized modifications is designated heterotypical cortex. Von Economo [25] classified the cerebral neocortex into five different Types designated: (1) Agranular, (2) Frontal, (3) Parietal, (4) Polar, and (5) Granular. Neocortical types 2, 3, and 4 are homotypical; Neocortical types 1 and 5 are heterotypical. Type 1 agranular cortex is specialized as a motor cortex with markedly diminished granular laminae (II and IV) and marked expansion of pyramidal neurons in layers III and V. In agranular neocortex, therefore, MRM shows poor definition of the individual cell layers and dense confluence of layers III and V. The precentral gyrus is the classic example of type 1 agranular neocortex (Fig. 4) [26]. Type 2 frontal type neocortex is thick and shows all the six layers well. Type 3 parietal neocortex also shows all six layers but is even more distinctive, because the two-granule cell layers II and IV have greater thickness and cell density. Type 4 polar neocortex still exhibits the six basic layers, but is thinner overall, and has a wealth of granule cells. Type 5 granular cortex is specialized as sensory cortex with maximally developed granular layers II and IV and poorly developed pyramidal layers III and V. Examples of granular cortex include the primary visual (calcarine) cortex (see Fig. 3), the primary somatosensory cortex of the postcentral gyrus (see Fig. 4), and the primary auditory cortex of Heschl’s gyrus (Fig. 5).

Brodmann recognized specific patterns of variation in the cortical cytoarchitecture, parcellated the cortex into cytoarchitectonic areas, numbered them, and tried to correlate their cortical architecture with function [24]. These regions are now designated as Brodmann areas (BA). Later investigators have redefined these initial divisions [25–40].

The allocortex

The allocortex includes the hippocampus proper, the dentate gyrus, and the olfactory cortex [8].

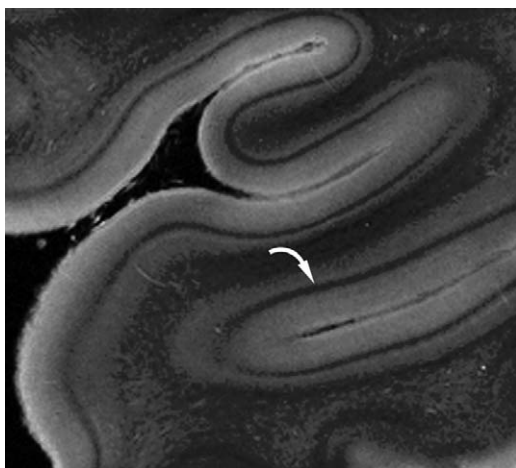


Fig. 3. Heterotypical sensory isocortex (calcarine cortex). Layer IVb contains the dense heavily myelinated plexus (external band of Baillarger) and appears as a prominent, dark gray band (curved arrow) on IW-MRM. Note that the cortex is normally thickest at the crown of the gyrus and thinnest at the depth of the sulcus. As judged from the position of layer IVb, this variation in cortical thickness can be seen to be because of changes in the thickness of layers V and VI, deep to the external band of Baillarger, rather than to variation in the thickness of the superficial layers I, II and III.

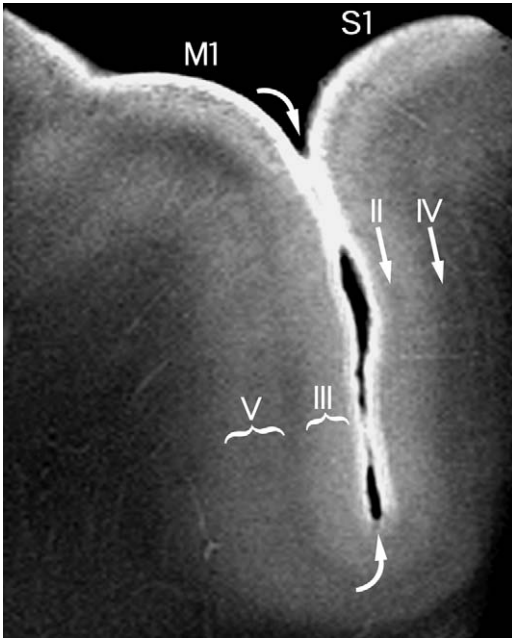


Fig. 4. Heterotypical sensorimotor isocortex cortex. (M1) Agranular (Motor) Cortex (Precentral gyrus). The agranular cortex is characterized by thick pyramidal cell layers III and V and very thin granular cell Layers II and IV. Layer IV is not easily appreciated, because it so thin. (S1) Granular Isocortex Cortex (Postcentral gyrus). The granular cortex is characterized by thick granular layers II and IV and thin pyramidal layers III and V. Note that the overall thickness of the gyrus, of the white matter, and of the cortex is greater in the precentral gyrus than in the postcentral gyrus. The curved arrow indicates the central sulcus.

Hippocampus proper (cornu ammonis CA1 to CA4)

From the ventricular cavity to the hippocampal sulcus, the cornu ammonis may be divided into six layers: the alveus, stratum oriens, stratum pyramidale, stratum radiatum, stratum lacunosum, and stratum moleculare (Fig. 6).

The alveus is a thin subependymal layer of white matter that is seen as a sharply marginated band of low signal on IW-MRM.

The stratum oriens is composed of scattered neurons (basket cells) crossed by axons from the adjacent stratum pyramidale. On IW-MRM, the stratum oriens is seen as a bright band that is difficult to differentiate from the underlying stratum pyramidale.

The stratum pyramidale is composed of prominent pyramidal cells and is organized into four cell fields, designated CA1 to CA4. On IW-

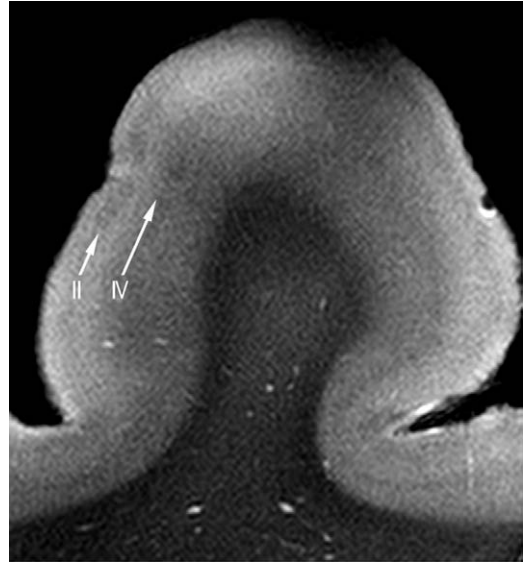


Fig. 5. Heterotypical sensory isocortex (Primary auditory cortex—Heschl's gyrus). This cortex is characterized by extreme prominence of the granular cell layers II and IV. These form two broad gray bands that give the cortex a speckled "dust-like" appearance that is designated koniocortex.

MRM, the stratum pyramidale is seen as a curvilinear bright band coursing lateral to the underlying gray stratum radiatum.

The stratum radiatum contains apical dendrites that arise from the pyramidal neurons of the stratum pyramidale. These dendrites display a parallel configuration that gives the layer its name. On MRM, the stratum radiatum appears as a nearly homogenous gray band.

The stratum lacunosum contains numerous fascicles of axons from the perforating fibers and the Schaffer collaterals. These course parallel to the surface of the cornu ammonis. On IW-MRM, the stratum lacunosum is seen as a thin dark gray band interposed between the stratum radiatum and stratum moleculare.

The stratum moleculare lies just lateral to the hippocampal sulcus. It contains only a few neurons and dendritic connections to the adjacent layers. On IW-MRM, the stratum moleculare is seen as a grayish heterogenous band interposed between the dark stratum lacunosum and dark hippocampal sulcus.

The cornu ammonis (CA) demonstrates a smoothly varying signal intensity because of regional differences in the size and density distribution of its pyramidal neurons [29,30].

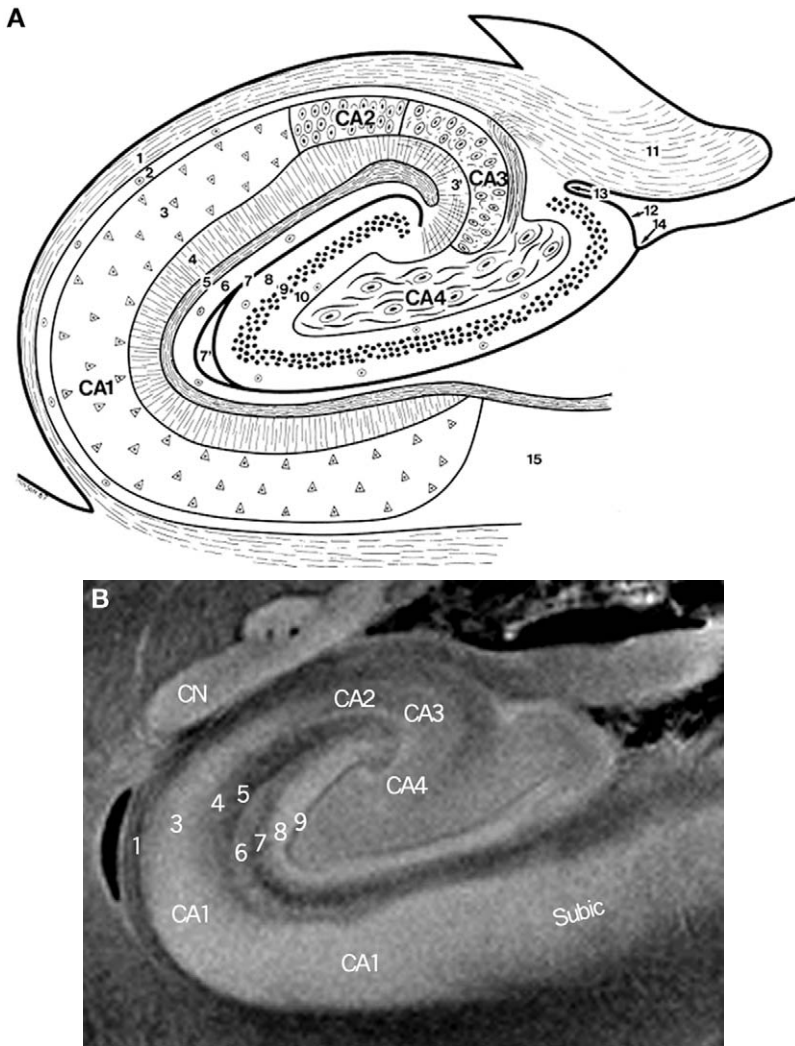


Fig. 6. Hippocampal formation—transverse section (A) diagram and (B) MRM. From lateral to medial, IW-MRM displays the layers of the hippocampal formation. 1. alveus, 2. stratum oriens—not distinctly seen on MRM, 3. stratum pyramidale—organized into four fields (CA1 to CA4) whose signal intensity varies in proportion to their cell densities, 4. stratum radiatum (*inhomogeneously gray*) 5. stratum lacunosum (*thin dark gray layer*) 6. stratum moleculare (*bright gray*) 7. hippocampal sulcus (*dark gray*) 8. stratum moleculare (*bright*) 9. stratum granulosum (*dark gray*) 10. polymorphic layer (*thin bright layer*) interposed between the dark stratum granulosum and the gray band of CA4. CN, caudate nucleus; subic, subiculum. Diagram (A) (From Duvernoy HM. The human hippocampus: an atlas of applied anatomy. Munich: J. F. Bergmann Verlag; 1988, with permission).

CA1 consists of scattered pyramidal cells and is seen as a bright band continuous with the subiculum. CA2 consists of a narrow band of densely packed pyramidal cells and is seen as a narrow darker gray band, distinct from the broader, brighter band of CA1. CA3 corresponds to the curve or the genu of the cornu ammonis as

it enters the concavity of the dentate gyrus. The bodies of the pyramidal cells of CA3 are more loosely packed than the bodies of the pyramidal cells of CA2 (ie, has lower cell density), so CA3 appears as a curvilinear gray band that is brighter than CA2. CA4 lies within the concavity of the dentate gyrus and contains scattered large ovoid

pyramidal cells and myelinated fibers, On IW-MRM, the more loosely packed cells of CA4 make CA4 appear a brighter gray than CA3.

Dentate gyrus

From the hippocampal sulcus to the Cornu Ammonis, the three strata of the dentate gyrus are designated the stratum moleculare, the stratum granulosum, and the polymorphic layer.

The stratum moleculare is thick, contains few granule cells, lies just deep to the hippocampal sulcus, and appears as a bright layer on IW-MRM.

The stratum granulosum (dentate granule cell basket) is a thin, sharply defined layer of densely packed, small, round, granule cells nearly devoid of myelin. On MRM, this appears as a thin, finely delineated, characteristically curvilinear dark gray band.

The polymorphic layer is the thinnest of the three dentate layers. It contains the axons that cross from the granule cell neurons of the dentate gyrus to the hippocampus proper. On IW-MRM, the polymorphic layer is seen as a thin bright band situated between the dark stratum granulosum and the Cornu Ammonis (CA4).

The transitional cortex

Transitional cortex (periallocortex, juxta-allo-cortex) is found in the retrosplenial region (BA 29 and 30), the anterior cingulate cortex (BA 23, 24a-c, and 25), and the ectosplenial cortex of area 26 (Fig. 7) [19,34,39,40]. This cortex shows features intermediate between allocortex and neocortex. In this region, the overall thickness of the cortex increases and the cortical layers begin to show individual definition.

Cerebellar cortex

The cerebellar cortex has three main strata, the molecular layer, the Purkinje cell layer, and the granular cell layer (Fig. 8) [11].

Molecular layer

The molecular layer is almost featureless, contains a sparse population of neurons and their fiber connections, and appears homogeneously bright on IW-MRM.

Purkinje cell layer

The Purkinje layer contains the large pear-shaped perikarya of the Purkinje cells, and

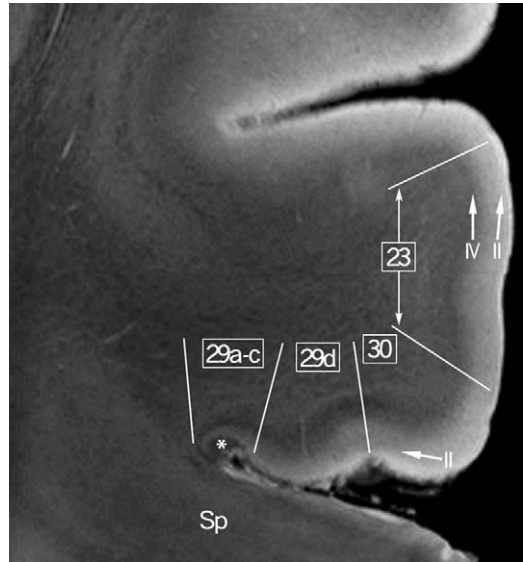


Fig. 7. Transitional cortex. IW-MRM demonstrates progressive thickening and increasing definition of the individual cortical layers as one proceeds from the periallocortical regions (BA 29, 30) into the adjacent isocortex (BA 23). BA 29 (a-c) is characterized by a thin cortex with prominent myelination (asterisk) in layer I. BA 30 shows emergence of a well-defined layer II, seen as a gray band, but no layer IV. In BA 23, layer IV also becomes definite and may be appreciated as a band of gray signal interposed between the bright layers III and V.

epithelial (Bergmann) glial cells. It appears as a band of intermediate gray signal on IW-MRM.

Granular cell layer

The granular layer contains a wealth of granular neurons and their fiber connections. On IW-MRM, it appears as a band of intermediate gray signal indistinguishable from the Purkinje layer.

Cerebellar nuclei

Four deep cerebellar nuclei are arrayed around the roof of the 4th ventricle on each side (Fig. 9). Closest to the midline dorsally are the paired fastigial nuclei. Next-most laterally and ventrally are the “interposed nuclei”, composed of the paired globose nuclei (more medially) and the paired emboliform nuclei (more laterally). Furthest laterally and ventrally are the largest pair of cerebellar nuclei designated the dentate nuclei. The dentate nuclei take the form of irregularly folded sheets of neurons, which encompass a mass of white fibers designated the “hilum”. The hilar

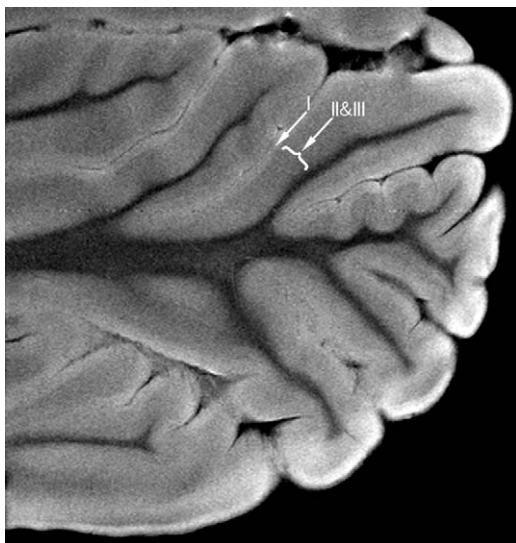


Fig. 8. Cerebellar cortex. From superficial to deep, IW-MRM displays the Molecular layer I: (*bright*) the Purkinje layer II: (*intermediate gray*) and the Granular cell layer III: (*intermediate gray*) indistinguishable from the superjacent layer II. The arbor vitae (central white matter) of the cerebellum branches extensively within the folia.

fibers extend cephalically to form a major portion of the superior cerebellar peduncles.

Basal ganglia

The basal ganglia constitute most of the subcortical gray matter and include the corpus striatum, the pallidum, the claustrum, and the amygdaloid complex [11]. The corpus striatum is divided into a larger dorsal division composed of the caudate nucleus and the putamen (Fig. 10) and a smaller ventral division composed of the nucleus accumbens septi and the olfactory tubercle (Fig. 11). The internal capsule extends through the basal ganglia as groups of fibers (fascicles) that *partially* subdivide the caudate from the putamen. Between the fascicles of the internal capsule, strands of gray matter (designated caudato-lenticular bridges of gray) still connect the caudate nucleus with the putamen “across” the internal capsule. The alternating layers of white fascicles and gray bridges form the stripes that give the caudate plus putamen the name: corpus striatum.

The globus pallidus forms the smaller inner portion of the lentiform nucleus. It is part of the basal ganglia, but not part of the corpus striatum.

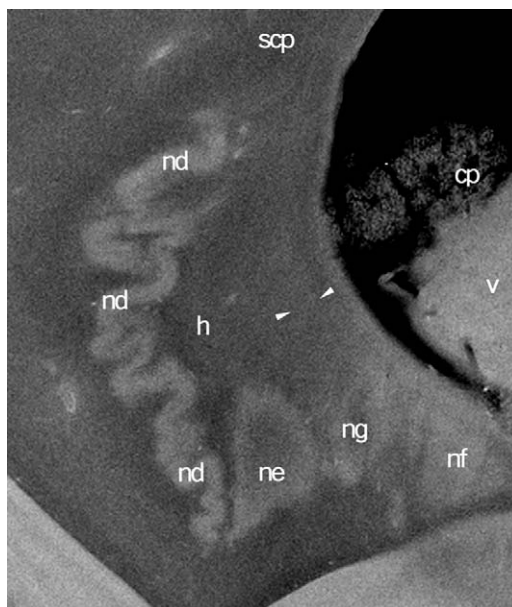


Fig. 9. Cerebellar nuclei. IW-MRM displays the cerebellar nuclei and key tracts arising from them: nd, nucleus dentatus; ne, nucleus emboliformis; nf, nucleus fastigii; ng, and nucleus globosus. The truncus uncinatus (*between arrowheads*) is composed primarily of the outflow tracts from the fastigial nuclei. The truncus uncinatus encircles the superior cerebellar peduncle (SCP, poorly identified) and projects to the reticular formation and the magnocellular vestibular nuclei. cp, choroids plexus; H, “hilus”; v, vermis; within the fourth ventricle.

The globus pallidus is subdivided into the globus pallidus externa and the globus pallidus interna. The external medullary lamina of the lentiform nucleus separates the globus pallidus externa from the putamen. The internal medullary lamina of the lentiform nucleus separates the globus pallidus externa from the globus pallidus interna.

The fiber connections arising from the basal ganglia arise as the thin radial fascicles of the caudate nuclei, the radial fascicles of the lenticular nuclei, and the radial fascicles of the globi pallidi and contribute to form the large fascicular outflow tracts designated the ansa lenticularis (AL), the fasciculus lenticularis (FL), and the fasciculus subthalamicus (FS) (Figs. 10, 12).

Thalamus

The thalamus is composed of masses of gray matter that are partitioned into separate groups of nuclei by thin sheets of white matter (the medullary

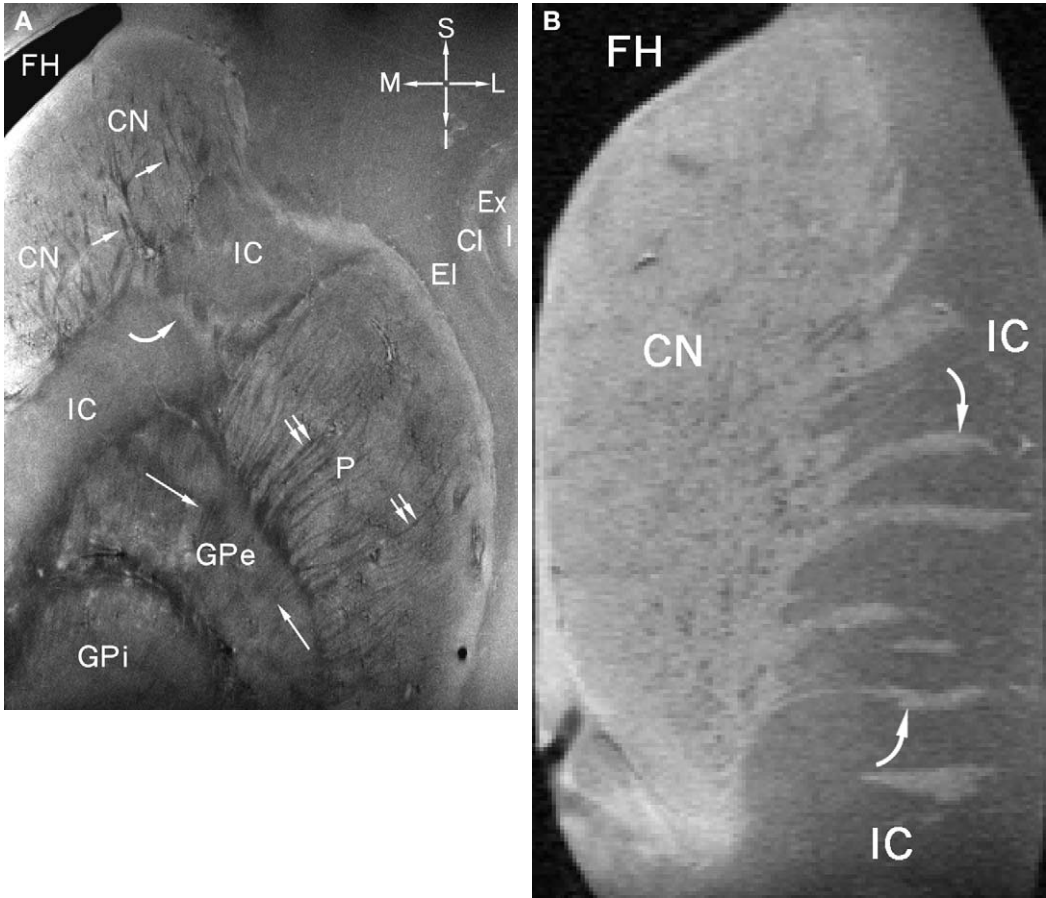


Fig. 10. Dorsal striatum. (A) Coronal IW-MRM demonstrates the caudate nucleus (CN) and the lentiform nucleus (LN) separated by the internal capsule (IC). The caudatolenticular bridges (*curved arrow*), seen better in (B) appear as short gray bands that connect the caudate and the putamen between individual fascicles of the internal capsule. The thin fasciculi radialis nuclei caudati (*single small arrows*), the fasciculi radialis nuclei lenticularis (*small double arrows*), and the fasciculi radialis pallidi (*long white arrows*) form part of the fascicular outflow tracts. CI, claustrum; EI, external capsule; Ex, extreme capsule; FH, frontal horn; GPe, globus pallidus externa; GPi, globus pallidus interna; I, insula; P, putamen.

laminae of the thalamus) (Fig. 13). The lateral surface of the thalamus is covered by the external medullary lamina. The interior of the thalamus is subdivided into major (and additional minor) nuclear groups by a vertically-oriented, Y-shaped internal medullary lamina. The thalamic nuclei may be grouped in diverse ways. In this report, they are considered to form three major groups of nuclei: the medial, the anterior, and the ventrolateral nuclear groups. The medial group lies medial to the internal medullary lamina and consists predominantly of the medial nucleus (dorsomedial nucleus). The anterior group lies within the opening arms of the Y-shaped internal medullary lamina, and consists predominantly of the large

anteroventral nucleus. The ventrolateral group forms the bulk of the lateral thalamus between the external medullary lamina and the internal medullary lamina. This group is further subdivided into lateral and ventral nuclear groups. The lateral group contains the lateral dorsal nucleus, the lateral posterior nucleus, and the pulvinar. The ventral nuclear group contains the ventral anterior nucleus, the ventral lateral nuclear complex and the ventral posterior nuclear complex.

Within the external medullary lamina there is an additional small group of reticular thalamic nuclei. Within the internal medullary lamina are a number of intralaminar nuclei, including the centromedian nucleus and small groups of anterior

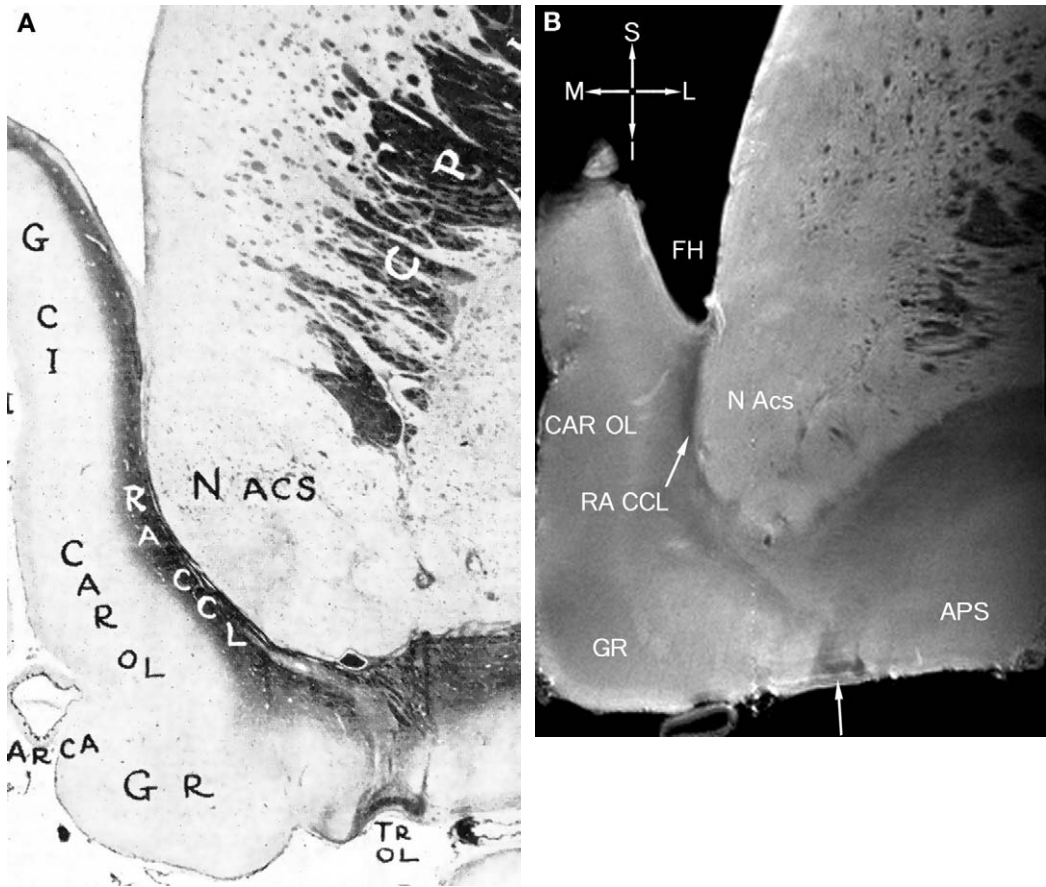


Fig. 11. Ventral striatum. (A) coronal myelin stain. (B) IW-MRM. Coronal IW-MRM demonstrates the nucleus accumbens (N Acs) as a bright structure situated just lateral to the “darkish gray” radiations of the corpus callosum (RA CCL). The olfactory tubercle (*arrow*) appears as a gray zone interposed between the gyrus rectus (GR) medially and the bright anterior perforated substance (APS) laterally. GCI, cingulate gyrus; CAROL, Carrefour olfactif, the junction of the gyrus rectus with the cingulate gyrus FH, frontal horn. (A) (From Riley HA. An atlas of basal ganglia, brainstem and spinal cord. Connecticut: Williams and Wilkinson, 1943, with permission.)

and posterior intralaminar nuclei. Far medially, a group of midline thalamic nuclei lie along the wall of the third ventricle and within the massa intermedia. The superior surface of the thalamus is covered by a thin sheet of white matter designated the striatum zonale.

The thalami are crossed superiorly by the paired striae medullares thalami that course anteroposteriorly to interconnect the septal region with the habenular nuclei. The thalami are pierced by the mammillothalamic tracts that ascend from the mammillary bodies to the anterior nuclei.

The major nuclear groups of the thalamus are successfully displayed by IW-MRM (Fig. 14).

Medial thalamic nuclei

On IW-MRM, the medial nucleus is seen as a large indistinct bright structure delimited laterally by the internal medullary lamina and medially by the midline thalamic nuclei.

Anterior thalamic nuclei

IW-MRM clearly displays the anteroventral nucleus as a large bright ovoid structure delimited laterally by the curvilinear gray mammillothalamic fasciculus and delimited superomedially by the stria medullaris thalami.

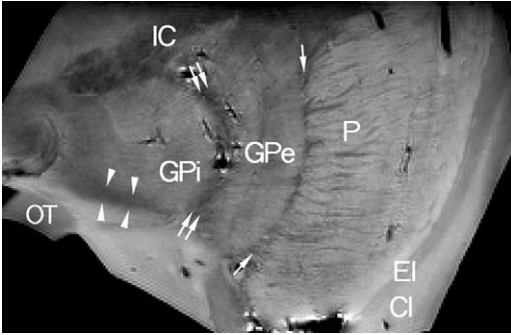


Fig. 12. Pallidum and ansa lenticularis. From lateral to medial, IW-MRM displays the inhomogenously gray putamen (P), dark external medullary lamina (*short single arrows*), gray globus pallidus externa (GPe), dark internal medullary lamina (*short double arrows*), and the gray globus pallidus interna (Gpi) of the lenticular nucleus. The ansa lenticularis (AL) (*arrowheads*) appears as a thin curvilinear gray band just inferior to the globus pallidus and superior to the optic tract (OT). FH: Frontal horn, IC: Internal capsule, Cl: Claustrum, and EL: External capsule.

Lateral thalamic nuclei

The lateral thalamic nuclei lie directly on the lateral surface of the internal medullary lamina behind the union of its open arms. The small lateral dorsal nucleus lies at and behind the open arms of the internal medullary lamina. The small

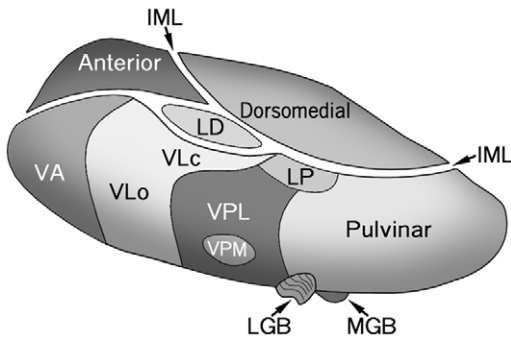


Fig. 13. Relationships of the thalamic nuclei to the internal medullary Lamina. Diagrammatic display. See text. Dorsomedial is a synonym for the medial nucleus. LD, lateral dorsal nucleus; LP, lateral posterior nucleus; VA, ventral anterior nucleus; VL, ventral lateral nucleus (subdivided into oral (o) and caudal (c) portions); VP, ventral posterior nucleus (subdivided into lateral (L) and medial (M) portions). LGB and MGB represent the lateral and medial geniculate bodies of the metathalamus. (Modified from Carpenter MB, Sutin J, editors. Human neuroanatomy. Williams & Wilkins, Baltimore, 1983, with permission).

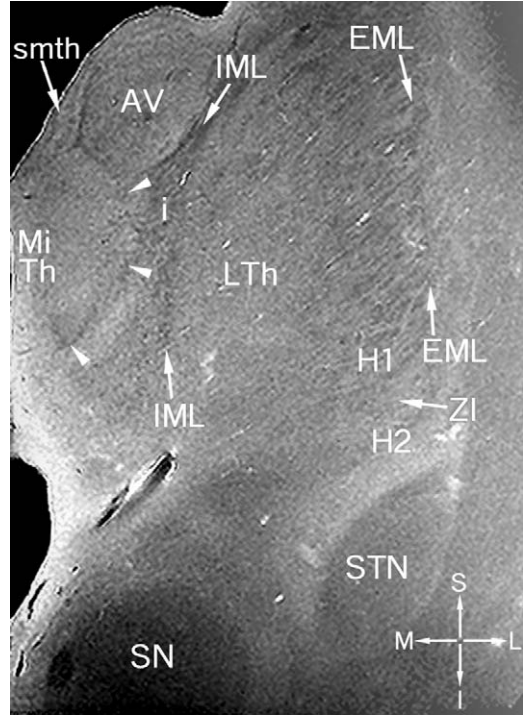


Fig. 14. Coronal MRM scan through the mamillo-thalamic fasciculus. The medial thalamic nucleus (*arrowhead*) appears as a bright structure indistinctly separated from the midline thalamic nuclei (MiTh) further medial. The medial thalamic nucleus is bordered laterally by the darkish gray internal medullary lamina (IML). The anteroventral thalamic nucleus (AV) forms a well-defined bright structure anterosuperior to the medial thalamic nuclei and lateral to the curvilinear gray stria medullaris thalami (smth). The internal medullary lamina (IML) splits to include an indistinct light gray zone representing the intralaminar nuclei (i). The lateral groups of thalamic nuclei (LTh) are interposed between the darkish gray internal medullary lamina (medially) and the relatively ill-defined inhomogenous gray external medullary lamina (EML) of the thalamus laterally. The reticular nucleus (RN), not clearly identified lies within the external medullary lamina. The numerous fiber tracts of the thalamocortical connections permeate the reticular nucleus. The internal capsule lies lateral to the reticular nucleus. Ventrally, the reticular nucleus continues into the zona incerta of the subthalamic region. H1, H2, fields of Forel; SN, substantia nigra; STN, subthalamic nucleus; ZI, zona incerta.

lateral posterior nucleus lies just behind that. The pulvinar expands markedly behind the lateral posterior nucleus to constitute the posterior pole of the thalamus. IW-MRM displays the lateral thalamic nuclei as an inhomogenously

bright structure adjoining the internal medullary lamina.

Ventral thalamic nuclei

The ventral nuclei form most of the thalamus lateral to the internal medullary lamina and anterior to the pulvinar. On IW-MRM, the ventral anterior group is seen as a bright structure delimited anteriorly by the internal capsule, posteriorly by the ventral lateral nucleus, medially by the internal medullary lamina, and laterally by the external medullary lamina. The ventral lateral and ventral posterior nuclei lie posterolateral to the ventral anterior group, and anterior to the pulvinar. They are less well delimited on IW-MRM.

Intralaminar nuclei

On IW-MRM, the intralaminar nuclei are seen as ill-defined bright areas embedded within the split fibers of the internal medullary lamina. The centromedian nucleus may be distinguished, but the other nuclei are not yet resolved individually.

Midline thalamic nuclei

IW-MRM displays the midline thalamic nuclei as bright structures arrayed along the lateral wall of the third ventricle and in the massa intermedia.

Subthalamus

The subthalamic nucleus, zona incerta, fields of Forel and a portion of the substantia nigra lie ventral to the thalamus. On IW-MRM, the subthalamic nucleus (STN) appears as a biconvex mass of gray matter situated ventral to the thalamus and medial to the internal capsule (Fig. 15). The zona incerta and the fields of Forel lie superior to the STN. The cerebral peduncle and substantia nigra lie inferolateral to the STN. The substantia nigra, a crescentic lamina of pigmented multipolar neurons forms an elongated slightly gray nucleus just inferomedial to the subthalamic nucleus (see Fig. 15). The substantia nigra is divisible into the dorsal pars compacta, which is intermingled with the fibers of the crus cerebri, and the ventral pars reticularis that is partially continuous with the globus pallidus.

Metathalamus

The metathalamus comprises the medial geniculate complex and the lateral geniculate body (Fig. 16).

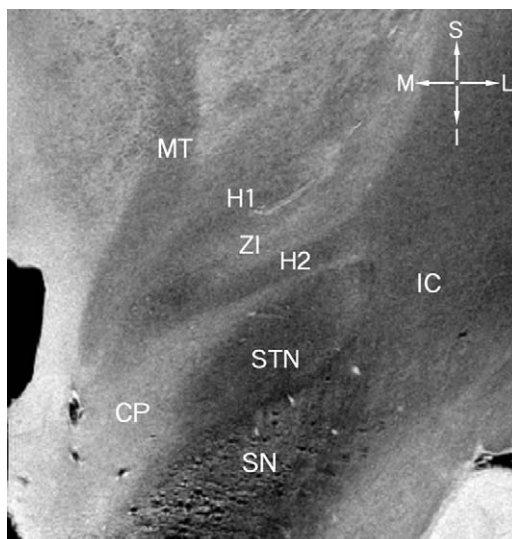


Fig. 15. Subthalamic nucleus. Coronal IW-MRM demonstrates the subthalamic nucleus as a lens-shaped gray mass that lies medial to the internal capsule, lateral to the thalamus, dorsolateral to the substantia nigra, and inferior to the zona incerta and fields of Forel. The prominent “staghorn” formed by the mammillothalamic tract (MT) serves as a landmark for the anterior portion of the subthalamic nucleus (STN). CP, cerebral peduncle; H1 & H2, fields of Forel; IC, internal capsule; SN, Substantia nigra; ZI, zona incerta.

Medial geniculate complex

The medial geniculate complex (MGC) forms a rounded elevation at the posterolateral aspect of the midbrain and cerebral peduncle, along the ventrolateral surface of the pulvinar. It contains three major medial geniculate nuclei: the medial, ventral, and dorsal nuclei. The brachium of the inferior colliculus separates the sparsely cellular medial nucleus from the densely cellular ventral nucleus. The dorsal nucleus overlies the ventral nucleus and expands posteriorly. For that reason, it may also be designated the posterior nucleus. The ventral nucleus is part of the classic tonotopic auditory relay. Within it, low-pitched sounds are represented laterally, and high-pitched sounds medially. The dorsal and medial nuclei receive both tonotopic and non-tonotopic input, and participate in non-classic polysensory pathways, including auditory spatial representation. IW-MRM displays the entire medial geniculate complex as a semilunar gray structure separated from the laminated lateral geniculate body by the dark geniculotemporal radiation. At present

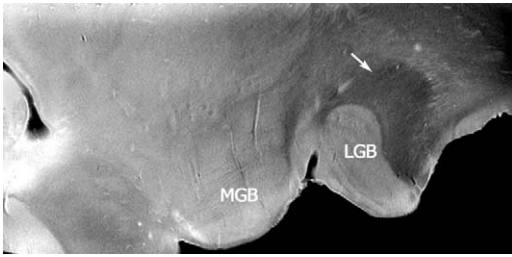


Fig. 16. Metathalamus. Coronal IM-MRM demonstrates the rounded configuration and near homogeneity of the medial geniculate body (MGB), and the Napoleon's hat configuration and laminated retinotopic organization of the lateral geniculate body (LGB). The geniculocalcarine radiation passes superolaterally from the lateral geniculate body (*arrow*).

IW-MRM resolves the individual nuclei of the MGC inconclusively.

Lateral geniculate body

The lateral geniculate body (LGB) is an elongated spatulate structure that projects ventrolaterally from the undersurface of the pulvinar. It is separated from the lateral aspect of the crus cerebri by the fibers of the optic tract. The brachium of the superior colliculus enters the posterior medial portion of the lateral geniculate dorsally, between the medial geniculate nucleus and the pulvinar. IW-MRM displays the LGB as a small structure, which takes a shape designated "Napoleon's hat", and which displays characteristic retinotopic layering.

Summary

MR microscopy at 9.4T depicts the architecture of the brain in exquisite detail, including the individual laminae of the cortex, the individual nuclei of the basal ganglia, the thalami, subthalamus and metathalamus, and the orientations and relationship among the dominant nuclei and white matter tracts of the brain. The authors believe that these anatomic relations will ultimately be displayed in vivo as clinical MR scanners begin to operate at field strengths of 4.7T, 7T, and 8T. Then, those familiar with this anatomy will be able to interpret patient images with far greater sophistication.

References

[1] Beuls E, Gelan J, Vandersteen M, Adriaensens P, Vanormelingen L, Palmers Y. Microanatomy of the

excised human spinal cord and the cervicomedullary junction examined with high-resolution MR imaging at 9.4 Tesla. *Am J Neuroradiol* 1993;14:699–707.

- [2] Vandersteen M, Beuls E, Gelan J, et al. High field magnetic resonance imaging of normal and pathologic medulla oblongata. *Anat Rec* 1994;238:277–86.
- [3] Benveniste H, Katie K, Zhang L, Johnson GA. Magnetic resonance microscopy of the C57BL mouse brain. *Neuroimage* 2000;11:601–11.
- [4] Burgess RE, Yu Y, Christoforidis GA, et al. Human leptomeningeal and cortical vascular anatomy of the cerebral cortex at 8 T. *J Comput Assist Tomogr* 1999;23:850–6.
- [5] Carpenter MB, Sutin J. *Human neuroanatomy: the cerebral cortex*. Baltimore: Williams & Wilkins; 1983. p. 643–705.
- [6] Daniels DL, Haughton VM, Naidich TP. *Cranial and spinal magnetic resonance imaging: an atlas and guide*. New York: Raven Press; 1987.
- [7] Nieuwenhuys R, Voogd J, van Huijzen C. *The human central nervous system: a synopsis and atlas*. 3rd revised edition. New York: Springer-Verlag; 1988.
- [8] Duvernoy HM. *The human hippocampus: an atlas of applied anatomy*. Munchen, Germany: J.F. Bergmann Verlag; 1988.
- [9] Duvernoy H. *The human brain: surface, three-dimensional sectional anatomy and MRI*. New York: Springer-Verlag Wien; 1991.
- [10] Ono M, Kubik S, Abernathy CD. *Atlas of the cerebral sulci*. New York: Thieme Medical Publishers, Inc.; 1990.
- [11] Berry M, Bannister LH, Standing SM. *Nervous System*. In: Williams PL (Deceased), Bannister LH, Berry M, Collins P, Dyson M, Dussek JE, Ferguson MWJ, editors. *Gray's anatomy*. 38th edition. Edinburgh: Churchill Livingstone; 1995. p. 901–1397.
- [12] Naidich TP, Daniels DH, Haughton VM, et al. The hippocampal formation and related structures of the limbic lobe. *Anatomic-MR correlations*. Part I. Surface features and coronal sections. *Radiology* 1987;162:747–54.
- [13] Naidich TP, Daniels DH, Haughton VM, et al. The hippocampal formation and related structures of the limbic lobe. *Anatomic-MR correlation*. Part II. Sagittal sections. *Radiology* 1987;162:755–61.
- [14] Naidich TP, Valavanis AG, Kubik S. *Anatomic relationships along the low-middle convexity: Part 1—normal specimens and magnetic resonance imaging*. *Neurosurgery* 1995;36:517–32.
- [15] Naidich TP, Valavanis AG, Kubik S, et al. *Anatomic relationships along the low-middle convexity. Part II. Lesion localization*. *Internat J Neuroradiol* 1997;3:393–409.
- [16] Naidich TP, Brightbill TC. *Systems for localizing fronto-parietal gyri and sulci on axial CT and MRI*. *International J Neuroradiol* 1996;2:313–38.
- [17] Yousry TA, Schmid UD, Alkadi H, et al. *Localization of the motor hand area to a knob on the*

- precentral gyrus: a new landmark. *Brain* 1997;120:141–157.
- [18] Yousry TA, Fesl G, Buttner A, et al. Heschl's Gyrus: anatomic description and methods of identification on magnetic resonance imaging. *Internat J Neuroradiol* 1997;3:2–12.
- [19] Vogt BA, Vogt LJ, Nimchinsky EA, et al. Chapter VIII Primate cingulate cortex, chemoarchitecture, and its disruption in Alzheimer's disease. In: Bloom FE, Björklund A, Hökfelt T. *Handbook of chemical neuroanatomy*, vol. 13. The primate nervous system, Part I. Amsterdam: Elsevier Science BV; 1997. p. 455–528.
- [20] Yasargil MG. *Microneurosurgery* in 4 volumes. IVA CNS tumors. Stuttgart, Germany: Georg Thieme Verlag; 1994.
- [21] Ture U, Yasargil DCH, Al-Mefty O, Yasargil MG. Topographic anatomy of the insular region. *J Neurosurg* 1999;90:720–33.
- [22] Talairach J, Tournoux P. *Co-planar stereotaxic atlas of the human brain. 3-Dimensional proportional system: an approach to cerebral imaging*. New York: Thieme Medical Publishers, Inc.; 1988.
- [23] Naidich TP, Hof PR, Yousry TAT, Yousry I. The motor cortex. *Anatomic Substrates of Function. Neuroimaging Clin N Am* 2001;11:171–93.
- [24] Brodmann K. *Vergleichende Lokalisationlehre der Grosshirnrinde in ihren Prinzipien dargestellt auf grund des Zellenbaues*. Leipzig, Barth; 1909.
- [25] von Economo C, Koskinas GN. *Die Cytoarchitektonik der Hirnrinde des erwachsenen Menschen*. Berlin: Springer; 1925.
- [26] Meyer JR, Roychowdhury S, Russell EJ, Callahan C, Gitelman D, Mesulam MM. Location of the central sulcus via cortical thickness of the precentral and postcentral gyri on MR. *AJNR Am J Neuroradiol* 1996;17:1699–706.
- [27] Vogt O. Die myeloarchitektonische Felderung des Menschlichen Stirnhirns. *J Psychol Neurol* 1910;15:221–232.
- [28] Vogt C, Vogt O. Allgemeinere Ergebnisse unserer Hirnforschung. *J Psychol Neurol* 1919;25:279–461.
- [29] Vogt C, Vogt O. Die vergleichend-architektonische und vergleichend-reizphysiologische Felderung der Grosshirnrinde unter besonderer Berücksichtigung der menschlichen Stirnhirns. *Naturwissenschaften* 1926;14:1190–4.
- [30] Lorente de No R. *Studies on the Structure of the Cerebral Cortex. I. The Area Entorhinalis*. *J Psychol Neurol* 1933;45:381–438.
- [31] Lorente de No R. *Studies on the Structure of the Cerebral Cortex. II. Continuation of the Study of the Ammonic System*. *J Psychol Neurol* 1934;46:113–77.
- [32] Foerster O. *Symptomatologie der Erkrankungen des Grosshirns. Motorische Felder und Bahnen*. In: Bumke O, Foerster O, editors. *Handbuch der Neurologie*, vol. 6. Berlin: Julius Springer; 1936:1–357.
- [33] DeFelipe J, Jones EG. *Cajal on the cerebral cortex: an annotated translation of the complete writings*. New York, Oxford: Oxford University Press; 1988.
- [34] Vogt BA, Nimchinsky EA, Vogt LJ, et al. Human cingulate cortex: Surface features, flat maps, and cytoarchitecture. *J Comp Neurol* 1995;359:490–506.
- [35] Zilles K, Schlaug G, Geyer S, et al. Anatomy and transmitter receptors of the supplementary motor areas in the human and nonhuman primate brain. *Adv Neurol* 1996;70:29–43.
- [36] Schleicher A, Amunts K, Geyer S, Morosan P, Zilles K. Observer-independent method for microstructural parcellation of cerebral cortex: A quantitative approach to cytoarchitectonics. *Neuroimage* 1999;9:165–77.
- [37] Schleicher A, Amunts K, Geyer S, Kowalski T, Schormann T, Palomero-Gallagher N, et al. A stereological approach to human cortical architecture: identification and delineation of cortical areas. *J Chem Neuroanat* 2000;20:31–47.
- [38] Amunts K, Zilles K. Advances in cytoarchitectonic mapping of the human cerebral cortex. *Neuroimaging Clin N Am* 2001;11:151–69.
- [39] Morris R, Paxinos G, Petrides M. Architectonic analysis of the human retrosplenial cortex. *J Comp Neurol* 2000;421:14–28.
- [40] Morris R, Paxinos G, Petrides M. Architectonic analysis of the human retrosplenial cortex. *Eur J Neurosci* 1999;11:2506–18.



Cumulative Index 2003

Volume 11

February	CARDIAC MR IMAGING, pages 1–191
May	MR IMAGING OF SPORTS-RELATED INJURIES, pages 193–378
August	MR NEUROIMAGING: CURRENT AND NEWER TECHNIQUES I, pages 379–527
November	MR NEUROIMAGING: CURRENT AND NEWER TECHNIQUES II, pages 529–671

Note: Page numbers of article titles are in **boldface** type.

A

- Abscess(es), on pons, diffusion-weighted MR imaging of, 385, 387
pyogenic, MR spectroscopy of, 422
- N*-Acetylaspartate, in evaluation of brain tumors, 419, 421
- Achilles tendon, injuries of, in athletic activities, 296
- Achilles tendonitis, 296–297
- Adductor insertion avulsion syndrome, 273
- Adductor muscle, strain of, 344, 346
- Alanine, in evaluation of brain tumors, 421
- Allocortex, MR microscopy of, 644–646
- Aneurysms, contrast-enhanced MR angiography in, 607–608
- Angiography, computed tomography, of carotid arteries, 589–591
of plaque evaluation of carotid arteries, 591–592
contrast-enhanced, of thoracic aorta, 136–137
magnetic resonance, coronary. *See Coronary magnetic resonance angiography.*
MR. *See Magnetic resonance angiography.*
- Angioma, frontal cavernous, functional MR imaging in, 534
- Angiosarcoma, cardiac, 179
- Ankle, accessory muscles of, 202–203
accessory ossicles and sesamoid bones of, 203
foot and, bony injury of, 295, 296
force on, during athletic activities, 295
sports injuries of, imaging of, **295–310**
sports protocols, for direct MR arthrography, 296
“high sprain” of, 300, 302
imaging of, after physical activity, 202
injuries of, in alpine skiing, 313, 314
lateral, ligamentous injury of, 299
ligaments and tendons of, asymptomatic findings about, 202
normal fluid collections in, 201
- Anterior cruciate ligament, ganglion cyst of, 290, 292
in meniscal and cruciate ligament injuries, **283–293**
normal fibrous bundles of, 287, 291
rupture of, 289, 291
sprains of, 289
tears of, 291–293
in alpine skiing, 312–313
MR imaging to diagnose, 291
- Aorta, coarctation of, MR imaging in, 31, 36, 37, 38
thoracic aortic stenosis caused by, 142, 144
thoracic. *See Thoracic aorta.*
- Aortic dissection, 140–142
type B, 138
with intramural hemorrhage, 139, 142
- Aortic flow, regurgitant, quantification of, by velocity-encoded cine MR imaging, 118–120, 121
- Aortic plaques, MR imaging of, 102–104
- Aortic regurgitation, and aortic stenosis, combined, 129

- Aortic regurgitation (*continued*)
 assessment of ventricular dysfunction in, 116
 causes of, 116–117
 cine gradient echo images in, 117
- Aortic stenosis, and aortic regurgitation,
 combined, 129
 causes of, 126
 evaluation of, MR imaging in, 126
 spin echo imaging in, 126
 thoracic, caused by coarctation of aorta, 142, 144
 postcoarctation repair in, 143, 144
- Aortic valve, abnormal motion of, evaluation of, 126–127
 MR imaging of, 30, 34, 35
- Apophyseal avulsion injuries, 343, 344
 clinical features of, 267
 MR imaging of, 267
 treatment of, 267
- Arachnoid cyst(s), in cerebellopontine angle cistern, diffusion-weighted MR imaging of, 386
 versus epidermoid tumor, diffusion-weighted MR imaging of, 383, 384
- Arrhythmogenic right ventricular dysplasia, MR imaging of, 10–12, 13, **163–171**
- Arterial dissection, MR angiography of neck for, 593–594
- Arteriovenous fistula, dural, MR angiography of, 569–573, 574
- Arteriovenous malformation, epidural, MR angiography of, 576–577
 intramedullary, MR angiography of, 573–575
- Artery(ies), atherothrombosis as systemic and diffuse disease of, 101
 carotid. *See Carotid artery(ies).*
 coronary, anomalies of, evaluation of,
 coronary MR angiography in, 89
 great, transposition of, 9, 10
 popliteal, high-resolution MR imaging of, 104
 pulmonary, MR imaging of, 33–34, 39, 44
- Arthritis, septic, of hip, 264
- Astrocytoma(s), high-grade, two-dimensional MR spectroscopy plot, 426–428
 low-grade, blood volume in, 407
 perfusion MR imaging in, 407
 MR spectroscopy of, 421
 surgical resection of, intraoperative MR imaging in, 437, 438
- Atherosclerotic disease, of carotid arteries, MR angiography in, 585
- Atherosclerotic ulcer, intramural hematoma in, 144
 penetrating, 140, 144
- Atherothrombosis, as systemic and diffuse disease of arterial system, 101
- Atherothrombotic plaques, MR imaging analysis of, 109
 MR imaging and molecular imaging in, 107–109
 noninvasive assessment of, MR imaging for, **101–113**
 future improvements in, 109–110
 progression and regression of, monitoring with MR imaging, 109
- Athletes, stress fractures in, imaging of, **323–339**
- Athletic pubalgia, 271–272
 MR imaging in, 272
- Atrial morphology, MR imaging of, 27–28
- Atrial septal defect, MR imaging of, 36–37, 40, 41, 42, 44
- Atrial situs, MR imaging in, 27–28, 29, 30
- Atrioventricular and ventriculoarterial connection, 29–30, 31, 32, 33
-
- B**
- Bankart lesions, 227, 229
- Basal ganglia, functional MR imaging in, 530, 531
 MR microscopy of, 648–649, 651, 652
- Baseball pitch, basic positions of, 226–227
- Bennett lesion, 230–231
- Biceps tendon, 250
 distal, rupture of, 250–251
- Biopsy, MR image-guided, in neurosurgery, 440–441
- Blood brain barrier, permeability of, perfusion weighted MR imaging in, 508–511
- Blood flow, cerebral, perfusion weighted MR imaging of, 503–508, 509, 510–511
- Blood oxygen level, high resolution venography dependent on, 633–636
- Blood vessels, intradural, abnormal, MR angiography of, 568, 569
 normal, MR angiography of, 567–568

- malformations of, MR angiography of, 568–569
- Blood volume, cerebral, perfusion weighted MR imaging of, 503–508, 509, 510–511
- Bobsledding, injuries associated with, 316, 317, 318
- Bone scintigraphy, in myositis ossificans, 356
in stress fractures, 332–334
- Brachial plexus, MR imaging of, 552, 553
neurofibroma of, MR imaging in, 554, 555
- Brain, hemodynamics of, prediction of, with conventional and perfusion MR imaging, 592–593
magnetoencephalography to assess, 529
normal human, MR microscopy of, **641–657**
positron emission tomography to assess, 529
traumatic injury to, diffusion tensor MR imaging in, 501–502, 505
- Brain tumor(s), detection of, diffusion-weighted MR imaging and, 383
diffusion-weighted and diffusion tensor MR imaging of, **379–401**
evaluation of, 382
 applications of neuroimaging to, 382–397
 functional MR imaging in, 439
 in pediatric patients, diffusion-weighted MR imaging of, 391–392
 in posterior fossa, diffusion-weighted MR imaging of, 391–392
 metabolites in evaluation of, 417–421
 metastases of, MR spectroscopy of, 423, 424
 MR spectroscopy of, **415–429**
 preoperative MR spectroscopy in, 439
 primary, MR spectroscopy for evaluation of, 421–422
 treatment planning in, 423–424
 ultrasmall superparamagnetic iron oxide contrast agent for evaluation of, 455–456
 resection of, intraoperative MR imaging in, 437–439
 solid, grading of, diffusion-weighted MR imaging and, 387–390
- Brainstem, lesions of, MR spectroscopy of, 422
- Bypass grafts, patency of, assessment of, coronary MR angiography in, 89–92
- C**
- Calf, hematoma of, imaging of, 342
- Capitellum, pseudodeflect of, elbow and, 196, 197
- Cardiac and pericardial malignancy, MR evaluation of, **173–186**
 techniques of, 173–174
- Cardiac fibromas, 177, 178
- Cardiac gating, and physiologic monitoring, 1–2
 for electrocardiogram lead placement, 2
- Cardiac looping, 29
- Cardiac magnetic resonance imaging, coronal and sagittal planes in, 3–4, 5
 expanding role of, 15
 horizontal long axis plane in, 5, 6
 imaging planes, 3
 in adult congenital heart disease, 7–8
 long axis view through aortic and mitral valves, 6, 7
 performance of, overview of, **1–18**
 pulse sequences, 2–3
 routine clinical studies with, 6–7
 scout planes in, 3, 4
 short axis plane in, 5, 7
 techniques of, principles of, 1
 vertical long axis plane in, 5, 6
- Cardiac magnetic resonance imaging report, used in clinical cardiac MR program, 25
- Cardiac myxoma, 175–177
- Cardiac neoplasms, benign, evaluation of, 175–178
 evaluation of, 175
- Cardiac pseudotumors, evaluation of, 174–175, 176
- Cardiac tumors, malignant, 178–181
- Cardiomyopathy, restrictive, constrictive pericarditis versus, 12–13
 MR imaging sequences in, 13–14
- Cardiovascular magnetic resonance imaging, of myocardial perfusion. See *Myocardial perfusion, cardiovascular MR imaging of.*
- Carotid artery(ies), atherosclerotic disease of, MR angiography in, 585
 computed tomography angiography of, 589–591
 evaluation of, MR angiography in, 585–589
 extracranial, MR angiography evaluation of, 585–589
 plaque circulation of, computed tomographic angiography of, 591–592

- Carotid plaques, MR imaging of, 102, 103
- Cell therapies, and drug delivery, MR image-guided, to central nervous system, 443
- Central nervous system, MR image-guided delivery of drug and cell therapies to, 443
- Cerebellar cortex, MR microscopy of, 647–648, 649
- Cerebellar nuclei, MR microscopy of, 648, 650
- Cerebellopontine angle cistern, arachnoid cyst in, diffusion-weighted MR imaging of, 386
- Cerebral cortex, MR microscopy of, 642 types of, 641–642
- Cerebral hematoma, temporal, HASTE image of, 478, 479
- Cervical ligament injury, 303, 304
- Cervical spine, HASTA image of, 479, 480
- Children. *See Pediatric patient(s).*
- Choline, as marker for proton MR spectroscopy, 458–460 in evaluation of brain tumors, 417, 419
- Cine gradient echo imaging, 116 signal void on, evaluation of, 126
- Circulation, extracranial, MR angiography of, **585–597** intracranial, contrast-enhanced MR angiography of, **599–613**
- Clinical cardiac MR imaging program. *See Magnetic resonance imaging program, clinical cardiac.*
- Coarctation of aorta, MR imaging in, 31, 36, 37, 38 thoracic aortic stenosis caused by, 142, 144
- Combindex, for imaging of head and neck, 453–455
- Compartment syndrome, 358–361 acute, 359 chronic, 359 diagnostic examinations of, 359–360 MR imaging of, 360–361 pathogenesis of, 359 symptoms and signs of, 359 treatment of, 361
- Computed tomography, in pericardial disease, 150–151 in sports-related muscle injuries, 355–356 in stress fractures, 330, 331, 334
- Computed tomography angiography, of carotid arteries, 589–591
- Connective tissue disorders, systemic, parotid gland in, mapping using apparent diffusion coefficients, 461–463
- Contrast agent(s), for perfusion MR imaging, 404 ultrasmall superparamagnetic iron oxide, 449, 452–458 for evaluation of metastatic lymph nodes, 457–458 for evaluation of primary brain tumors, 455–456
- Contrast-enhanced angiography, of thoracic aorta, 136–137
- Contrast-enhanced magnetic resonance angiography. *See Magnetic resonance angiography, contrast-enhanced.*
- Contrast-enhanced magnetic resonance imaging, 8–9
- Coracoid impingement syndrome, 230
- Coronary artery, anomalies of, evaluation of, coronary MR angiography in, 89
- Coronary magnetic resonance angiography, 3D segmented K-space echoplanar, 87–89 3D segmented K-space gradient echo, 87 cardiac motion suppression in, 82 clinical applications of, 15, 89–94 and imaging of coronary artery disease, **81–99** contrast-to-noise ratio considerations in, 85–86 future developments in, 94–95 respiratory motion suppression in, 82–85 signal-to-noise ratio considerations in, 85 technical considerations in, 81–86 techniques for clinical imaging in, 86–89
- Coronary plaques, high-resolution MR imaging of, 104–105
- Coronary stenosis, native vessel, identification of, coronary MR angiography in, 92–93
- Cortex, cerebellar, MR microscopy of, 647–648, 649 cerebral, MR microscopy of, 642 types of, 641–642 transitional, MR microscopy of, 646, 648

Cortical dysplasia, focal, FLAIR in, 483, 484

Coxa saltans, 270–271
MR imaging in, 271

Creatine, as marker for proton MR spectroscopy, 458–460
in evaluation of brain tumors, 418–421

Cruciate ligament, anterior. See *Anterior cruciate ligament*.
injuries of, and meniscal injuries, MR imaging of, **283–293**
posterior, injuries of, 291, 292, 293

Cystic masses, intraaxial, characterization of, diffusion-weighted MR imaging in, 385–387

Cyst(s), pericardial, 158, 159, 181

D

Delayed onset muscle soreness, 302

Deltoid ligament, tears of, 298

Dentate gyrus, MR microscopy of, 646

Deuterium oxide, for perfusion MR imaging, 404

Diffusion tensor MR imaging, 381–382, 622–624
diffusion tensor ellipsoid, 382
high angular resolution, 503, 506
in pediatric patients, 499–503
of brain tumors, **379–401**
tractology in neonate using, 502–503, 506

Diffusion-weighted MR imaging, and apparent diffusion coefficient maps, 381
basic concepts and techniques of, 379–382
for posttreatment assessment, 395–397
in pediatric patients, 493–499
of brain tumors, **379–401**
physical basis of diffusion and, 379
process of, 380–381
rising interest in diffusion and, 379–380
to assess effectiveness of therapy, 395–397
to assess extent of residual epidermoid tumor, 395, 396–397
to diagnose posttreatment complications, 397
to predict patterns of tumor spread, 397

Dobutamine, MR imaging using, 73–77
stress echocardiography using, 75

Drugs, delivery of, and cell therapies, MR image-guided, to central nervous system, 443

Dynamic contrast-enhanced MR imaging, 449–452
clinical utility of, 450–451

in cancers of head and neck, 451, 452–453, 454–455
limitations of, 452
of cervical lymph nodes, in squamous cell carcinoma, 451
technical background of, 450

Dysplasia, of hip, osteoarthritis and, 257–258

E

Echo planar imaging, 69

Echocardiography, in constrictive pericarditis, 158
in pericardial disease, 149–150
stress, using dobutamine, 75

Elbow, capsule anatomy and pathology of, 241–242
common extensor tendon, and lateral muscles, 248
dislocation of, posterolateral rotary instability and, 245–247
epicondylitis and overuse syndromes of, 248–250
flexor tendon of, and medial muscles, 248
fracture dislocations of, 246–247, 248
imaging of, normal variants and pitfalls of, 196–197
instability at, 243–244
lateral muscles of, common extensor tendon and, 248
ligamentous anatomy and pathology of, 242–247
medial muscles of, flexor tendon and, 248
osseous anatomy and pathology of, 239–241
osteochondral lesions of, 240–241
posterolateral rotary instability of, and dislocation, 245–247
pseudodeflect of capitellum and, 196, 197
sports injuries of, **239–253**
subluxation or dislocation of, 246–247, 248
tendons of, anatomy and pathology of, 247–252
valgus stress at, 240, 242
varus stress at, 245, 246

Electrocardiogram, lead placement for, cardiac gating as, 2

Empyema, subdural, and frontal sinusitis, diffusion tensor MR imaging in, 497–498, 503

Encephalomyelitis, acute disseminated, diffusion tensor MR imaging in, 497, 500

- Endocarditis, and valvular morphology, MR imaging of, 130–131
- Epicondylitis, and overuse syndromes of elbow, 248–250
- Epidermoid tumor(s), diffusion-weighted MR imaging of, 392–394
residual, diffusion-weighted MR imaging to assess, 395, 396–397
versus arachnoid cysts, diffusion-weighted MR imaging of, 383, 384
- Epilepsy, neurosurgery in, MR imaging guidance in, 443
- Exercise, for enhancement of MR imaging, 343
- Extraaxial masses, characterization of, diffusion-weighted MR imaging in, 383–385
- Extracranial circulation, MR angiography of, **585–597**
-
- F**
- Femoral neck, stress fractures of, 336–337
- Femoroacetabular impingement, in osteoarthritis of hip, 263
- Ferumoxides, for imaging of head and neck, 455
- Ferumoxtran-10, for imaging of head and neck, 453–455
- Fibrocartilage, asymptomatic triangular, 197–198
- Fibroelastoma, papillary, 177
- Fibromas, cardiac, 177, 178
- Fibrosarcoma, cardiac, 180–181
- Fistula, dural arteriovenous, MR angiography of, 569–573, 574
- Fluid-attenuated inversion recovery (FLAIR),
basic principles of, 480
clinical applications of, 482–487
disadvantage of, 481
in cerebral embolic infarcts, 482, 483
in focal cortical dysplasia, 483, 484
in glioblastoma multiforme, 486
in head trauma, 484
in inflammation of maxillary sinus, 487
in multiple sclerosis, 482, 483
in orbital pseudotumor, 485–486
in subarachnoid hemorrhage, 485, 486
magnetization transfer, and HASTE, **471–492**
- Foot, and ankle, bony injury of, 295, 296
force on, during athletic activities, 295
sports injuries of, imaging of, **295–310**
sports protocols, for direct MR arthrography, 296
injuries of, associated with snowboarding, 315
in alpine skiing, 313, 314
normal fluid collections in, 201
- Foramen sublabrum, 224
- Forefoot, asymptomatic findings in, 203
- Fourier transformation, proton MR spectroscopy after, 415, 417
- Frame-based and frameless navigational systems, disadvantage of, 431
- Free induction decay signal, 415, 416
- Functional magnetic resonance imaging, 631–633
auditory stimulation paradigms, 532, 533
clinical application of, 529
clinical preoperative, 530
cognitive paradigms and, 536–538
cortical motor control for, 530–531
image-guided, in neurosurgery, 441–443
in basal ganglia, 530, 531
in brain tumors, 439
in children, 515–517
in frontal cavernous angioma, 534
in parietal low grade glioma, 530, 531
interpretation of, 538–540
language paradigms and, 533–536
memory function and, 537–538
paradigms for clinical preoperative mapping, **529–542**
routine session of, 530
tactile stimulation paradigms, 531–532
visual stimulation paradigm, 533, 534
whole-brain volumetric, capability of, 529–530
-
- G**
- Gadolinium, signal intensity and, 417
- Gadolinium contrast-enhanced cardiovascular magnetic resonance imaging, of myocardial perfusion, 55–61
- Gadolinium enhancement, of magnetic resonance imaging, 342–343
- Gadopentetate dimeglumine, in perfusion MR imaging, 404, 405, 406
- Ganglion cyst, of anterior cruciate ligament, 290, 292

- Gastrocnemius muscle, residual hematoma in, 347, 350
 strain injury of, 352–353
- Geniculate body, lateral, 654
- Geniculate complex, medial, 652–653
- Glenohumeral instability, atraumatic, 228
 classification of, 227
 traumatic, 227–228
- Glenohumeral joint, microinstability of, 228
 posterolateral instability of, 234–235
- Glenohumeral ligament(s), 222
 humeral avulsion of, 227, 229
 inferior, 224
 middle, 223–224
 superior, 223
- Glial tumor, malignant, perfusion weighted MR imaging in, 509, 513
- Glioblastoma(s), blood volume in, 407, 408
- Glioblastoma multiforme, diffusion-weighted MR imaging of, 397, 398
 FLAIR in, 486
- Glioma(s), differentiation of, diffusion-weighted MR imaging of, 387–390
 high-grade, debulking of, intraoperative MR imaging in, 439
 low-grade, intraoperative MR imaging in, 438
 parietal low grade, functional MR imaging in, 530, 531
 perfusion MR imaging, 407–409
 pontine, MR spectroscopy of, 421
 representative myo-inositol spectra for, 419–420, 421
 surgical resection of, intraoperative MR imaging in, 437
 treatment planning in, 423, 424
- Glutamate, in evaluation of brain tumors, 421
- Glutamine, in evaluation of brain tumors, 421
- Gradient echo imaging, in magnetic resonance imaging, 342
- Gradient recalled echo sequences, 3
- Groin pain, acute, in athletes, 271–272
- H**
-
- Haglund's deformity, 297, 298
- Half-Fourier acquisition single-shot turbo spin echo (HASTE), for brain imaging, 478
 for fetal neuroimaging, 479, 481
 magnetization transfer, and FLAIR imaging, **471–492**
 of cervical spine, 479, 480
 of temporal cerebral hematoma, 478–479
 technique of, 477–478
- Hamstring muscles, strain injury of, 349–352
- Hand, imaging of, normal variants and pitfalls of, 197–198
- Head and neck, cancers of, dynamic contrast-enhanced MR imaging in, 451, 452–453, 454–455
 MR angiography of, for arterial dissection, 593–594
 MR imaging techniques for, newer, **449–469**
 tumors of, monitoring of, and recurrence detection, proton MR spectroscopy for, 461
- Head trauma, FLAIR in, 484
- Headache, mapping of parotid gland in, spinal cord values for, 462, 463
- Heart, function of, assessment of, with MR imaging, **67–80**
 metastatic disease of. See also *Pericardium, and heart, metastatic disease of.*
 and cardiac tumors, 14
 MR sequences in, 14–15
 size and function of, acquisition techniques for quantifying, 67
 gradient echo of, 67
 spin echo imaging of, 67
 tissue tagging to assess, 67–68
 tumors of, and metastatic disease, 14
 MR sequences in, 14–15
 univentricular, MR imaging of, 45–46, 47
- Heart disease, congenital, adult, cardiac MR imaging in, 7–8
 general MR imaging in, 8
 MR imaging of, **27–48**
- Hematoma, and pseudotumor appearance, 347–348, 349, 350
 intramural, in atherosclerotic ulcer, 144
 of calf, imaging of, 342
 residual, in gastrocnemius muscle, 347, 350
 temporal cerebral, HASTE image of, 478, 479
- Hemorrhage, subarachnoid, FLAIR in, 485, 486

High resolution blood oxygen level dependent venography, 633–636

Hip, arthroscopy of, indications for, and contraindications to, 255–256

technique of, and complications of, 256

bursae of, and bursitis of, 267–270

disorders of, sports-related, MR imaging of, **255–281**

dysplasia of, osteoarthritis and, 257–258

extra-articular derangement of, protocol for, 257

extrinsic ligaments of, anatomy and function of, 261

MR imaging of, 261

instability of, clinical manifestations of, 261

internal derangement of, imaging protocol for, 256–257

joint effusion of, 261–262

ligaments of, and ligament injuries, 260–261

MR imaging of, 198

technical considerations for, 256–257

musculotendinous injuries of, 270–273

osseous injuries of, 265–267

osteoarthritis of. See *Osteoarthritis, of hip.*

osteochondral injury of, 262

septic arthritis of, 264

stress fracture of, 265–266

Hippocampus, MR microscopy of, 644–646, 647

Histiocytoma, malignant fibrous, 179–180

Hydrogen protons, in MR spectroscopy, 415, 416

I

Ice hockey, injuries associated with, 319

Iliopsoas bursa, and bursitis, 268

Iliotibial band friction syndrome, joint effusion in knee versus, 201, 202

Interosseous ligament, lesions of, 197–198

Intersesamoid ligament, rupture of, 306, 307

Intracardiac shunts, MR imaging of, 36

Intracoronary stents, coronary MR angiography in, 93–94

Intracranial circulation, contrast-enhanced MR angiography of, **599–613**

Intracranial neoplasm(s), MR imaging in, 407

perfusion MR imaging in, 406–407

tumor angiogenesis in, 406

Intradural vessels, abnormal, MR angiography of, 568, 569

normal, MR angiography of, 567–568

Intramedullary arteriovenous malformation, MR angiography of, 573–575

Ischemic stroke, contrast-enhanced MR angiography in, 605–606

Isocortex, heterotypical sensory, MR microscopy of, 644

human cerebral, MR microscopy of, 641–642, 643

J

Joints, injuries of, related to sports, MR imaging in. See specific joints.

Jumper's knee, high signal in patellar tendon versus, 201

Juxta-allocortex, MR microscopy of, 646, 648

K

Kawasaki disease, assessment of, coronary MR angiography in, 89

Kearns-Sayre syndrome, diffusion tensor MR imaging in, 497, 501

Knee, chondrocalcinosis of, versus meniscal tear of, 199, 200

joint effusion in, versus iliotibial band friction syndrome, 201, 202

meniscal tear of, versus chondrocalcinosis of, 199, 200

MR imaging of, normal variants and pitfalls in, 199–201

transverse ligament of, 199, 200

L

Labrum, acetabular, variability of, 198, 199

anatomic variations in, 260

anatomy and function of, 257

glenoid, 222–223

MR imaging of, 260

posterior tear of, 227–228, 230

superior, lesions of, 231–234

rotator cuff tears in, 231

tear(s) of, classification of, 258–259

clinical features of, 257

diagnostic criteria for, 258

- secondary findings in, 259–260
- treatment of, and prognosis in, 260
- Lactate, in evaluation of brain tumors, 419, 421
- Leiomyosarcoma, cardiac, 180
- Ligamentum teres, anatomy and function of, 260
 - arthroscopy of, 261
 - derangements of, 260
 - MR imaging of, 261
- Lipids, in evaluation of brain tumors, 419, 421
- Lisfranc ligament, anatomy of, 304
 - injury of, 304–305
- Luge, injuries associated with, 316–317
- Lymph nodes, metastatic, ultrasmall superparamagnetic iron oxide contrast agent for evaluation of, 457–458
- Lymphoma(s), MR spectroscopy of, 422, 423
 - non-Hodgkin's, MR imaging in, 554, 556
 - of central nervous system, diffusion-weighted MR imaging of, 390, 391, 392
 - primary cerebral, 409–410
 - perfusion MR imaging in, 410

M

- Macroadenoma, of pituitary gland, transsphenoidal resection of, MR imaging for, 439–440
- Magnetic resonance angiography,
 - contrast-enhanced, applications of, 599–600
 - as invasive class of MR angiography, 601–602
 - clinical applications of, 605–610
 - dynamic, 603–604
 - in aneurysms, 607–608
 - in ischemic stroke, 605–606
 - in moyamoya disease, 610
 - in vascular malformations, 608–610
 - of intracranial circulation, **599–613**
 - post-contrast, 602–603
 - time-resolved approaches to, 604–605
 - when to use, 600–601
 - coronary. See *Coronary magnetic resonance angiography*.
 - 3D contrast-enhanced, 559
 - postprocessing, 564–567
 - fast 3D contrast-enhanced, 563–564
 - for evaluation of carotid arteries, 585–589
 - for evaluation of extracranial carotid arteries, 585–589
 - history of, 599
 - non-contrast-enhanced, advantages of, 600–601
 - disadvantages of, 601
 - of carotid artery atherosclerotic disease, 585
 - of extracranial circulation, **585–597**
 - of neck, for arterial dissection, 593–594
 - of spine, **559–584**
 - spinal intradural vessels on, 567–581
 - standard 3D contrast-enhanced, 559–563
 - techniques of, 599
 - using 3T scanner, 618–620
- Magnetic resonance arthrography, direct, foot and ankle sports protocols for, 296
 - of rotator cuff tears, 212
- Magnetic resonance imaging, assessment of cardiac function with, **67–80**
 - cardiac. See *Cardiac magnetic resonance imaging*.
 - cardiovascular, of myocardial perfusion. See *Myocardial perfusion, cardiovascular MR imaging of*.
 - contrast-enhanced, 8–9
 - conventional and perfusion, prediction of brain hemodynamics with, 592–593
 - diffusion tensor, 622–624. See *Diffusion tensor MR imaging*.
 - diffusion-weighted. See *Diffusion-weighted MR imaging*.
 - dynamic contrast-enhanced, 449–452
 - exercise enhancement of, 343
 - for noninvasive of atherothrombotic plaques, **101–113**
 - for transsphenoidal tumor resections, 439–440
 - functional. See *Functional magnetic resonance imaging*.
 - gadolinium enhancement of, 342–343
 - general, in congenital heart disease, 8
 - gradient echo imaging in, 342
 - high field, and phased array surface coils, 517–518
 - intraoperative, **431–447**
 - applications of, 437–443
 - biplanar magnet design, 434–435
 - cylindrical superconducting systems for, 433–434
 - devices for, 432–437
 - double-donut configuration, 433, 434
 - for brain tumor resection, 437–439
 - new developments in, 435
 - new techniques in, application in pediatric patients, **493–522**

Magnetic (*continued*)

- of arrhythmogenic right ventricular dysplasia, 10–12, 13, **163–171**
- of cardiac and pericardial malignancy, **173–186**
- of congenital heart disease, **27–48**
- of head and neck, newer techniques for, **449–469**
- of instability injuries of shoulder, **221–238**
- of joint, artifacts in, 193–194
 - magic angle phenomenon in, 194
 - truncation artifacts in, 193–194
 - variants in, related to sports injury, **193–205**
- of meniscal and cruciate ligament injuries, **283–293**
- of myocardial perfusion and viability, **49–66**
- of peripheral nerves, 550–557
 - and MR myelography of spine, **543–558**
- of sports injuries to rotator cuff, **207–219**
- of sports-related hip disorders, **255–281**
- of stress fractures, 326–331
- of thoracic aorta, **135–148**
- percutaneous interventional, 436
- perfusion. See *Perfusion magnetic resonance imaging*.
- perfusion weighted. See *Perfusion weighted MR imaging*.
- phase contrast, 68
- practical techniques for, 341–343
- real-time, 69
- report, used in clinical cardiac MR program, 25
- routine protocol for, 341–342
- sequences in, in cardiac tumors and metastatic disease, 14–15
 - in restrictive cardiomyopathy, 13–14
- spinal intradural vessels on, 567–581
- supplemental scans, 342–343
- supplemental technical developments in, 435–437
- 3T, applications of, 618
 - improving spatial resolution, 617–618
 - of healthy neonates, 620–622
 - practical considerations for, **615–639**
 - shortening data acquisition times and, 616–617
 - signal-to-noise ratio and, 615, 616–626
 - specific absorption rate and, 636–638
 - susceptibility and, basic physics of, 626–627
 - correction of effects of, 630–631
 - effects on MR images, 627–629
 - geometric distortion and, 628–629
 - phase dispersion and, 627–628
- to classify osseous stress injury, 327
 - to guide biopsy in neurosurgery, 440–441
 - using dobutamine, 73–77
- Magnetic resonance imaging program, clinical cardiac, billers in, 22
 - cardiac MR imaging report used in, 25
 - current trends in, 24–26
 - financial issues and “turf battles” in, 24–26
 - hospital-based versus private practice, 24
 - nurses in, 22
 - personnel for, 19–22
 - physicians in, 19–21
 - credentialing criteria for, 19, 20
 - reimbursement (in US) of, 22
 - codes for, 23
 - schedulers in, 22
 - setting up of, **19–26**
 - space and equipment for, 23–24
 - technologists in, 21
 - core competencies for, 21
- Magnetic resonance imaging proton spectroscopy, 458–461
- Magnetic resonance microscopy, of cerebral cortex, 642
 - of normal human brain, **641–657**
- Magnetic resonance myelography, of spine, 543–550, 551, 552
 - and MR peripheral nerve imaging, **543–558**
- Magnetic resonance plaque imaging, multicontrast, 101–102, 105–107
- Magnetic resonance spectroscopy. See *Spectroscopy, MR*.
- Magnetization transfer, HASTE, and FLAIR imaging, **471–492**
 - qualitative applications of, 473–475
 - quantitative applications of, 475–477
- Magnetoencephalography, to assess brain, 529
- Malleolus, medial, stress fractures of, 333
- Maxillary sinus, inflammation of, FLAIR in, 487
- MCA dissection(s), diffusion-weighted MR imaging in, 494, 495
 - perfusion weighted MR imaging in, 508
- Medulloblastoma, diffusion tensor MR imaging in, 497–498, 502
 - diffusion-weighted MR imaging of, 391
- Meningioma(s), diffusion-weighted MR imaging in, 384–385
 - dynamic perfusion MR imaging of, 406, 410
 - MR spectroscopy of, 422

- Meniscocapsular separation, 200
- Meniscofemoral ligaments, 199, 200
- Meniscus, injuries of, and cruciate ligament injuries, MR imaging of, **283–293**
 ossifications of, 200–201
 postoperative, 200
 tear(s) of, 284–291
 asymptomatic, 199
 mimics of, 199
- Metastases, diffusion-weighted MR imaging of, 390–391
- Metastatic tumors, perfusion MR imaging of, 409
- Metatarsal stress fracture, 306, 308
- Metathalamus, MR microscopy of, 652–654, 655
- Microscopy, MR, of cerebral cortex, 642
 of normal human brain, **641–657**
- Mitral regurgitation, causes of, 120
 measurements of, imaging modalities in, 120–123
- Mitral stenosis, causes of, 129
 cine gradient echo imaging in, 129, 130
- Molecular imaging, and MR imaging, in atherothrombotic plaques, 107–109
- Motor seizures, focal right, high field imaging with phased array surface coils showing, 517, 518
- Moyamoya disease, contrast-enhanced MR angiography in, 610
 perfusion weighted MR imaging in, 508, 512
- Multicontrast MR imaging, 101–102, 105–107
- Multiple sclerosis, FLAIR in, 482, 483
- Multivalvular regurgitation, definition of, 126
 imaging in, 125–126
- Muscle(s), and tendons, of elbow, 248
 denervation of, 362–363
 herniation of, 356–358
 imaging in, 358
 location of, 357
 symptoms and signs of, 357–358
 treatment of, 358
 injuries of, sports-related, apophyseal avulsion, 343, 344
 delayed-onset muscle soreness in, 353
 differential diagnosis of, 362, 363
 first-degree strain, 344–345, 346
 hematoma and pseudotumor
 appearance, 347–348, 349, 350
 injuries of, **341–371**
 muscle contusion in, 353–354
 myositis ossificans, 354–355
 myotendinous strain injury, 344–345, 346
 radiography and computed tomography in, 355–356
 second-degree strain, 345–347
 specific, 348–353
 third-degree strain, 347, 348
 lacerations of, 356, 357
- Musculotendinous injuries, of hip, 270–273
- Myelography, MR, of spine, 543–550, 551, 552
 of spine and MR peripheral nerve imaging, **543–558**
- Myelopathy, MR imaging in, 545, 551
- Myo-Inositol, in evaluation of brain tumors, 417, 419
- Myocardial perfusion, and viability, MR imaging of, 16–17, **49–66**
 cardiovascular MR imaging of, 49
 analysis of studies, 51–52
 clinical implications of, 52
 contrast media for, 50
 for assessment of myocardial viability, 52–62
 gadolinium contrast-enhanced, 55–61
 pharmacologic vasodilation for, 51
 technical requirements for, 49–50
- Myocardium, ischemia of, detection of, 73–75
 dobutamine MR imaging in, 73–75
 viability of, and myocardial perfusion, MR imaging of, **49–66**
 definitions of, 54
 detection of, dobutamine MR imaging in, 76–77
- Myositis ossificans, 354–356
 bone scintigraphy in, 356
 MR imaging in, 356, 357
 treatment of, 356
- Myotendinous strain injury, 344–345, 346
- Myxoma, cardiac, 14, 175–177
- N**
- Nasopharynx, squamous cell carcinoma of, proton MR spectroscopy in, 458, 459
- Navicular stress fracture(s), 306, 308, 335

- Neck. See *Head and neck*.
- Neocortex, lamination of, MR microscopy of, 642
- Neonates, healthy, 3T MR imaging of, 620–622
- Neoplasms, benign and malignant, differentiation of, proton MR spectroscopy for, 460–461
cardiac, benign, evaluation of, 175–178
evaluation of, 175
intracranial. See *Intracranial neoplasm(s)*.
of brain. See *Brain tumor(s)*.
- Nerve(s). See also specific nerves.
compression of, MR imaging in, 554–557
peripheral, injuries of, two groups of, 554
MR imaging of, 550–557
and MR myelography of spine, **543–558**
sciatic, MR imaging of, 552, 553
tibial, neurofibroma of, MR imaging in, 554, 556
- Neurofibroma, of brachial plexus, MR imaging in, 554, 555
of tibial nerve, MR imaging in, 554, 556
- Neurosurgery, in epilepsy, MR imaging guidance in, 443
MR image-guided, history of, 431
MR image-guided biopsy in, 440–441
MR image-guided functional imaging in, 441–443
- NF1, perfusion weighted MR imaging in, 508, 512
- Non-Hodgkin's lymphoma, MR imaging in, 554, 556

O

- Obsessive-compulsive disorder, psychosurgery in, 442
- Oligoastrocytoma, MR spectroscopy of, 421–422
- Oligoendroglioma, MR spectroscopy of, 421–422
- Orbital pseudotumor, FLAIR in, 485–486
- Osteitis pubis, 273
- Osteoarthritis, of hip, clinical features of, 262–263
differential diagnosis of, 264
dysplasia and, 257–258
femoroacetabular impingement in, 263
MR imaging of, 263–264
treatment of, 264
- Overuse syndromes, of elbow, epicondylitis and, 248–250

P

- Papillary fibroelastoma, 177
- Parotid gland, mapping of, in diffuse systemic connective tissue disorders, 461–463
- Patellar tendon, high signal in, versus jumper's knee, 201
- Patent ductus arteriosus, 145, 146
MR imaging in, 10, 11, 32–33, 39
vascular shunts in, 145, 146
- Pectoralis major muscle, strain injury of, 348–349, 351
- Pediatric patient(s), application of new MR techniques in, **493–522**
diffusion tensor MR imaging in, 499–503
diffusion-weighted MR imaging in, 493–499
functional MR imaging in, 515–517
perfusion weighted MR imaging in, 503–515
- Perfusion magnetic resonance imaging, basic principles and clinical applications of, **403–413**
clinical applications of, 406–411
contrast agents for, 404
dynamic contrast-enhanced, advantages of, 403
applications of, 403
image processing in, 405
in gliomas, 407–409
in intracranial neoplasms, 406–407
in meningiomas, 406, 410
in metastatic tumors, 409
in primary cerebral lymphomas, 409–410
in tumefactive demyelinating lesions, 410, 411
in tumor-mimicking lesions, 410–411
sequence consideration and imaging protocol in, 404–405
susceptibility contrast and radiotracer kinetic theory of, 403–404
technical considerations in, 403–406
technical pitfalls and limitations of, 405–406
- Perfusion weighted MR imaging, 503–515
arterial spin labeling and, 511–515
blood brain barrier permeability and, 508–511
cerebral hemodynamics and, 503–508
intravenous paramagnetic contrast techniques in, 503–511
- Periallocortex, MR microscopy of, 646, 648
- Pericardial cyst(s), 158, 159, 181
- Pericardial effusion(s), 153–154, 155, 156, 184

- Pericarditis, constrictive, clinical presentation of, 155–156, 157
 echocardiography in, 158
 imaging in, 156, 159
 versus restrictive cardiomyopathy, 12–13
 MR imaging findings in, 154, 156
- Pericardium, adhesions of, imaging in, 158
 anatomy of, 149, 150
 and heart, metastatic disease of, 181
 direct invasion of, 183
 hematogenous spread of, 182, 183
 MR imaging in, 181–182
 retrograde lymphatic extension of, 182
 transvenous extension of, 182–183
 congenital absence of, 159–161
 disease of, computed tomography in, 150–151
 echocardiography in, 149–150
 imaging of, **149–162**
 MR imaging technique in, 151–153
 hematoma of, imaging in, 154, 155
 malignancies of, 159, 160, 161
 normal, 150, 153
 thickened, imaging of, 156
- Peripheral nerve(s), injuries of, two groups of, 554
 MR imaging of, 550–557
 and MR myelography of spine, **543–558**
- Peroneus brevis splits syndrome, 300, 303
- Phase contrast magnetic resonance imaging, 68
- Phased array surface coils, high field MR imaging and, 517–518
- Pigmented villonodular synovitis, 265
- Pituitary gland, macroadenoma of, transsphenoidal resection of, MR imaging for, 439–440
- Plantar fasciitis, 300–301, 303
- Plantar nerve, impingement of, 301–302, 303
- Plantaris tendon, rupture of, with muscle strain, 352, 353
- Plaque, characterization of, using contrast agents, 105–106
- Positron emission tomography, to assess brain, 529
- Posterior cruciate ligament, injuries of, 291, 292, 293
- Posterosuperior impingement syndrome, 234
- Prosthetic valves, cine gradient echo imaging in, 132
- Proton, path length of, 379, 380
- Proton magnetic resonance spectroscopy. See *Spectroscopy, proton MR.*
- Pseudo dorsal intercalated segment instability, 197, 198
- Pseudotumors, cardiac, evaluation of, 174–175, 176
- Psychosurgery, in obsessive-compulsive disorder, 442
- Pulmonary regurgitation, causes of, 124
 MR imaging modalities in, 124–125
- Pulmonary stenosis, cine gradient echo imaging in, 129–130, 131
 congenital, MR imaging of, 34–36, 40
- Pulmonary veins, anomalous, MR imaging of, 10, 11
-
- R**
- Radial collateral ligament complex, 244–245, 247
- Radiation necrosis, delayed, perfusion MR imaging in, 408–409
- Radiculopathy, bilateral, MR imaging in, 545, 549–550
- Radiography, in sports-related muscle injuries, 355–356
 in stress fractures, 324–326
- Radionuclide imaging, of tibial stress fracture, 337–338
- Rapid gradient-echo pulse sequences, 436
- Real-time magnetic resonance imaging, 69
- Respiratory arrest, perfusion weighted MR imaging in, 507–508, 510–511
- Restrictive cardiomyopathy, constrictive pericarditis versus, 12–13
 MR imaging sequences in, 13–14
- Rhabdoid tumor, atypical teratoid, diffusion tensor MR imaging in, 497–498, 502
- Rhabdomyomas, 177
- Rhabdomyosarcoma, 180
- Rotator cuff, contusion of, 214
 injuries of, MR imaging of, 213–218

Rotator (*continued*)

- instability of, secondary impingement and, 208–209
- macrotrauma of, from contact sports, 209, 211
- normal interval, 225
- normal MR imaging appearance of, 211, 212–213
- posterior impingement of, 209
- primary impingement of, 207–208
- secondary impingement of, and instability, 208–209
- sports injuries to, categories of, 207
 - MR imaging of, **207–219**
- strain of, 214
- tear(s) of, 214
 - conventional MR imaging technique in, 210, 211–212
 - in older athlete, 211
 - in SLAP lesion, 231
 - MR arthrography of, 212
 - posterolateral impingement, 215–218
 - rim-rem, 213, 214–215
 - standard, 214
- tensile overload of, 211

S

-
- Scanner, 3T, MR angiography using, 618–620
 - Sciatic nerve, MR imaging of, 552, 553
 - Sensitivity encoding scheme, 69
 - Septic arthritis, of hip, 264
 - Shin splints, 328–329
 - Shoulder, acute traumatic instability of, 234
 - Buford complex versus labral tear of, 195
 - injuries of, in alpine skiing, 313–314
 - instability injuries of, MR imaging of, **221–238**
 - labral variability in, MR imaging of, 194
 - MR imaging of, in normal anatomy and biomechanics, 222–227
 - pathophysiology and, 227
 - strategies for, 221–222
 - muscles around, 225
 - os acromiale versus acromial fracture, 195–196
 - pain in, causes of, 207
 - postoperative, imaging of, 196
 - primary disease of, 230–231
 - sublabral hole versus labral tear of, 194–195
 - sublabral recess versus superior labrum anteroposterior lesion, 195, 196
 - Sickle cell disease, diffusion-weighted MR imaging in, 494–495, 496
 - perfusion weighted MR imaging in, 507, 509
 - Signal-to-noise ratio, 3T MR imaging and, 615, 616–626
 - Sinerem, for imaging of head and neck, 455
 - Sinus tarsi syndrome, posttraumatic, 303, 304
 - Sinusitis, frontal, and subdural empyema, diffusion tensor MR imaging in, 497–498, 503
 - Skiing, alpine (downhill), events grouped as, 311–312
 - knee injuries associated with, 312–313
 - mechanisms of injury in, 312
 - risk of injury from, 312
 - nordic (cross-country), risk of injury in, 314
 - Snapping hip syndrome, 270–271
 - MR imaging in, 271
 - Snowboarding, foot injuries associated with, 315
 - risk of injury in, 314–315
 - spinal injuries associated with, 315–316
 - upper extremity injuries in, 315, 317
 - Spectroscopy, MR, chemical shift imaging, for treatment monitoring, 425, 427
 - for treatment monitoring, 424–425, 426
 - of brain tumors, **415–429**
 - two-dimensional, to improved specificity, 426–428
 - MR preoperative, in brain tumors, 439
 - proton MR, 458–461
 - after Fourier transformation, 415, 417
 - clinical utility of, 460–461
 - for differentiation of benign from malignant neoplasms, 460–461
 - for tumor monitoring and recurrence detection, 461
 - technical background of, 458–460
 - technical challenges in, 460
 - Speedskating, injuries associated with, 318, 319–320
 - Spinal vascular imaging, noninvasive, new developments in, 559
 - Spine, intradural vessels of, MR angiography of, 567–581
 - MR imaging of, 567–581
 - MR angiography of, **559–584**
 - MR myelography of, 543–550, 551, 552
 - and MR peripheral nerve imaging, **543–558**
 - Sports injuries, hip disorders related to, MR imaging of, **255–281**

- in winter sports, 2002 Winter Olympics experience, **311–321**
of elbow, **239–253**
of foot and ankle, imaging of, **295–310**
of muscle, imaging of, **341–371**
related to joint, MR imaging of, variants in, **193–205**
to rotator cuff, MR imaging of, **207–219**
- Squamous cell carcinoma, nasopharyngeal, proton MR spectroscopy in, 458, 459
of head and neck, dynamic contrast-enhanced MR imaging in, 451, 452–453, 455–456
- Status epilepticus, diffusion-weighted MR imaging in, 496, 499
- Stents, intracoronary, coronary MR angiography in, 93–94
- Stress echocardiography, using dobutamine, 75
- Stress fracture(s), bone scintigraphy in, 332–334
clinical features of, 324
computed tomography in, 330, 331, 334
in athlete, imaging of, **323–339**
mechanism of injury in, 323–324
MR imaging of, 326–331
navicular, 306, 308, 335
of femoral neck, 336–337
of hip, 265–266
of medial malleolus, 333
pathogenesis of, 323–324
radiography in, 324–326
sites of, 335–338
tibial, 328, 329, 330, 331, 337–338
ulnar, 332
- Stress injury, osseous, MR imaging classification of, 327
- Stroke, ischemic, contrast-enhanced MR angiography in, 605–606
neonatal, diffusion tensor MR imaging in, 501, 504
perfusion weighted MR imaging in, 507
- Stroke-like episodes, diffusion-weighted MR imaging in, 495, 498
- Sublabral recess, 224
- Subthalamus, MR microscopy of, 652, 655
- Synovial (osteo)chondromatosis, idiopathic, 264–265
- Synovial plicae, 197
- Synovitis, pigmented villonodular, 265
- Syringomyelia, MR myelography in, 548, 552
- Systemic lupus erythematosus, mapping of parotid gland in, 462, 463
-
- ## T
-
- Tachycardia, ventricular outflow tract, evaluation of, MR imaging of, 166–167
technique of, 167–170
- Talar dome, osteochondral defect of, 308, 309
pseudodeflect of, 203
- Tarsal tunnel syndrome, 302–303
- Tendonitis, Achilles, 296–297
- Tendonosis, 214
- Tendons, of elbow, anatomy and pathology of, 247–252
- Tennis leg, 352
- Tetralogy of Fallot, MR imaging of, 9–10, 38–44, 45, 46
- Thalamus, MR microscopy of, 649–651, 653, 654
- Thoracic aorta, abnormalities of, 138, 139, 140–146
aneurysms of, 141, 144
MR imaging of, **135–148**
black blood techniques in, 136
contrast-enhanced angiography in, 136–137
conventional CE-MRA in, 137
phased contrast MRA in, 137
sensitivity encoding in, 137–138
simultaneous acquisition of spatial harmonics in, 137–138
T1-weighted gradient echo fat-saturated imaging in, 136
techniques of, 135–139
temporally resolved subsecond CE-MRA in, 136–137
time-resolved imaging of contrast kinetics in, 138
TrueFISP technique in, 135–136
pseudocoarctation of, 144–146
stenosis of, 142, 143, 144
- Thrombus, characterization of, using contrast agents, 106–107
- Tibia, stress fractures of, 328, 329, 330, 331
longitudinal, 337–339
- Tibial nerve, neurofibroma of, MR imaging in, 554, 556
- Tibiofibular syndesmotc injury, 300, 302

Tissue segmentation, using 3T MR imaging, 624–626

Tractography, white matter, diffusion-weighted MR imaging and, 394, 395

Transitional cortex, MR microscopy of, 646, 648

Transsphenoidal tumors, resection of, MR imaging for, 439–440

Transverse acetabular ligament, 261

Trauma X, diffusion-weighted MR imaging in, 495, 497

Triceps tendon, rupture of, 251–252

Tricuspid atresia, MR imaging of, 45, 46

Tricuspid regurgitation, evaluation of, imaging modalities in, 123–124

Trochanteric bursae, and lateral hip pain, 268–270

Trochlear groove, variations of, 197

True fast imaging with steady-state precession, 68–69
sequences in, 3, 15–16

Tumefactive demyelinating lesions, perfusion MR imaging in, 410, 411

Turf toe injury, 305, 306

U

Ulcer, atherosclerotic, 140, 144

Ulna, stress fractures of, 332

Ulnar collateral ligament, tears of, in alpine skiing, 314

Ulnar collateral ligament complex, 242

Ultrasmall superparamagnetic iron oxide contrast agent, 449, 452–458
for evaluation of metastatic lymph nodes, 457–458
for evaluation of primary tumors, 455–456

V

Valve disease, assessment of, cine MR imaging in, 116
flow-sensitive imaging technique for, 116
imaging techniques for, 115–116
qualitative and quantitative, **115–134**
spin echo and fast echo techniques for, 115–116
MR imaging in, 15, 16

Valvular regurgitation, cine gradient echo imaging in, 117–118

Vascular malformations, contrast-enhanced MR angiography in, 608–610
MR angiography of, 568–569
posttreatment, MR angiography of, 575–576, 577–582

Vascular occlusive disease, MR angiography of, 577–579

Vascular tumors, MR angiography of, 577–579

Veins, pulmonary, anomalous, MR imaging of, 10, 11

Velocity-encoded magnetic resonance imaging, 115
quantification of transvalvular pressure gradient by, 127–129

Venography, high resolution blood oxygen level dependent, 633–636

Ventricles, left, function of, assessment of, 15–16
dynamic measures of, 73–77
strain of, 72–73
volume and ejection fraction of, 69–70, 71
wall motion abnormalities of, evaluation of, 16
wall thickening of, 70–72
left and right, function at rest, measurement of, 69–73
morphology of, 29, 31
right, arrhythmogenic dysplasia of, MR imaging of, 10–12, 13, **163–171**
function of, 73

Ventricular dysplasia, arrhythmogenic right, MR imaging of, **163–171**
for evaluation, 163–166
in diagnosis, 163, 164, 165, 168
technique of, 167–170

Ventricular outflow tract tachycardia, evaluation of, MR imaging of, 166–167
technique of, 167–170

Ventricular septal defect, MR imaging of, 10, 37, 43–44

Ventricular volumes, regurgitant fraction calculations of, fast cine gradient echo in, 118

Volkman's ischemic contracture, 358–359

W

White matter tractography, diffusion-weighted
MR imaging and, 394, 395

Winter sports, injuries associated with, alpine
skiing and, 311–314
 bobsledding and, 316
 ice hockey and, 319
 luge and, 316–317

nordic (cross-country) skiing and, 314
skeletal, 317
snowboarding and, 311–314
speedskating and, 318, 319–320
study population for, 311
2002 Winter Olympics experience, **311–321**

Wrist, imaging of, normal variants and pitfalls of,
197–198